

SPECTROSCOPIC INVESTIGATION OF ATMOSPHERICALLY SIGNIFICANT
CRIEGEE INTERMEDIATES AND HYDROXYL RADICALS

Amy M. Green

A DISSERTATION

in

Chemistry

Presented to the Faculties of the University of Pennsylvania

in

Partial Fulfillment of the Requirements for the

Degree of Doctor of Philosophy

2017

Supervisor of Dissertation

Marsha I. Lester, Edmund J. Kahn Distinguished Professor

Graduate Group Chairperson

Gary A. Molander, Hirschmann-Makineni Professor of Chemistry

Dissertation Committee

Feng Gai, Edmund J. and Louise W. Kahn Endowed Term Professor of Chemistry

Andrew M. Rappe, Blanchard Professor of Chemistry

Michael R. Topp, Professor of Chemistry

SPECTROSCOPIC INVESTIGATION OF ATMOSPHERICALLY SIGNIFICANT
CRIEGEE INTERMEDIATES AND HYDROXYL RADICALS

COPYRIGHT

2017

Amy M. Green

This work is licensed under the
Creative Commons Attribution-
NonCommercial-ShareAlike 3.0
License

To view a copy of this license, visit

<http://creativecommons.org/licenses/by-nc-sa/3.0/>

To my family

ACKNOWLEDGMENT

I'd like to thank my advisor, Prof. Marsha Lester, for her patience, guidance, and support over the past several years. The opportunity to work alongside such an inspirational scientist with an unparalleled passion for research has been amazing. I also want to thank my committee, Prof. Feng Gai, Prof. Andrew Rappe, and Prof. Michael Topp for asking the hard questions.

I'd like to thank our collaborator, Dr. Stephen Klippenstein, for running the best calculations. Thank you to Prof. Patrick Walsh, Prof. William Dailey, and Prof. David Chenoweth for helpful synthesis discussions. I appreciate all the help I've received over the years from several people in the Walsh Group and Chenoweth Group, especially from: Nisalak Trongsirawat, Dr. Robert Rarig, Dr. Yitao Zhang, Dr. Sung-Eun Suh, Dr. Roy Malamakal, and Daniel Wu. Thank you to Dr. George Furst, Dr. Jun Gu, Dr. Rakesh Kohli, and Dr. Charles Ross III for helping with analysis of synthesized precursors.

I couldn't have done any of this without the friendship and many helpful discussions with past and present Lester Group members: Dr. Fang Liu, Dr. Hongwei Li, Dr. Yi Fang, Dr. Joseph Beames, Dr. Julia Lehman, Dr. Greg Drozd, Dr. Nathanael Kidwell, Dr. Barbara Marchetti, Dr. Shubhrangshu Pandit, Victoria Barber, and Mike Vansco, and Lu Lu. No quantity of cakes could express my appreciation for all of you.

Thank you to my friends and family, for their love and support. I want to thank my grandparents especially, for always listening. I was very fortunate to have several

great mentors that got me started on this path and I can't thank them enough, in particular: Pearl Raikin, Mary Engels, Prof. Christopher Abelt, and Prof. John Poutsma.

ABSTRACT

SPECTROSCOPIC INVESTIGATION OF ATMOSPHERIC OXIDANTS: CRIEGEE INTERMEDIATES AND HYDROXYL RADICALS

Amy M. Green

Marsha I. Lester

Alkene ozonolysis generates Criegee intermediates (carbonyl oxides) that decay to several products including hydroxyl (OH) radicals, the primary oxidant of trace atmospheric species. In the laboratory, an alternative method allows for efficient generation of stabilized Criegee intermediates upon photolysis of synthesized diiodo alkane precursors and reaction with O₂. Following supersonic expansion, the Criegee intermediates are photoionized with fixed vacuum ultraviolet radiation (VUV, 118 nm) and detected on their parent mass channels in a time-of-flight mass spectrometer (TOF-MS). Significant ultraviolet (UV) induced depletions of (CH₃)₂COO and CH₃CH₂CHOO photoionization signals are attributed to strong characteristic $\pi^* \leftarrow \pi$ transitions localized on the carbonyl oxide group. Using a similar approach, synthesis of a suitable precursor has enabled production of a vinyl-substituted Criegee intermediate, methylvinylketone oxide (MVK-OO), which would be formed upon isoprene ozonolysis in the atmosphere. MVK-OO is detected by VUV photoionization on the parent mass channel. OH radical products are cooled to X²Π_{3/2} (v=0) in the expansion and detected concurrently using a resonance-enhanced UV+VUV ionization scheme via the OH A²Σ⁺ (v=1) state. Another study used tunable VUV radiation generated by four-wave mixing to examine the origin

of the enhanced ionization efficiency observed for OH radicals prepared in specific $A^2\Sigma^+$ intermediate levels. The enhancement is shown to arise from resonant excitation to distinct rotational and fine structure levels of two newly identified $^2\Pi$ Rydberg states with an $A^3\Pi$ cationic core and a $3d$ electron, followed by ionization. Finally, synthesis of a partially deuterated CD_3CHI_2 precursor is used to produce selectively deuterated *syn*- CD_3CHOO Criegee intermediates in an analogous manner. Vibrational activation of *syn*- CD_3CHOO is shown to result in deuterium atom transfer and release of OD radical products. Direct time-resolved measurement of the rate of appearance of OD products reveals a 10-fold slower rate for unimolecular decay of *syn*- CD_3CHOO in the vicinity of the transition state barrier compared to *syn*- CH_3CHOO . The equivalent kinetic isotope effect of ca. 10 is attributed primarily to the decreased probability of D-atom vs. H-atom transfer arising from tunneling.

TABLE OF CONTENTS

ACKNOWLEDGMENT	iv
ABSTRACT.....	vi
LIST OF TABLES	xi
LIST OF FIGURES	xiii
Introduction.....	1
References	12
UV + VUV DOUBLE-RESONANCE STUDIES OF AUTOIONIZING RYDBERG STATES OF THE HYDROXYL RADICAL	19
I. Introduction.....	20
II. Experimental Methods.....	22
III. Results.....	24
IV Discussion	34
A. Assignments and spectroscopic constants	34
B. Deviations from Hund's case (a): Uncoupling phenomena	38
C. Comparison with fixed VUV REMPI studies	40
V. Conclusion.....	42
Acknowledgements.....	44
References	45
UV SPECTROSCOPIC CHARACTERIZATION OF DIMETHYL- AND ETHYL-SUBSTITUTED CARBONYL OXIDES	48
I. Introduction.....	49
II. Methods.....	53

III. Results.....	55
IV. Discussion	64
V. Conclusions	75
Acknowledgements.....	76
References	77

SELECTIVE DEUTERATION ILLUMINATES THE IMPORTANCE OF TUNNELING IN THE UNIMOLECULAR DECAY OF CRIEGEE INTERMEDIATES TO HYDROXYL RADICAL PRODUCTS..... 83

I. Introduction.....	84
II. Results	89
III. Discussion	99
IV. Materials and Methods.....	106
Acknowledgements.....	106
References	107

SYNTHESIS OF PRECURSORS AND EXPERIMENTAL STUDIES OF LARGER CRIEGEE INTERMEDIATES 113

I. Introduction.....	114
II. Experimental Methods.....	117
A. Synthetic Methods.....	117
B. Generation of Criegee intermediates from the corresponding precursors.....	124
III. Results and Discussion	125
IV. Future Directions	136
Acknowledgements.....	136
References	137

OBSERVATION OF AN ISOPRENE-DERIVED CRIEGEE INTERMEDIATE: METHYL VINYLKETONE OXIDE..... 141

I. Introduction.....	142
-----------------------------	------------

II. Materials and Methods	147
A. Synthesis and characterization of precursor	147
B. Generation of MVK-OO and Detection in a TOF-MS.....	152
C. Theoretical Calculations	155
III. Results and Discussion	156
IV. Conclusions and Future Directions	171
Acknowledgements.....	173
References	173
UV + VUV DOUBLE-RESONANCE STUDIES OF AUTOIONIZING RYDBERG STATES OF THE HYDROXYL RADICAL SUPPLEMENTARY MATERIAL .	180
SELECTIVE DEUTERATION ILLUMINATES THE IMPORTANCE OF TUNNELING IN THE UNIMOLECULAR DECAY OF CRIEGEE INTERMEDIATES TO HYDROXYL RADICAL PRODUCTS SUPPLEMENTARY MATERIAL	188
A. Synthesis and characterization of precursor.....	200
B. Experimental and theoretical methods	201
References	204
SYNTHESIS OF PRECURSORS AND EXPERIMENTAL STUDIES OF LARGER CRIEGEE INTERMEDIATES SUPPLEMENTARY MATERIAL	206
OBSERVATION OF AN ISOPRENE-DERIVED CRIEGEE INTERMEDIATE: METHYL VINYLKETONE OXIDE SUPPLEMENTARY MATERIAL.....	215

LIST OF TABLES

CHAPTER 2

Table 1. Spectroscopic constants derived for the OH $^2\Pi_{\text{upper}}$ ($v=0$) Rydberg state with an $A^3\Pi$ cationic core and a $3d$ electron based on the Hund's case (a) approximation 37

CHAPTER 3

Table 1. Photoionization signals for OH radicals relative to those for Criegee intermediates measured concurrently are compared with OH yields reported from ozonolysis of alkenes..... 70

Table 2. Stationary points computed along the reaction coordinate from Criegee intermediates to vinyl hydroperoxide and OH + vinoxy products using CCSD(T)/6-311+G(2d,p) 73

CHAPTER 5

Table 1. Relative intensity of photoionization signals for diiodoalkane precursors and corresponding Criegee intermediates at ca. 25 °C 131

CHAPTER 6

Table 1. Relative energies and Gibbs free energies (at 1300 K) of MVK-OO conformers calculated at the CCSD/6-311+G(d,p) level of theory, including estimated population based on a Boltzmann distribution..... 160

Table 2. Calculated vertical ionization energies at the CCSD/6-311+G(d,p) and B3LYP/6-311+G(d,p) levels of theory for each MVK-OO conformer 163

Table 3. Vertical B-X excitation energies, absorption wavelength, and transition strengths calculated at the CASPT2/aug-cc-pVTZ level of theory for each MVK-OO conformer and CH₂OO..... 166

Table 4. Relative OH yield for each Criegee intermediate observed in a TOF-MS compared to reported OH yields from ozonolysis 172

APPENDIX I

Table S1. Peak positions, FWHM, and assignments of OH Rydberg levels and VUV transitions observed from initially prepared OH $A^2\Sigma^+$ ($v'=1, J', N', F_i'$) levels via specific OH $A^2\Sigma^+ - X^2\Pi$ transitions..... 184

Table S2. Relative energies of observed $^2\Pi$ Ryd levels, sorted by rotational level (J) and parity (+/-) 187

APPENDIX II

Table S1. Fundamental harmonic and anharmonic vibrational frequencies and descriptions computed for *syn*-CD₃CDOO, *syn*-CD₃CHOO, and *anti*-CD₃CHOO in C_s symmetry..... 193

Table S2. Strongest IR transitions predicted with second order vibrational perturbation theory using B2PLYPD3/cc-pVTZ level of theory for *syn*-CD₃CDOO, *syn*-CD₃CHOO, and *anti*-CD₃CHOO from 3900 to 6300 cm⁻¹ with assignments, wavenumbers and intensities 195

Table S3. Computed harmonic and anharmonic frequencies for the transition states (TS) of *syn*-CD₃CHOO and *syn*-CD₃CDOO 196

Table S4. RRKM rates and lifetimes calculated for unimolecular decay of *syn*-CD₃CHOO and *syn*-CD₃CDOO using asymmetric Eckart or semi-classical transition state theory (SCTST) model for tunneling..... 197

APPENDIX IV

Table S1. Calculated vibrational modes for (*Z*)-1,3-diiodobut-2-ene and (*E*)-1,3-diiodobut-2-ene at the B3LYP/6-311+G(d,p) level of theory 219

LIST OF FIGURES

CHAPTER 1

Figure 1. Schematic of alkene ($R_1R_2C=CR_3R_4$) ozonolysis..... 3

CHAPTER 2

Figure 1. Tunable VUV scan accessing OH [$A^3\Pi$, $3d$] ($v=0$) Rydberg states from the OH $A^2\Sigma^+$ ($v'=1$, $J'=0.5$, $N'=0$, F_1') intermediate level with detection of OH^+ on the $m/z=17$ mass channel . 26

Figure 2. VUV spectra accessing OH [$A^3\Pi$, $3d$] ($v=0$) Rydberg states from OH $A^2\Sigma^+$ ($v'=1$, $N'=1$) intermediate levels with ($J'=0.5$, F_2') or ($J'=1.5$, F_1') and OH^+ detection..... 28

Figure 3. VUV spectra accessing OH [$A^3\Pi$, $3d$] ($v=0$) Rydberg states from OH $A^2\Sigma^+$ ($v'=1$, $N'=2$) levels with ($J'=1.5$, F_2') and ($J'=2.5$, F_1') and OH^+ detection 29

Figure 4. VUV spectra accessing OH [$A^3\Pi$, $3d$] ($v=0$) Rydberg states from OH $A^2\Sigma^+$ ($v'=1$, $N'=3$) levels with ($J'=2.5$, F_2') and ($J'=3.5$, F_1') and OH^+ detection 30

Figure 5. VUV spectrum accessing OH [$A^3\Pi$, $3d$] ($v=0$) Rydberg states from OH $A^2\Sigma^+$ ($v'=1$, $N'=4$, $J'=4.5$, F_1') level and OH^+ detection..... 31

Figure 6. Energy level diagram and assignments of observed rotational and fine structure levels, labeled with J and $+/-$, in OH $^2\Pi$ Rydberg states with an $A^3\Pi$ cationic core and a $3d$ electron.... 43

CHAPTER 3

Figure 1. Minimum energy structures for $(CH_3)_2COO$ and CH_3CH_2CHOO computed using B3LYP/6-311+G(2d,p) 56

Figure 2. Time-of-flight mass spectra for $(CH_3)_2COO$ and CH_3CH_2CHOO , separately detected at $m/z=74$, arising from single photon ionization at 118 nm 57

Figure 3. Experimental absorption spectra for jet-cooled $(CH_3)_2COO$ and CH_3CH_2CHOO derived from UV-induced depletion of the VUV ionization signals 60

Figure 4. Hydroxyl radical photoionization signals detected concurrently with the Criegee intermediates: $\text{CH}_3\text{CH}_2\text{CHOO}$, $(\text{CH}_3)_2\text{COO}$, CH_3CHOO , and CH_2OO 63

Figure 5. Reaction coordinates for decomposition of Criegee intermediates *syn*- CH_3CHOO , $(\text{CH}_3)_2\text{COO}$, and *syn*- $\text{CH}_3\text{CH}_2\text{CHOO}$ via 1,4-H shift to vinyl hydroperoxides and OH radical products..... 72

CHAPTER 4

Figure 1. Energies and geometries of stationary points along the unimolecular decay pathway from the *syn*- CD_3CHOO Criegee intermediate to OD products 85

Figure 2. Calculated anharmonic IR stick spectra for three isotopologues of the *syn* methyl-substituted Criegee intermediate at the B2PLYPD3/cc-pVTZ level of theory 90

Figure 3. Experimental IR spectral feature observed at 6055.0 cm^{-1} for *syn*- CD_3CHOO with UV LIF detection of OD products and simulated rotational band contour..... 92

Figure 4. Temporal appearance profile and fit of OD products arising from IR activation of *syn*- CD_3CHOO at 6055.0 cm^{-1} compared to the temporal profile of OH products arising from IR activation of *syn*- CH_3CHOO at 5709.0 cm^{-1} 94

Figure 5. Energy-dependent unimolecular decay rates $k(E)$ for *syn* methyl-substituted Criegee intermediates and associated kinetic isotope effects for selectively and fully deuterated systems on semi-log scales 97

Figure 6. Asymmetric Eckart potentials of the transition state critical oscillator for reaction of *syn*- CH_3CHOO and *syn*- CD_3CHOO to vinyl hydroperoxide and vinyl deuteroperoxide via 1,4 H- and D-atom transfer, respectively 101

Figure 7. Thermal decay rates $k(T)$ predicted between 200 and 350 K for *syn* methyl-substituted Criegee intermediates and associated kinetic isotope effects upon deuteration..... 105

CHAPTER 5

Figure 1. Synthesis of 1,1-diodoethane (CH_3CHI_2) from 1,1-dichloroethane (Method 1). 118

Figure 2. Synthesis of 1,1-diodoethane (CH_3CHI_2) from acetaldehyde (Method 2). 120

Figure 3. Synthesis of 2,2-diiodopropane-*d*₆ ((CD₃)₂CI₂) from acetone-*d*₆ (Method 3). 122

Figure 4. (Upper) Mass spectrum of CD₃CDI₂, (CD₃)₂CI₂, and CH₂I₂ precursors, and corresponding Criegee intermediates detected with VUV photoionization in a TOF-MS..... 129

Figure 5. Vapor pressure of 1-iodoalkanes as a function of temperature are predicted using published coefficients in the Antoine equation..... 133

CHAPTER 6

Figure 1. Summary of products and branching fractions from isoprene ozonolysis..... 144

Figure 2. Synthesis of (*Z/E*)-1,3-diiodobut-2-ene precursor from but-2-yn-1-ol..... 149

Figure 3. UV-Vis spectra for (*Z/E*)-1,3-diiodobut-2-ene and CH₂I₂ in hexanes 150

Figure 4. Schematic for generation of methylvinylketone oxide (MVK-OO) Criegee intermediates from (*Z/E*)-1,3-diiodobut-2-ene precursors 154

Figure 5. TOF mass spectrum of (*Z/E*)-1,3-diiodobut-2-ene precursor sample and corresponding MVK-OO Criegee intermediate detected with 118 nm VUV photoionization..... 158

Figure 6. Relative energies of MVK-OO conformers evaluated at the CCSD/6-311+G(d,p) level of theory and previously published *syn/anti* and *cis/trans* isomerization barriers..... 161

Figure 7. Depletions on the MVK-OO *m/z* = 86 mass channel observed at three UV wavelengths: 281 nm, 317 nm, 350 nm 165

Figure 8. Mechanism for formation of a cyclic dioxole isomer that may be formed from reaction of O₂ with iodoalkene radicals (C₄H₆I) 169

Figure 9. 1 + 1' REMPI photoionization of OH radicals detected concurrently with MVK-OO Criegee intermediates in a TOF-MS 170

APPENDIX I

Figure S1. Schematic diagram illustrating the twelve allowed transitions from the OH $A^2\Sigma^+$ ($v'=1, J'=3.5, N'=3, F_1'$) state or OH $A^2\Sigma^+$ ($v'=1, J'=2.5, N'=3, F_2'$) state to OH $^2\Pi_{\Omega}$ ($v=0$) Ryd states..... 181

Figure S2. VUV spectrum accessing OH [$A^3\Pi, 3d$] ($v=0$) Rydberg states from OH $A^2\Sigma^+$ ($v'=1, N'=4, J'=3.5, F_2'$) level with OH⁺ detection 182

Figure S3. Enhancement factors (REMPI/LIF) previously reported for main branch and satellite lines in the OH $A^2\Sigma^+$ - $X^2\Pi$ (1,0) region, accessing F_1' and F_2' fine structure levels of the OH $A^2\Sigma^+$ state 183

APPENDIX II

Figure S1. Temporal profile of OD products arising from IR excitation of the *syn*-CD₃CHOO Criegee intermediate at 6055.0 cm⁻¹ as a function of IR-UV time delay with 50 ns steps 189

Figure S2. Calculated anharmonic IR stick spectrum for *syn*- and *anti*- conformers of selectively deuterated CD₃CHOO at the B2PLYPD3/cc-pVTZ level of theory and observed experimental IR action spectral features for OH and OD products detected by LIF 190

Figure S3. Density of reactant states per cm⁻¹ for *syn*-CH₃CHOO, *syn*-CD₃CHOO and *syn*-CD₃CDOO..... 191

Figure S4. Schematic of Synthesis of 1,1-diiodoethane-2,2,2-*d*3 192

APPENDIX III

Figure S1. ¹HNMR of CH₃CHI₂ in CDCl₃..... 207

Figure S2. GC-MS (EI) of CD₃CDI₂..... 208

Figure S3. ²HNMR of CD₃CDI₂ in CHCl₃..... 209

Figure S4. ¹HNMR of (CH₃)₂CI₂ in CDCl₃..... 210

Figure S5. GC-MS (EI) of $(\text{CD}_3)_2\text{Cl}_2$	211
Figure S6. $^1\text{HNMR}$ of $(\text{CD}_3)_2\text{Cl}_2$ in CDCl_3	212
Figure S7. $^1\text{HNMR}$ of $\text{CH}_3\text{CH}_2\text{CHI}_2$ in CDCl_3	213
Figure S8. $^1\text{HNMR}$ of $(\text{CH}_3\text{CH}_2)(\text{CH}_3)\text{Cl}_2$ in CDCl_3	214

APPENDIX IV

Figure S1. $^1\text{HNMR}$ of (Z/E) -1,3-diiodobut-2-ene mixture in CDCl_3 indicates a 5:1 ratio of $Z:E$ conformers.	216
Figure S2. FTIR spectrum of (Z) -1,3-diiodobut-2-ene and (E) -1,3-diiodobut-2-ene mixture from 400-3200 cm^{-1}	217
Figure S3. (Z) -1,3-diiodobut-2-ene and (E) -1,3-diiodobut-2-ene precursor geometries with number labeling of atoms.....	218

CHAPTER 1

Introduction

Hydroxyl radicals (OH) play an important role in the oxidative removal of trace atmospheric species and are often called the atmosphere's "detergent."¹ OH radicals are constantly being generated and consumed and this results in a low atmospheric steady state concentration of approximately 10^5 - 10^6 molecules cm^{-3} .^{1,2} Daytime production of OH in pristine environments is dominated by photolysis of ozone to form $\text{O}(^1\text{D})$ which undergoes subsequent reaction with water:¹



In polluted environments with high NO_x concentrations, another important source of hydroxyl radical is photolysis of nitrous acid:¹



Unlike reactions (1a,1b) and (2), alkene ozonolysis is a non-photolytic source of OH radicals. Field measurements from the 2003 TORCH campaign in London and the 1999-2000 PUMA campaign in Birmingham indicate that alkene ozonolysis is responsible for nearly a third of OH production in the daytime,³ and nearly all of OH generated under low light conditions such as nighttime or wintertime.^{4,5}

Emissions of smaller alkenes such as ethylene, propylene, and butenes are on the order of 30-60 Tg/yr and originate primarily from anthropogenic sources (i.e. fossil fuel use or biomass burning).⁶ In comparison, emissions of larger alkenes such as isoprene, pinene, and limonene are primarily from biogenic sources (i.e. foliar emissions).^{6,7}

Isoprene is the most abundant non-methane volatile organic compound in the atmosphere.⁷

Ozonolysis proceeds via addition of ozone across a C=C double bond of an alkene ($R_1R_2C=CR_3R_4$) in a highly exothermic process ($\sim 50 \text{ kcal mol}^{-1}$) that forms an energized primary ozonide, as shown in Figure 1.² The ozonide rapidly decomposes to produce a carbonyl compound and corresponding carbonyl oxide species (R_1R_2COO or R_3R_4COO), called the Criegee intermediate. The resultant Criegee intermediate is generated with high internal excitation and can decay to several products including OH radical.⁸⁻¹⁰ The OH yield from alkene ozonolysis increases with increasing substitution, approaching unity for highly branched alkenes such as 2,3-dimethyl-2-butene.^{1, 11} A portion of the Criegee intermediates may be collisionally stabilized¹²⁻¹⁴ and undergo subsequent bimolecular reaction,¹⁵⁻¹⁹ thermalized unimolecular decay,²⁰⁻²² or solar photolysis to produce other atmospherically important species.^{23, 24} Criegee intermediates have also been implicated in the generation of aerosols,^{25, 26} which have a significant impact on global climate.²⁷

Monoalkyl substituted Criegee intermediates such as CH_3CHOO have two configurations, *syn* and *anti*, separated by a substantial interconversion barrier.⁹ The more stable *syn* alkyl-substituted conformer contains an alkyl group on the same side of the carbonyl as the terminal oxygen and exhibits an intramolecular interaction between an α -hydrogen and terminal oxygen, which has a stabilizing effect.²⁴ The dominant atmospheric loss process for a prototypical *syn* alkyl-substituted Criegee intermediate (i.e. *syn*- CH_3CHOO) is an intramolecular 1,4 H-atom transfer mechanism to a vinyl

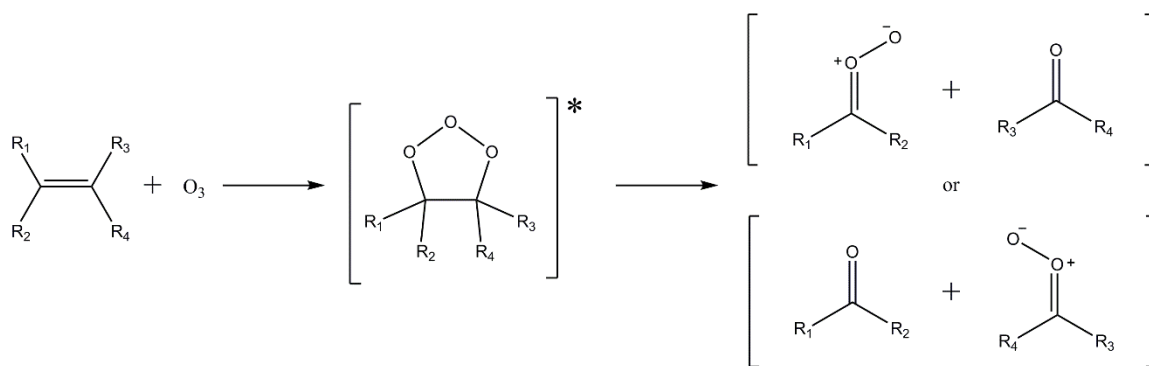


Figure 1. Schematic of alkene ($R_1R_2C=CR_3R_4$) ozonolysis. Addition of O_3 produces an energized primary ozonide which undergoes prompt decomposition by breaking the C-C bond and either O-O bond to yield one of two possible Criegee intermediates (R_1R_2COO or R_3R_4COO) and the corresponding carbonyl coproduct (R_3R_4CO or R_1R_2CO).

hydroperoxide (VHP) species which undergoes unimolecular decay to OH + vinyloxy radical products.^{12, 28, 29} Stabilized *anti*-CH₃CHOO and the simplest Criegee intermediate, CH₂OO, are primarily removed from the atmosphere via reaction with water dimer.^{16, 17, 19}

Ozonolysis reaction rate constants range from ca. 10⁻¹⁸ cm³ molecule⁻¹ s⁻¹ for the simplest alkene ethylene³⁰ to 10⁻¹⁵ cm³ molecule⁻¹ s⁻¹ for highly branched alkenes such as 2,3-dimethyl-2-butene³¹ under atmospheric conditions. Despite conformer dependence, several bimolecular processes of Criegee intermediates with trace atmospheric species, such as water dimer or SO₂, have reaction rate constants that are orders of magnitude larger than that of ozonolysis.^{17, 19, 32, 33} Due to the slow ozonolysis reaction rate and several rapid processes that remove the Criegee intermediate population, the steady-state concentration of Criegee intermediates is estimated to be extremely low (ca. 10³-10⁶ molecules cm⁻³), making them difficult to detect.³⁴

Direct detection of the simplest Criegee intermediate (CH₂OO) generated from ethylene ozonolysis has been observed via Fourier transform microwave (FTMW) spectroscopy.³⁵ Criegee intermediates generated from ozonolysis of β-pinene, a larger branched alkene, have been directly observed by Fourier transform infrared (FTIR) spectroscopy.³⁶

Observation of Criegee intermediates generated from alkene ozonolysis in the laboratory has largely relied on indirect methods with scavenger species such as hexafluoroacetone, 5,5-dimethyl-pyrroline *N*-oxide (DMPO) or acetic acid.³⁷⁻³⁹ Reaction of Criegee intermediates with these scavengers forms covalent bonds and generate a

stable adduct, which is then analyzed by FTIR, electron paramagnetic resonance, proton-transfer reaction mass spectrometry, or chemical ionization mass spectrometry (CIMS).³⁷⁻

39

Major advancements in the study of Criegee intermediates are largely due to an alternative synthetic method using geminal diiodoalkane precursors such as CH_2I_2 .⁴⁰



Laser photolysis of the precursor $\text{R}_1\text{R}_2\text{CI}_2$ results in C-I bond dissociation.⁴¹ Dissociation of the C-I bond also occurs in an electric discharge source.^{42, 43} In both cases, a monoiodoalkyl radical is formed and the remaining iodine is displaced by O_2 to produce a Criegee intermediate. A portion of the newly formed Criegee intermediates may be collisional stabilized and studied. Due to the internal excitation of the monoiodoalkyl radical,⁴¹ the remaining energized Criegee intermediates will promptly decay to products, such as OH radicals.

Many research groups have coupled this alternative synthetic method with direct detection techniques such as UV absorption,^{33, 44} cavity ring-down spectroscopy,²⁰ FTIR spectroscopy,^{45, 46} and FTMW spectroscopy^{42, 43, 47, 48} for conformational and kinetic studies of Criegee intermediates. This laboratory has implemented the alternative synthesis in a quartz capillary reactor coupled with a supersonic expansion to prepare collisionally stabilized, jet-cooled Criegee intermediates that are detected by vacuum ultraviolet (VUV) photoionization in a time-of-flight mass spectrometer (TOF-MS). Synthesis of a series of alkyl-substituted Criegee intermediate precursors, $\text{R}_1\text{R}_2\text{CI}_2$, has

allowed for the characterization and study of R_1R_2COO Criegee intermediates with different R_1 and R_2 alkyl groups, including $-H$, $-CH_3$ and $-CH_2CH_3$.

A recent sensitive and state-selective ionization method has been developed for detection of the OH radical that utilizes UV excitation on the $A^2\Sigma^+-X^2\Pi$ transition followed by fixed 118 nm VUV radiation to access autoionizing Rydberg states.^{49, 50} In **Chapter 2**, tunable VUV radiation generated by four-wave mixing is used to examine the origin of the enhanced ionization efficiency observed for OH radicals prepared in specific $A^2\Sigma^+$ intermediate levels. The enhancement is shown to arise from resonant excitation to distinct rotational and fine structure levels of two newly identified $^2\Pi$ Rydberg states with an $A^3\Pi$ cationic core and a $3d$ electron followed by ionization. Spectroscopic constants are derived and effects due to uncoupling of the Rydberg electron are revealed for the OH $^2\Pi$ Rydberg states. The linewidths indicate a Rydberg state lifetime due to autoionization on the order of a picosecond.

The UV + VUV double-resonance OH detection scheme described in **Chapter 2** has been coupled with methods which allow for further ion manipulation of hydroxyl radicals and provide mass selectivity. This technique has been applied to concurrent detection of OH products following unimolecular decay of energized Criegee intermediates generated from diiodoalkane precursors, to show that increased alkylation is correlated with increased OH yield.²⁴ In this group, velocity map imaging (VMI) of OH radicals following IR-activation of Criegee intermediates has shown an isotropic angular distribution of OH products indicative of slow unimolecular decay relative to the rotational period.^{51, 52} Most recently, this ionization scheme has been coupled with a

Stark decelerator and used to characterize the spatial density distribution of OH radicals in a trap.⁵³

In **Chapter 3**, dimethyl- and ethyl-substituted Criegee intermediates, $(\text{CH}_3)_2\text{COO}$ and $\text{CH}_3\text{CH}_2\text{CHOO}$, are photolytically generated from diiodo precursors, detected by VUV photoionization at 118 nm, and spectroscopically characterized via UV-induced depletion of the $m/z = 74$ signals under jet-cooled conditions. In each case, UV excitation resonant with the B–X transition results in significant ground-state depletion, reflecting the large absorption cross section and rapid dynamics in the excited B state. The broad UV absorption spectra of both $(\text{CH}_3)_2\text{COO}$ and $\text{CH}_3\text{CH}_2\text{CHOO}$ peak at ~ 320 nm with absorption cross sections approaching $\sim 4 \times 10^{-17} \text{ cm}^2 \text{ molec}^{-1}$. The UV absorption spectra for $(\text{CH}_3)_2\text{COO}$ and $\text{CH}_3\text{CH}_2\text{CHOO}$ are similar to that reported previously for *syn*- CH_3CHOO , suggesting analogous intramolecular interactions between the α -H and terminal O of the COO groups. Hydroxyl radical products generated concurrently with the Criegee intermediates are detected by $1 + 1'$ resonance enhanced multiphoton ionization, as described in **Chapter 2**. The OH signals, scaled relative to those for the Criegee intermediates, are compared with prior studies of OH yield from alkene ozonolysis. The stationary points along the reaction coordinates from the alkyl-substituted Criegee intermediates to vinyl hydroperoxides and OH products are also computed to provide insight on the OH yields.

The benchmark UV studies of $(\text{CH}_3)_2\text{COO}$ and $\text{CH}_3\text{CH}_2\text{CHOO}$ presented in **Chapter 3** as well as previous UV studies in this group of CH_3CHOO ²⁴ and CH_2OO ²³ have been followed by several direct UV absorption studies.^{44, 54-56} The characteristic

strong UV absorption has become a standard method to directly monitor Criegee intermediates for kinetic studies in the laboratory.^{17, 20, 33, 44, 54}

Concurrent detection of Criegee intermediates and OH products has led to a series of experiments regarding the unimolecular decay of Criegee intermediates. Ground state alkyl-substituted Criegee intermediates are IR-activated to induce a 1,4 H-atom transfer to form a vinyl hydroperoxide (VHP) species which decays to OH products detected via laser-induced fluorescence (LIF).^{57, 58} Observation of OH at excitation energies in the vicinity of the isomerization barrier match statistical RRKM calculations when tunneling is taken into account.^{28, 29} OH radicals observed following IR excitation at energies well below the barrier are classically forbidden, further supporting the importance of tunneling in the unimolecular decay of Criegee intermediates.^{59, 60} However, the typical test to verify tunneling is via deuteration.

Ozonolysis of alkenes, an important nonphotolytic source of hydroxyl (OH) radicals in the atmosphere, proceeds through unimolecular decay of Criegee intermediates. In **Chapter 4**, we report a large kinetic isotope effect associated with the rate-limiting hydrogen transfer step that releases OH radicals for a prototypical Criegee intermediate, CH₃CHOO. IR excitation of selectively deuterated *syn*-CD₃CHOO is shown to result in deuterium atom transfer and release OD radical products. Vibrational activation of *syn*-CD₃CHOO is coupled with direct time-resolved detection of OD products to measure a 10-fold slower rate of unimolecular decay upon deuteration in the vicinity of the transition state barrier, which is confirmed by microcanonical statistical theory that incorporates quantum mechanical tunneling. The equivalent kinetic isotope

effect of ca. 10 is attributed primarily to the decreased probability of D-atom vs. H-atom transfer arising from tunneling. Master equation modeling is utilized to compute the thermal unimolecular decay rates for selectively and fully deuterated *syn* methyl-substituted Criegee intermediates under atmospheric conditions. At 298 K (1 atm), tunneling is predicted to enhance the thermal decay rate of *syn*-CH₃CHOO to OH radicals by a factor of 100 and result in a significant kinetic isotope effect of ca. 50 upon deuteration.

Recent spectroscopic and dynamical investigations of Criegee intermediates in this laboratory^{24, 28, 29, 51, 57-59, 61-63} have relied on the alternative synthetic method utilizing non-commercial diiodoalkane precursors (i.e. CD₃CHI₂, (CH₃)₂CI₂, CH₃CH₂CHI₂).

Chapter 5 details methods and lessons learned in synthesis of geminal diiodoalkane precursors with different substituent groups based on the methods of Pross and Sternhell⁶⁴ and Friedrich et. al.⁶⁵ The general procedures of these two methods involves two steps: (1) generation of a hydrazone species from a ketone or aldehyde and (2) oxidation of the hydrazone species by iodine. A third method developed by Letsinger and Kammeyer⁶⁶ was found to be efficient for the generation of 1,1-diodoethane (CH₃CHI₂) from 1,1-dichloroethane. The investigation of Criegee intermediates with increasing number of carbons requires utilizing diiodoalkane precursors with greater mass and lower vapor pressure.⁶⁷ The reduction in photoionization signal of both precursor and Criegee intermediate mass channels with increasing molecular mass is attributed to the decrease in vapor pressure. This can be overcome by heating the precursor sample.

The most important non-methane volatile organic compound emitted into the atmosphere is isoprene (ca. 500 Tg/yr).^{6, 7} Nearly 90% of isoprene emissions are from biogenic sources.⁷ An important process in the oxidative removal of atmospheric isoprene is rapid addition of OH to a C=C double bond (rate constant of ca. 10^{-10} cm³ molecule⁻¹ s⁻¹).⁶⁸ Another significant oxidative process is ozonolysis.⁷ Isoprene ozonolysis has a slow reaction rate constant (ca. 10^{-18} cm³ molecule⁻¹ s⁻¹) relative to OH addition.⁶⁸ However, the sheer abundance of both isoprene (2 ppb or 5×10^{11} molecules cm⁻³) and ozone (20 ppb or 5×10^{11} molecules cm⁻³) makes understanding isoprene ozonolysis and subsequent decay of the corresponding Criegee intermediates crucial to understanding fundamental atmospheric chemistry.^{7, 69} According to a global atmospheric model, over 60% of stabilized Criegee intermediates in the troposphere are due to ozonolysis of isoprene (and subsequent ozonolysis of resultant isoprene ozonolysis products, such as methylvinylketone and methacrolein).⁷⁰ There has been no prior study in which a four-carbon isoprene-derived Criegee intermediate has been directly detected.

Addition of ozone to one of two possible double bonds of isoprene (2-methyl-1,3-butadiene, CH₂=C(CH₃)-CH=CH₂) may yield three possible Criegee intermediates: formaldehyde oxide (CH₂OO), methacrolein oxide (MACR-OO, CH₃(CH₂=)CCH(OO)), and methylvinylketone oxide (MVK-OO, CH₂=CHC(CH₃)OO). Isoprene ozonolysis is predicted to have a substantial branching fraction to MVK-OO.⁷¹ **Chapter 6** describes the synthesis of a diiodobutene precursor suitable for generation of the MVK-OO Criegee intermediate. Generation of MVK-OO from the diiodobutene precursor is similar to the previously described method.⁴⁰ Photolysis of a *Z/E*-1,3-

diiodobut-2-ene species will break the weak allylic C-I bond and produce an allylic monoiodoalkene radical species.⁷² The monoiodoalkene radical species has two resonance structures, the more stable of which will generate MVK-OO upon reaction with O₂. Collaboration with Prof. Patrick Walsh and his group has resulted in the successful synthesis this diiodoalkene precursor. This alternative synthetic method is demonstrated to generate stabilized MVK-OO. Detection of MVK-OO is achieved on the parent mass channel in a TOF-MS with 118 nm VUV photoionization. UV-induced depletion of the ground state population, resulting in a decrease in the photoionization signal suggests that MVK-OO has a characteristic strong UV absorption, similar to previously studied Criegee intermediates.^{23, 24, 62} Due to the presence of a methyl group and a vinyl group, MVK-OO has four conformers, each with different peak absorption between ca. 350 nm and 400 nm based on theoretical predictions. Depletion of the ground state population upon 350 nm UV excitation is attributed to a strong $\pi^* \leftarrow \pi$ transition. Previous theoretical calculations^{9, 73} predict that the two *syn* conformers of MVK-OO, in which the methyl group is on the same side of the carbonyl as the terminal oxygen, may yield OH products, as has been observed for other *syn* alkyl-substituted Criegee intermediates.^{28, 29, 57, 58} Concurrent observation of OH products is indicative of unimolecular decay of energized MVK-OO. This work is promising for future spectroscopic, kinetic, and dynamic studies of isoprene-derived Criegee intermediates.

References

- ¹ B. J. Finlayson-Pitts, and J. N. Pitts, *Chemistry of the Upper and Lower Atmosphere* (Academic Press, San Diego, 2000).
- ² D. Johnson, and G. Marston, *Chem. Soc. Rev.* **37**, 699 (2008).
- ³ K. M. Emmerson, N. Carslaw, D. C. Carslaw, J. D. Lee, G. McFiggans, W. J. Bloss, T. Gravesstock, D. E. Heard, J. Hopkins, T. Ingham, M. J. Pilling, S. C. Smith, M. Jacob, and P. S. Monks, *Atmos. Chem. Phys.* **7**, 167 (2007).
- ⁴ R. M. Harrison, J. Yin, R. M. Tilling, X. Cai, P. W. Seakins, J. R. Hopkins, D. L. Lansley, A. C. Lewis, M. C. Hunter, D. E. Heard, L. J. Carpenter, D. J. Creasey, J. D. Lee, M. J. Pilling, N. Carslaw, K. M. Emmerson, A. Redington, R. G. Derwent, D. Ryall, G. Mills, and S. A. Penkett, *Sci. Total. Environ.* **360**, 5 (2006).
- ⁵ K. M. Emmerson, and N. Carslaw, *Atmos. Environ.* **43**, 3220 (2009).
- ⁶ J. O. Nriagu, *Gaseous pollutants: Characterization and cycling* (John Wiley & Sons, Inc, New York, 1992), Vol. 24.
- ⁷ F. Pacifico, S. P. Harrison, C. D. Jones, and S. Sitch, *Atmos. Environ.* **43**, 6121 (2009).
- ⁸ J. H. Kroll, S. R. Sahay, J. G. Anderson, K. L. Demerjian, and N. M. Donahue, *J. Phys. Chem. A* **105**, 4446 (2001).
- ⁹ K. T. Kuwata, M. R. Hermes, M. J. Carlson, and C. K. Zogg, *J. Phys. Chem. A* **114**, 9192 (2010).
- ¹⁰ C. Yin, and K. Takahashi, *Phys. Chem. Chem. Phys.* **19**, 12075 (2017).
- ¹¹ IUPAC, IUPAC Subcommittee on Gas Kinetic Data Evaluation. Data Sheet Ox_VOC3, 2005, http://iupac.pole-ether.fr/htdocs/datasheets/pdf/Ox_VOC3_O3_alkene.pdf.

- ¹²G. T. Drozd, T. Kurten, N. M. Donahue, and M. I. Lester, *J. Phys. Chem. A* **121**, 6036 (2017).
- ¹³J. P. Hakala, and N. M. Donahue, *J. Phys. Chem. A* **120**, 2173 (2016).
- ¹⁴A. Novelli, L. Vereecken, J. Lelieveld, and H. Harder, *Phys. Chem. Chem. Phys.* **16**, 19941 (2014).
- ¹⁵R. L. Mauldin III, T. Berndt, M. Sipila, P. Paasonen, T. Petaja, S. Kim, T. Kurten, F. Stratmann, V. M. Kerminen, and M. Kulmala, *Nature* **488**, 193 (2012).
- ¹⁶L.-C. Lin, H.-T. Chang, C.-H. Chang, W. Chao, M. C. Smith, C.-H. Chang, J. Jr-Min Lin, and K. Takahashi, *Phys. Chem. Chem. Phys.* **18**, 4557 (2016).
- ¹⁷W. Chao, J.-T. Hsieh, C.-H. Chang, and J. J.-M. Lin, *Science* **347**, 751 (2015).
- ¹⁸H.-L. Huang, W. Chao, and J. J.-M. Lin, *Proc. Natl. Acad. Sci.* **112**, 10857 (2015).
- ¹⁹T. R. Lewis, M. A. Blitz, D. E. Heard, and P. W. Seakins, *Phys. Chem. Chem. Phys.* **17**, 4859 (2015).
- ²⁰R. Chhantyal-Pun, O. Welz, J. D. Savee, A. J. Eskola, E. P. F. Lee, L. Blacker, H. R. Hill, M. Ashcroft, M. A. H. Khan, G. C. Lloyd-Jones, L. Evans, B. Rotavera, H. Huang, D. L. Osborn, D. K. W. Mok, J. M. Dyke, D. E. Shallcross, C. J. Percival, A. J. Orr-Ewing, and C. A. Taatjes, *J. Phys. Chem. A* **121**, 4 (2017).
- ²¹T.-N. Nguyen, R. Putikam, and M. C. Lin, *J. Chem. Phys.* **142**, 124312 (2015).
- ²²M. C. Smith, W. Chao, K. Takahashi, K. A. Boering, and J. J.-M. Lin, *J. Phys. Chem. A* **120**, 4789 (2016).
- ²³J. M. Beames, F. Liu, L. Lu, and M. I. Lester, *J. Am. Chem. Soc.* **134**, 20045 (2012).
- ²⁴J. M. Beames, F. Liu, L. Lu, and M. I. Lester, *J. Chem. Phys.* **138**, 244307 (2013).

- ²⁵ J. H. Kroll, and J. H. Seinfeld, *Atmos. Environ.* **42**, 3593 (2008).
- ²⁶ C. J. Percival, O. Welz, A. J. Eskola, J. D. Savee, D. L. Osborn, D. O. Topping, D. Lowe, S. R. Utembe, A. Bacak, G. M c Figgans, M. C. Cooke, P. Xiao, A. T. Archibald, M. E. Jenkin, R. G. Derwent, I. Riipinen, D. W. K. Mok, E. P. F. Lee, J. M. Dyke, C. A. Taatjes, and D. E. Shallcross, *Farad. Discuss.* **165**, 45 (2013).
- ²⁷ M. C. Jacobson, H. C. Hansson, K. J. Noone, and R. J. Charlson, *Rev. Geophys.* **38**, 267 (2000).
- ²⁸ Y. Fang, F. Liu, V. P. Barber, S. J. Klippenstein, A. B. McCoy, and M. I. Lester, *J. Chem. Phys.* **144**, 061102 (2016).
- ²⁹ Y. Fang, F. Liu, S. J. Klippenstein, and M. I. Lester, *J. Chem. Phys.* **145**, 044312 (2016).
- ³⁰ M. S. Alam, M. Camredon, A. R. Rickard, T. Carr, K. P. Wyche, K. E. Hornsby, P. S. Monks, and W. J. Bloss, *Phys. Chem. Chem. Phys.* **13**, 11002 (2011).
- ³¹ A. A. Presto, and N. M. Donahue, *J. Phys. Chem. A* **108**, 9096 (2004).
- ³² C. A. Taatjes, O. Welz, A. J. Eskola, J. D. Savee, A. M. Scheer, D. E. Shallcross, B. Rotavera, E. P. F. Lee, J. M. Dyke, D. K. W. Mok, D. L. Osborn, and C. J. Percival, *Science* **340**, 177 (2013).
- ³³ L. Sheps, A. M. Scully, and K. Au, *Phys. Chem. Chem. Phys.* **16**, 26701 (2014).
- ³⁴ A. Novelli, K. Hens, C. Tatum Ernest, M. Martinez, A. C. Nölscher, V. Sinha, P. Paasonen, T. Petäjä, M. Sipilä, T. Elste, C. Plass-Dülmer, G. J. Phillips, D. Kubistin, J. Williams, L. Vereecken, J. Lelieveld, and H. Harder, *Atmos. Chem. Phys.* **17**, 7807 (2017).

- ³⁵ C. C. Womack, M.-A. Martin-Drumel, G. G. Brown, R. W. Field, and M. C. McCarthy, *Sci. Adv.* **1**, (2015).
- ³⁶ J. Ahrens, P. T. M. Carlsson, N. Hertl, M. Olzmann, M. Pfeifle, J. L. Wolf, and T. Zeuch, *Angew. Chem.* **53**, 715 (2014).
- ³⁷ G. T. Drozd, J. Kroll, and N. M. Donahue, *J. Phys. Chem. A* **115**, 161 (2011).
- ³⁸ C. Giorio, S. J. Campbell, M. Bruschi, F. Tampieri, A. Barbon, A. Toffoletti, A. Tapparo, C. Paijens, A. J. Wedlake, P. Grice, D. J. Howe, and M. Kalberer, *J. Am. Chem. Soc.* **139**, 3999 (2017).
- ³⁹ R. Yajima, Y. Sakamoto, S. Inomata, and J. Hirokawa, *J. Phys. Chem. A* **Accepted**, (2017).
- ⁴⁰ O. Welz, J. D. Savee, D. L. Osborn, S. S. Vasu, C. J. Percival, D. E. Shallcross, and C. A. Taatjes, *Science* **335**, 204 (2012).
- ⁴¹ J. H. Lehman, H. Li, and M. I. Lester, *Chem. Phys. Lett.* **590**, 16 (2013).
- ⁴² M. Nakajima, and Y. Endo, *J. Chem. Phys.* **140**, 011101 (2014).
- ⁴³ M. Nakajima, and Y. Endo, *J. Chem. Phys.* **139**, 101103 (2013).
- ⁴⁴ M. C. Smith, W.-L. Ting, C.-H. Chang, K. Takahashi, K. A. Boering, and J. J.-M. Lin, *J. Chem. Phys.* **141**, 074302 (2014).
- ⁴⁵ H.-Y. Lin, Y.-H. Huang, X. Wang, J. M. Bowman, Y. Nishimura, H. A. Witek, and Y.-P. Lee, *Nat. Commun.* **6**, 7012 (2015).
- ⁴⁶ Y.-T. Su, Y.-H. Huang, H. A. Witek, and Y.-P. Lee, *Science* **340**, 174 (2013).
- ⁴⁷ C. Cabezas, J.-C. Guillemin, and Y. Endo, *J. Chem. Phys.* **145**, 224314 (2016).
- ⁴⁸ C. Cabezas, J.-C. Guillemin, and Y. Endo, *J. Chem. Phys.* **146**, 174304 (2017).

- ⁴⁹ J. M. Beames, F. Liu, and M. I. Lester, *Mol. Phys.* **112**, 897 (2014).
- ⁵⁰ J. M. Beames, F. Liu, M. I. Lester, and C. Murray, *J. Chem. Phys.* **134**, 241102 (2011).
- ⁵¹ N. M. Kidwell, H. Li, X. Wang, J. M. Bowman, and M. I. Lester, *Nat. Chem.* **8**, 509 (2016).
- ⁵² H. Li, N. Kidwell, X. Wang, J. Bowman, and M. I. Lester, **145**, 104307 (2016).
- ⁵³ J. M. Gray, J. A. Bossert, Y. Shyur, and H. J. Lewandowski, *Phys. Rev. A* **96**, 023416 (2017).
- ⁵⁴ L. Sheps, *Phys. Chem. Lett.* **4**, 4201 (2013).
- ⁵⁵ Y.-P. Chang, C.-H. Chang, K. Takahashi, and J. J.-M. Lin, *Chem. Phys. Lett.* **653**, 155 (2016).
- ⁵⁶ W.-L. Ting, Y.-H. Chen, W. Chao, M. C. Smith, and J. J.-M. Lin, *Phys. Chem. Chem. Phys.* **16**, 10438 (2014).
- ⁵⁷ F. Liu, J. M. Beames, and M. I. Lester, *J. Chem. Phys.* **141**, 234312 (2014).
- ⁵⁸ F. Liu, J. M. Beames, A. S. Petit, A. B. McCoy, and M. I. Lester, *Science* **345**, 1596 (2014).
- ⁵⁹ Y. Fang, F. Liu, V. P. Barber, S. J. Klippenstein, A. B. McCoy, and M. I. Lester, *J. Chem. Phys.* **145**, 234308 (2016).
- ⁶⁰ Y. Fang, V. P. Barber, S. J. Klippenstein, A. B. McCoy, and M. I. Lester, *J. Chem. Phys.* **146**, 134307 (2017).
- ⁶¹ H. Li, Y. Fang, N. M. Kidwell, J. M. Beames, and M. I. Lester, *J. Phys. Chem. A* **119**, 8328 (2015).

- ⁶² F. Liu, J. M. Beames, A. M. Green, and M. I. Lester, *J. Phys. Chem. A* **118**, 2298 (2014).
- ⁶³ F. Liu, Y. Fang, M. Kumar, W. H. Thompson, and M. I. Lester, *Phys. Chem. Chem. Phys.* **17**, 20490 (2015).
- ⁶⁴ A. Pross, and S. Sternhell, *Aust. J. Chem.* **23**, 989 (1970).
- ⁶⁵ E. C. Friedrich, S. N. Falling, and D. E. Lyons, *Synth. Commun.* **5**, 33 (1975).
- ⁶⁶ R. L. Letsinger, and C. W. Kammeyer, *J. Am. Chem. Soc.* **73**, 4476 (1951).
- ⁶⁷ N. M. Donahue, S. A. Epstein, S. N. Pandis, and A. L. Robinson, *Atmos. Chem. Phys.* **11**, 3303 (2011).
- ⁶⁸ M. Karl, T. Brauers, H. P. Dorn, F. Holland, M. Komenda, D. Poppe, F. Rohrer, L. Rupp, A. Schaub, and A. Wahner, *Geophys. Res. Lett.* **31**, (2004).
- ⁶⁹ J. Lelieveld, T. M. Butler, J. N. Crowley, T. J. Dillon, H. Fischer, L. Ganzeveld, H. Harder, M. G. Lawrence, M. Martinez, D. Taraborrelli, and J. Williams, *Nature* **452**, 737 (2008).
- ⁷⁰ J. R. Pierce, M. J. Evans, C. E. Scott, S. D. D'Andrea, D. K. Farmer, E. Swietlicki, and D. V. Spracklen, *Atmos. Chem. Phys.* **13**, 3163 (2013).
- ⁷¹ T. B. Nguyen, G. S. Tyndall, J. D. Crouse, A. P. Teng, K. H. Bates, R. H. Schwantes, M. M. Coggon, L. Zhang, P. Feiner, D. O. Miller, K. M. Skog, J. C. Rivera-Rios, M. Dorris, K. F. Olson, A. Koss, R. J. Wild, S. S. Brown, A. H. Goldstein, J. A. de Gouw, W. H. Brune, F. N. Keutsch, J. H. Seinfeld, and P. O. Wennberg, *Phys. Chem. Chem. Phys.* **18**, 10241 (2016).
- ⁷² N. Isaacs, *Physical Organic Chemistry* (Longman Scientific & Technical, 1995).

⁷³ K. T. Kuwata, L. C. Valin, and A. D. Converse, *J. Phys. Chem. A* **109**, 10725 (2005).

CHAPTER 2

UV + VUV double-resonance studies of autoionizing Rydberg states of the hydroxyl radical

This research has been published in the *Journal of Chemical Physics*, **144**, 184311 (2016). The research and was performed with postdoctoral researcher Dr. Fang Liu and Prof. Marsha I. Lester in the *Department of Chemistry, University of Pennsylvania*.

I. Introduction

The hydroxyl radical (OH) plays a significant role in atmospheric, interstellar, and combustion chemistry.^{1,2} For example, OH acts as a key oxidizing agent that initiates numerous free radical chain reactions, which lead to oxidative breakdown of most trace species in the atmosphere. OH radicals are most often detected by laser-induced fluorescence (LIF), utilizing the well-characterized OH $A^2\Sigma^+ - X^2\Pi$ band system,³⁻⁵ in laboratory studies of inelastic collisions, reaction dynamics, and weakly bound complexes.⁶⁻⁸ Nevertheless, it is still desirable to develop a sensitive and state-selective ionization method for OH radical detection, which offers mass selectivity when coupled with a mass spectrometer that cannot be achieved with fluorescence measurements. In addition, it allows for further ion manipulation required for many modern experimental techniques such as velocity map imaging (VMI),⁹ which affords information regarding angular and kinetic energy distributions of ions or electrons.

The ionization efficiency in a multiphoton ionization process is typically enhanced by resonant intermediate states. Several resonance enhanced multiphoton ionization (REMPI) schemes have been developed for detection of OH radicals, including 2+1 REMPI schemes that rely on resonant $D^2\Sigma^+$ or $3^2\Sigma^-$ Rydberg intermediate states.¹⁰ However, these intermediate states exhibit significant coupling to nearby repulsive potentials,¹¹⁻¹³ resulting in rapid electronic predissociation and reducing the sensitivity of these schemes.

A state-selective 1+1' REMPI scheme has recently been developed for OH $X^2\Pi$ radical detection utilizing the intermediate OH $A^2\Sigma^+$ ($v'=1$ or 2) valence state followed by

fixed 118 nm VUV (10.5 eV) photoionization.^{14, 15} The fixed-frequency VUV radiation is generated by frequency-tripling the third harmonic of a Nd:YAG laser in a Xe gas cell, enabling this 1+1' REMPI scheme to be readily implemented using typical laboratory laser setups. The 1+1' REMPI scheme is practical and has already been applied in photoionization mass spectrometry^{16, 17} and VMI⁹ studies of OH products from unimolecular decay of Criegee intermediates.

While easy to implement, the underlying ionization mechanism for the 1+1' OH REMPI scheme is not as straightforward. Although the energy of the combined UV and VUV photons is well above the ionization threshold (13.01 eV),¹⁸ the ground cationic state $\text{OH}^+ X^3\Sigma^- (1\sigma^2 2\sigma^2 3\sigma^2 1\pi^2)$ is not accessible from the intermediate $\text{OH } A^2\Sigma^+ (1\sigma^2 2\sigma^2 3\sigma^1 1\pi^4)$ state via a one-photon, one-electron process. The lowest allowed cationic state is $\text{OH}^+ A^3\Pi$, which lies at much higher energy (16.48 eV).¹⁸ However, the combined energy (ca. 14.88 eV) of the UV and VUV photons coincides with a previously identified autoionizing $\text{OH } [A^3\Pi, 3d] (v=0)$ Rydberg state converging on the $\text{OH}^+ A^3\Pi$ cationic core.¹⁹ Therefore, it was postulated that VUV excitation from the $\text{OH } A^2\Sigma^+ (v'=1)$ state accesses the $\text{OH } [A^3\Pi, 3d] (v=0)$ Rydberg state, which undergoes autoionization and yields $\text{OH}^+ X^3\Sigma^-$ ground state cations. This assignment is consistent with the lack of photoionization signal upon VUV excitation from the lowest vibrational level of $\text{OH } A^2\Sigma^+ (v'=0)$, where the combined UV and VUV photon energies are not sufficient to access the autoionizing Rydberg state.

Previous work compared the 1+1' photoionization signals with near simultaneous LIF measurements accessing the same $\text{OH } A^2\Sigma^+$ levels, and derived an enhancement

factor from the ratio of the REMPI to LIF signal intensities.¹⁴ The enhancement factor is indicative of the ionization efficiency with fixed VUV excitation from selected rotational and fine structure levels in the OH $A^2\Sigma^+$ ($v'=1$) state. For main branch $A^2\Sigma^+ - X^2\Pi$ transitions, the enhancement factor profile was found to be similar to the constant ionic state (CIS) photoelectron spectrum for the transition from the ground state directly to the autoionizing OH [$A^3\Pi$, $3d$] ($v=0$) Rydberg state.^{14, 19} In both cases, the breadth suggested that autoionization is rapid, possibly allowing for relaxed resonance conditions of the VUV excitation.

The previous studies provided only a small window on the OH $A^2\Sigma^+$ to Rydberg transition, starting from specific OH $A^2\Sigma^+$ rovibrational and fine structure levels and utilizing fixed 118 nm VUV radiation to access the Rydberg state. This work uses tunable VUV radiation to continuously scan over a broad frequency region to access the OH [$A^3\Pi$, $3d$] ($v=0$) Rydberg state from specific rotational levels of the OH $A^2\Sigma^+$ ($v'=1$) state. Total symmetry permits several electronic state configurations that contain the $A^3\Pi$ core and a $3d$ Rydberg electron: $^2\Sigma^\pm$, two $^2\Pi$, $^2\Delta$, and $^2\Phi$ states. Of these states, only the $^2\Sigma^+$ and two $^2\Pi$ states are accessible from the intermediate OH $A^2\Sigma^+$ state. The present study spectroscopically characterizes these Rydberg states with rotational resolution and provides new insight on the 1+1' REMPI ionization scheme for OH radicals previously implemented with fixed VUV radiation.

II. Experimental Methods

OH radicals are produced by photolysis of nitric acid and detected by 1+1' REMPI in a Wiley-McLaren linear time-of-flight mass spectrometer (TOF-MS, RM

Jordan). Fuming nitric acid (Puritan Products, 98%) vapor seeded in He (30 psi) is pulsed from a solenoid valve and photolyzed at the throat of a free jet expansion by the focused output of a 193 nm ArF excimer laser (Coherent COMPex 102, 15 mJ/pulse) to yield OH radicals. The OH radicals are cooled in the expansion ($T_{\text{rot}} \sim 200$ K) and probed approximately 7.5 cm downstream. The OH radicals are excited on specific $A^2\Sigma^+ - X^2\Pi$ (1,0) lines with unfocused UV radiation crossing perpendicular to the unskimmed expansion in the ionization region of the TOF-MS. The UV radiation (0.2 mJ/pulse) is the frequency-doubled output of a Nd:YAG pumped dye laser (Innolas Narrowscan, Rhodamine 590). All lasers are calibrated with a wavemeter (Coherent Wavemaster).

Tunable VUV radiation is generated via two-photon resonant four-wave mixing ($\omega_{\text{VUV}} = 2\omega_1 - \omega_2$) with $2\omega_1$ fixed on the $5p'[1/2]_0 \leftarrow 1S_0$ Kr resonance at 98855.1 cm^{-1} ,²⁰ building on analogous studies by Pratt and coworkers.²¹ The fixed ω_1 radiation (< 1 mJ/pulse) is generated from the frequency-tripled output of a Nd:YAG pumped dye laser (Continuum Powerlite 9000 and ND6000, Rhodamine 640, 8 ns FWHM). The tunable ω_2 radiation (7-18 mJ/pulse) is the fundamental output of a Nd:YAG pumped dye laser (Continuum 7020 with ND6000, LDS 698, 7 ns FWHM). The ω_1 and ω_2 pulses are temporally overlapped and spatially combined using a dichroic mirror, before being focused with a $f=25$ cm CaF_2 lens into a 33 cm stainless steel cell containing Kr gas (35 torr). The resultant tunable VUV radiation is focused into the ionization region of the TOF-MS using an $f=25$ cm MgF_2 lens without polarization selection. The tunable VUV is introduced counterpropagating to the UV after a 60 ns delay.

OH⁺ ions generated by the 1+1' REMPI scheme are extracted perpendicular to the expansion and detected on the m/z = 17 mass channel. Excimer photolysis, UV excitation, and VUV generation (utilizing ω_1 , ω_2 , and Kr gas) are required to obtain OH⁺ ionization signals. The ion signal is processed with a digital oscilloscope (LeCroy WaveRunner 6050A) and transferred to a PC for averaging and further analysis. An electric field of ~400 V/cm is used in the interaction region. Variation of this electric field in the 70-700 V/cm range was found to have no observable effect on the position or width of the VUV features within experimental resolution.

III. Results

A sequential UV-VUV double-resonance excitation technique is used to access individual rovibronic levels of OH [$A^3\Pi$, $3d$] ($v=0$) Rydberg states. The UV transition prepares OH in specific rovibronic levels of the $A^2\Sigma^+$ ($v'=1$) intermediate state; the tunable VUV radiation generated by four-wave mixing promotes the OH radicals to autoionizing levels of two newly identified Rydberg states with an $A^3\Pi$ cationic core and $3d$ electron, both $^2\Pi$ in character, hereafter denoted as $^2\Pi$ Ryd. Spectra of the OH $^2\Pi$ Ryd - $A^2\Sigma^+$ transitions are obtained by scanning the VUV radiation and mass-selectively detecting the resultant OH⁺ ions (m/z=17) using a TOF-MS. The transition frequencies, intensities, and linewidths are utilized to characterize the OH $^2\Pi$ Ryd states and gain insight on previously reported UV+VUV (1+1') REMPI transitions observed with fixed 118 nm VUV radiation.

Various OH A-X (1,0) lines are used to prepare specific rotational (N') and spin component (F_1') levels of the intermediate OH $A^2\Sigma^+$ ($v'=1$, J' , N' , F_1') state. Standard

spectroscopic notation for the OH $A^2\Sigma^+$ state is briefly summarized in Ref. 22, and augmented here with the total angular momentum J' to help in assigning $^2\Pi$ Ryd - $A^2\Sigma^+$ transitions. Notation for $^2\Pi - ^2\Sigma^+$ electronic transitions is summarized in Ref. 23. The UV transitions originate from OH X $^2\Pi_\Omega$ ($v''=0, J'', F_1'', +/-$) levels, labels defined in Ref. 24, that are populated upon photolysis of HNO_3 and partially relaxed in the He expansion. To the extent possible, specific intermediate OH $A^2\Sigma^+$ ($v'=1, J', N', F_1'$) levels are prepared using two different A-X transitions and scanning the VUV radiation to verify $^2\Pi$ Ryd - $A^2\Sigma^+$ assignments. It should be noted that OH A-X (1,0) R_1 and Q_1 lines have nearby satellite lines, particularly from low J'' , which are not resolved from main branch lines at the experimental linewidth, and may simultaneously prepare two closely-spaced spin-rotation (F_1') sublevels in the OH $A^2\Sigma^+$ state. This, in turn, may give rise to additional lines and/or overlapping lines in the VUV scans.

The VUV scans shown in Figures 1-5 reveal spectroscopic lines associated with $^2\Pi$ Ryd - $A^2\Sigma^+$ transitions originating from specific intermediate OH $A^2\Sigma^+$ ($v'=1, J', N', F_1'$) levels with $N'=0-4$, respectively. The positions, widths, and assignments of the observed lines and $^2\Pi$ Ryd levels are listed in Table S1.²⁵ In Figure 1, the intermediate state is OH $A^2\Sigma^+$ ($v'=1, J'=0.5, N'=0, F_1'$). In Figures 2-4 with $N'=1-3$, there are two nearly degenerate (spin-rotation) intermediate levels that are accessed for each N' , which are shown as separate panels. Figures 2-4 also show VUV scans obtained using two different A-X lines to reach the same intermediate level; these VUV scans are denoted by

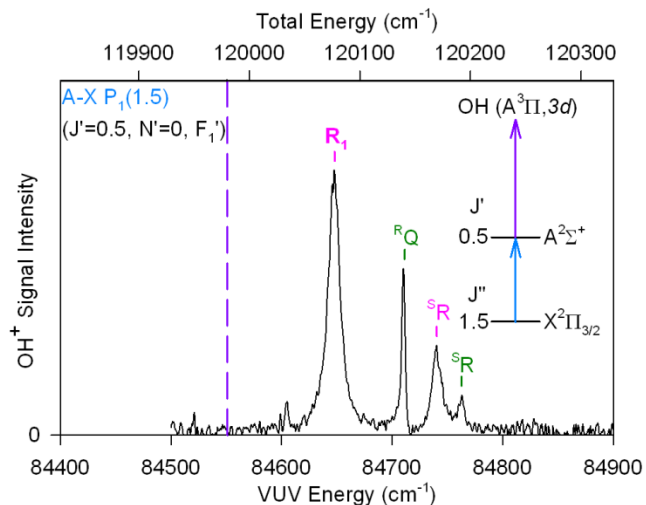


Figure 1. Tunable VUV scan accessing OH [$A^3\Pi$, $3d$] ($v=0$) Rydberg states from the OH $A^2\Sigma^+$ ($v'=1$, $J'=0.5$, $N'=0$, F_1') intermediate level with detection of OH^+ on the $m/z=17$ mass channel. The intermediate level is prepared by UV excitation on the OH $A^2\Sigma^+ - X^2\Pi(1,0) P_1(1.5)$ transition as indicated in the schematic energy level diagram (right, blue arrow) and labels (upper left). Spectroscopic transitions from OH $A^2\Sigma^+$ to the $^2\Pi_{3/2, \text{lower}}$ and $^2\Pi_{1/2, \text{lower}}$ Rydberg states are indicated with ticks and labeled (see Ref. 33) using bold and normal pink font, respectively. Transitions from OH $A^2\Sigma^+$ to a separate $^2\Pi_{1/2, \text{upper}}$ Rydberg state are labeled using normal green font. The top axis refers to the total energy of the $^2\Pi$ Rydberg state relative to the lowest rovibrational level ($v''=0$, $J''=1.5$, F_1'' , -) of the ground $X^2\Pi_{3/2}$ electronic state. The energy of the fixed VUV radiation (118 nm) used in prior OH $1+1'$ REMPI studies is indicated by the dashed purple line.

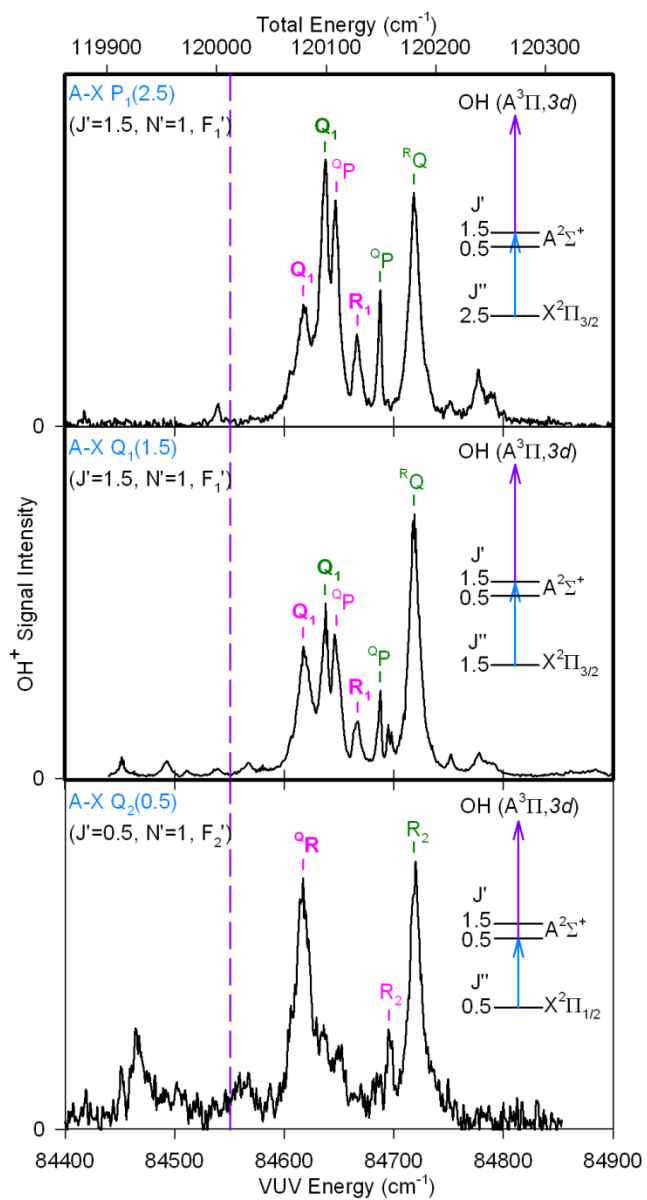


Figure 2. VUV spectra accessing OH [$A^3\Pi, 3d$] ($v=0$) Rydberg states from OH $A^2\Sigma^+$ ($v'=1, N'=1$) intermediate levels with ($J'=0.5, F_2'$) or ($J'=1.5, F_1'$) and OH^+ detection. The intermediate level is prepared by UV excitation on the OH $A^2\Sigma^+ - X^2\Pi$ (1,0) $Q_2(0.5)$, $Q_1(1.5)$, or $P_1(2.5)$ lines as indicated in the schematic energy level diagram (right, blue arrow) and labels (upper left) on each panel. The thicker box outline indicates VUV scans originating from the same intermediate level prepared using two different A-X lines. Transitions from OH $A^2\Sigma^+$ to the $^2\Pi_{3/2, \text{lower}}$ and $^2\Pi_{1/2, \text{lower}}$ Rydberg states are indicated with ticks and labeled (see Ref. 33) using bold and normal pink font, respectively, while those to the $^2\Pi_{3/2, \text{upper}}$ and $^2\Pi_{1/2, \text{upper}}$ Rydberg states are labeled using bold and normal green font, respectively. The energy of the fixed VUV radiation (118 nm) used in prior OH 1+1' REMPI studies is indicated by the dashed purple line.

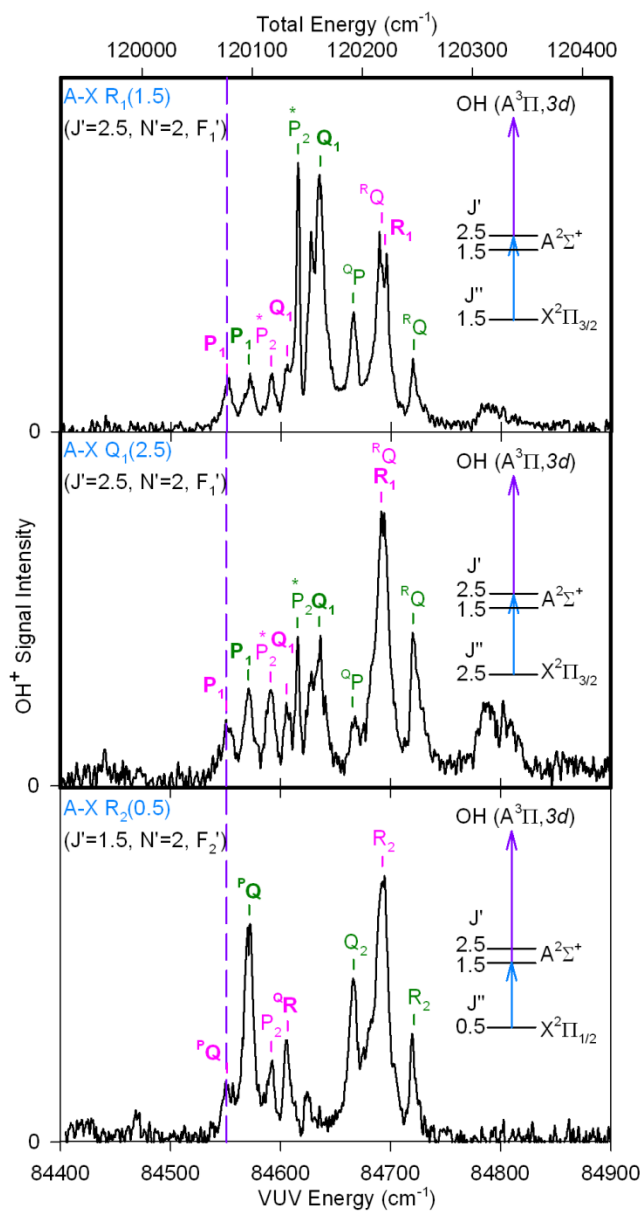


Figure 3. VUV spectra accessing OH [$A^3\Pi, 3d$] ($v=0$) Rydberg states from OH $A^2\Sigma^+$ ($v'=1, N'=2$) levels with ($J'=1.5, F_2'$) and ($J'=2.5, F_1'$) and OH^+ detection. The intermediate level is prepared by UV excitation on the OH $A^2\Sigma^+ - X^2\Pi(1,0) R_2(0.5)$, $Q_1(2.5)$, or $R_1(1.5)$ lines. See Figure 2 caption for additional details.

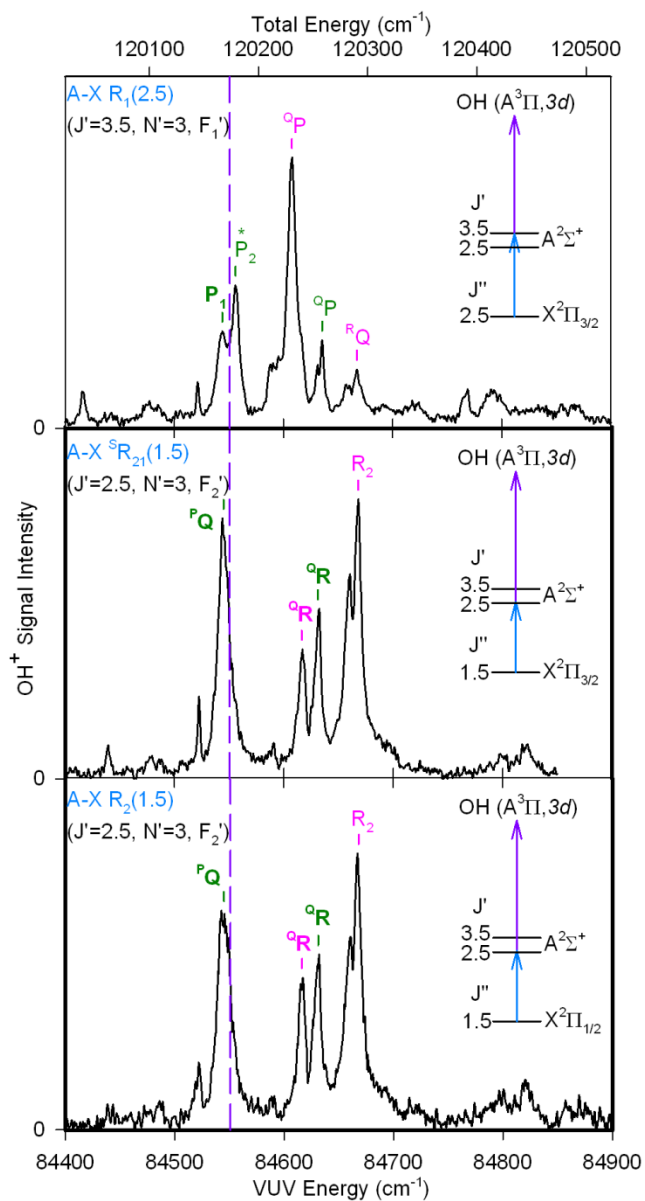


Figure 4. VUV spectra accessing OH [A³Π, 3d] (v=0) Rydberg states from OH A²Σ⁺ (v'=1, N'=3) levels with (J'=2.5, F₂') and (J'=3.5, F₁') and OH⁺ detection. The intermediate level is prepared by UV excitation on the OH A²Σ⁺ - X²Π (1,0) R₂(1.5), ^sR₂₁(1.5), or R₁(2.5) lines. See Figure 2 caption for additional details.

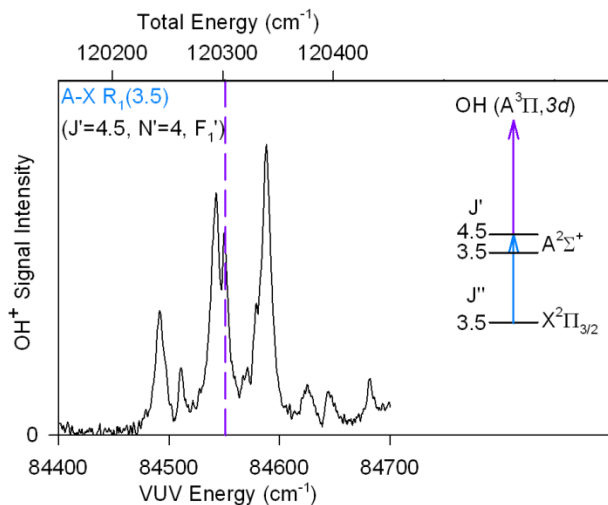


Figure 5. VUV spectrum accessing OH [$A^3\Pi$, $3d$] ($v=0$) Rydberg states from OH $A^2\Sigma^+$ ($v'=1$, $N'=4$, $J'=4.5$, F_1') level and OH⁺ detection. Prominent lines are tentatively attributed to Q_1 (and/or P_1) lines terminating in the lower and upper $^2\Pi_{3/2}$ states and $^oP_{21}$ lines terminating in the lower and upper $^2\Pi_{1/2}$ states. The intermediate level is prepared by UV excitation on the OH $A^2\Sigma^+$ - $X^2\Pi$ (1,0) $R_1(3.5)$ line. See Figure 2 caption for additional details.

thicker box outlines. The OH A-X lines utilized and the intermediate $A^2\Sigma^+$ ($v'=1, J', N', F_1'$) levels accessed are identified in each figure and Table S1.²⁵ The VUV scans encompass a 500 cm^{-1} region from 84400 to 84900 cm^{-1} . The assigned transitions lie in the central region of the VUV spectra; only weak lines are seen below 84500 cm^{-1} and above 84800 cm^{-1} and are not assigned. The purple dashed lines in Figures 1-5 indicate the fixed 118 nm VUV radiation (10.5 eV) utilized in prior OH $1+1'$ REMPI studies.^{14, 15} Finally, the total energy²⁶ shown on the top axes of Figures 1-5 refers to the energy of the level prepared in the $^2\Pi$ Ryd state relative to the lowest rovibrational level ($v''=0, J''=1.5, F_1'', -$) of the ground $X^2\Pi_{3/2}$ electronic state.

Figure 1 shows 4 distinct lines in the VUV scan originating from OH $A^2\Sigma^+$ ($v'=1, J'=0.5, N'=0, F_1'$) and accessing two newly identified $^2\Pi_{\Omega}$ Ryd states, each with two spin-orbit manifolds $\Omega=3/2$ (F_1) and $\Omega=1/2$ (F_2). One line at 84710 cm^{-1} is noticeably narrower than the others. Based on $\Delta J=0, \pm 1$ selection rules, some lines will not be observed; for example, P-lines are absent. One anticipates up to 6 lines in the spectrum accessing $J=0.5, 1.5$ for $^2\Pi_{1/2}$ and $J=1.5$ for $^2\Pi_{3/2}$ in each $^2\Pi_{\Omega}$ Ryd state. Only 4 of the 6 possible lines are observed because of unusual intensity patterns arising from several effects (e.g. l-uncoupling) discussed later.

The bottom panel of Figure 2 shows 3 lines (of the 6 possible $\Delta J=0, \pm 1$ transitions indicated above) in the VUV scan originating from OH $A^2\Sigma^+$ ($v'=1, J'=0.5, N'=1, F_2'$). Again, P-lines are absent in transitions to the $^2\Pi_{\Omega}$ Ryd states. The top and middle panels of Figure 2 show VUV scans from the OH $A^2\Sigma^+$ ($v'=1, J'=1.5, N'=1, F_1'$) intermediate

level, which is prepared by two different A-X transitions. The same 6 lines are observed in both spectra, although transitions to $J=1.5, 2.5$ for ${}^2\Pi_{3/2}$ and $J=0.5, 1.5, 2.5$ for ${}^2\Pi_{1/2}$ are anticipated for each of the two ${}^2\Pi$ Ryd states (totaling 10 lines).

In Figure 3, starting again with the bottom panel, the VUV scan reveals many lines, but not all lines anticipated from $\Delta J=0, \pm 1$ selection rules, originating from the OH $A^2\Sigma^+$ ($v'=1, J'=1.5, N'=2, F_2'$) level. The top and middle panels show VUV scans starting from the adjacent OH $A^2\Sigma^+$ ($v'=1, J'=2.5, N'=2, F_1'$) level prepared by two different A-X transitions, which give rise to a rich spectrum composed of the same spectral lines, albeit with somewhat different intensities. Extra lines (indicated by *) and/or overlapping lines that impact relative intensities in the VUV spectra are attributed to simultaneous preparation of nearly degenerate $A^2\Sigma^+$ levels in the A-X excitation step.

The bottom and middle panels of Figure 4 show the same 4 distinct lines and intensity profiles in the VUV scan originating from the OH $A^2\Sigma^+$ ($v'=1, J'=2.5, N'=3, F_2'$) level, which is prepared by two distinct A-X transitions. The VUV scan in the top panel of Figure 4 originates from the adjacent OH $A^2\Sigma^+$ ($v'=1, J'=3.5, N'=3, F_1'$) level and accesses additional rotational levels of the ${}^2\Pi_{\Omega}$ Ryd states. In each VUV scan, only a few of the possible ${}^2\Pi$ Ryd - $A^2\Sigma^+$ (0,1) lines are observed. Figure S1 provides a schematic diagram showing allowed transitions from OH $A^2\Sigma^+$ ($v'=1, N'=3$) to OH ${}^2\Pi_{\Omega}$ Rydberg states.²⁵

Figure 5 shows a VUV scan originating from the next higher OH $A^2\Sigma^+$ ($v'=1, J'=4.5, N'=4, F_1'$) intermediate level. The prominent features in this region span ~ 250 cm^{-1} from 84450 to 84700 cm^{-1} . The VUV lines are only tentatively identified (see

caption), although similar transitions are anticipated as those assigned from lower N' levels of the intermediate OH $A^2\Sigma^+$ ($v'=1$) state. Of particular interest are VUV transitions that would be resonant with fixed 118 nm radiation, as discussed below.

The lines observed in the VUV scans from specific OH $A^2\Sigma^+$ ($v'=1, J', N', F_i'$) levels are assigned as transitions to two OH $^2\Pi_\Omega$ Ryd ($v=0$) states. The peak positions and full width at half maximum (FWHM) of each line in the VUV spectra are determined from a multiplex fitting algorithm embedded within the Igor program software, and are listed in Table S1.²⁵ The extracted linewidths vary from 3.2 to 15.3 cm^{-1} (FWHM) and are attributed primarily to homogeneous lifetime broadening, which likely results from autoionization. These linewidths correspond to OH Rydberg state lifetimes of 1.8-0.3 ps. The assignments for the narrower lines observed in the VUV scans are discussed in the next section. While the linewidth of the tunable VUV is not measured directly, analogous four-wave mixing schemes have been reported that generate VUV with a linewidth in the 0.1-1.0 cm^{-1} range, utilizing a similar dye laser setup with Kr as the nonlinear medium.²⁷⁻²⁹ This suggests that the narrowest lines may prepare OH $^2\Pi_\Omega$ Ryd levels with slightly longer lifetimes (ca. +0.1 ps) than indicated above.

IV Discussion

A. Assignments and spectroscopic constants

Rydberg states accessible from the resonant intermediate OH $A^2\Sigma^+$ state are $^2\Sigma^+$ from the $[A^3\Pi, 3d\pi]$ configuration and two $^2\Pi$ states from $[A^3\Pi, 3d\sigma]$ and $[A^3\Pi, 3d\delta]$ configurations. In a simple case without perturbations, the $3d\sigma$ would be lower in energy than $3d\delta$, although perturbations described below preclude definitive assignment of the

two ${}^2\Pi$ states.³⁰ Based on selection rules ($\Delta\Lambda = 0, \pm 1$, $\Delta J = 0, \pm 1$ and $+ \leftrightarrow -$), combination differences, and energy spacings, the VUV photoionization spectra (Figures 1-5) are assigned to transitions from OH $A^2\Sigma^+$ to the two ${}^2\Pi$ Ryd states, denoted as ${}^2\Pi_{\text{upper}}$ and ${}^2\Pi_{\text{lower}}$. As discussed below, the prominent lines observed in the VUV scans can be assigned to allowed transitions accessing rotational levels in these two ${}^2\Pi$ Ryd states, each of which has two spin-orbit manifolds, $\Omega=3/2$ (F_1) and $\Omega=1/2$ (F_2), from initially prepared intermediate OH $A^2\Sigma^+$ ($v'=1, J', N', F_1'$) levels.

The assignments for each of the observed OH ${}^2\Pi$ Ryd - $A^2\Sigma^+$ transitions and corresponding ${}^2\Pi_{\Omega}$ Ryd levels accessed are listed in Table S1.²⁵ Based on these assignments, an energy level diagram of the rotational levels observed in the ${}^2\Pi_{\Omega}$ Ryd states can be generated, as shown in Figure 5, and corresponding energies are listed in Table S2. The lowest observed levels of the two ${}^2\Pi$ Ryd states are separated by approximately 20 cm^{-1} , which is smaller than the spacings between the lowest observed levels of the two spin-orbit manifolds in each ${}^2\Pi$ Ryd state (31.8 and 43.6 cm^{-1} for ${}^2\Pi_{\text{lower}}$ and ${}^2\Pi_{\text{upper}}$, respectively), thereby making the spectra very congested. In each case, the ${}^2\Pi_{3/2}$ component is lower in energy than the ${}^2\Pi_{1/2}$ component, which is analogous to the inverted spin-orbit splitting of the OH $X^2\Pi$ ground electronic state. Utilizing the Hund's case (a) limit, the rotational levels are denoted with total angular momentum J and Λ -doubling splits each rotational level into two levels with \pm total parity within each ${}^2\Pi_{\Omega}$ Ryd manifold.

Spectroscopic constants are derived for the ${}^2\Pi$ Ryd states based on the following standard equations for Hund's case (a) rotational energy levels in a ${}^2\Pi_{\Omega}$ state:³¹

$$E_{3/2}(J) = \frac{A_{eff}}{2} + B_{3/2(eff)} \left(\left(J + \frac{1}{2} \right)^2 - 1 \right) \quad (1)$$

$$E_{1/2}(J) = -\frac{A_{eff}}{2} + B_{1/2(eff)} \left(\left(J + \frac{1}{2} \right)^2 - 1 \right) \quad (2)$$

The spectroscopic constants are obtained from a weighted least squares fit of the observed rotational energy levels $E_{\Omega}(J)$ in the ${}^2\Pi_{\Omega}$ manifolds. This analysis neglects centrifugal distortion and perturbations in low rotational levels of the OH ${}^2\Pi_{\Omega}$ Ryd states. Here, A_{eff} is the effective spin-orbit coupling constant, and $B_{3/2(eff)}$ and $B_{1/2(eff)}$ are the effective rotational constants within each ${}^2\Pi_{\Omega}$ component. The resultant spectroscopic constants are listed in Table 1 for the ${}^2\Pi_{upper}$ Ryd state. The ${}^2\Pi_{lower}$ Ryd state is found to deviate significantly from the Hund's case (a) limit for reasons discussed below.

Averaging $B_{3/2(eff)}$ and $B_{1/2(eff)}$ from the two spin-orbit manifolds of the ${}^2\Pi_{upper}$ Ryd state yields an effective rotational constant of $B_{upper} = 13.4 \pm 0.6 \text{ cm}^{-1}$. This rotational constant is similar to that of the OH $A^3\Pi$ cationic core, $B_{OH^+} = 13.35 \text{ cm}^{-1}$,³² consistent with the nonbonding nature of a Rydberg electron.

The spin-orbit coupling constant (A) is evaluated from $A = A_{eff} - 2B$ and yields a value of $-60.1 \pm 6.0 \text{ cm}^{-1}$ for the ${}^2\Pi_{upper}$ state. The spin orbit coupling constant is a measure of the separation between the two spin-orbit ${}^2\Pi_{3/2}$ and ${}^2\Pi_{1/2}$ components, which is much smaller for the ${}^2\Pi$ Ryd state than that of the ground state OH $X^2\Pi$ ($A = -139$

Table 1. Spectroscopic constants (cm^{-1}) derived for the OH ${}^2\Pi_{\text{upper}}$ ($v=0$) Rydberg state with an $A^3\Pi$ cationic core and a $3d$ electron based on the Hund’s case (a) approximation.^a

Spectroscopic constants are defined in Section IV. A.

Spectroscopic Constant	${}^2\Pi_{\text{upper}}$
$B_{1/2(\text{eff})}$	13.5 ± 1.1
$B_{3/2(\text{eff})}$	13.3 ± 0.6
B	13.4 ± 0.6
A_{eff}	-86.9 ± 5.9
A	-60.1 ± 6.0
$v_{0, 1/2}$	84705.7 ± 5.1
$v_{0, 3/2}$	84618.9 ± 2.8
p	-4.8 ± 0.9
q	-0.04 ± 0.13

^a Notable deviations from the Hund’s case (a) limit, particularly for the ${}^2\Pi_{\text{lower}}$ ($v=0$) Rydberg state, are described in the text.

cm⁻¹), indicating significantly less coupling of the electronic spin with the internuclear axis in the Rydberg state.

The rotational constant B and spin-orbit coupling constant A are further utilized to evaluate the sub-band origins, $\nu_{0, 3/2}$ and $\nu_{0, 1/2}$, for the ${}^2\Pi_{\Omega}$ Ryd - OH $A^2\Sigma^+$ transition:³³

$${}^2\Pi_{3/2} : \Delta\nu = \nu_{0,3/2} + B_{eff}J(J+1) - B'(J'+0.5)(J'-0.5) \quad (3)$$

$${}^2\Pi_{1/2} : \Delta\nu = \nu_{0,1/2} + B_{eff}J(J+1) - B'(J'+0.5)(J'+1.5) \quad (4)$$

The Λ -doubling constants, p and q , which describe the Λ -doublet energy level splitting $\Delta\nu_{dc}$ for each rotational level (J) of the ${}^2\Pi$ Rydberg state, are evaluated as follows:³⁴

$${}^2\Pi_{1/2} : \Delta\nu_{dc} = p(J+0.5) \quad (5)$$

$${}^2\Pi_{3/2} : \Delta\nu_{dc} = -\left(\frac{p}{Y^2} + \frac{2q}{Y}\right)(J-0.5)(J+0.5)(J+1.5), \text{ with } Y = A/B \quad (6)$$

The resultant values for ν_0 , p and q are listed in Table 1. The Λ -doublet spacings are larger for ${}^2\Pi_{1/2}$ than ${}^2\Pi_{3/2}$ components, as expected,³³ supporting the assignments of the ${}^2\Pi_{\Omega}$ manifolds. Significant Λ -doublet splitting is observed for the Rydberg states compared to the ground state OH $X^2\Pi$, which is likely due to an l-uncoupling effect in the Rydberg states, as discussed below.

B. Deviations from Hund's case (a): Uncoupling phenomena

Thus far, the spectroscopic analysis has been based on a Hund's case (a) limit. As discussed in Herzberg and other sources,^{31, 33} both the orbital angular momentum and spin are strongly coupled with the internuclear axis in Hund's case (a) limit. Deviations from this limit may arise from decoupling of spin from the internuclear axis, decoupling of orbital angular momentum from the internuclear axis, or decoupling of spin and orbital

angular momentum from the internuclear axis.³³ The VUV spectra of the $^2\Pi$ Ryd states reveal three distinct effects indicative of deviations from Hund's case (a).

In the first case where the spin is decoupled from the internuclear axis, the rotational energy levels may be better described by $B[N(N+1)-1]$. This can also be evident by a switch in the +/- parity pattern³⁵ between the two Λ -doublets within a $^2\Pi_{1/2}$ manifold, which is observed beginning at the $^2\Pi_{1/2,lower}$, $J=1.5$ level (Figure 5) and indicates significant deviation from the Hund's case (a) limit at low J for the $^2\Pi_{lower}$ Ryd state.

In the second case, which is common for Rydberg states, orbital angular momentum becomes decoupled from the internuclear axis (l-uncoupling) as the Rydberg electron is farther from the electronic core.³⁰ The l-uncoupling may lead to perturbations in the $^2\Pi$ levels due to interaction with nearby $^2\Sigma^\pm$ (or possibly $^2\Delta$) states, which are not directly observed. Parity-dependent interaction between $^2\Pi$ and $^2\Sigma^\pm$ states, arising from l-uncoupling, likely contributes to the significant Λ -doublet splittings observed in the $^2\Pi$ Rydberg states.³⁶ The observed Λ -doublet splittings are on the order of several wavenumbers in the OH Rydberg states, which is substantially larger than the Λ -doublet splittings in the OH $X^2\Pi$ ground state, the latter being much less than a wavenumber.³⁷

In addition, constructive or destructive interference due to the mixing of states can affect the intensity patterns for rovibronic transitions with $\Delta J = \pm 1$.³⁰ For example, if the interference is constructive for P-branch lines, it will be destructive for R-branch lines. In the present study, R-branch lines in $^2\Pi_\Omega$ Ryd - OH $A^2\Sigma^+$ transitions to the upper OH $^2\Pi_{3/2}$ ($v=0$, J , F_1 , +/-) Rydberg manifold are not observed, likely due to destructive

interference from the mixing of states arising from l-uncoupling. (The associated P-branch lines are observed.)

C. Comparison with fixed VUV REMPI studies

Previous implementation of the OH 1+1' REMPI scheme combined OH A²Σ⁺ - X²Π (1,0) excitation with fixed 118 nm VUV excitation that resulted in ionization. Ionization efficiencies from intermediate OH A²Σ⁺ (v'=1, J', N', F₁') levels were represented by an enhancement factor,¹⁴ which was defined as the ratio of photoionization to LIF signal intensities. For OH A²Σ⁺ (v'=1, J', N', F₁') levels prepared on main branch lines of the A²Σ⁺ - X²Π (1,0) transition, the enhancement factor profile was found to peak at the J'=4.5 level of the OH A²Σ⁺ state. The peak and breadth of the enhancement profile was consistent with an OH [A³Π, 3d] Rydberg state observed in CIS photoelectron spectra with OH⁺ X³Σ⁻ (v=0) detection. Some anomalies were observed in enhancement factors derived from OH A²Σ⁺ (v'=1, J', N', F₂') levels prepared via satellite lines of the A²Σ⁺ - X²Π transition, suggesting a parity-dependence of the OH A²Σ⁺ (v'=1) to Rydberg state transitions.

In Figures 1-5, the dashed purple line indicates the energy of the fixed (118 nm) VUV excitation. There is clearly overlap with prominent lines in the tunable VUV scans originating from OH A²Σ⁺ (v'=1) with N'=2-4 (Figures 3-5), consistent with the strong enhancement factors reported previously for these intermediate levels.¹⁴ (Figure S3 shows an adapted version of the enhancement factor plots from Ref. 14, which indicates the intermediate levels examined in the present work.²⁵) This demonstrates that the 1+1' REMPI with fixed (118 nm) VUV excitation is enhanced by accidental overlap with

rotationally resolved ${}^2\Pi$ Ryd - $A^2\Sigma^+$ transitions, followed by ionization. There is not an apparent resonance in the tunable VUV spectrum from OH $A^2\Sigma^+$ ($v'=1$) with $N'=0$ or 1, in accord with smaller enhancement factors, yet ionization still occurs. This suggests the possibility of excitation of weak (unassigned) transitions to autoionizing Rydberg states or possibly direct coupling to the ionization continuum.

In previous investigations, the lifetime of the autoionizing OH [$A^3\Pi$, $3d$] ($v=0$) Rydberg state was estimated from the breadth of the enhancement factor profile or CIS photoelectron spectrum to be on the order of tens of femtoseconds.^{14, 19} The resolution of the prior spectra precluded identification of rotational and fine structure levels in the ${}^2\Pi_{\Omega}$ Rydberg states. In this study, a broad range of linewidths (3.2 to 15.3 cm^{-1}) and corresponding lifetimes (1.8-0.3 ps) have been observed in the VUV spectra accessing rotational levels of the two OH ${}^2\Pi$ Rydberg states. Notably, the narrowest lines with a FWHM of $\sim 3 \text{ cm}^{-1}$ and longer lifetime, ca. 2 ps, arise from transitions to $J=0.5$ levels in the ${}^2\Pi_{1/2, \text{upper}}$ state. The lifetimes of the OH ${}^2\Pi$ Rydberg states can be affected by perturbation from nearby repulsive states leading to predissociation, as well as population loss associated with autoionization. A theoretical investigation of the dynamics of these Rydberg states would be helpful in unraveling the ionization mechanism.

This 1+1' OH REMPI detection method utilizing fixed VUV radiation has already been coupled with modern experimental techniques such as TOF-MS and VMI to gain a deeper understanding of OH generation from the unimolecular decay of Criegee intermediates ($R_1R_2\text{COO}$).^{9, 16, 17} The angular and velocity distributions of OH $X^2\Pi$ ($v''=0, J''=3.5, F_1$) products are probed in the VMI studies, taking advantage of the

enhancement factor in ionization that peaks at the OH $A^2\Sigma^+$ ($v'=1, J'=4.5, N'=4, F_1'$) level (see Figure S3).²⁵ Tunable VUV excitation from this OH $A^2\Sigma^+$ intermediate level accesses higher Λ -doublet and/or rotational levels in the $^2\Pi_\Omega$ Rydberg manifolds than assigned in the present work (Figure 6). The fixed 118 nm VUV radiation overlaps a strong line at 84551 cm^{-1} , tentatively assigned as $^Q P_{21}(4.5)$, which accesses the $^2\Pi_{1/2,lower}$ ($v=0, J=3.5, F_2, -$) level of the $[A^3\Pi, 3d]$ Rydberg state. In contrast, the VUV scan originating from the nearly degenerate (spin-rotation) OH $A^2\Sigma^+$ ($v'=1, J'=3.5, N'=4, F_2$) level, shown in Figure S2,²⁵ indicates that fixed 118 nm VUV radiation lacks significant overlap with the prominent lines. This is consistent with a dip observed in the enhancement factor profile from the corresponding OH $A^2\Sigma^+$ state level (see Figure S3).²⁵

V. Conclusion

Rotationally resolved spectra have been obtained for two distinct OH $^2\Pi$ Rydberg states with an $A^3\Pi$ cationic core and $3d$ electron using tunable VUV excitation (10.46-10.53 eV) from specifically prepared OH $A^2\Sigma^+$ ($v'=1, J', N', F_i'$) levels. The sequential OH $A^2\Sigma^+ - X^2\Pi$ and Ryd - $A^2\Sigma^+$ excitation results in autoionization and enables OH⁺ detection. The VUV transitions exhibit a range of linewidths, indicating that the Rydberg state lifetimes due to autoionization are on the order of a picosecond. Spectroscopic constants for one of the newly identified OH $^2\Pi$ Rydberg states are derived from fits of the observed energy levels in the Hund's case (a) limit. As is common in Rydberg states,³⁰ uncoupling of spin and/or orbital angular momentum (l -uncoupling) from the internuclear axis results in deviations from the Hund's case (a) limiting case. This is

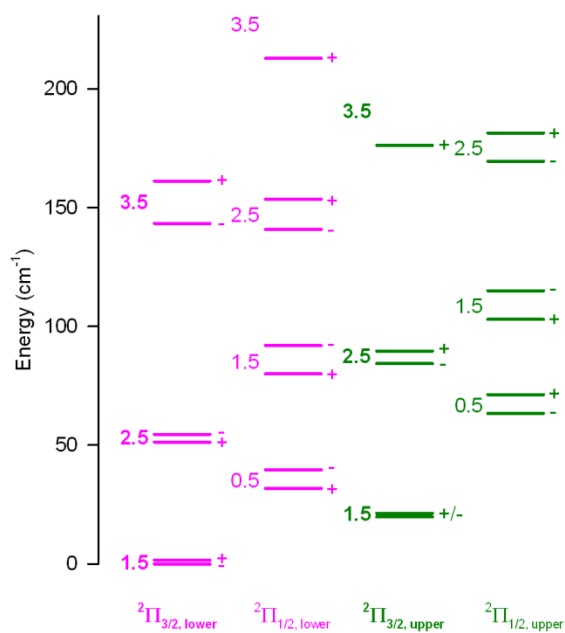


Figure 6. Energy level diagram and assignments of observed rotational and fine structure levels, labeled with J and +/-, in OH $^2\Pi$ Rydberg states with an $A^3\Pi$ cationic core and a 3d electron. Two $^2\Pi$ Ryd states, denoted lower and upper, each of which has two spin-orbit manifolds, $\Omega=3/2$ and $\Omega=1/2$, are accessed from intermediate OH $A^2\Sigma^+$ ($v'=1, J', N', F_1'$) levels. The $^2\Pi_{\text{lower}}$ and $^2\Pi_{\text{upper}}$ Ryd states are shown in pink and green, respectively, with bold and regular fonts indicating $^2\Pi_{3/2}$ and $^2\Pi_{1/2}$ manifolds, respectively. Energies are relative to lowest level assigned in $^2\Pi$ Ryd states and are listed in Table S2

evident in several ways, most notably in significant Λ -doublet splittings, suggesting interaction of the observed $^2\Pi$ Rydberg states with a nearby (unobserved) $^2\Sigma^\pm$ state.

The OH [$A^3\Pi$, $3d$] ($v=0$) Rydberg state had previously been accessed in a $1+1'$ REMPI scheme with OH $A^2\Sigma^+ - X^2\Pi$ (1,0) excitation and fixed VUV (118 nm) radiation.^{13, 14} The present study demonstrates that the OH $1+1'$ REMPI scheme is enhanced by accidental overlap of the fixed VUV radiation with distinct $^2\Pi$ Ryd - $A^2\Sigma^+$ transitions having well-defined rotational and fine structure components, followed by ionization. The overlap of fixed VUV (118 nm) radiation with prominent lines in VUV scans originating from specific OH $A^2\Sigma^+$ ($v'=1$, J' , N' , F_1') levels corroborates the previously reported enhancement factors for REMPI to LIF signals. In particular, a resonant transition ascribed to the $^2\Pi_{1/2, \text{lower}}$ Rydberg state gives rise to the largest enhancement factor for the OH $A^2\Sigma^+$ ($v'=1$, $J'=4.5$, $N'=4$, F_1') intermediate level, which has been utilized with VMI for detection of OH products from Criegee intermediates.⁹ In the future, it would be highly desirable to use photoelectron imaging to further unravel the ionization mechanism.

Acknowledgements

This research was supported by the U.S. Department of Energy-Basic Energy Sciences under grant DE-FG02-87ER13792. The authors thank Stephen Pratt (Argonne National Laboratory) for helpful discussions regarding generation of tunable VUV radiation and Joseph Beames (Cardiff University) for insights on the spectroscopic analysis.

References

- ¹ B. J. Finlayson-Pitts and J. N. Pitts, *Chemistry of the Upper and Lower Atmosphere* (Academic Press, San Diego, 2000).
- ² D. Stone, L. K. Whalley, and D. E. Heard, *Chem. Soc. Rev.* **41**, 6348 (2012).
- ³ J. A. Coxon, *Can. J. Phys.* **58**, 933 (1980).
- ⁴ J. Luque and D. R. Crosley, *J. Chem. Phys.* **109**, 439 (1998).
- ⁵ K. L. Steffens, J. Luque, J. B. Jeffries, and D. R. Crosley, *J. Chem. Phys.* **106**, 6262 (1997).
- ⁶ L. P. Dempsey, C. Murray, P. A. Cleary, and M. I. Lester, *Phys. Chem. Chem. Phys.* **10**, 1424 (2008).
- ⁷ P. Soloveichik, B. A. O'Donnell, M. I. Lester, J. S. Francisco, and A. B. McCoy, *J. Phys. Chem. A* **114**, 1529 (2010).
- ⁸ F. Ausfelder and K. G. McKendrick, *Prog. React. Kinet. Mec.* **25**, 299 (2000).
- ⁹ N. Kidwell, H. Li, X. Wang, J. M. Bowman, and M. I. Lester, *Nat. Chem.*, published online (2016) DOI: 10.1038/NCHEM.2488.
- ¹⁰ M. E. Greenslade, M. I. Lester, D. Č. Radenović, A. J. A. van Roij, and D. H. Parker, *J. Chem. Phys.* **123**, 074309 (2005).
- ¹¹ E. F. van Dishoeck and A. Dalgarno, *J. Chem. Phys.* **79**, 873 (1983).
- ¹² E. F. van Dishoeck, S. R. Langhoff, and A. Dalgarno, *J. Chem. Phys.* **78**, 4552 (1983).
- ¹³ M. P. J. van der Loo and G. C. Groenenboom, *J. Chem. Phys.* **123**, 074310 (2005).
- ¹⁴ J. M. Beames, F. Liu, and M. I. Lester, *Mol. Phys.* **112**, 897 (2013).
- ¹⁵ J. M. Beames, F. Liu, M. I. Lester, and C. Murray, *J. Chem. Phys.* **134**, 241102 (2011).

- ¹⁶ J. M. Beames, F. Liu, L. Lu, and M. I. Lester, *J. Chem. Phys.* **138**, 244307 (2013).
- ¹⁷ F. Liu, J. M. Beames, A. M. Green, and M. I. Lester, *J. Phys. Chem. A* **118**, 2298 (2014).
- ¹⁸ H. Vanlonkhuyzen and C. A. Delange, *Mol. Phys.* **51**, 551 (1984).
- ¹⁹ J. D. Barr, A. De Fanis, J. M. Dyke, S. D. Gamblin, N. Hooper, A. Morris, S. Stranges, J. B. West, and T. G. Wright, *J. Chem. Phys.* **110**, 345 (1999).
- ²⁰ V. Kaufman, *J. Res. Natl. Inst. Stan.* **98**, 717 (1993).
- ²¹ H. Xu and S. T. Pratt, *J. Phys. Chem. A* **117**, 9331 (2013).
- ²² The OH $A^2\Sigma^+$ state is well described using Hund's case (b) notation with quantum number for vibration (v'), total angular momentum (J'), and rotation without spin (N'). The rotational levels are shifted slightly due to spin-rotation coupling, with fine-structure labeling of $J'=N'+0.5$ for the F_1' spin component and $J'=N'-0.5$ for the F_2' spin component.
- ²³ Spectroscopic transitions use ΔJ notation with superscript ΔN , if $\Delta N \neq \Delta J$. Subscripts denote the spin component(s) of the upper level and, if different, the lower level. For example, a main branch R_1 line for a $\Delta N = \Delta J = +1$ transition involves the F_1 spin components of the upper and lower states, while satellite line $^S R_{21}$ for a $\Delta N = +2$ and $\Delta J = +1$ transition involves F_2 (upper) and F_1 (lower) spin components. Figure S1 illustrates labels for $^2\Pi_\Omega$ Ryd - $A^2\Sigma^+$ (0,1) transitions using Hund's case (a) notation.
- ²⁴ The OH $X^2\Pi_\Omega$ state is denoted with vibration (v''), rotation (J''), spin-orbit (Ω or F_i'), and parity (+/-) labels. The same notation (without primes) is used for $^2\Pi$ Ryd states.

- ²⁵ See supplementary material at <http://dx.doi.org/10.1063/1.4948640> E-JCPSA6-144-042618 for further information on the $^2\Pi$ Ryd- $A^2\Sigma^+$ transitions, an additional VUV spectrum originating from $N'=4$, and enhancement factors.
- ²⁶ Total energies are rigorous for F_1' components, and will differ by less than 1 cm^{-1} for F_2' components of the $^2\Pi$ Ryd states.
- ²⁷ R. Hilbig, G. Hilber, A. Lago, B. Wolff, and R. Wallenstein, *Comments At. Mol. Phys* **18**, 157 (1986).
- ²⁸ J. P. Marangos, N. Shen, H. Ma, M. H. R. Hutchinson, and J. P. Connerade, *J. Opt. Soc. Am. B* **7**, 1254 (1990).
- ²⁹ W. Kong, D. Rodgers, and J. W. Hepburn, *J. Chem. Phys* **99**, 8471 (1993).
- ³⁰ C. Jungen, *J. Chem. Phys.* **53**, 4168 (1970).
- ³¹ P. F. Bernath, *Spectra of Atoms and Molecules* (Oxford University Press, New York, 1995).
- ³² A. J. Merer, D. N. Malm, R. W. Martin, M. Horani, and J. Rostas, *Can. J. Phys.* **53**, 251 (1975).
- ³³ G. Herzberg, *Molecular Spectra and Molecular Structure: Spectra of Diatomic Molecules* (Van Nostrand Reinhold Company, New York, 1950).
- ³⁴ R. S. Mulliken and A. Christy, *Phys. Rev.* **38**, 87 (1931).
- ³⁵ J. M. Brown, M. Kaise, C. M. L. Kerr, and D. J. Milton, *Mol. Phys.* **36**, 553 (1978).
- ³⁶ H. Lefebvre-Brion and R. W. Field, *Perturbations in the Spectra of Diatomic molecules* (Academic Press, Inc., New York, 1986).
- ³⁷ G. H. Dieke and H. M. Crosswhite, *J. Quant. Spectrosc. Radiat. Transfer* **2**, 97 (1961).

CHAPTER 3

UV spectroscopic characterization of dimethyl- and ethyl-substituted carbonyl oxides

This research has been published in the Journal of Physical Chemistry A, **118**(12), 2298 (2014). The research and was performed with graduate student Fang Liu, postdoctoral researcher Dr. Joseph Beames, and Prof. Marsha I. Lester in the *Department of Chemistry, University of Pennsylvania*.

I. Introduction

A major loss pathway for alkenes in the troposphere is through their reaction with ozone, which generates oxygenated compounds and free radicals of atmospheric significance, including OH, HO₂, CO, CO₂, CH₃, and H₂CO.¹ Ozonolysis of large alkenes, such as terpenes, which dominate global alkene emissions, yields semi-volatile products that are likely to be partitioned into the condensed phase and lead to the formation of secondary organic aerosols.² Gas phase ozonolysis is generally understood to proceed through the Criegee mechanism,³ which is initiated by cycloaddition of ozone across the alkene double bond producing an internally excited primary ozonide. The primary ozonide undergoes rapid unimolecular dissociation to carbonyl and carbonyl oxide species, the latter known as Criegee intermediates. The Criegee intermediates are produced with a large degree of internal excitation that often results in unimolecular decay to OH radicals.⁴ The internally excited Criegee intermediates can also undergo collisional stabilization and/or reaction with other atmospheric species, such as NO₂, SO₂, HO_x and H₂O.⁵⁻⁷ Recent experiments in this laboratory have revealed an additional daytime loss pathway arising from solar photolysis.⁸⁻⁹

Naturally abundant alkenes vary widely in size and complexity, ranging from the simplest ethene to larger terpenes, and upon ozonolysis generate Criegee intermediates with a variety of substituent groups. Terminal alkenes are most abundant,¹⁰⁻¹¹ and generate the simplest Criegee intermediate CH₂OO. Alkenes with internal double bonds account for a smaller portion of the total emissions from anthropogenic and biogenic sources; nevertheless, ozonolysis of these internal alkenes may contribute significantly to

the tropospheric HO_x budget.¹² Ozonolysis of branched internal alkenes with (CH₃)₂C=C structural unit such as terpinolene, a monoterpene associated with secondary organic aerosol formation,² will yield a dimethyl-substituted Criegee intermediate (CH₃)₂COO. An ethyl-substituted Criegee intermediate CH₃CH₂CHOO can be generated from some linear internal alkenes or 1-butene, a common emission from fuel combustion and biomass burning.¹⁰ Asymmetric alkenes will yield two different Criegee intermediates with substituents from each side of the original C=C bond. As a result, when considering alkene sources of (CH₃)₂COO and CH₃CH₂CHOO, we will refer to ozonolysis of the symmetric alkenes 2,3-dimethyl-2-butene and *E*-3-hexene. The nature and location of the substituents on the Criegee intermediate are expected to influence their atmospheric fate, including UV photolysis rate,⁸ bimolecular reaction rates with NO₂, SO₂ and H₂O,^{7, 13} and unimolecular decomposition into OH.^{4, 14}

Ozone-alkene reactions have long been a subject of atmospheric interest as a non-photolytic source of OH. The OH radical yield has been investigated for a series of alkenes, and the OH yield is found to increase from ethene to alkyl substituted alkenes, approaching unity in highly branched alkenes.^{1, 14-15} The OH radical products are believed to be generated from unimolecular decomposition of Criegee intermediates. The increased OH yields for the larger Criegee intermediates are indicative of faster rates for unimolecular decay to OH relative to other channels, e.g. collisional stabilization, bimolecular reactions, and/or solar photolysis.

Six prototypical Criegee intermediates have been identified as characteristic of the dominant carbonyl oxide species in the atmosphere.⁶ Three of these have recently been

detected by VUV photoionization under thermal and/or jet-cooled conditions: CH₂OO and *syn*- and *anti*-CH₃CHOO.^{8-9, 13, 16} Of these, both CH₂OO and *syn*-CH₃CHOO have been further characterized by their UV absorption spectra under jet-cooled conditions in this laboratory.⁸⁻⁹ There is also a recent report of the UV absorption spectrum for CH₂OO under thermal conditions.¹⁷ The latter may have hot band contributions to the spectrum in analogy with isoelectronic ozone.¹⁸⁻²⁰ In addition, CH₂OO has been characterized using Fourier transform IR and MW spectroscopy by the Y.P. Lee, Nakajima and Endo, and McCarthy groups;²¹⁻²³ Nakajima and Endo have also reported the pure rotational spectrum of *syn*-CH₃CHOO.²⁴

This paper presents the first identification of the fourth prototypical Criegee intermediate (CH₃)₂COO as well as its structural isomer CH₃CH₂CHOO via VUV photoionization and UV absorption spectroscopy. The methyl- and ethyl-substituted Criegee intermediates CH₃CHOO, (CH₃)₂COO, and CH₃CH₂CHOO can be viewed as proxies for carbonyl oxides with longer alkyl side chains. Weak electron-donating alkyl substituents may influence the π electron density localized on the COO subunit of the Criegee intermediate, potentially changing the biradical vs. zwitterionic character, and thus the C-O and O-O bond lengths.⁷ We utilize the strong $\pi^* \leftarrow \pi$ transition for identification and characterization of the alkyl-substituted carbonyl oxides.

Previous studies in this laboratory have investigated the UV absorption spectra of jet-cooled CH₂OO and CH₃CHOO, which are generated from diiodo precursors in a quartz capillary reactor and detected in a time-of-flight mass spectrometer with fixed frequency VUV ionization at 118 nm (10.5 eV).⁸⁻⁹ UV excitation resonant with the B-X

transition depletes the ground state population and results in reduced ion signals for the Criegee intermediates, which enables laboratory measurements of their UV absorption spectra. The absorption spectra of CH₂OO and CH₃CHOO peak at 335 nm and 320 nm, respectively, with large absorption cross sections ($\sim 5 \times 10^{-17} \text{ cm}^2 \text{ molec}^{-1}$). The excited B state potential energy surface is repulsive along the O-O coordinate, which results in rapid dissociation of the jet-cooled Criegee intermediates upon electronic excitation from 280-420 nm. At the lowest dissociation asymptote, the photolysis products are singlet aldehydes and O ¹D.⁸⁻⁹ A recent study in this laboratory utilized velocity map imaging to characterize the velocity and angular distributions of the O ¹D products following UV photodissociation of CH₂OO, and determine an upper limit for the CH₂OO X ¹A' dissociation energy of 54 kcal mol⁻¹.²⁵

The present study focuses on the UV absorption spectra of the dimethyl- and ethyl-substituted Criegee intermediates, (CH₃)₂COO and CH₃CH₂CHOO, under jet-cooled conditions, and comparison of their spectra with those previously reported for the CH₂OO and CH₃CHOO Criegee intermediates.⁸⁻⁹ The solar photolysis rates for the alkyl-substituted Criegee intermediates are then derived and compared with that for CH₂OO. In our experimental setup, OH radicals are detected simultaneously with the Criegee intermediates in the mass spectrum. The OH yields are scaled relative to the parent Criegee intermediates and compared for different substituents. Finally, the stationary points along the reaction coordinate from the Criegee intermediate to OH products are computed to facilitate comparison among the systems.

II. Methods

The Criegee intermediates are generated and detected following the procedures described previously for CH_2OO and CH_3CHOO .⁸⁻⁹ In this study, $(\text{CH}_3)_2\text{COO}$ and $\text{CH}_3\text{CH}_2\text{CHOO}$ are produced from 2,2-diiodopropane $(\text{CH}_3)_2\text{CI}_2$ and 1,1-diiodopropane $\text{CH}_3\text{CH}_2\text{CHI}_2$ precursors, respectively, which are synthesized using the method outlined below. The precursors are seeded in 20% O_2/Ar carrier gas at 25 psi and pulsed from a solenoid valve into a quartz capillary tube (1 mm ID) reactor. The precursors are photolyzed with 248 nm radiation from an excimer laser (Coherent, COMPex 102) along the length of the capillary tube and the iodo-propyl fragments subsequently react with O_2 to produce the Criegee intermediates. The resultant gas mixture undergoes supersonic expansion on exiting the capillary tube and travels ~4 cm downstream to the interaction region of a time-of-flight mass spectrometer (TOF-MS), where it is intersected at right angles by counter-propagating UV and 118 nm VUV laser beams.

Fixed frequency VUV radiation at 118 nm is generated by frequency tripling the third harmonic of an Nd:YAG laser (Continuum Powerlite 9010) at 355 nm (50 mJ/pulse) in a phase-matched Xe/Ar gas mixture. The 118 nm VUV laser is used for one photon ionization of the Criegee intermediates and the resultant $m/z=74$ ions are detected by TOF-MS. For UV spectroscopic studies, an unfocussed UV laser fires ~100 ns prior to the VUV photoionization laser. The UV laser excites the Criegee intermediates to the B state, which induces depletion of the ionization signal. The tunable UV radiation is generated by frequency doubling the output of Nd:YAG (Continuum Surelite II) pumped dye laser (ND 6000) using various dyes (Rhodamine 590, 610, 640; DCM; LDS 698, 750

and dye mixtures) and calibrated with a wavemeter (Coherent Wavemaster) and a power meter (RJ-F7100, Laser Precision Corp.). The measurements are performed at UV wavelengths near the peak output of each laser dye, enabling the dye laser to function with optimum efficiency and stability.

Hydroxyl radicals are ionized using a state-selective 1+1' resonance enhanced multiphoton ionization scheme (REMPI),²⁶⁻²⁷ which combines resonant OH A-X (1,0) excitation on the R₁(1.5) line at 281.5 nm with VUV ionization at 118 nm, the latter being the same VUV laser utilized for single-photon ionization of the Criegee intermediates. As a result, OH radicals can be detected at m/z=17 concurrently with the Criegee intermediates in the TOF-MS.

The 2,2-diiodopropane and 1,1-diiodopropane precursors are synthesized following a slightly adapted version of the methods developed by Pross and Sternhell.²⁸ Acetone (Fisher Scientific, ≥99.5%) or propionaldehyde (Acros Organics, 99+%) is added dropwise to hydrazine monohydrate (Acros Organics, 100%) to obtain crude hydrazones. Triethylamine (Acros Organics, 99.7%) and a saturated iodine (Acros Organics) solution in ether are added to the hydrazine to obtain the final products, which are isolated by Kugelrohr distillation. The diiodo products are confirmed by ¹H NMR.

Vertical ionization energies are obtained by single point energy calculations of neutral and cationic species at the CCSD(T)/aug-cc-pVTZ level of theory based on B3LYP/aug-cc-pVTZ optimized neutral ground state geometries. Energetics of the Criegee intermediates, transition states, and vinylhydroperoxides are determined from CCSD(T)/6-311+G(2d,p) single point calculations with geometries optimized at the

B3LYP/6-311+G(2d,p) level. The CCSD(T) energies at each stationary point are zero point energy (ZPE) corrected using DFT frequencies, and the dissociation limit is further corrected for basis set superposition error at the CCSD(T) level. The calculations are carried out with the Gaussian 09 suite of programs.²⁹

III. Results

The dimethyl- and ethyl-substituted Criegee intermediates, $(\text{CH}_3)_2\text{COO}$ and $\text{CH}_3\text{CH}_2\text{CHOO}$, illustrated in Figure 1, are separately generated in a pulsed supersonic expansion by 248 nm photolysis of $(\text{CH}_3)_2\text{Cl}_2$ and $\text{CH}_3\text{CH}_2\text{CHI}_2$ precursors, respectively, and reaction with O_2 in a quartz capillary tube. The Criegee intermediates are ionized by fixed frequency VUV radiation at 118 nm (10.5 eV) and detected on the parent mass channel at $m/z=74$ in a TOF-MS. The photon energy exceeds the calculated vertical ionization energies of 8.71 eV for $(\text{CH}_3)_2\text{COO}$ and 9.14 eV and 8.96 eV for the *syn* and *anti* conformers of $\text{CH}_3\text{CH}_2\text{CHOO}$. The generation and detection of the Criegee intermediates are analogous to prior studies of the smaller Criegee intermediates CH_2OO and CH_3CHOO .⁸⁻⁹ Since $(\text{CH}_3)_2\text{COO}$ and $\text{CH}_3\text{CH}_2\text{CHOO}$ are detected using the same mass channel, blank measurements are performed between each sample change to eliminate any interference from the other isomeric species. Figure 2 shows representative ion signals arising from single photon VUV ionization of $(\text{CH}_3)_2\text{COO}$ and $\text{CH}_3\text{CH}_2\text{CHOO}$.

Significant depletion of the ion signals is observed when unfocused UV laser radiation is introduced prior to the VUV photoionization laser as described above using a UV wavelength near the peak of the absorption spectrum for each Criegee intermediate.

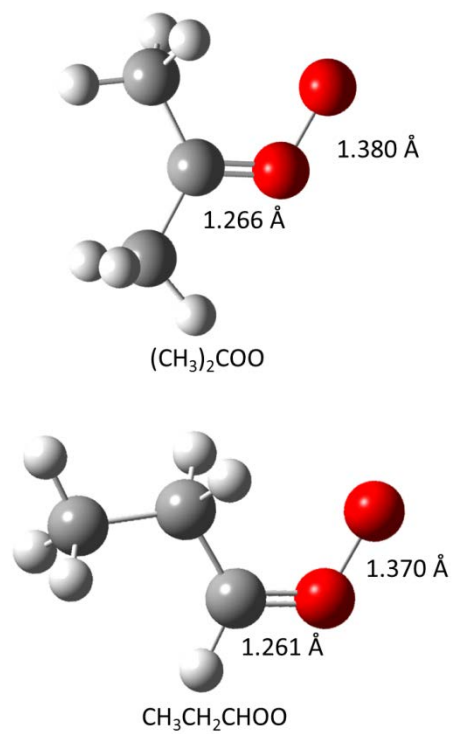


Figure 1. Minimum energy structures for (CH₃)₂COO and CH₃CH₂CHOO computed using B3LYP/6-311+G(2d,p). The O-O and C-O bond lengths are reported as descriptors of the π -character of the systems.

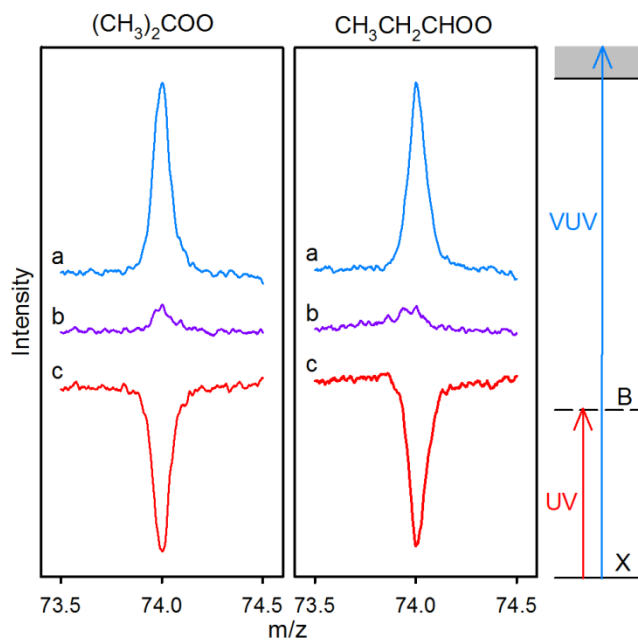


Figure 2. Time-of-flight mass spectra for $(\text{CH}_3)_2\text{COO}$ and $\text{CH}_3\text{CH}_2\text{CHOO}$, separately detected at $m/z=74$, arising from single photon ionization at 118 nm. The top traces (a) correspond to the photoionization signal of the Criegee intermediates. The middle traces (b) show the significantly depleted photoionization signals for $(\text{CH}_3)_2\text{COO}$ and $\text{CH}_3\text{CH}_2\text{CHOO}$ upon UV excitation at 323 and 322 nm, respectively. The bottom traces (c) illustrate the depletion [UV on (trace b) – UV off (trace a)] induced by UV excitation. The UV excitation and VUV ionization scheme is illustrated at right.

As shown in Figure 2, depletions far in excess of 50% are observed for $(\text{CH}_3)_2\text{COO}$ and $\text{CH}_3\text{CH}_2\text{CHOO}$ when excited at 323 and 322 nm, respectively. Similarly large depletions were observed previously for CH_2OO and CH_3CHOO when excited near the peak of their respective B-X transitions.⁸⁻⁹ Both experiment and theory indicate that excitation of CH_2OO to the B $^1\text{A}'$ state leads to dissociation,^{9,25} while *ab initio* calculations indicate that excitation of *syn*- and *anti*- CH_3CHOO to their B electronic states also leads to dissociation.⁸ The large depletions shown in Figure 3 indicate that promotion of the dimethyl- and ethyl-substituted Criegee intermediates on an analogous electronic transition also results in rapid dynamics, and likely leads to O-O bond cleavage as seen for CH_2OO .

The fractional (or percentage) depletion is determined as the change in the ion signal upon UV irradiation, $(N_0-N)/N_0$ (or multiplied by 100%), where N_0 and N correspond to the integrated ion signal intensity before and after UV irradiation, respectively. The magnitude of the UV-induced depletion is measured as a function of wavelength over the 288 to 368 nm range to obtain the absorption spectrum for each Criegee intermediate. The absorbance, $-\ln(N/N_0)$, signal scales linearly with UV laser power over the range utilized for spectroscopic measurements, indicating a one-photon process. The unfocussed UV laser power is typically set at ~ 1 mJ/pulse near the peak of the absorption profile; at much higher laser powers (e.g. ~ 2.5 mJ/pulse), the ground state depletion can approach 100%.

The absorption cross section $\sigma(\lambda)$ for each Criegee intermediate is then evaluated using $\sigma(\lambda) = -\ln(N/N_0)/\varphi(\lambda)$. Here, $\varphi(\lambda)$ is the UV photon fluence, which is the number of

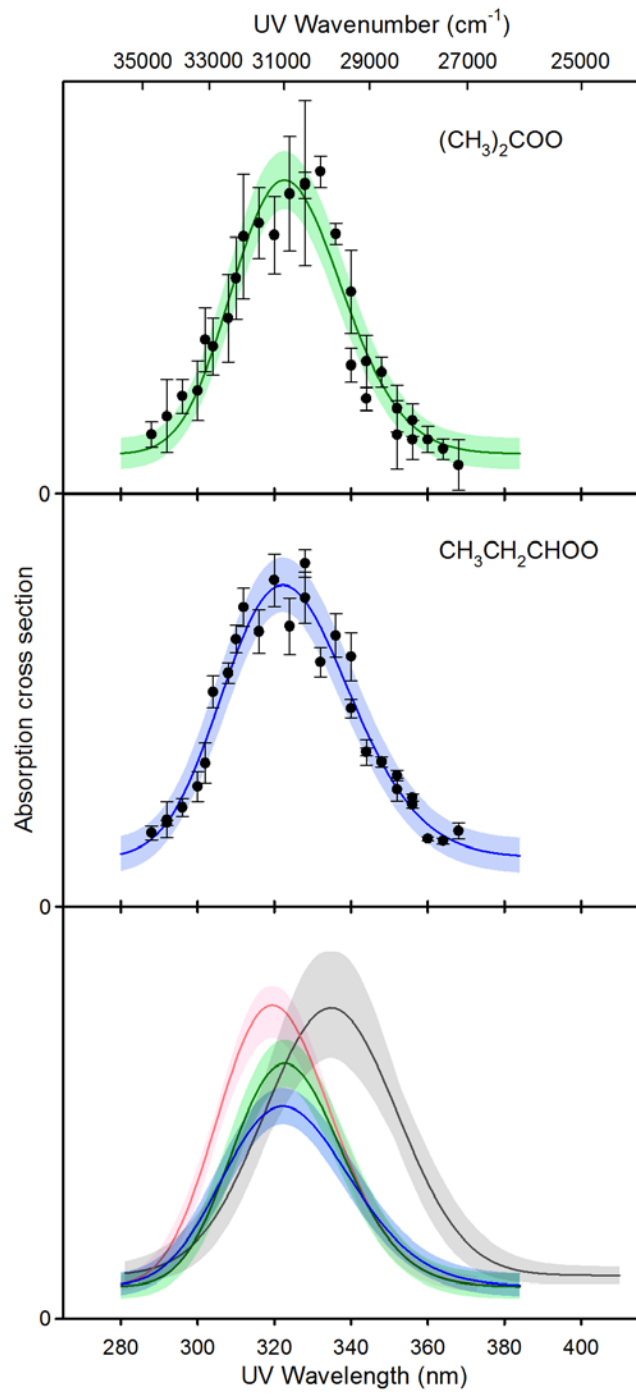


Figure 3. Experimental absorption spectra for jet-cooled $(\text{CH}_3)_2\text{COO}$ (upper panel) and $\text{CH}_3\text{CH}_2\text{CHOO}$ (middle panel) derived from UV-induced depletion of the VUV ionization signals at $m/z=74$. The smooth curves through the experimental data points correspond to Gaussian fits of the absorption spectra with the uncertainty in the fit indicated by the shaded regions. The fits to the UV spectra for $(\text{CH}_3)_2\text{COO}$ (green) and $\text{CH}_3\text{CH}_2\text{CHOO}$ (blue) are also compared with those reported previously⁸⁻⁹ for CH_3CHOO (red) and CH_2OO (black) Criegee intermediates (bottom panel).

UV photons per unit area ($\sim 6 \text{ mm}^2$ at 320 nm) in the interaction region. (A similar methodology has been utilized in determining the absorption cross section for ClOOCl.³⁰) Figure 3 shows the resultant broad UV absorption spectra of the Criegee intermediates $(\text{CH}_3)_2\text{COO}$ and $\text{CH}_3\text{CH}_2\text{CHOO}$ plotted as absorption cross section $\sigma(\lambda)$ vs. UV wavelength. The standard deviations (1σ) derived from repeated measurements at each wavelength are illustrated by the vertical error bars. Greater depletions of the Criegee intermediate signals are found near the peak wavelength (50%-60% at 320 nm) than those obtained at wavelengths on either side of the maximum (20%-30% at 290 and 360 nm) with similar UV pulse energies ($\sim 1 \text{ mJ}$). Each absorption spectrum is then fit using a simple Gaussian function with an offset; the nonzero offset arises from the detection limit of the depletion measurements ($\sim 3\%$). The experimental data and Gaussian fits for $(\text{CH}_3)_2\text{CO}$ and $\text{CH}_3\text{CH}_2\text{CHOO}$ are shown in separate panels in Figure 3, along with the uncertainty in each fit represented by shaded regions. The UV spectrum for $(\text{CH}_3)_2\text{COO}$ peaks at 323(2) nm with a breadth of 35 nm (3340 cm^{-1}) FWHM derived from the fit. The UV spectrum is quite similar for $\text{CH}_3\text{CH}_2\text{CHOO}$ with peak at 322(2) nm and FWHM of 39 nm (3740 cm^{-1}). The peak absorption cross sections for $(\text{CH}_3)_2\text{COO}$ and $\text{CH}_3\text{CH}_2\text{CHOO}$ are separately estimated to be ~ 4 and $\sim 3.5 \times 10^{-17} \text{ cm}^2 \text{ molec}^{-1}$. Clearly, the magnitude of the peak absorption cross sections indicates that these Criegee intermediates are strong UV absorbers, as found previously for CH_2OO and CH_3CHOO .⁸⁻

⁹ Experimental factors, such as inhomogeneity of the UV laser beam, suggest an uncertainty in the absolute cross sections on the order of a factor of 2.

The hydroxyl radical is an important unimolecular decay product of highly excited Criegee intermediates.^{4, 31-33} In our experimental setup, OH radicals are ionized using a state-selective 1+1' REMPI scheme²⁶⁻²⁷ that utilizes OH A-X (1-0) excitation as the resonant step followed by fixed frequency VUV ionization at 10.5 eV, which is the same laser utilized for photoionization of Criegee intermediates. This yields an OH ion signal at $m/z=17$ well separated from the Criegee intermediates ($m/z=74$) by flight time, and therefore enables direct, simultaneous detection of hydroxyl radicals along with the Criegee intermediates in a single time-of-flight mass spectrum. Since the OH radicals generated in the quartz capillary undergo cooling in the supersonic expansion before ionization, the OH A-X (1,0) UV excitation wavelength is fixed at the $R_1(1.5)$ line to probe the population in the ground rovibrational state. (Prior studies have demonstrated that the OH products are effectively cooled in the expansion.⁸) Figure 4 compares the OH signals ($m/z=17$) detected concurrently with the Criegee intermediates $(\text{CH}_3)_2\text{COO}$ and $\text{CH}_3\text{CH}_2\text{CHOO}$, and the OH signals detected in an analogous manner with the other smaller Criegee intermediates, CH_2OO and CH_3CHOO , as reported previously.⁸ No OH^+ signal is observed when UV laser is turned off or tuned off-resonance from the OH A-X $R_1(1.5)$ transition, verifying the assignment of the $m/z=17$ mass ion peak to OH radical. The amount of different Criegee intermediates generated in the molecular beam varies due to the vapor pressures of the diiodo precursors, photolysis efficiencies of the precursors at 248 nm, and possibly other factors. To compare the amount of OH produced with different Criegee intermediates, the integrated OH signal intensities are normalized to the Criegee intermediate mass signals in the same TOF-MS. Following

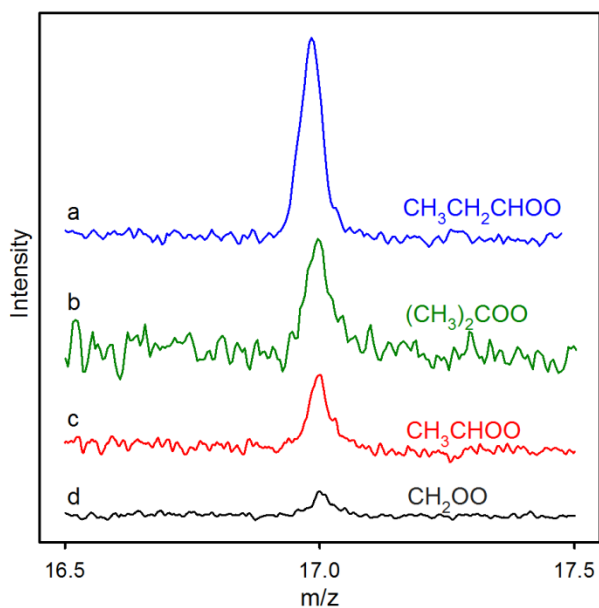


Figure 4. Hydroxyl radical photoionization signals detected concurrently with the Criegee intermediates (a) $\text{CH}_3\text{CH}_2\text{CHOO}$, (b) $(\text{CH}_3)_2\text{COO}$, (c) CH_3CHOO , and (d) CH_2OO ; the latter two were reported previously.⁸ OH radicals are detected by a 1+1' REMPI scheme utilizing OH A-X (1,0) $R_1(1.5)$ excitation and fixed frequency VUV ionization at 118 nm. The OH signals are scaled relative to the corresponding Criegee intermediate ion signals arising solely from VUV photoionization.

this procedure, $\text{CH}_3\text{CH}_2\text{CHOO}$ is found to be associated with the largest OH signal, followed by $(\text{CH}_3)_2\text{COO}$, and both are larger than that of CH_3CHOO and CH_2OO . The ratio of their normalized OH signal intensities are 10:6:4:1 (Table 1). The observed trend in OH signal intensities can be compared with the reported OH yields from alkene ozonolysis, as discussed below.

IV. Discussion

This laboratory has previously reported the intense UV absorptions on the B-X transitions of two smaller Criegee intermediates CH_2OO and CH_3CHOO under jet-cooled conditions, which peak at 320 and 335 nm with similar maximum absorption cross sections of $\sim 5 \times 10^{-17} \text{ cm}^2 \text{ molec}^{-1}$.⁸⁻⁹ The absorption features of CH_2OO and CH_3CHOO are relatively broad due to the repulsive nature of the upper B state in the O-O stretching coordinate. The methyl-substituted Criegee intermediate CH_3CHOO has two conformers, *syn* and *anti*, with a high interconversion barrier, $\sim 29\text{-}38 \text{ kcal mol}^{-1}$,^{4,34} due to the partial π -bonding character in the C-O bond.⁴ In the *syn* conformer, the methyl group lies on the same side as the terminal O atom, whereas in the *anti* conformer, they are on different sides. An intramolecular interaction between the terminal O and methyl H atoms stabilizes the ground state of *syn*- CH_3CHOO , which makes it the dominant species under both flow cell and free jet environments;^{8,13} this intermolecular interaction also destabilizes the excited B state by extending the π^* character of the carbonyl oxide onto the methyl hydrogens. The combined effect results in a conformer-specific spectral shift of the B-X transition for the *syn*-conformer of CH_3CHOO to shorter wavelength.⁸

The *syn* conformer of CH₃CHOO is predominant in photoionization, UV, and FTMW spectra.^{8, 13, 24}

The minimum energy structures for (CH₃)₂COO and CH₃CH₂CHOO are illustrated in Figure 1. The *syn*-conformer of CH₃CH₂CHOO is the global minimum and is expected to be prevalent in experiments. The *anti*-conformer of CH₃CH₂CHOO with the terminal O pointing away from the ethyl group lies ~1000 cm⁻¹ higher in energy. The structures are annotated with their respective C-O and O-O bond lengths. The bond lengths in (CH₃)₂COO are in good accord with those reported previously by Anglada et al.⁷ The ratio of O-O and C-O bond lengths has been proposed to be an effective probe of the π -system character, and an indicator of the relative zwitterionic vs. biradical nature of a Criegee intermediate. Both of these carbonyl oxides have an O-O to C-O bond length ratio of ~1.09, signifying that they have similar amounts of zwitterionic character as CH₃CHOO, but more zwitterionic character than CH₂OO (O-O/C-O ratio of ~1.076), as predicted for alkyl substituted Criegee intermediates.⁷

The overall absorption features for (CH₃)₂COO and CH₃CH₂CHOO (Figure 3) are very similar in their breadths and peak positions to the methyl-substituted Criegee intermediate CH₃CHOO. When a mixture of two diiodo precursors ((CH₃)₂CI₂ or CH₃CH₂CHI₂ with CH₃CHI₂) is prepared to probe the relative absorptions of different Criegee intermediates simultaneously, the UV-induced depletion on each Criegee intermediate mass peak differs, confirming their different absorption cross sections. Although their peak absorption cross sections are slightly lower, (CH₃)₂COO and

CH₃CH₂CHOO are still very strong UV absorbers with $\sigma_{\max} \sim 4$ and $\sim 3.5 \times 10^{-17}$ cm² molec⁻¹.

The agreement in peak position of CH₃CH₂CHOO with the conformer-specific shift of *syn*-CH₃CHOO is an experimental indication that CH₃CH₂CHOO is also likely formed predominantly in the *syn* conformation. The similarities of the peak positions also suggest analogous intramolecular interactions between the α -H and terminal O atoms in the Criegee intermediates (CH₃)₂COO and CH₃CH₂CHOO as found for *syn*-CH₃CHOO. This is confirmed by preliminary TDDFT calculations, in which the vertical excitation energy computed for *syn*-CH₃CH₂CHOO is shifted to higher energy than other conformers. Given the similarity of the spectra, it would be difficult to distinguish between these Criegee intermediates with different alkyl substitutions via UV spectroscopy.

The calculated ionization energies for (CH₃)₂COO and CH₃CH₂CHOO indicate that both Criegee intermediates can be detected with the fixed frequency VUV radiation. Other isomers with $m/z=74$ can also be ionized by a single 118 nm (10.5 eV) VUV photon process, notably dioxiranes, propanoic acid and methyl acetate. Specifically, dimethyl- and ethyl-substituted dioxiranes are calculated to have ionization energies of 10.24 and 10.47 eV, respectively. The ionization energies for stable isomers CH₃COOCH₃ (methyl acetate) and CH₃CH₂COOH (propanoic acid) have been previously determined to be 10.25 and 10.44 eV, respectively.³⁵ However, the possible contributions of these other isomers to the mass spectra can be eliminated based on the UV spectroscopic characterization. The absorption spectrum of dimethyl dioxirane peaks

at $\lambda_{\text{max}}=335$ nm ($\epsilon=10$) with a cross section in the order of 10^{-20} $\text{cm}^2\text{molec}^{-1}$,³⁶ ~3 orders of magnitude lower than that of the Criegee intermediates, and dioxirane species were not observed in previous photoionization studies with tunable VUV radiation.^{37, 21}

Carboxylic acids and esters have absorptions much further into the UV at ~200 nm,³⁸ which is outside of the current wavelength range (280-400 nm). Most importantly, the present UV absorption features attributed to $(\text{CH}_3)_2\text{COO}$ and $\text{CH}_3\text{CH}_2\text{CHOO}$ are consistent with other Criegee intermediates identified in previous studies in the laboratory performed under jet-cooled conditions with mass- and isomer-selectivity.⁸⁻⁹

The UV absorption of stabilized Criegee intermediates overlaps with the UV sunlight radiation penetrating the upper atmosphere to reach the troposphere, which will result in daytime photolysis of Criegee intermediates. The photochemical loss rate due to solar irradiation, k_p , can be estimated by combining the UV absorption cross section of the Criegee intermediates, $\sigma(\lambda)$, and the solar actinic flux for a 0° zenith angle at the Earth's surface, $F(\lambda)$:

$$k_p = \int_{\lambda} \varphi(\lambda)\sigma(\lambda)F(\lambda)d\lambda$$

where the photodissociation quantum yield $\varphi(\lambda)$ is assumed to be unity. The integration is carried out in the UV wavelength window (280-380 nm) over which the Criegee intermediates have a large absorption cross section under jet-cooled conditions, using a Gaussian fit of the UV absorption cross section $\sigma(\lambda)$ and a 6th order polynomial fit of the solar actinic flux $F(\lambda)$. The corresponding solar photolysis lifetime $\tau = (k_p)^{-1}$ obtained for $(\text{CH}_3)_2\text{COO}$ and $\text{CH}_3\text{CH}_2\text{CHOO}$ are predicted to be ~1.1 s and ~1.3 s respectively, whereas the lifetime of CH_2OO and CH_3CHOO calculated in the same manner are

estimated to be ~ 0.5 s and ~ 1 s, respectively. These photolysis lifetimes supersede our previous estimates.⁸⁻⁹ The photolysis lifetimes of the larger alkyl substituted Criegee intermediates $(\text{CH}_3)_2\text{COO}$ and $\text{CH}_3\text{CH}_2\text{CHOO}$ are quite similar to that of CH_3CHOO , and a little longer than CH_2OO , as expected based on the shift of the absorption to shorter wavelength, resulting in decreased overlap with the solar actinic flux, as well as the slightly reduced peak absorption cross sections. Note that the solar photolysis rates of Criegee intermediates may increase under thermal conditions in the atmosphere due to hot band contributions on the red edge of the absorption spectrum.¹⁷

The photolysis rates of the Criegee intermediates can be compared with the bimolecular loss rate from reactions with other atmospheric species. These reactions have been extensively investigated in the theoretical literature,⁵⁻⁷ and direct experimental determinations of the bimolecular loss rate constants have been reported for the reaction of SO_2 and NO_2 with CH_2OO and *syn/anti*- CH_3CHOO and reaction of water with *anti*- CH_3CHOO .^{13, 16, 37} Given an average atmospheric concentration (2 ppb SO_2 , 11 ppb NO_2), the corresponding loss rates of Criegee intermediates in the troposphere can be estimated to be approximately $1\text{-}2\text{ s}^{-1}$, which is comparable to the solar photolysis rate ($\sim 1\text{ s}^{-1}$).^{1, 8-9} The reactivity of the Criegee intermediates is predicted to be strongly influenced by the nature and location of the substituents.⁶⁻⁷ In a theoretical study on the reaction of Criegee intermediates with water, some large alkyl substitutions were found to reduce the reaction rates by several orders of magnitude.⁷ However, the nature of the alkyl substituent (methyl, dimethyl, ethyl) does not appear to significantly change the characteristic UV absorption spectrum of the Criegee intermediates or solar photolysis

rate. This suggests that the relative rates for bimolecular reaction and solar photolysis may change upon alkyl substitution.

Energized Criegee intermediates are known to produce OH radicals via unimolecular decomposition.^{4, 31-33, 39} In our experimental setup, OH radicals are produced concurrently with the Criegee intermediates in the capillary reactor tube prior to supersonic expansion, and detected in the same mass spectrum as the Criegee intermediates. The absolute yield of OH radicals is not determined because the ionization efficiencies for OH and the Criegee intermediates are not known; nevertheless, the signal intensities for OH relative to the Criegee intermediates are measured and compiled in Table 1. This data is compared with the reported OH yields from ozonolysis of symmetrical alkenes that exclusively produce the Criegee intermediates of interest.^{11, 15, 40} For the Criegee intermediates CH₂OO, CH₃CHOO and (CH₃)₂COO, the relative OH signal intensities are consistent with the trend of OH yields in the ozonolysis reactions. However, a greater amount of OH is observed with the ethyl-substituted Criegee intermediate CH₃CH₂CHOO than expected based on the OH yield reported for ozonolysis of *E*-3-hexene.^{11, 40}

Two unimolecular reaction mechanisms are predicted for OH formation from Criegee intermediates. CH₂OO and *anti*-conformers of CH₃CHOO and CH₃CH₂CHOO are expected to produce OH through isomerization to dioxirane with a high activation barrier,⁴⁰⁻⁴² resulting in a relatively low OH yield. The production of OH from (CH₃)₂COO and the *syn* conformers is predicted to preferentially follow a vinyl hydroperoxide (VHP, with general structure R₁R₂C=C(R₃)-OOH) channel, where the

Table 1. Photoionization signals for OH radicals relative to those for Criegee intermediates measured concurrently are compared with OH yields reported from ozonolysis of alkenes.

Criegee intermediate	Alkene	Reported OH yield	OH signal ratio ^c
CH ₂ OO	Ethene	0.16 ^a	1
CH ₃ CHOO	<i>E</i> -2-Butene	0.64 ^a	4
(CH ₃) ₂ COO	2,3-Dimethyl-2-Butene	0.90 ^a	6
CH ₃ CH ₂ CHOO	<i>E</i> -3-Hexene	0.53 ^b	10

^a Ref. 15

^b Refs. 11, 40

^c Relative OH ion signals scaled to that observed with CH₂OO.

migration of an α -H on the alkyl group to the terminal O leads to formation of VHP, which subsequently dissociates to OH + vinoxy radicals by breaking the O-O bond.^{4, 41-42} The VHP channel is predicted to be more favorable because of its lower activation barrier.^{1, 4, 31} An increased OH yield is reported for ozonolysis of internal alkenes and highly branched alkenes via formation and unimolecular dissociation of alkyl-substituted Criegee intermediates, presumably through the VHP channel.^{1, 11, 15}

The VHP channel consists of two steps: VHP formation and homolysis as illustrated in Figure 5. The barriers (TS) connecting the Criegee intermediates to the associated VHP have been investigated in previous computational studies, with barrier heights estimated to be ~ 14.8 - 21.2 kcal mol⁻¹;⁵ the barriers are predicted to be similar (within ± 1 kcal mol⁻¹) for CH₃CHOO and (CH₃)₂COO.^{32-33, 42-43} However, the barrier separating CH₃CH₂CHOO from its corresponding VHP has not been reported previously.

In the present work, the barriers between the Criegee intermediates and associated VHP are computed for (CH₃)₂COO, *syn*-CH₃CHOO and *syn*-CH₃CH₂CHOO using the same electronic structure method/basis [CCSD(T)/6-311+G(2d,p)//B3-LYP/6-311+G(2d,p)] to facilitate comparison, and the results are given in Table 2. *Syn*-CH₃CH₂CHOO forms the *trans*-VHP species CH₃CH=CHOOH. The transition state (TS) geometry has a 5-membered ring structure, with an H atom bridged between the α -carbon atom and terminal O. After including zero-point energy corrections at the transition state, the barriers for (CH₃)₂COO, CH₃CHOO and CH₃CH₂CHOO are similar at ~ 17 kcal mol⁻¹. The ZPE corrected barrier for CH₃CHOO is consistent with a recently published value (17.91 kcal mol⁻¹),⁴⁴ yet lower than the predicted barrier for

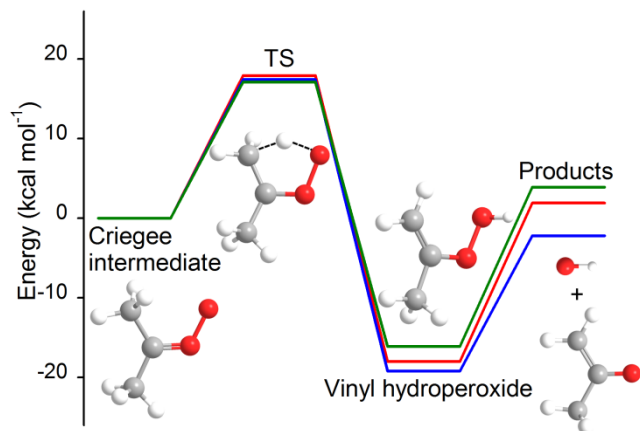


Figure 5. Reaction coordinates for decomposition of Criegee intermediates *syn*-CH₃CHOO (red), (CH₃)₂COO (green), and *syn*-CH₃CH₂CHOO via 1,4-H shift to vinyl hydroperoxides (VHP) and OH radical products. The geometric structures of the stationary points for the (CH₃)₂COO system are shown. All energies are obtained at the ZPE-CCSD(T)/6-311+G(2d,p) level, and are shown relative to Criegee intermediates (set to zero).

Table 2. Stationary points computed along the reaction coordinate from Criegee intermediates (set to zero) to vinyl hydroperoxide (VHP) and OH + vinoxy products using CCSD(T)/6-311+G(2d,p) and including zero-point energy (ZPE) corrections. Product asymptotes are corrected for basis set superposition error. Comparisons with recent computational results are shown where available.

Criegee intermediate	Energy (kcal mol ⁻¹)			
	TS ^a	VHP	Products	
CH ₃ CHOO	17.9 (17.9 ^b , 16.7 ^c)	-18.0 (-17.62 ^b)	1.9	19.9 ^d (26.4 ^e)
(CH ₃) ₂ COO	17.1 (16) ^c	-16.1 (-13.9) ^f	3.9	20.0 ^d (26.3 ^e)
CH ₃ CH ₂ CHOO	17.4	-19.2	-2.2	17.0 ^d (22.7 ^e)

^a TS is the barrier separating the Criegee intermediate from VHP.

^b Ref. 44

^c Ref. 33

^d Energy of products relative to VHP.

^e Ref. 45; energy of products relative to VHP and without ZPE corrections.

^f Ref. 42

interconversion between *syn* and *anti* conformers ($\sim 29\text{-}38\text{ kcal mol}^{-1}$ for CH_3CHOO).^{4, 34} Moreover, the transition state is significantly lower than the energy released upon ozonolysis of alkenes ($\sim 50\text{ kcal mol}^{-1}$).³¹ Due to the similarity of the barriers at the transition state, similar rates of formation for VHP can be expected from the Criegee intermediates $(\text{CH}_3)_2\text{COO}$, CH_3CHOO and $\text{CH}_3\text{CH}_2\text{CHOO}$ in the first step.

The second step involves O-O bond breakage of VHP leading to OH and vinyloxy products. The energetics of this dissociative process have been computed for each of the Criegee intermediates under investigation in this work and are shown both in Figure 1 and Table 2. A recent computational study by Kurten et al.⁴⁵ also investigated the reaction coordinate for the dissociation of several alkyl-substituted VHPs, deriving asymptotic dissociation energies and identifying a submerged barrier in the dissociation coordinate. Their results with energies relative to VHP are included for comparison in Table 2. Both the current study and the previous theoretical investigation show the product asymptotes are lower for $\text{CH}_3\text{CH}_2\text{CHOO}$ than for $(\text{CH}_3)_2\text{COO}$ and CH_3CHOO .⁴⁵ Most significantly, the $\text{CH}_3\text{CH}_2\text{CHOO}$ VHP dissociation asymptote is exothermic relative to the stabilized Criegee intermediate. For $\text{CH}_3\text{CH}_2\text{CHOO}$, the terminal methyl substitution on R_1 or R_2 in $\text{R}_1\text{R}_2\text{C}=\text{C}(\text{R}_3)\text{-OOH}$ was found to stabilize the vinyloxy products and lower the net reaction energy.⁴⁵ The lower product asymptote for the ethyl- vs. methyl-substituted systems may increase the OH yield relative to VHP stabilization. This would be consistent with our observation of a larger OH signal from the ethyl-substituted Criegee intermediate $\text{CH}_3\text{CH}_2\text{CHOO}$ than $(\text{CH}_3)_2\text{COO}$ and CH_3CHOO . However, the reported OH yield from ozonolysis of *E*-3-hexene is not consistent with this

trend,^{11, 40} suggesting the need for direct detection of the Criegee intermediates and OH products arising from alkene ozonolysis.

V. Conclusions

Very strong UV absorption spectra arising from the B-X transitions, nominally $\pi^* \leftarrow \pi$ transitions localized on the carbonyl oxide group, of the alkyl-substituted Criegee intermediates $(\text{CH}_3)_2\text{COO}$ and $\text{CH}_3\text{CH}_2\text{CHOO}$ are observed with peaks at ~ 320 nm and cross sections approaching $\sim 4 \times 10^{-17} \text{ cm}^2 \text{ molec}^{-1}$. In both cases, the UV absorption is detected as a significant depletion of the $m/z=74$ ion signal obtained by subsequent VUV photoionization at 10.5 eV. The large depletions – approaching 100% – are indicative of rapid dynamics in the excited B state, most likely due to direct dissociation as found for CH_2OO .^{9, 25} The UV spectra are analogous to that obtained previously for *syn*- CH_3CHOO ,⁸ although shifted relative to CH_2OO ,⁹ indicating a similar intramolecular interaction between an α -H and the terminal O of the COO group in the alkyl-substituted Criegee intermediates. This interaction may facilitate a 1,4-hydrogen shift and lead to OH production upon unimolecular dissociation of the VHP intermediate.^{4, 8, 33} Solar photochemical loss rates for $(\text{CH}_3)_2\text{COO}$ and $\text{CH}_3\text{CH}_2\text{CHOO}$ are estimated, assuming unit photodissociation quantum yields, which suggest different daytime vs. nighttime behavior for these alkyl-substituted Criegee intermediates. OH radical products are observed concurrently with the Criegee intermediates $(\text{CH}_3)_2\text{COO}$ and $\text{CH}_3\text{CH}_2\text{CHOO}$. The OH^+ signals relative to those of the corresponding Criegee intermediates are compared with the reported OH yields in the reactions of alkenes with ozone.^{8, 11, 15, 40} The trends are consistent with OH products increasing according to $\text{CH}_2\text{OO} <$

$\text{CH}_3\text{CHOO} < (\text{CH}_3)_2\text{COO}$. However, the OH signal observed with $\text{CH}_3\text{CH}_2\text{CHOO}$ is greater than expected based on the OH yield from ozonolysis of *E*-3-hexene.^{11,40} The stationary points along the reaction coordinates leading to VHP intermediates and OH products are computed at the same level of theory for the methyl-, dimethyl-, and ethyl-substituted Criegee intermediates to facilitate comparison. A more energetically favorable dissociation to OH products may help explain the greater OH yield from $\text{CH}_3\text{CH}_2\text{CHOO}$, although modeling of the competition between VHP stabilization and dissociation is still required. Further experimental studies with direct detection of the Criegee intermediates and OH products arising from alkene ozonolysis are also needed.

Acknowledgements

This research was supported, in part, through the National Science Foundation under Grant CHE-1112016. J.M.B. acknowledges support through the Dreyfus Postdoctoral Program in Environmental Chemistry (EP-12-025). Acknowledgment is made to the Donors of the American Chemical Society Petroleum Research Fund for partial support of this research (ACS PRF 53320-ND6). The authors thank David Chenoweth and his group for help in synthesis of the diiodo precursors. The authors thank Jim Lin (Academia Sinica) for sharing his UV absorption spectrum of CH_2OO under thermal conditions prior to publication.

References

- ¹ Finlayson-Pitts, B. J.; Pitts, J. N. *Chemistry of the Upper and Lower Atmosphere*. Academic Press: San Diego, 2000.
- ² Kroll, J. H.; Seinfeld, J. H. Chemistry of Secondary Organic Aerosol: Formation and Evolution of Low-Volatility Organics in the Atmosphere. *Atmos. Environ.* **2008**, *42*, 3593-3624.
- ³ Criegee, R. Mechanism of Ozonolysis. *Angew. Chem., Int. Ed.* **1975**, *14*, 745-752.
- ⁴ Johnson, D.; Marston, G. The Gas-Phase Ozonolysis of Unsaturated Volatile Organic Compounds in the Troposphere. *Chem. Soc. Rev.* **2008**, *37*, 699-716.
- ⁵ Vereecken, L.; Francisco, J. S. Theoretical Studies of Atmospheric Reaction Mechanisms in the Troposphere. *Chem. Soc. Rev.* **2012**, *41*, 6259-6293.
- ⁶ Vereecken, L.; Harder, H.; Novelli, A. The Reaction of Criegee Intermediates with NO, RO₂, and SO₂, and Their Fate in the Atmosphere. *Phys. Chem. Chem. Phys.* **2012**, *14*, 14682-14695.
- ⁷ Anglada, J. M.; Gonzalez, J.; Torrent-Sucarrat, M. Effects of the Substituents on the Reactivity of Carbonyl Oxides. A Theoretical Study on the Reaction of Substituted Carbonyl Oxides with Water. *Phys. Chem. Chem. Phys.* **2011**, *13*, 13034-13045.
- ⁸ Beames, J. M.; Liu, F.; Lu, L.; Lester, M. I. UV Spectroscopic Characterization of An Alkyl Substituted Criegee Intermediate CH₃CHOO. *J. Chem. Phys.* **2013**, *138*, 244307.
- ⁹ Beames, J. M.; Liu, F.; Lu, L.; Lester, M. I. Ultraviolet Spectrum and Photochemistry of the Simplest Criegee Intermediate CH₂OO. *J. Am. Chem. Soc.* **2012**, *134*, 20045-20048.

- ¹⁰ Nriagu, J. O. *Gaseous Pollutants: Characterization and Cycling*. John Wiley & Sons, Inc: New York, 1992; Vol. 24.
- ¹¹ Orzechowska, G. E.; Paulson, S. E. Production of OH Radicals from the Reactions of C4-C6 Internal Alkenes and Styrenes with Ozone in the Gas Phase. *Atmos. Environ.* **2002**, *36*, 571-581.
- ¹² Paulson, S. E.; Orlando, J. J. The Reactions of Ozone with Alkenes: An Important Source of HO_x in the Boundary Layer. *Geophys. Res. Lett.* **1996**, *23*, 3727-3730.
- ¹³ Taatjes, C. A.; Welz, O.; Eskola, A. J.; Savee, J. D.; Scheer, A. M.; Shallcross, D. E.; Rotavera, B.; Lee, E. P. F.; Dyke, J. M.; Mok, D. K. W., et al. Direct Measurements of Conformer-Dependent Reactivity of the Criegee Intermediate CH₃CHOO. *Science* **2013**, *340*, 177-180.
- ¹⁴ Fenske, J. D.; Hasson, A. S.; Ho, A. W.; Paulson, S. E. Measurement of Absolute Unimolecular and Bimolecular Rate Constants for CH₃CHOO Generated by the Trans-2-Butene Reaction with Ozone in the Gas Phase. *J. Phys. Chem. A* **2000**, *104*, 9921-9932.
- ¹⁵ IUPAC Subcommittee for Gas Kinetic Data Evaluation, Data sheet Ox_VOC3_O3, 2005. http://www.iupac-kinetic.ch.cam.ac.uk/datasheets/pdf/Ox_VOC3_O3_alkene.pdf
- ¹⁶ Taatjes, C. A.; Welz, O.; Eskola, A. J.; Savee, J. D.; Osborn, D. L.; Lee, E. P. F.; Dyke, J. M.; Mok, D. W. K.; Shallcross, D. E.; Percival, C. J. Direct Measurement of Criegee Intermediate (CH₂OO) Reactions with Acetone, Acetaldehyde, and Hexafluoroacetone. *Phys. Chem. Chem. Phys.* **2012**, *14*, 10391-10400.
- ¹⁷ Sheps, L. Absolute Ultraviolet Absorption Spectrum of a Criegee Intermediate CH₂OO. *J. Phys. Chem. Lett.* **2013**, *4*, 4201-4205.

- ¹⁸ Burrows, J. P.; Richter, A.; Dehn, A.; Deters, B.; Himmelmann, S.; Orphal, J. Atmospheric Remote-Sensing Reference Data from GOME - 2. Temperature-Dependent Absorption Cross Sections of O₃ in the 231-794 nm Range. *J. Quant. Spectrosc. Radiat. Transfer* **1999**, *61*, 509-517.
- ¹⁹ Orphal, J. A Critical Review of the Absorption Cross-Sections of O₃ and NO₂ in the Ultraviolet and Visible. *J. Photochem. Photobiol., A* **2003**, *157*, 185-209.
- ²⁰ Voigt, S.; Orphal, J.; Bogumil, K.; Burrows, J. P. The Temperature Dependence (203-293 K) of the Absorption Cross Sections of O₃ in the 230-850 nm Region Measured by Fourier-Transform Spectroscopy. *J. Photochem. Photobiol., A* **2001**, *143*, 1-9.
- ²¹ Su, Y.-T.; Huang, Y.-H.; Witek, H. A.; Lee, Y.-P. Infrared Absorption Spectrum of the Simplest Criegee Intermediate CH₂OO. *Science* **2013**, *340*, 174-176.
- ²² Nakajima, M.; Endo, Y. Communication: Determination of the Molecular Structure of the Simplest Criegee Intermediate CH₂OO. *J. Chem. Phys.* **2013**, *139*, 101103.
- ²³ McCarthy, M. C.; Cheng, L.; Crabtree, K. N.; Martinez, O.; Nguyen, T. L.; Womack, C. C.; Stanton, J. F. The Simplest Criegee Intermediate (H₂C=O-O): Isotopic Spectroscopy, Equilibrium Structure, and Possible Formation from Atmospheric Lightning. *J. Phys. Chem. Lett.* **2013**, *4*, 4133-4139.
- ²⁴ Nakajima, M.; Endo, Y. Spectroscopic Characterization of An Alkyl Substituted Criegee Intermediate Syn-CH₃CHOO Through Pure Rotational Transitions. *J. Chem. Phys.*, *submitted* **2013**.

- ²⁵ Lehman, J. H.; Li, H. W.; Beames, J. M.; Lester, M. I. Communication: Ultraviolet Photodissociation Dynamics of the Simplest Criegee Intermediate CH₂OO. *J. Chem. Phys.* **2013**, *139*, 141103.
- ²⁶ Beames, J. M.; Liu, F.; Lester, M. I.; Murray, C. Communication: A New Spectroscopic Window on Hydroxyl Radicals Using UV Plus VUV Resonant Ionization. *J. Chem. Phys.* **2011**, *134*, 241102.
- ²⁷ Beames, J. M.; Liu, F.; Lester, M. I. 1+1' Resonant Multiphoton Ionisation of OH Radicals Via the A²Σ⁺ State: Insights from Direct Comparison with A-X Laser-Induced Fluorescence Detection. *Mol. Phys.* **2013**, DOI: 10.1080/00268976.2013.822592 (Published online: 18 Sep 2013).
- ²⁸ Pross, A.; Sternhell, S. Oxidation of Hydrazones with Iodine in Presence of Base. *Aust. J. Chem.* **1970**, *23*, 989-1003.
- ²⁹ Frisch, M. J.; Trucks, G. W.; Schlegel, H. B.; Scuseria, G. E.; Robb, M. A.; Cheeseman, J. R.; Scalmani, G.; Barone, V.; Mennucci, B.; Petersson, G. A.; et al. Gaussian 09, Revision D.01; Gaussian, Inc.: Wallingford CT, 2009.
- ³⁰ Chen, H. Y.; Lien, C. Y.; Lin, W. Y.; Lee, Y. T.; Lin, J. J. UV Absorption Cross Sections of ClOOCl Are Consistent with Ozone Degradation Models. *Science* **2009**, *324*, 781-784.
- ³¹ Donahue, N. M.; Drozd, G. T.; Epstein, S. A.; Presto, A. A.; Kroll, J. H. Adventures in Ozoneland: Down the Rabbit-Hole. *Phys. Chem. Chem. Phys.* **2011**, *13*, 10848-10857.
- ³² Kroll, J. H.; Clarke, J. S.; Donahue, N. M.; Anderson, J. G.; Demerjian, K. L. Mechanism of HO_x Formation in the Gas-Phase Ozone-Alkene Reaction. 1. Direct,

Pressure-Dependent Measurements of Prompt OH Yields. *J. Phys. Chem. A* **2001**, *105*, 1554-1560.

³³ Kroll, J. H.; Sahay, S. R.; Anderson, J. G.; Demerjian, K. L.; Donahue, N. M. Mechanism of HO_x Formation in the Gas-Phase Ozone-Alkene Reaction. 2. Prompt Versus Thermal Dissociation of Carbonyl Oxides to Form OH. *J. Phys. Chem. A* **2001**, *105*, 4446-4457.

³⁴ Kuwata, K. T.; Kujala, B. J.; Morrow, Z. W.; Tonc, E. Quantum Chemical and RRKM/Master Equation Studies of Cyclopropene Ozonolysis. *Comput. Theor. Chem.* **2011**, *965*, 305-312.

³⁵ Lias, S. G.; Bartmess, J. E.; Liebman, J. F.; Holmes, J. L.; Levin, R. D.; Mallard, W. G. In "Ion Energetics Data" in *NIST Chemistry WebBook, NIST Standard Reference Database Number 69*, Eds. P.J. Linstrom and W.G. Mallard, National Institute of Standards and Technology, Gaithersburg MD, 20899, <http://webbook.nist.gov>.

³⁶ Adam, W.; Chan, Y. Y.; Cremer, D.; Gauss, J.; Scheutzow, D.; Schindler, M. Spectral and Chemical-Properties of Dimethyldioxirane as Determined by Experiment and Abinitio Calculations. *J. Org. Chem.* **1987**, *52*, 2800-2803.

³⁷ Welz, O.; Savee, J. D.; Osborn, D. L.; Vasu, S. S.; Percival, C. J.; Shallcross, D. E.; Taatjes, C. A. Direct Kinetic Measurements of Criegee Intermediate (CH₂OO) Formed by Reaction of CH₂I with O₂. *Science* **2012**, *335*, 204-207.

³⁸ Feinstein, K. *Guide to Spectroscopic Identification of Organic Compounds*. CRC press: Boca Raton, 1995.

- ³⁹ Liu, Y.; Bayes, K. D.; Sander, S. P. Measuring Rate Constants for Reactions of the Simplest Criegee Intermediate (CH₂OO) by Monitoring the OH Radical. *J. Phys. Chem. A* **2014**, *118*, 741-747.
- ⁴⁰ Kroll, J. H.; Donahue, N. M.; Cee, V. J.; Demerjian, K. L.; Anderson, J. G. Gas-Phase Ozonolysis of Alkenes: Formation of OH from Anti Carbonyl Oxides. *J. Am. Chem. Soc.* **2002**, *124*, 8518-8519.
- ⁴¹ Anglada, J. M.; Bofill, J. M.; Olivella, S.; Solé, A. Unimolecular Isomerizations and Oxygen Atom Loss in Formaldehyde and Acetaldehyde Carbonyl Oxides. A Theoretical Investigation. *J. Am. Chem. Soc.* **1996**, *118*, 4636-4647.
- ⁴² Gutbrod, R.; Kraka, E.; Schindler, R. N.; Cremer, D. Kinetic and Theoretical Investigation of the Gas-Phase Ozonolysis of Isoprene: Carbonyl Oxides as an Important Source for OH Radicals in the Atmosphere. *J. Am. Chem. Soc.* **1997**, *119*, 7330-7342.
- ⁴³ Gutbrod, R.; Schindler, R. N.; Kraka, E.; Cremer, D. Formation of OH Radicals in the Gas Phase Ozonolysis of Alkenes: The Unexpected Role of Carbonyl Oxides. *Chem. Phys. Lett.* **1996**, *252*, 221-229.
- ⁴⁴ Kuwata, K. T.; Hermes, M. R.; Carlson, M. J.; Zogg, C. K. Computational Studies of the Isomerization and Hydration Reactions of Acetaldehyde Oxide and Methyl Vinyl Carbonyl Oxide. *J. Phys. Chem. A* **2010**, *114*, 9192-9204.
- ⁴⁵ Kurten, T.; Donahue, N. M. MRCISD Studies of the Dissociation of Vinylhydroperoxide, CH₂CHOOH: There Is a Saddle Point. *J. Phys. Chem. A* **2012**, *116*, 6823-6830.

CHAPTER 4

Selective deuteration illuminates the importance of tunneling in the unimolecular decay of Criegee intermediates to hydroxyl radical products

This research has been published in the Proceedings of the National Academy of Sciences (2017, DOI: 10.1073/pnas.1715014114). The experimental research and was performed with graduate students Victoria Barber, Yi Fang, and Prof. Marsha I. Lester in the *Department of Chemistry, University of Pennsylvania*. Theoretical calculations were performed in collaboration with Stephen J. Klippenstein in the *Chemical Sciences and Engineering Division, Argonne National Laboratory*.

I. Introduction

Ozonolysis of volatile alkenes originating from biogenic and anthropogenic sources is an important source of hydroxyl radicals (OH), a key oxidant in the troposphere (1). The TORCH Campaign near London showed that $\sim 1/3$ of daytime OH and essentially all of nighttime OH are produced by alkene ozonolysis, while the PUMA field campaign near Birmingham, United Kingdom, attributed nearly half of OH radicals in the summertime and most of the OH radicals in wintertime to this mechanism (2–4). Alkene ozonolysis occurs by addition of ozone across the C=C double bond to form a primary ozonide, which rapidly decomposes to an energized Criegee intermediate (R_1R_2COO) and carbonyl coproduct in a highly exothermic process (1). Under atmospheric conditions, the Criegee intermediates may undergo unimolecular decay to OH and other products (1, 5–9). Alternatively, collisional stabilization and bimolecular reaction of the Criegee intermediates may occur with water vapor, SO_2 , and other atmospheric species (10–15). The relative importance of the unimolecular and bimolecular processes depends on the size and conformation of the Criegee intermediate as well as the atmospheric abundance of the reaction partners.

Unimolecular decay of *syn* alkyl-substituted Criegee intermediates, such as *syn*- CH_3CHOO , proceeds via a 1,4 hydrogen atom transfer mechanism. An α -hydrogen on the *syn*-alkyl group transfers to the terminal O atom via a five-membered cyclic transition state (TS) to form vinyl hydroperoxide (VHP), which is followed by rapid homolysis of the O–O bond to release OH + vinoxy radical products (6, 16, 17), as illustrated for *syn* CH_3CHOO in Fig. 1. For *syn*- CH_3CHOO and $(CH_3)_2COO$, a

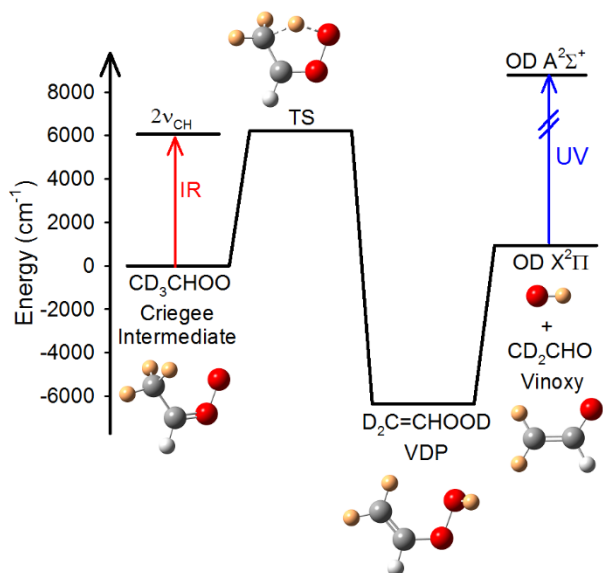


Figure 1. Energies and geometries of stationary points along the unimolecular decay pathway from the syn- CD_3CHOO Criegee intermediate to OD products. The reaction follows a 1,4-deuterium atom transfer mechanism to vinyl deuteroperoxide (VDP, $\text{D}_2\text{C}=\text{CHOOD}$) via a cyclic transition state (TS), followed by prompt dissociation to OD + vinoxy (CD_2CHO) products. In the experiment, the IR laser is resonant with a CH stretch overtone ($2\nu_{\text{CH}}$). The resulting OD products are detected by UV laser-induced fluorescence (LIF) on the OD $\text{A}^2\Sigma^+ - \text{X}^2\Pi_{3/2}$ (1,0) $\text{Q}_1(3.5)$ transition. In the molecular structures, the D-atoms are indicated in gold, while the H-atom is shown as white.

combination of prompt and thermal unimolecular decay to OH products is the dominant atmospheric loss process (7, 18–20). For example, recent master equation modeling of 2,3-dimethyl-2-butene ozonolysis under atmospheric conditions (1 atm, 298 K) was shown to produce chemically activated $(\text{CH}_3)_2\text{COO}$ (average energy of $\sim 24 \text{ kcal mol}^{-1}$) that decays to OH products on prompt (10^{-9} s) and thermal (10^{-3} s) timescales with comparable yields (7). On the other hand, Criegee intermediates that lack a *syn* alkyl group (i.e., CH_2OO and *anti* CH_3CHOO) are predicted to decay via a ring closure pathway through a dioxirane intermediate (three-membered cyclic peroxide) to a complex array of products including OH radicals (8, 21). For CH_2OO and *anti*- CH_3CHOO , bimolecular reaction with water dimer is the primary atmospheric decay pathway (12–14).

Recently, this laboratory carried out microcanonical rate measurements for the unimolecular decay of the more stable *syn* conformers of alkyl-substituted Criegee intermediates—namely, *syn* CH_3CHOO , $(\text{CH}_3)_2\text{COO}$, and *syn*- $\text{CH}_3\text{CH}_2\text{CHOO}$ —to OH radical products at energies in the vicinity of the TS barrier ($\sim 6,000 \text{ cm}^{-1}$) (20, 22). The experiments were conducted by IR activation of the Criegee intermediates in the CH stretch overtone region ($2\nu_{\text{CH}}$) and time-resolved detection of the resultant OH products under collision-free conditions. The experimental OH appearance rates were in excellent agreement with complementary statistical Rice–Ramsperger–Kassel–Marcus (RRKM) theory that incorporates quantum mechanical tunneling (20). Subsequently, OH radical products were observed following vibrational activation of combination bands involving CH stretch and another lower-frequency mode of *syn*- CH_3CHOO and $(\text{CH}_3)_2\text{COO}$ at

energies as much as $\sim 2,000 \text{ cm}^{-1}$ below the TS barrier (18, 19). At these energies, the 1,4 H-atom transfer reaction is classically forbidden and must proceed exclusively via quantum mechanical tunneling. Direct IR-UV time-domain measurements revealed much slower rates of appearance for OH products, which were generally in very good agreement with statistical RRKM theory, including tunneling. In addition, the experimentally validated microcanonical decay rates $k(E)$ for the *syn* alkyl-substituted Criegee intermediates were extended by using master equation modeling to derive thermal decay rates $k(T)$ in the high pressure limit. The resultant thermal decay rates (18–20, 22), which are in accord with other recent experimental and computational studies (23–26), were also found to have significant contribution from tunneling under atmospheric conditions.

The quintessential assessment to verify the role of tunneling in a chemical reaction is via isotopic (H/D) substitution, which increases the mass of the particle and slows tunneling through the TS barrier. When tunneling is important, deuteration of the *syn* methyl-substituted Criegee intermediate is expected to significantly slow the rate of 1,4 D-atom transfer, leading to OD products. Deuteration decreases the imaginary frequency along the reaction coordinate, effectively increasing the breadth of the barrier (in mass-weighted coordinates), and slightly increases the barrier height due to zero-point energy (ZPE) effects, both of which slow tunneling. Deuteration also lowers the frequencies of other vibrational modes—e.g., CD stretches ($\sim 2,200 \text{ cm}^{-1}$) compared with CH stretches ($\sim 3,000 \text{ cm}^{-1}$)—which increases the density of reactant states at a given

energy $N(E)$ and slows unimolecular decay (27). In addition, deuteration slows the thermal decay rate (23, 24, 28).

The present study examines the importance of tunneling in the unimolecular decay of *syn*-CH₃CHOO by using selectively deuterated *syn*-CD₃CHOO, which maintains a CH stretch (ν_1) and associated vibrational overtone transition ($2\nu_1$) at $\sim 6,000\text{ cm}^{-1}$ in the vicinity of the TS barrier, as shown in Fig. 1. As will be shown, the vibrationally activated *syn*-CD₃CHOO undergoes 1,4 D-atom transfer from the CD₃ group to the terminal O atom, resulting in release of OD products. A direct time-domain measurement of the appearance of OD products yields the unimolecular decay rate for *syn*-CD₃CHOO in the vicinity of the TS barrier. Complementary RRKM calculations of $k(E)$, including tunneling, are carried out for selectively deuterated *syn*-CD₃CHOO at energies near the TS barrier and compared with the experimental rate of appearance of OD products. The importance of H/D tunneling through the TS barrier is evaluated by detailed comparisons with previous experimental and theoretical studies of the unimolecular decay rate for *syn*-CH₃CHOO (19, 20). In addition, thermal decay rates $k(T)$ for deuterated systems are computed by using master equation modeling. Finally, a significant kinetic isotope effect, $\text{KIE} = k_H/k_D$, is elucidated (27), demonstrating the importance of quantum mechanical tunneling in the unimolecular decay of *syn* CH₃CHOO to hydroxyl radical products.

II. Results

Unimolecular decay of selectively deuterated *syn*-CD₃CHOO Criegee intermediates to OD + vinoxy radical products is examined experimentally and theoretically. Two types of experiments are performed: (i) An IR action spectrum of *syn*-CD₃CHOO is obtained by scanning the IR pump laser in the CH stretch overtone ($2\nu_{\text{CH}}$) region at a fixed IR pump–UV probe delay of 100 ns; and (ii) direct time-domain measurements of the rate of appearance of OD products are recorded following vibrational activation of *syn*-CD₃CHOO. In this case, the IR-UV time delay is stepped in 2- or 50-ns increments. In both types of experiments, the OD X²Π_{3/2} ($v = 0, J = 3.5$) products are detected by laser-induced fluorescence (LIF) on the OD A²Σ⁺ – X²Π_{3/2} (1,0) Q₁(3.5) transition. Complementary theoretical calculations are carried out to predict the IR absorption spectrum of selectively deuterated *syn*-CD₃CHOO and fully deuterated *syn*-CD₃CDOO, along with RRKM calculations of the microcanonical unimolecular decay rates for the deuterated Criegee intermediates.

Anharmonic frequencies and IR intensities in the 3,900- to 6,300-cm⁻¹ region are computed at the B2PLYPD3/cc-pVTZ level (29, 30), with second-order vibrational perturbation theory (VPT2) for *syn*-CH₃CHOO, fully deuterated *syn*-CD₃CDOO, and selectively deuterated *syn*-CD₃CHOO Criegee intermediates and shown in Fig. 2. As reported (17, 19, 20), IR transitions involving two quanta of CH stretch excitation (e.g., $2\nu_1$) of *syn*-CH₃CHOO are located in the 5,600- to 6,100-cm⁻¹ region in the vicinity of the TS barrier (17.05 kcal mol⁻¹; 5,960 cm⁻¹). Another group of IR transitions is predicted in the 3,900- to 4,600-cm⁻¹ region at energies as much as 2,000 cm⁻¹ below the

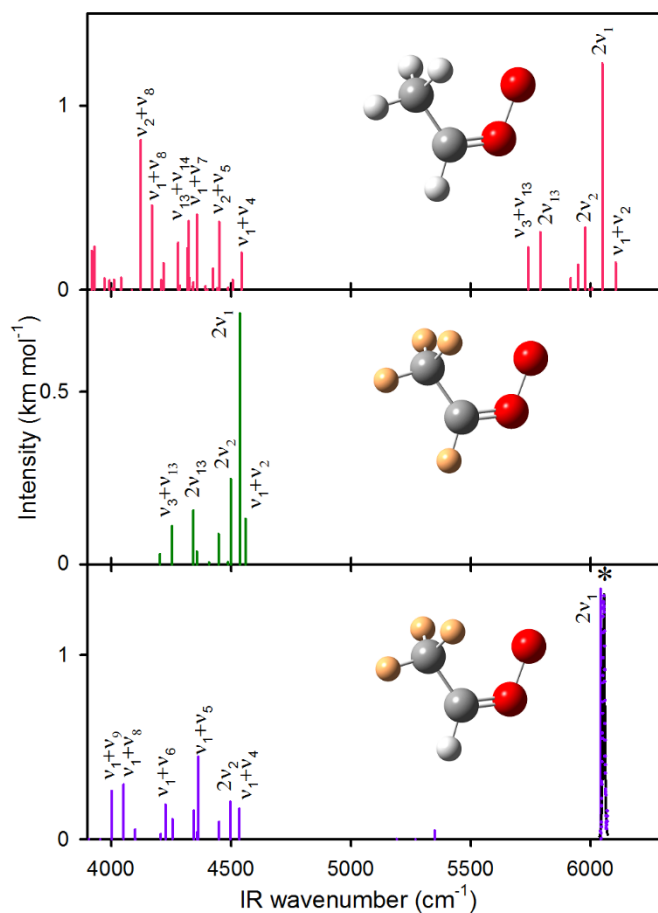


Figure 2. Calculated anharmonic IR stick spectra for three isotopologues of the *syn* methyl-substituted Criegee intermediate at the B2PLYPD3/cc-pVTZ level of theory. Upper Panel: *syn*-CH₃CHOO (red) from Ref. 19. Middle panel: *syn*-CD₃CDOO (green). Lower panel: *syn*-CD₃CHOO (purple). The lower panel also shows the experimental feature observed at 6055.0 cm⁻¹ (purple data, black fit) via IR action spectroscopy with OD LIF detection.

TS barrier, which corresponds to combination bands composed of one quantum each of CH stretch and another lower-frequency mode (e.g., $\nu_1 + \nu_4$). For comparison, the fully deuterated *syn*-CD₃CDOO Criegee intermediate is predicted to exhibit an analogous set of IR transitions. The reduction in CH fundamental frequencies from 3,000– 3,200 to 2,100–2,300 cm⁻¹ upon deuteration (Table S1) shifts the approximately twofold weaker IR transitions involving two quanta of CD stretch excitation of *syn*-CD₃CDOO to the 4,200- to 4,600- cm⁻¹ region (Fig. 2 and Table S2). IR transitions involving three quanta of CD stretch excitation of *syn*-CD₃CDOO are anticipated in the vicinity of ~6,000 cm⁻¹; however, their IR transition strengths are expected to be at least an order of magnitude weaker.

In selectively deuterated *syn*-CD₃CHOO, the focus of the present study, a similar set of IR transitions are anticipated for the carbonyl oxide CH (ν_1) stretch and various methyl CD (ν_2, ν_3, ν_{13}) stretches (Table S1). As shown in Fig. 2 (Table S2), a strong CH stretch overtone ($2\nu_1$) is predicted at 6,042.5 cm⁻¹. Several other weaker transitions are located in the 4,000- to 4,600-cm⁻¹ range involving two quanta of CD stretch (e.g., $2\nu_2$) or combination bands involving CH stretch and a lower-frequency mode (e.g., $\nu_1 + \nu_5$). Additional very weak transitions are predicted in the 5,100- to 5,400-cm⁻¹ region. The weaker transitions are not expected to be observable.

Experimentally, the IR action spectrum of *syn*-CD₃CHOO was scanned in the 6,030- to 6,080-cm⁻¹ range with UV LIF detection of the resultant OD products with an IR-UV time delay of 100 ns. One feature is observed at 6,055.0 cm⁻¹, as shown in Fig. 3. Only one IR transition of *syn*-CD₃CHOO is anticipated near 6,000 cm⁻¹ (Fig. 2), and thus

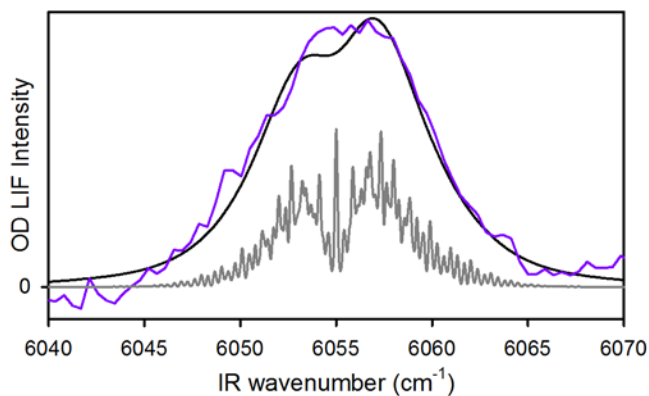


Figure 3. Experimental IR spectral feature (purple) observed at 6055.0 cm^{-1} (band origin) for *syn*- CD_3CHOO with UV LIF detection of OD products. The superimposed simulation (black) of the rotational band contour utilizes calculated rotational constants, a/b-type transition (1:2 a:b), homogeneous broadening with Lorentzian linewidth of 2.7 cm^{-1} , and rotational temperature of 10 K. A simulation at the 0.15 cm^{-1} laser bandwidth (gray) is also displayed.

the observed feature is ascribed to the strong CH stretch overtone ($2\nu_1$) transition predicted at $6,042.5\text{ cm}^{-1}$. No OH products are detected upon excitation of *syn*-CD₃CHOO at $6,055.0\text{ cm}^{-1}$, confirming that unimolecular decay arises from D-atom transfer and leads exclusively to OD products.

The assignment is further validated by simulation of the rotational band contour by using the PGOPHER spectral simulation program (31). The simulation is generated by using calculated rotational constants for *syn*-CD₃CHOO ($A = 0.524\text{ cm}^{-1}$, $B = 0.208\text{ cm}^{-1}$, $C = 0.157\text{ cm}^{-1}$), which differ only slightly from the experimental rotational constants for *syn*-CH₃CHOO (32), and the hybrid a/b-type transition (a:b = 1:2) predicted by theory for $2\nu_1$. As shown in Fig. 3, a simulation with band origin at $6,055.0\text{ cm}^{-1}$, rotational temperature of $\sim 10\text{ K}$, and homogeneous broadening with a Lorentzian linewidth of 2.7 cm^{-1} , corresponding to an intramolecular vibrational redistribution (IVR) lifetime of $\sim 2\text{ ps}$, is in good accord with the experimental band contour.

The experimental rate of appearance of OD products is obtained from direct time-domain measurements following CH stretch overtone ($2\nu_1$) excitation at $6,055.0\text{ cm}^{-1}$ of the selectively deuterated *syn*-CD₃CHOO Criegee intermediate. As shown in Fig. 4, scanning the IR-UV time delay in 2-ns steps reveals a slower exponential appearance of OD products from unimolecular decay of IR-activated *syn*-CD₃CHOO than the more rapid appearance of OH products arising from IR-activated *syn*-CH₃CHOO at a similar energy ($5,709.0\text{ cm}^{-1}$) (20).

The OD product temporal profile from IR-activated *syn*-CD₃CHOO is also measured with 50-ns IR-UV time-delay increments to capture the long time behavior as

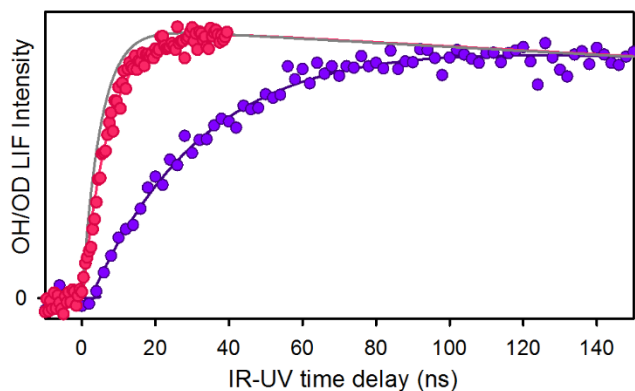


Figure 4. Temporal appearance profile and fit of OD products arising from IR activation of *syn*-CD₃CHO at 6055.0 cm⁻¹ (purple). The temporal profile of OH products arising from IR activation of *syn*-CH₃CHO at 5709.0 cm⁻¹ (red) from Ref. 20 is shown for comparison. A laser limited OH appearance curve (gray) derived from the IR and UV laser pulse widths and experimental fall off (Figure S1) is also shown.

shown in Fig. S1. The overall temporal profile is well represented by a dual exponential function that encompasses the rise (k_{rise}) and fall (k_{fall}) rate constants, as well as the laser time resolution of 5.0 ± 0.1 ns (20). k_{rise} is the rate constant for appearance of OD products and corresponding unimolecular decay of *syn*-CD₃CHOO. k_{fall} is purely experimental in nature, which arises from the molecules moving out of the UV probe volume due to the terminal velocity of the free jet expansion and the kinetic energy release to the OD products following unimolecular decay (33, 34). At long time delays, the temporal profile is dominated by the exponential falloff term. Repeated measurements yield $k_{fall} = 8.0 \pm 0.5 \times 10^5$ s⁻¹, which is fixed in the subsequent determination of k_{rise} . The exponential rise rate constant is then separately determined to be $k_{rise} = 3.0 \pm 0.3 \times 10^7$ s⁻¹, corresponding to an OD appearance time of 33.3 ± 2.8 ns. The uncertainty ($\pm 1\sigma$) in k_{rise} is derived from repeated measurements and takes into account the uncertainty ($\pm 1\sigma$) in k_{fall} .

The microcanonical dissociation rate constants $k(E)$ for the selectively deuterated *syn*-CD₃CHOO Criegee intermediate are also computed with RRKM theory. Tunneling is taken into account by using semiclassical TS theory (SCTST) (35) and asymmetric Eckart (36) models that incorporate anharmonic frequencies. The D-atom transfer step is taken to be rate-limiting for unimolecular decay to OD products.

The RRKM calculations are based on previous high-level electronic structure calculations of the TS barrier for *syn*-CH₃CHOO (20) and changes in the anharmonic frequencies and ZPE of the Criegee intermediate reactant and TS upon deuteration (Tables S1 and S3). Upon selective deuteration of *syn*-CD₃CHOO, the TS barrier

increases to 17.74 kcal mol⁻¹ (6,205 cm⁻¹), and the imaginary frequency associated with 1,4 D-atom transfer decreases to 1,325i cm⁻¹; see below for comparison of these parameters with other isotopologues. The computed RRKM rate coefficients using Eckart and SCTST tunneling models are predicted to be 2.94×10^7 and 2.62×10^7 s⁻¹ (corresponding to lifetimes of 34.0 and 38.2 ns), respectively, for selectively deuterated *syn*-CD₃CHOO at 6,055.0 cm⁻¹, which are in very good agreement with the experimental measurement. The agreement of experiment with statistical RRKM theory for the unimolecular decay rate of *syn*-CD₃CHOO further validates the computed TS barrier and demonstrates the importance of quantum mechanical tunneling. The agreement also shows that the initial CH stretch overtone excitation ($2\nu_1$) is rapidly randomized by IVR before unimolecular decay. The energy-dependent RRKM unimolecular decay rates for selectively deuterated *syn*-CD₃CHOO are predicted over a wide range of energies, as shown in Fig. 5 (Table S4).

The *anti* conformer of CD₃CHOO is expected to undergo unimolecular decay through a three-membered ring closure to form a dioxirane intermediate and ultimately yield many products, including OH (1). Selective deuteration allows one to distinguish between *syn*-CD₃CHOO that yields OD and *anti*-CD₃CHOO that produces OH, as shown in hexene ozonolysis (37). As a result, the vibrational frequencies and IR spectrum of *anti*-CD₃CHOO are also computed at the B2PLYPD3/cc-pVTZ level of theory (Fig. S2 and Tables S1 and S2). An experimental search is conducted for the strongest $2\nu_1$ transition predicted at 5,986.1 cm⁻¹ by using action spectroscopy with OH LIF detection on the A-X (1,0) Q₁(3.5) line. Indeed, a weak transition is observed at 5,979.0 cm⁻¹ that

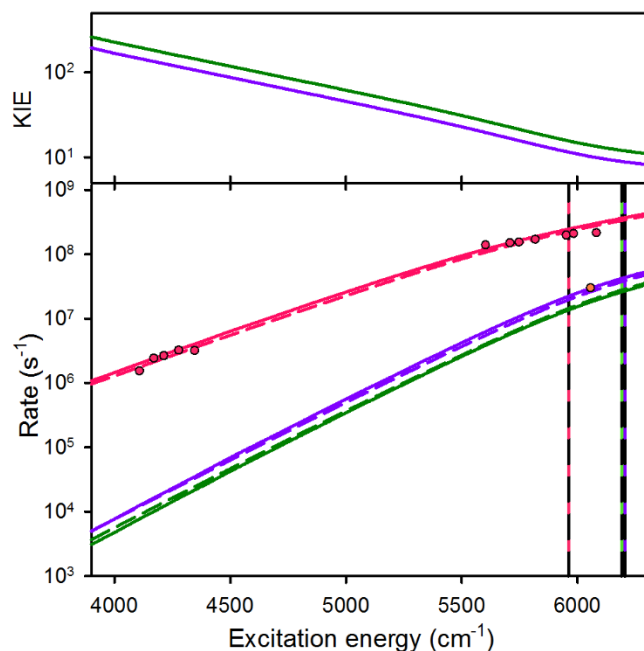


Figure 5. Energy-dependent unimolecular decay rates $k(E)$ for *syn* methyl-substituted Criegee intermediates and associated kinetic isotope effects (KIE) for selectively and fully deuterated systems on semi-log scales. Lower panel: Experimental OD appearance rate for IR activated *syn*-CD₃CDOO (purple symbol) and OH appearance rates for *syn*-CH₃CHOO (red symbols, Refs. 19, 20) are shown, along with computed RRKM rates for unimolecular decay of *syn*-CH₃CHOO (red), *syn*-CD₃CHOO (purple), and *syn*-CD₃CDOO (green) with asymmetric Eckart (solid lines) and semi-classical transition state (SCTST, dashed lines) tunneling models. The transition state (TS) barrier energies (vertical dashed lines) for *syn*-CH₃CHOO (red and black), *syn*-CD₃CHOO (purple and black), and *syn*-CD₃CDOO (green and black) are also indicated. Upper panel: KIE reveals the relative unimolecular decay rates for *syn*-CH₃CHOO compared to *syn*-CD₃CHOO (purple) or *syn*-CD₃CDOO (green) at each energy.

is tentatively ascribed to *anti*-CD₃CHOO. The OH products are rapidly formed within the time resolution of the lasers (≤ 5 ns), which is consistent with RRKM calculations based on theoretically predicted TS barriers to dioxirane (21, 28, 38).

III. Discussion

Selective deuteration of *syn*-CH₃CHOO provides an effective means to examine the kinetic isotopic effect associated with H/D atom transfer from the methyl group to the terminal O atom. The energy-specific activation of *syn*-CD₃CHOO is afforded by IR excitation of a strong CH stretch overtone ($2\nu_1$) transition at 6,055.0 cm⁻¹, which is followed by statistical unimolecular decay of *syn*-CD₃CHOO to OD + CD₂CHO products on a 33.3 ± 2.8 -ns timescale with $k(E) = 3.0 \pm 0.3 \times 10^7$ s⁻¹. Additional IR transitions arising from CD stretch overtone and combination bands are predicted to occur in the 4,000- to 4,600-cm⁻¹ energy range. However, these excitation energies are in the deep tunneling regime, where RRKM calculations including tunneling indicate unimolecular decay rates for *syn*-CD₃CHOO to OD products that are orders of magnitude slower (10^3 to 10^5 s⁻¹; Fig. 5 and Table S4). The latter are too slow to measure under the current experimental conditions, which is limited by the timescale (~ 1 – 2 μ s) for molecules moving out of the probe laser detection region (18, 19) and will not be observed in the IR action spectrum. In addition, the weak IR transitions of *syn*-CD₃CHOO predicted in the 5,100- to 5,400-cm⁻¹ region will result in slow unimolecular decay (10^5 to 10^6 s⁻¹) and are not expected to be observable in the IR action spectrum.

Selectively deuterated *syn*-CD₃CHOO differs from the previously studied *syn*-CH₃CHOO system in that the rate-limiting H-atom transfer step leading to OH products is now a D-atom transfer process that yields OD products. At 6,055.0 cm⁻¹, the unimolecular decay time of *syn*-CD₃CHOO is 33.3 ± 2.8 ns, while that of *syn*-CH₃CHOO was limited by the laser time resolution (20). Since experiment and RRKM theory are in

excellent accord for *syn*-CD₃CHOO at 6,055.0 cm⁻¹ and for *syn*-CH₃CHOO at slightly lower energies, we utilize RRKM theory with tunneling for the unimolecular decay time for *syn*-CH₃CHOO at 6,055.0 cm⁻¹ (3.7 ns) to deduce a 10-fold increase in lifetime upon selective deuteration of the methyl-substituted Criegee intermediate. Equivalently, this corresponds to a kinetic isotope effect (KIE) of ~10. A portion of this increase, specifically a factor of 3.4, can be explained by the increase in $N(E)$ at 6,055.0 cm⁻¹ upon selective deuteration (Fig. S3). The balance is primarily due to the decreased probability of tunneling through the TS barrier for D-atom vs. H-atom transfer.

The rate of change of the unimolecular decay rate with energy is also greater for selectively deuterated *syn*-CD₃CHOO than *syn*-CH₃CHOO. As shown in Fig. 5, the unimolecular decay rate for *syn*-CD₃CHOO increases 10,000-fold from 3,900 to 6,300 cm⁻¹ (Table S4), while that for *syn*-CH₃CHOO increases by a factor of 400 (see table S4 of ref. 19). The KIE changes from 8 to 200 across this energy range, with the largest KIE at energies significantly below the TS barrier in the deep tunneling regime. A small portion of this effect can be attributed to the increase in $N(E)$ (by a factor of 2.8–3.4) upon selective deuteration at these energies (Fig. S3). The large KIE at these energies demonstrates the importance of quantum mechanical tunneling, which is much less probable for D-atom vs. H-atom transfer.

Deuteration of the methyl-group of the Criegee intermediate results in changes in the TS barrier height and imaginary frequency. Fig. 6 shows an anharmonic ZPE-corrected asymmetric Eckart potential in mass-weighted coordinates to illustrate these changes. The TS barrier increases by ~4% from 17.05 kcal mol⁻¹ (5,960 cm⁻¹) for

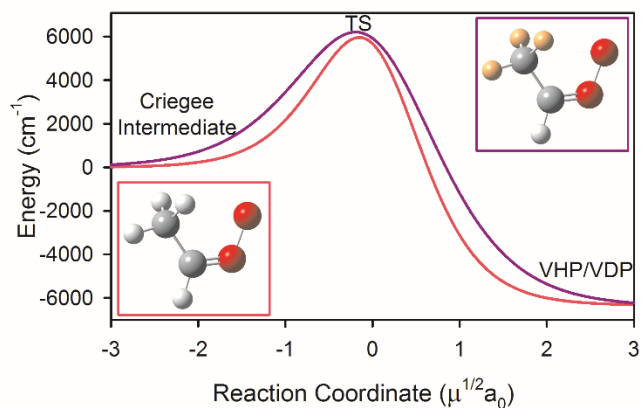


Figure 6. Anharmonic zero-point corrected asymmetric Eckart potentials plotted in mass-weighted coordinates (reduced mass μ and distance a_0) of the transition state critical oscillator for reaction of *syn*-CH₃CHOO (red) and *syn*-CD₃CHOO (purple) to vinyl hydroperoxide (VHP, H₂C=CHOOH) and vinyl deuteroperoxide (VDP, D₂C=CHOOD) via 1,4 H- and D-atom transfer, respectively. The curvature of the potential barrier at the transition state (TS) is determined by the imaginary frequency of $1696i$ cm⁻¹ for *syn*-CH₃CHOO (Ref. 20) and $1325i$ cm⁻¹ for *syn*-CD₃CHOO. Small change in TS barrier height and negligible change in VHP/VDP asymptote arise from changes in ZPE.

syn-CH₃CHOO to 17.74 kcal mol⁻¹ (6,205 cm⁻¹) for selectively deuterated *syn*-CD₃CHOO. This is a result of a larger reduction in the ZPE of the reactant than that of the TS upon deuteration. The imaginary frequency along the reaction coordinate for H/D atom transfer also decreases by ~22% from 1,696i cm⁻¹ for *syn*-CH₃CHOO (20) to 1,325i cm⁻¹ for *syn*-CD₃CHOO. The imaginary frequency is related to the curvature at the top of the barrier and results in an increase in the breadth of the Eckart potential (in mass-weighted coordinates) for *syn*-CD₃CHOO. These factors reduce the probability of tunneling through the TS barrier associated with D-atom transfer for *syn*-CD₃CHOO compared with that for H-atom transfer in *syn*-CH₃CHOO.

The $k(E)$ for fully deuterated *syn*-CD₃CDOO is also computed with RRKM theory by using the Eckart and SCTST tunneling models. For fully deuterated *syn*-CD₃CDOO, both the ZPE corrected TS barrier (17.72 kcal mol⁻¹; 6,199 cm⁻¹) and imaginary frequency (1,321i cm⁻¹) are nearly identical to those for selectively deuterated *syn*-CD₃CHOO. The resultant Eckart potential (Fig. 6) is essentially unchanged for the fully deuterated and selectively deuterated systems. As a result, the tunneling probability at a given energy will be approximately the same for the selectively and fully deuterated systems. However, $k(E)$ for fully deuterated *syn*-CD₃CDOO is slower by a factor of ~1.5 compared with *syn*-CD₃CHOO, as shown in Fig. 5 (Table S4), due to the slightly higher $N(E)$ for *syn*-CD₃CDOO (Fig. S3). Specifically, at 6,055.0 cm⁻¹, the unimolecular decay rate (lifetime) computed for fully deuterated *syn*-CD₃CDOO is 1.80×10^7 s⁻¹ (55.6 ns) and 1.93×10^7 s⁻¹ (51.8 ns) for the Eckart and SCTST tunneling models, respectively, and yields a KIE of 14. The KIE changes from 11 to 260 across the energy range from

6,300 to 3,900 cm^{-1} as tunneling becoming increasingly important. The large KIE signifies the reduced probability of tunneling upon deuteration, although a small portion of this change is due to the increase in $N(E)$ (by a factor of 3.8–5.1).

The slow unimolecular decay rate of fully deuterated *syn*- CD_3CDOO to OD products makes it difficult to detect via IR action spectroscopy. The RRKM calculations indicate that *syn*- CD_3CDOO excited on IR transitions in the 4,200- to 4,600- cm^{-1} range (Fig. 2), assigned to transitions involving two quanta of CD stretch excitation, will decay too slowly to OD products ($\sim 10^4$ to 10^5 s^{-1}) to be observed under the current experimental conditions. While *syn*- CD_3CDOO prepared with three quanta of CD stretch (e.g., $3\nu_1$) near $\sim 6,000 \text{ cm}^{-1}$ would have appropriate unimolecular decay rates ($\sim 10^7 \text{ s}^{-1}$) for experimental observation, these IR transitions are anticipated to be at least an order of magnitude weaker than those involving two quanta of CD stretch excitation (e.g., $2\nu_1$). Preliminary attempts to obtain an IR action spectrum of the fully deuterated *syn*- CD_3CDOO Criegee intermediate in the $2\nu_{\text{CD}}$ and $3\nu_{\text{CD}}$ energy regions were not successful.

The thermal unimolecular decay rates $k(T)$ for the selectively and fully deuterated *syn* methyl-substituted Criegee intermediates have been computed under atmospheric conditions by using master equation modeling; thermal rates for *syn*- CH_3CHOO have been reported (19, 20, 25, 26). Under these conditions, the rates are predicted to be in the high pressure limit, where the thermal rate can be expressed as a Boltzmann-weighted average over $k(E)$ and $N(E)$, $k(T) \propto \int k(E)N(E)\exp(-E/k_B T)dE$ (39). Note that the higher $N(E)$ for the fully deuterated *syn*- CD_3CDOO compared with selectively deuterated

syn-CD₃CHOO results in essentially the same thermal rates, aside from a minor effect due to their slightly different TS barriers arising from ZPE corrections. Over the 200–350 K (1 atm) range, the thermal rates for *syn*-CD₃CHOO (Fig. 7) and *syn*-CD₃CDOO are nearly indistinguishable. The thermal decay rates for *syn*-CH₃CHOO (Fig. 7) are significantly faster than the deuterated systems, primarily due to enhanced tunneling for H-atom transfer. At 298 K, the thermal decay rates for both deuterated Criegee intermediates are $\sim 3 \text{ s}^{-1}$ compared with 166 s^{-1} for *syn*-CH₃CHOO (19, 20). By contrast, the effective first-order rate constants for *syn*- and *anti*-CH₃CHOO with water vapor are estimated to be $\sim 10^1$ and $\sim 10^4 \text{ s}^{-1}$, respectively, at typical atmospheric concentrations of $[\text{H}_2\text{O}] = 1 \times 10^{17}$ to $5 \times 10^{17} \text{ cm}^{-3}$ (14). Thus, thermal unimolecular decay will be the primary atmospheric loss process for *syn*-CH₃CHOO, while bimolecular reaction with water vapor is expected to be the main atmospheric decay pathway for the less stable *anti*-CH₃CHOO conformer.

As shown in Fig. 7, the thermal rates without tunneling follow simple Arrhenius behavior with slopes indicative of the TS barrier heights. Thermal rates incorporating tunneling show significantly enhanced rates with strong curvature evident in the Arrhenius plots at lower temperatures, which can be represented by modified Arrhenius expressions (SI Materials and Methods). At 298 K, tunneling enhances the thermal decay rate of *syn*-CH₃CHOO by a factor of 100 and to a lesser degree (10-fold) for *syn*-CD₃CHOO and *syn*-CD₃CDOO. The *syn* methyl-substituted Criegee intermediate is predicted to have a large KIE of 52 at 298 K upon deuteration and ranges from 15 (350 K) to $>4,200$ (200 K) at temperatures relevant to the troposphere.

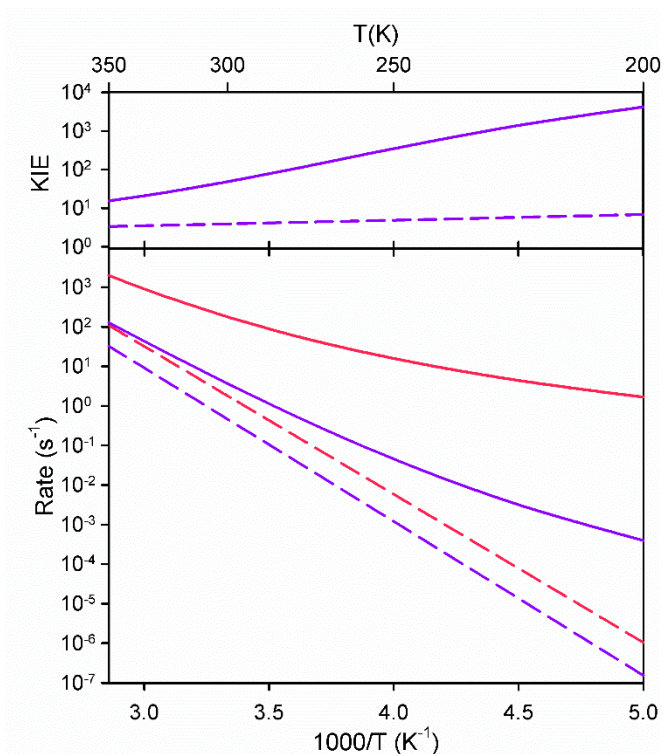


Figure 7. Thermal decay rates $k(T)$ predicted for *syn* methyl-substituted Criegee intermediates and associated kinetic isotope effects (KIE) upon deuteration on semi-log scales. Lower panel: Arrhenius plots of thermal decay rates computed using master equation modeling in the high pressure limit as a function of inverse temperature from 200 to 350 K. Thermal rates for *syn*-CD₃CHOO (purple) are compared with those for *syn*-CH₃CHOO (red; Ref. 20) incorporating tunneling (solid lines) and neglecting tunneling (dashed lines). Upper panel: KIE reveals the thermal decay rates for *syn*-CH₃CHOO compared to *syn*-CD₃CHOO (purple) incorporating tunneling (solid line) and neglecting tunneling (dashed line).

This work demonstrates the importance of quantum mechanical tunneling in the energy-dependent ($3,900\text{--}6,300\text{ cm}^{-1}$) and thermal (200–350 K) unimolecular decay rates of *syn*-CH₃CHOO to OH radical products. Selective deuteration of *syn*-CD₃CHOO is shown to slow the rate of unimolecular decay to OD products by 10-fold in the vicinity of the TS barrier, primarily due to the decreased probability of tunneling in D-atom vs. H-atom transfer. Moreover, deuteration is shown to give rise to a large KIE of ~ 50 in the thermal unimolecular decay rate of *syn*-CH₃CHOO at 298 K. The large KIE emphasizes the importance of tunneling in enhancing the thermal decay rate of the *syn* methyl-substituted Criegee intermediate to OH products, which needs to be taken into account in atmospheric models of OH production.

IV. Materials and Methods

The methods utilized for IR action spectroscopy and time-resolved dynamics of *syn*-CH₃CHOO to OH radical products have been described (17, 19, 20). In the present study, the 1,1-diiodoethane-2,2,2-*d*₃ (CD₃CHI₂) precursor is prepared by using the general procedures of Friedrich et al. (40), starting from acetaldehyde-2,2,2-*d*₃ (99% purity, 98% D; Sigma Aldrich). ¹H, ²H, and ¹³C NMR and high-resolution mass spectrometry confirm selective deuteration of the methyl group. Additional details are given in SI Materials and Methods.

Acknowledgements

We thank Prof. Anne B. McCoy (University of Washington) and Prof. David M. Chenoweth (University of Pennsylvania) for helpful discussions and Dr. Jun Gu

(University of Pennsylvania) and Dr. Charles W. Ross III (University of Pennsylvania) for help in analytical characterization of the precursor. This work was primarily supported by National Science Foundation Grants CHE-1362835 and CHE-1664572 (to M.I.L.). This material is also based on work supported by the US Department of Energy, Office of Science, Office of Basic Energy Sciences, Division of Chemical Sciences, Geosciences, and Biosciences at Argonne under Contract DE-AC02-06CH11357 (to S.J.K.).

References

1. Johnson D, Marston G (2008) The gas-phase ozonolysis of unsaturated volatile organic compounds in the troposphere. *Chem Soc Rev* 37:699–716.
2. Emmerson KM, et al. (2007) Free radical modelling studies during the UK TORCH campaign in summer 2003. *Atmos Chem Phys* 7:167–181.
3. Emmerson KM, Carslaw N (2009) Night-time radical chemistry during the TORCH campaign. *Atmos Environ* 43:3220–3226.
4. Harrison RM, et al. (2006) Measurement and modelling of air pollution and atmospheric chemistry in the U.K. West Midlands conurbation: Overview of the PUMA Consortium project. *Sci Total Environ* 360:5–25.
5. Kroll JH, Sahay SR, Anderson JG, Demerjian KL, Donahue NM (2001) Mechanism of HO_x formation in the gas-phase ozone-alkene reaction. 2. Prompt versus thermal dissociation of carbonyl oxides to form OH. *J Phys Chem A* 105:4446–4457.

6. Donahue NM, Drozd GT, Epstein SA, Presto AA, Kroll JH (2011) Adventures in ozoneland: Down the rabbit-hole. *Phys Chem Chem Phys* 13:10848–10857.
7. Drozd GT, Kurtén T, Donahue NM, Lester MI (2017) Unimolecular decay of the dimethyl-substituted Criegee intermediate in alkene ozonolysis: Decay time scales and the importance of tunneling. *J Phys Chem A* 121:6036–6045.
8. Nguyen TL, Lee H, Matthews DA, McCarthy MC, Stanton JF (2015) Stabilization of the simplest Criegee intermediate from the reaction between ozone and ethylene: A high level quantum chemical and kinetic analysis of ozonolysis. *J Phys Chem A* 119:5524–5533.
9. Novelli A, Vereecken L, Lelieveld J, Harder H (2014) Direct observation of OH formation from stabilised Criegee intermediates. *Phys Chem Chem Phys* 16:19941–19951.
10. Mauldin RL, 3rd, et al. (2012) A new atmospherically relevant oxidant of sulphur dioxide. *Nature* 488:193–196.
11. Hakala JP, Donahue NM (2016) Pressure-dependent Criegee intermediate stabilization from alkene ozonolysis. *J Phys Chem A* 120:2173–2178.
12. Chao W, Hsieh J-T, Chang C-H, Lin JJ-M (2015) Atmospheric chemistry. Direct kinetic measurement of the reaction of the simplest Criegee intermediate with water vapor. *Science* 347:751–754.
13. Lewis TR, Blitz MA, Heard DE, Seakins PW (2015) Direct evidence for a substantive reaction between the Criegee intermediate, CH₂OO, and the water vapour dimer. *Phys Chem Chem Phys* 17:4859–4863.

14. Lin L-C, et al. (2016) Competition between H_2O and $(\text{H}_2\text{O})_2$ reactions with $\text{CH}_2\text{OO}/\text{CH}_3\text{CHOO}$. *Phys Chem Chem Phys* 18:4557–4568.
15. Huang H-L, Chao W, Lin JJ-M (2015) Kinetics of a Criegee intermediate that would survive high humidity and may oxidize atmospheric SO_2 . *Proc Natl Acad Sci USA* 112:10857–10862.
16. Vereecken L, Francisco JS (2012) Theoretical studies of atmospheric reaction mechanisms in the troposphere. *Chem Soc Rev* 41:6259–6293.
17. Liu F, Beames JM, Petit AS, McCoy AB, Lester MI (2014) Infrared-driven unimolecular reaction of CH_3CHOO Criegee intermediates to OH radical products. *Science* 345:1596–1598.
18. Fang Y, Barber VP, Klippenstein SJ, McCoy AB, Lester MI (2017) Tunneling effects in the unimolecular decay of $(\text{CH}_3)_2\text{COO}$ Criegee intermediates to OH radical products. *J Chem Phys* 146:134307.
19. Fang Y, et al. (2016) Deep tunneling in the unimolecular decay of CH_3CHOO Criegee intermediates to OH radical products. *J Chem Phys* 145:234308.
20. Fang Y, et al. (2016) Communication: Real time observation of unimolecular decay of Criegee intermediates to OH radical products. *J Chem Phys* 144:061102.
21. Nguyen T-N, Putikam R, Lin MC (2015) A novel and facile decay path of Criegee intermediates by intramolecular insertion reactions via roaming transition states. *J Chem Phys* 142:124312.

22. Fang Y, Liu F, Klippenstein SJ, Lester MI (2016) Direct observation of unimolecular decay of $\text{CH}_3\text{CH}_2\text{CHOO}$ Criegee intermediates to OH radical products. *J Chem Phys* 145:044312.
23. Chhantyal-Pun R, et al. (2017) Direct measurements of unimolecular and bimolecular reaction kinetics of the Criegee intermediate $(\text{CH}_3)_2\text{COO}$. *J Phys Chem A* 121:4–15.
24. Smith MC, Chao W, Takahashi K, Boering KA, Lin JJ-M (2016) Unimolecular decomposition rate of the Criegee intermediate $(\text{CH}_3)_2\text{COO}$ measured directly with UV absorption spectroscopy. *J Phys Chem A* 120:4789–4798.
25. Long B, Bao JL, Truhlar DG (2016) Atmospheric chemistry of Criegee intermediates: Unimolecular reactions and reactions with water. *J Am Chem Soc* 138:14409–14422.
26. Nguyen TL, McCaslin L, McCarthy MC, Stanton JF (2016) Communication: Thermal unimolecular decomposition of *syn*- CH_3CHOO : A kinetic study. *J Chem Phys* 145:131102.
27. Baer T, Hase WL (1996) *Unimolecular Reaction Dynamics Theory and Experiments* (Oxford Univ Press, New York).
28. Yin C, Takahashi K (2017) How does substitution affect the unimolecular reaction rates of Criegee intermediates? *Phys Chem Chem Phys* 19:12075–12084.
29. Kozuch S, Gruzman D, Martin JML (2010) DSD-BLYP: A general purpose double hybrid density functional including spin component scaling and dispersion correction. *J Phys Chem C* 114:20801–20808.
30. Biczysko M, Panek P, Scalmani G, Bloino J, Barone V (2010) Harmonic and anharmonic vibrational frequency calculations with the double-hybrid B2PLYP method:

Analytic second derivatives and benchmark studies. *J Chem Theory Comput* 6:2115–2125.

31. Western CM (2017) PGOPHER, a Program for Simulating Rotational Structure (University of Bristol, Bristol, UK). Available at pgopher.chm.bris.ac.uk.

32. Nakajima M, Endo Y (2014) Communication: Spectroscopic characterization of an alkyl substituted Criegee intermediate *syn*-CH₃CHOO through pure rotational transitions. *J Chem Phys* 140:011101.

33. Kidwell NM, Li H, Wang X, Bowman JM, Lester MI (2016) Unimolecular dissociation dynamics of vibrationally activated CH₃CHOO Criegee intermediates to OH radical products. *Nat Chem* 8:509–514.

34. Li H, Kidwell NM, Wang X, Bowman JM, Lester MI (2016) Velocity map imaging of OH radical products from IR activated (CH₃)₂COO Criegee intermediates. *J Chem Phys* 145:104307.

35. Miller WH, Hernandez R, Handy NC, Jayatilaka D, Willetts A (1990) Ab initio calculation of anharmonic constants for a transition state, with application to semiclassical transition state tunneling probabilities. *Chem Phys Lett* 172:62–68.

36. Johnston HS, Heicklen J (1962) Tunneling corrections for the unsymmetrical Eckart potential energy barriers. *J Phys Chem* 66:532–533.

37. Kroll JH, Donahue NM, Cee VJ, Demerjian KL, Anderson JG (2002) Gas-phase ozonolysis of alkenes: Formation of OH from anti carbonyl oxides. *J Am Chem Soc* 124: 8518–8519.

38. Kuwata KT, Hermes MR, Carlson MJ, Zogg CK (2010) Computational studies of the isomerization and hydration reactions of acetaldehyde oxide and methyl vinyl carbonyl oxide. *J Phys Chem A* 114:9192–9204.
39. Levine RD, Bernstein RB (1987) *Molecular Reaction Dynamics and Chemical Reactivity* (Oxford Univ Press, New York).
40. Friedrich EC, Falling SN, Lyons DE (1975) A convenient synthesis of ethylidene iodide. *Synth Commun* 5:33–36.

CHAPTER 5

Synthesis of precursors and experimental studies of larger Criegee intermediates

The experimental research was performed with Prof. Marsha I. Lester in the *Department of Chemistry, University of Pennsylvania*.

I. Introduction

Criegee intermediates (carbonyl oxides), generated from alkene ozonolysis, decompose to several products including hydroxyl (OH) radicals, an important oxidant of trace atmospheric species.^{1,2} Alkene ozonolysis is a slow process with reaction rate constants ranging from ca. 10^{-18} cm³ molecules⁻¹ s⁻¹ for ethylene³ to ca. 10^{-15} cm³ molecules⁻¹ s⁻¹ for highly substituted alkenes such as tetramethylethylene (TME) under atmospheric conditions.⁴ Ozonolysis proceeds by addition of ozone across the C=C double bond of an alkene ($R_1R_2C=R_3R_4$) to form a 5-membered ring structure, called the primary ozonide, in a highly exothermic process (ca. 50 kcal mol⁻¹).² The primary ozonide promptly decays to form a Criegee intermediate (R_1R_2COO or R_3R_4COO) and a corresponding carbonyl cofragment (R_3R_4CO or R_1R_2CO).

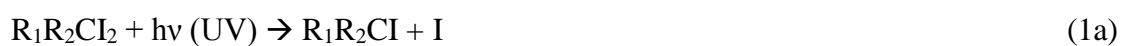
In the atmosphere, some fraction of newly formed energized Criegee intermediates will undergo prompt unimolecular decay to OH and other products.^{5,6} The remaining Criegee intermediates are collisionally stabilized⁷ and undergo thermal unimolecular decay,^{5,6,8,9} bimolecular reaction,^{10,11} or solar photolysis.¹²⁻¹⁴ Generation of Criegee intermediates from alkene ozonolysis depends on the concentrations of ozone and alkene, temperature, and pressure. Similarly, bimolecular processes that remove Criegee intermediates from the atmosphere depend on the temperature, pressure, conformer the Criegee intermediate, and the concentration of both reaction partners. However, some removal processes have reaction rate constants that are orders of magnitude faster than alkene ozonolysis.^{10-13,15} For example, $CH_2OO + (H_2O)_2$ has a reaction rate constant of ca. 10^{-12} cm³ molecule⁻¹ s⁻¹, nearly six orders of magnitude

greater than that of ethylene ozonolysis, under atmospheric conditions.¹⁶ This results in a low estimated steady-state concentration of Criegee intermediate, ca. 10^3 to 10^6 molecules cm^{-3} in the atmosphere.¹⁷ Therefore, observation of Criegee intermediates generated from alkene ozonolysis under atmospheric conditions is challenging.^{2, 18-20}

Some laboratories have indirectly observed Criegee intermediates via detection of H_2SO_4 or OH radicals.^{21, 22} Criegee intermediates may oxidize SO_2 to produce SO_3 and a carbonyl coproduct.²¹ Subsequent reaction of SO_3 with H_2O produces H_2SO_4 , which can be detected by chemical ionization mass spectroscopy (CIMS).²¹ OH radicals generated from unimolecular decay of Criegee intermediates are often detected with the use of a scavenger species (i.e. cyclohexane) that can react with OH to generate a new product (i.e. cyclohexanone) that is detected.²³ Another method for detecting OH radicals is by measuring the loss of a tracer species (i.e. 1,3,5-trimethylbenzene) due to reaction with OH radicals.²³ OH radicals can also be directly detected by laser-induced fluorescence (LIF).²²

CH_2OO , generated from ethylene ozonolysis, has been directly observed via Fourier-transform microwave spectroscopy (FTMW) and found to have significantly lower concentrations than other stable reaction products (i.e. formaldehyde, formic acid, dioxirane, etc.).²⁴ Recently, Criegee intermediates generated from ozonolysis of α -pinene or ethylene have been shown to undergo rapid reaction with 5,5-dimethyl-pyrroline *N*-oxide or acetic acid, producing an adduct that may be detected by proton-transfer mass spectrometry or CIMS.^{19, 20}

Direct detection of Criegee intermediates became possible in 2012 with development of an alternative synthetic method,²⁵ which efficiently generates Criegee intermediates, coupled with photoionization mass spectroscopy for detection. This alternative synthetic method begins with UV excitation of a geminal diiodoalkane precursor that results in dissociation of a C-I bond to produce a monoiodoalkane radical.²⁶ Subsequent reaction of the monoiodoalkane radical with molecular oxygen produces the Criegee intermediate:



This method has been extended to study a series of prototypical Criegee intermediates with alkyl substituents including -H, -CH₃, and -CH₂CH₃. Aside from CH₂I₂ and CH₃CHI₂, geminal diiodoalkane precursors are not commercially available and must be synthesized.

This chapter describes several procedures for synthesis of geminal diiodoalkane precursors (CH₃CHI₂, (CH₃)₂CI₂, CH₃CH₂CHI₂, (CH₃CH₂)(CH₃)CI₂) and some deuterated analogs (CD₃CDI₂, CD₃CHI₂, (CD₃)₂CI₂). The methyl-substituted diiodoalkane precursor (CH₃CHI₂) can be prepared via halogen exchange of 1,1-dichloroethane with iodoethane. The CH₃CHI₂ and other alkyl-substituted precursors are prepared from a two-step synthesis whereby: (1) A hydrazone species is formed from a ketone or aldehyde. (2) Subsequent oxidation of the hydrazone species with iodine results in production of the corresponding geminal diiodoalkane precursor. All of the precursors are light sensitive and require a dark storage environment due to the weak

nature of C-I bonds. Diiodoalkane precursors are characterized by nuclear magnetic resonance (NMR) spectroscopy and gas-chromatography mass spectrometry (GC-MS), which are provided in Figures S1-S8 of Supplementary Materials.

Ab initio calculations indicate that reaction (1b) is a nearly thermoneutral process for CH_2OO .²⁷ Internal energy (ca. 35 kcal mol⁻¹) of the monoiodoalkane (CH_2I) radical species produced from reaction (1a) will result in internal excitation of the CH_2OO product.²⁶ In this laboratory, the alternative synthetic method is utilized in a quartz capillary reactor coupled with a supersonic expansion to permit the study of collisionally stabilized, rotationally cooled (typically 10 K) Criegee intermediates. Both the diiodoalkane precursor and the Criegee intermediate species are detected concurrently on their parent mass channels in a time-of-flight mass spectrometer (TOF-MS).

II. Experimental Methods

A. Synthetic Methods

CH_3CHI_2 Synthesis, Method 1:

A methyl-substituted geminal diiodoalkane precursor, CH_3CHI_2 , was synthesized following the general procedures of Letsinger and Kammeyer,²⁸ as shown in Figure 1. A mixture of CH_3CHCl_2 (8.4 mL, >95% purity, TCI America), $\text{CH}_3\text{CH}_2\text{I}$ (24.0 mL, 99% purity, Sigma Aldrich), and anhydrous AlCl_3 (0.53 g) was refluxed at 100°C for 3 hours with rapid stirring. The reaction mixture was quenched in water (200 mL), washed with a saturated sodium bisulfite solution (1x 200 mL, 1x 100 mL), and dried over magnesium sulfate. The drying agent was filtered via Buchner filtration and rinsed several times with ether. The combined filtrate and ether rinses were concentrated in vacuo. The desired

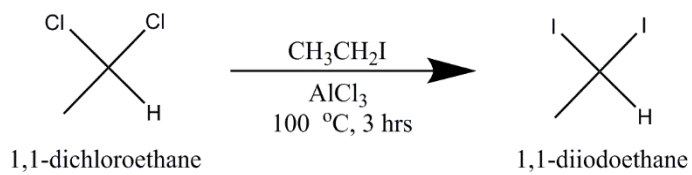


Figure 1. Synthesis of 1,1-diiodoethane (CH_3CHI_2) from 1,1-dichloroethane following the procedures of Letsinger and Kammemeyer²⁸ (Method 1).

product was purified via Kugelrohr distillation to give a pale yellow liquid (17.8 g, 64% yield). $^1\text{H NMR}$ (500 MHz, CDCl_3) δ 2.9 (d, 3H), 5.2 (q, 1H).

CH_3CHI_2 Synthesis, Method 2:

A methyl-substituted diiodoalkane precursor, CH_3CHI_2 , was also synthesized following the procedures of Friedrich et al.,²⁹ as shown in Figure 2. Acetaldehyde (15 mL, $\geq 99.5\%$ purity, Sigma Aldrich) chilled to 0°C was added dropwise to hydrazine monohydrate (25 mL, $>99\%$ purify, Alfa Aesar) maintained at approximately -20°C in a NaCl/ice bath (~1:3) with rapid stirring to produce the acetaldehyde hydrazone species. The reaction was allowed to stir for 15 minutes. The crude hydrazone species was extracted with dichloromethane (6 x 10mL, 0°C) and dried over sodium sulfate. The hydrazone was diluted in dichloromethane (250 mL) and chilled in an ice water bath. Triethylamine (62 mL) was added and the mixture was chilled in an ice bath. Solid iodine was added slowly with rapid stirring until no more N_2 gas was evolved and the solution was a deep red/brown color. The mixture was washed with water until the water layer was clear. The mixture was washed with a saturated sodium thiosulfate solution until the organic layer was a pale yellow. The mixture was washed with 3N HCl until the water layer was acidic. The mixture was washed with a brine solution until the pH was ~7. The mixture was dried over magnesium sulfate, concentrated in vacuo, and purified via Kugelrohr distillation to yield a pale yellow liquid (19.0 g, 33% yield). $^1\text{H NMR}$ (360 MHz, CDCl_3) δ 2.9 (d, 3H), 5.2 (q, 1H).

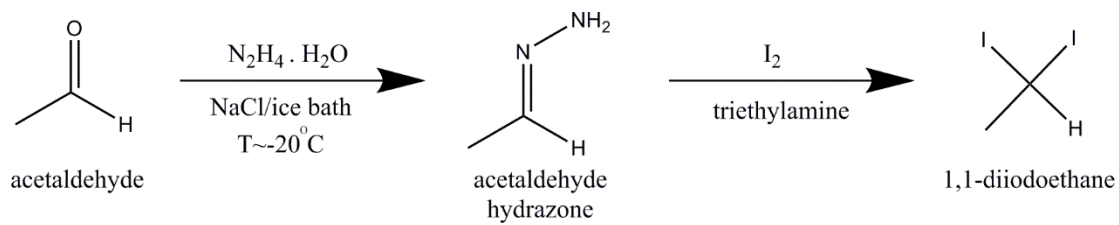


Figure 2. Synthesis of 1,1-diiodoethane (CH_3CHI_2) from acetaldehyde following the procedures of Friedrich et al.²⁹ (Method 2).

CD₃CDI₂ Synthesis:

A fully deuterated analog of the methyl-substituted geminal diiodoalkane precursor, CD₃CDI₂ was produced from CD₃CDO (98% purity, 99% D, Cambridge Isotope Laboratories) with a 34% yield by following the methods of Friederich et al.²⁹ (Method 2). ²HNMR (77 MHz, CHCl₃) δ 2.9 (s, 3D), 5.2 (s, 1D). GC-MS (EI) 286 (CD₃CDI₂, 100%).

(CH₃)₂CI₂ Synthesis:

The dimethyl-substituted diiodoalkane precursor, (CH₃)₂CI₂, was made starting from (CH₃)₂CO (99.8% purity, ACROS Organics) with an 18% yield following the methods of Friedrich et al.²⁹ (Method 2). The (CH₃)₂CI₂ product was verified via ¹HNMR (360 MHz, CDCl₃) δ 3.0 (s, 6H)

CD₃CHI₂ Synthesis:

The selectively deuterated methyl-substituted precursor, CD₃CHI₂, was made starting from CD₃CHO (99% purity, 98% D, Sigma Aldrich) with a 26% yield following the methods of Friedrich et al. (Method 2). Detailed methods and analytic spectra can be found in the Supplementary Materials of Chapter 4.

(CD₃)₂CI₂ Synthesis, Method 3:

A fully deuterated analog of the dimethyl-substituted geminal diiodoalkane precursor, (CD₃)₂CI₂, was synthesized following the general methods of Pross and Sternhell,³⁰ as shown in Figure 3. Acetone-*d*₆ (12.5 mL, ≥99% purity, ≥99.9% D, Sigma Aldrich) was added dropwise to hydrazone monohydrate (19 mL, >99% purity, Alfa Aesar). The mixture was refluxed at 100°C for 1 hr to yield an acetone hydrazone

species. The crude hydrazone was extracted in chloroform (200 mL), washed with water (2 x 20 mL), dried over potassium carbonate, and concentrated in vacuo. The hydrazone was then dilute into 5 mL ether. Triethylamine (2.5 mL) was added to the mixture. A saturated solution of iodine in ether was added slowly with rapid stirring until the solution was red/brown in color. The crude product was diluted in ether (30 mL) and was washed with a 5% sodium thiosulfate solution (2 x 50 mL), 3N HCl (15 mL), a 5% sodium carbonate solution (2 mL), and brine (2 x 50 mL). The product was dried over potassium carbonate and concentrated in vacuo. The crude product was purified via Kugelrohr distillation to yield a pale yellow liquid $(\text{CD}_3)_2\text{CI}_2$ with very low yield (0.4 g, 0.8% yield). Unfortunately, no $^2\text{HNMR}$ was obtained; however the presence of some small $\sim \delta$ 3.0 ppm shift in the $^1\text{HNMR}$ (360 MHz, CDCl_3) suggests some loss of deuteration. GC-MS (EI) 302 ($(\text{CD}_3)_2\text{CI}_2$, 90%), 301 ($(\text{CD}_3)(\text{CD}_2\text{H})\text{CI}_2$, 10%).

$(\text{CH}_3)_2\text{CI}_2$ Synthesis:

The dimethyl-substituted diiodoalkane precursor, $(\text{CH}_3)_2\text{CI}_2$, was also synthesized from $(\text{CH}_3)_2\text{CO}$ (99.8% purity, ACROS Organics) with an 8% yield following the methods of Pross and Sternhell³⁰ (Method 3). The $(\text{CH}_3)_2\text{CI}_2$ product was verified via $^1\text{HNMR}$ (360 MHz, CDCl_3) δ 3.0 (s, 6H).

$\text{CH}_3\text{CH}_2\text{CHI}_2$ Synthesis:

An ethyl-substituted diiodoalkane species, $\text{CH}_3\text{CH}_2\text{CHI}_2$, was produced from $\text{CH}_3\text{CH}_2\text{CHO}$ () with a 15% yield following the methods of Pross and Sternhell³⁰ (Method 3). The $\text{CH}_3\text{CH}_2\text{CHI}_2$ product was verified via $^1\text{HNMR}$ (360 MHz, CDCl_3) δ 1.0 (t, 3H), 2.4 (m, 2H), 5.1 (t, 1H).

(CH₃CH₂)(CH₃)Cl₂ Synthesis:

A methylethyl- substituted diiodoalkane precursor, (CH₃CH₂)(CH₃)Cl₂ and a mixture of isomeric iodobutenes, was made starting from (CH₃CH₂)(CH₃)CO ($\geq 99.7\%$ purity, Sigma Aldrich), with an 8% yield following the methods of Pross and Sternhell³⁰ (Method 3). Inability to separate the iodobutenes from the desired diiodoalkane product is consistent with the previously reported results.³⁰ The (CH₃CH₂)(CH₃)Cl₂ product was verified via ¹HNMR (360 MHz, CDCl₃) δ 1.1 (t, 3H), 2.2 (q, 2H), 3.0 (s, 3H). The relative yields of diiodoalkane precursor CH₃CH₂(CH₃)Cl₂ (73%) to cis/trans-2-iodobut-2-ene (27%) was determined via ¹HNMR.

Synthesis of the (CH₃CH₂)(CH₃)Cl₂ precursor has also been generated from (CH₃CH₂)(CH₃)CO by Cabezas et al. using a slightly modified Method 2 procedure.³¹ The ketone and hydrazine mixture was heated to 50 °C for 15 minutes prior to addition of iodine.³¹ The precursor was purified via distillation in vacuo (40°C).³¹ The NMR spectra and presence of iodoalkene byproducts was not reported.

B. Generation of Criegee intermediates from the corresponding precursors

As described previously,¹²⁻¹⁴ a geminal diiodoalkane precursor (R₁R₂Cl₂) seeded in a 20% O₂/Ar carrier gas is pulsed from a solenoid valve into a quartz capillary reactor where it is photolyzed by the focused 248 nm output of a KrF excimer laser to produce the monoiodoalkane radical (R₁R₂Cl). Reaction of the monoiodoalkane radical with O₂ displaces the remaining iodine atom to produce the corresponding Criegee intermediate (R₁R₂COO). The Criegee intermediates are collisionally stabilized in the capillary, cooled in a free jet expansion, probed 4 cm downstream by 118 nm VUV radiation and

detected in a TOF-MS on the parent mass channel. The VUV radiation is generated by frequency tripling the third harmonic (355 nm, 40 mJ/pulse) of a Nd:YAG laser (Continuum Powerlite 9010) in a phase-matched Xe/Ar (~ 1:10) gas mixture.

The geminal diiodoalkane precursor is loaded in the armature of the pulsed valve (Parker General Valve Series 9). In some cases the valve was heated to increase the vapor pressure of the precursor sample. The valve was encased in an aluminum block that makes thermal contact with a Peltier thermoelectric module (Laird Technologies, PC4), which maintains a temperature differential between the two sides of the module. The temperature of the cool side is maintained by thermal contact with a water line. Thermal silicone compound (Wakefield-Vette) is applied at every interface to permit thermal contact. The temperature was monitored with a thermocouple (Cole-Parmer, Type K digital thermometer).

III. Results and Discussion

The synthetic methods to produce a variety of geminal diiodoalkane species and their deuterated analogs have permitted immense advancements in characterizing fundamental reactions of Criegee intermediates. The method of Letsinger et al.²⁸ (Method 1) generates geminal diiodoethane (CH_3CHI_2) via halogen exchange between dichloroethane with iodoethane and with reproducible yields (ca. 60%). Buchner filtration was necessary to filter the magnesium sulfate drying agent from the product. Ether readily dissolves the diiodoethane product and was thus used to rinse the magnesium sulfate drying agent. Furthermore, ether is easily removed by concentrating

the product *in vacuo*. Efficient synthesis and purification provides CH_3CHI_2 product at a fraction of the cost of commercial vendors.

In addition to CH_3CHI_2 , several diiodoalkane species ($(\text{CH}_3)_2\text{CI}_2$, $\text{CH}_3\text{CH}_2\text{CHI}_2$, $(\text{CH}_3\text{CH}_2)(\text{CH}_3)\text{CI}_2$) and deuterated analogs (CD_3CDI_2 , CD_3CHI_2 , $(\text{CD}_3)_2\text{CI}_2$) can be prepared via generation of a hydrazone from the corresponding ketone or aldehyde followed by reaction of the hydrazone species with iodine. Two similar techniques have been applied to produce the same geminal diiodoalkane precursor from the corresponding ketone or aldehyde: the procedure reported by Pross and Sternhell³⁰ (Method 3) and the procedure presented by Friedrich et al.²⁹ (Method 2), which is found to be more efficient. The main difference between these two methods is the temperature at which the hydrazone is generated, 100 °C and -20 °C, respectively. Yields reported herein are a factor of 3 to 5 lower than the ca. 35-45% yields reported by Pross and Sternhell for synthesis of $(\text{CH}_3)_2\text{CI}_2$, $\text{CH}_3\text{CH}_2\text{CHI}_2$, and $(\text{CH}_3\text{CH}_2)(\text{CH}_3)\text{CI}_2$.³⁰ The published ca. 35% yield of Friedrich et al.²⁹ is reproduced for synthesis of CH_3CHI_2 . The first step in these synthetic methods, preparation of a hydrazone species, is known to be challenging due to formation of an azine byproduct as well as spontaneous decomposition of the hydrazone.³² Increased yield of diiodoalkane product was observed upon chilling the ketone/aldehyde and hydrazine reaction mixture in the first step. A possible explanation is that lower temperatures may catalyze formation of the hydrazone species. This enhancement is consistent with similar chemistry observed in oxime ligation.³³ It is hypothesized that freezing initiates formation of ice crystals that results in locally high concentrations of hydrazine and thereby favor hydrazone formation.³³ In addition to

reproducible yields, the Friedrich et al.²⁹ method is significantly faster, as it does not require dropwise addition of the aldehyde/ketone to the hydrazine in the first step.

The successful synthesis of a series of diiodoalkane precursors enables preparation and spectroscopic studies of the corresponding Criegee intermediates with substituents including –H, –CH₃, and –CH₂CH₃. The CH₃CHI₂, (CH₃)₂CI₂ and CH₃CH₂CHI₂ precursors yield the corresponding Criegee intermediates CH₃CHOO, (CH₃)₂COO, and CH₃CH₂CHOO via the alternative synthetic method and have been detected by VUV photoionization in a TOF-MS as previously reported.¹²⁻¹⁴

Recent synthesis and TOF-MS detection of fully deuterated analogs of the methyl- and dimethyl- substituted precursors, CD₃CDI₂ and (CD₃)₂CI₂, has been successful. Although synthesis begins with a deuterated starting material, it is possible that H/D exchange with non-deuterated solvents can occur. However, no significant loss of deuteration is found. This is confirmed via NMR and GC-MS. H/D exchange between deuterated precursors and the non-deuterated solvent requires isomerization of the ketone or aldehyde starting material to the “enol” configuration. The process of keto-enol tautomerization has a significant barrier (70-90 kcal/mol) and thus the “enol” configuration is not accessible, and significant loss of deuteration is not observed.³⁴

The TOF mass spectrum of CD₃CDI₂, (CD₃)₂CI₂, and CH₂I₂ seeded in an O₂/Ar backing gas and photoionized with VUV radiation is shown in the upper panel of Figure 4. Observation of the parent (m/z = 268 CH₂I₂, m/z = 286 CD₃CDI₂ and m/z = 302 (CD₃)₂CI₂) as well as –I (m/z = 141 CH₂I, m/z = 159 CD₃CDI and m/z = 175 (CD₃)₂CI) mass channels demonstrate photoionization of the fully deuterated methyl- and dimethyl-

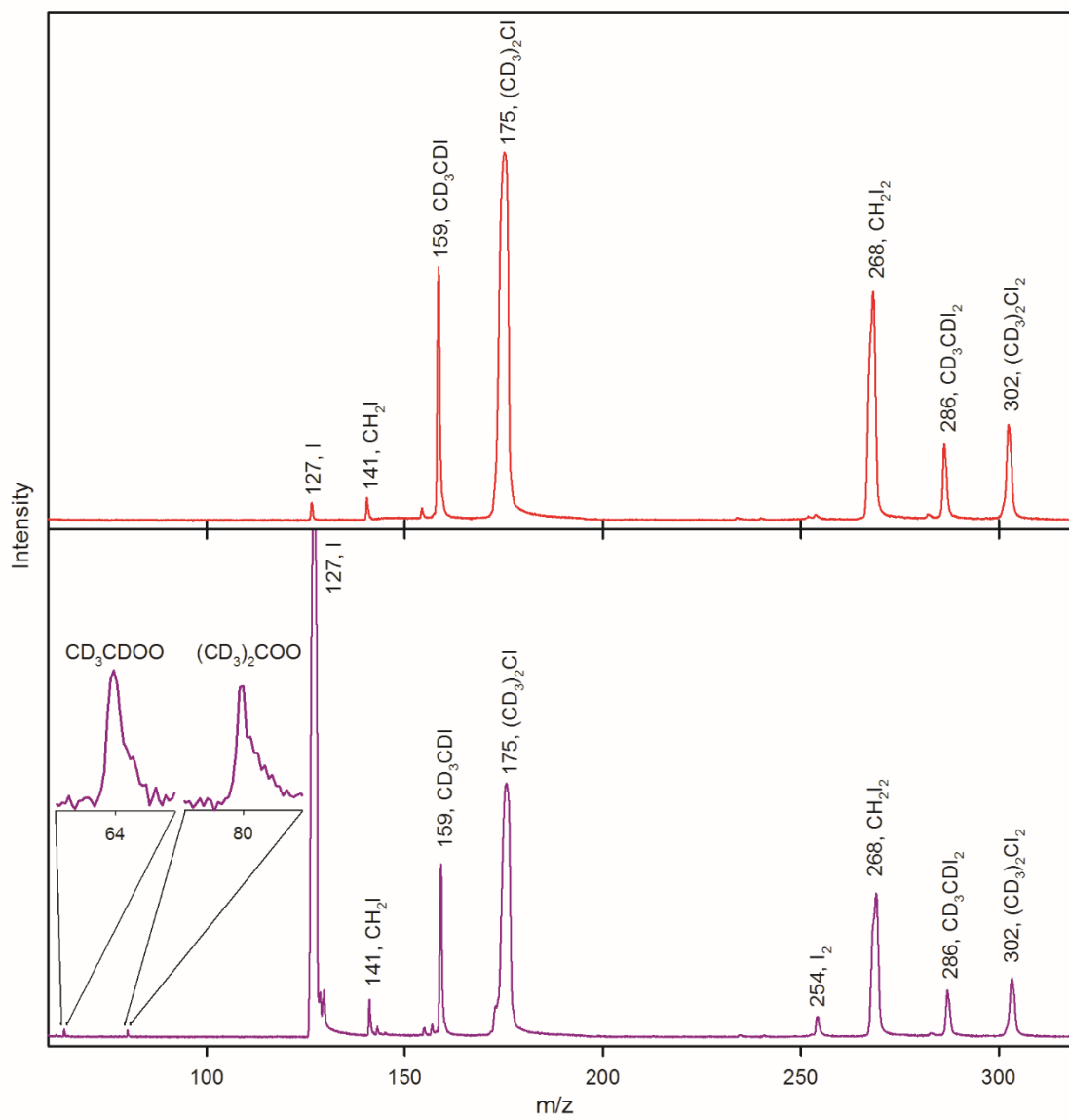


Figure 4. (Upper) Mass spectrum of CD_3CDI_2 , $(\text{CD}_3)_2\text{CI}_2$, and CH_2I_2 precursors, seeded in an O_2/Ar backing gas, with VUV photoionization in a TOF-MS. Mass channels ($m/z = 302$ $(\text{CD}_3)_2\text{CI}_2$, $m/z = 175$ $(\text{CD}_3)_2\text{CI}$, $m/z = 286$ CD_3CDI_2 , $m/z = 159$ CD_3CDI , $m/z = 268$ CH_2I_2 , $m/z = 141$ CH_2I) show that CD_3CDI_2 , $(\text{CD}_3)_2\text{CI}_2$, and CH_2I_2 precursors are photoionized. I ($m/z = 127$) mass channel are also observed. (Lower) Mass spectrum of CD_3CDI_2 , $(\text{CD}_3)_2\text{CI}_2$, and CH_2I_2 precursors with 248 nm photolysis along the capillary reactor prior to photoionization. Significant enhancement of the I -atom ($m/z = 127$) and I_2 ($m/z = 254$) mass channels upon 248 nm photolysis of the diiodoalkane precursor is attributed to C-I bond dissociation. Inset shows mass channels $m/z = 64$ and $m/z = 80$ assigned to fully deuterated Criegee intermediates CD_3CDOO and $(\text{CD}_3)_2\text{COO}$, respectively. This confirms generation of the monoiodoalkane radical and subsequent reaction with O_2 to displace the remaining iodine atom and produce Criegee intermediates. Multiple precursors are seeded in the backing gas to compare relative precursor and Criegee intermediate photoionization signal intensities.

substituted precursors. The lower panel of Figure 4 shows the mass spectrum upon 248 nm photolysis of diiodoalkane precursors along the length of the capillary prior to direct detection in a TOF-MS. Upon 248 nm photolysis, significant increase of the I ($m/z = 127$) mass channel and appearance of the corresponding Criegee intermediate mass channels ($m/z = 46$ CH_2OO , $m/z = 64$ CD_3CDOO and $m/z = 80$ $(\text{CD}_3)_2\text{COO}$) are observed as described by reactions (1a) and (1b).²⁵ Synthesis of deuterated Criegee intermediates allows for investigation of kinetic isotope effects in bimolecular reaction and unimolecular decay.^{15, 35, 36}

Seeding multiple precursors in the backing gas allows for simultaneous observation of the precursors and corresponding Criegee intermediates with 10.5 eV VUV photoionization. The relative intensities of the precursor and Criegee intermediate signals at ca. 25 °C is shown in Table 1. Several factors affect the intensity of the diiodo precursor including the vapor pressure, photoionization efficiency, and possible photofragmentation. Both CD_3CDI_2 and $(\text{CD}_3)_2\text{CI}_2$ precursors exhibit significantly more photofragmentation than CH_2I_2 , as observed by the significant CD_3CDI ($m/z = 159$) and $(\text{CD}_3)_2\text{CI}$ ($m/z = 175$) mass channels in the absence of excimer photolysis, as shown in the upper panel of Figure 4. The relative Criegee intermediate photoionization signal intensity depends on the vapor pressure of the precursor, precursor absorption at 248 nm, efficiency of the collisional stabilization of Criegee intermediates, and subsequent photoionization, and possible photofragmentation upon 10.5 eV VUV irradiation.

Initial detection of the four-carbon methylethyl- substituted $(\text{CH}_3\text{CH}_2)(\text{CH}_3)\text{CI}_2$ diiodoalkane precursor and corresponding $(\text{CH}_3\text{CH}_2)(\text{CH}_3)\text{COO}$ Criegee intermediate

Table 1. Relative intensity of photoionization signals for diiodoalkane precursors and corresponding Criegee intermediates at ca. 25 °C (no heating).

Diiodoalkane Precursor (room temperature)	Relative Precursor Intensity (scaled to CH ₂ I ₂)	Relative Criegee Intermediate Intensity (scaled to CH ₂ OO)	Criegee Intermediate
CH ₂ I ₂	1.00	1.00	CH ₂ OO
CH ₃ CHI ₂	0.23	0.24	CH ₃ CHOO
(CH ₃) ₂ CI ₂	0.06	0.02	(CH ₃) ₂ COO
(CH ₃ CH ₂)(CH ₃)CI ₂	0.01	0.02	(CH ₃ CH ₂)(CH ₃)COO
CD ₃ CDI ₂	0.26	0.42	CD ₃ CDOO
(CD ₃) ₂ CI ₂	0.55	0.77	(CD ₃) ₂ COO

resulted in very weak photoionization signals, as shown in Table 1. It is evident that the photoion signal of the precursor species gets smaller with increasing carbon number. In general, increasing the number of carbons is expected to result in a decrease in vapor pressure,³⁷ which will affect the partial pressure of the precursor carried in the backing gas. The relationship between vapor pressure and carbon number for a similar class of compounds, 1-iodoalkanes, is predicted from the Antoine coefficients and shown in Figure 5 as a function of temperature.³⁸ The precursor vapor pressure can be increased via heating, assuming no decomposition.

Due to the low vapor pressure of diiodoalkane precursors with increasing carbon number, the methylethyl- substituted precursor, $(\text{CH}_3\text{CH}_2)(\text{CH}_3)\text{Cl}_2$, was heated to 44 °C at the valve. The mass spectrum of the heated $(\text{CH}_3\text{CH}_2)(\text{CH}_3)\text{Cl}_2$ precursor seeded in an O_2/Ar backing gas is shown in the upper panel of Figure 6. Detection of the parent ($m/z = 310 \text{ C}_4\text{H}_8\text{I}_2$) and $-\text{I}$ ($m/z = 183 \text{ C}_4\text{H}_8\text{I}$) mass channels show that $(\text{CH}_3\text{CH}_2)(\text{CH}_3)\text{Cl}_2$ is photoionized by the VUV radiation. The lower panel shows the mass spectrum upon 248 nm photolysis of the precursor in the reactor tube prior to photoionization. Enhancement of the I ($m/z = 127$) mass channel indicates that 248 nm induced photolysis of the C-I bond generates a monoiodoalkane $(\text{CH}_3\text{CH}_2)(\text{CH}_3)\text{Cl}$ radical. The appearance of the $m/z = 88$ mass channel suggests subsequent reaction of the monoiodoalkane radical with O_2 to displace the remaining iodine atom and generate the $(\text{CH}_3\text{CH}_2)(\text{CH}_3)\text{COO}$ Criegee intermediate.

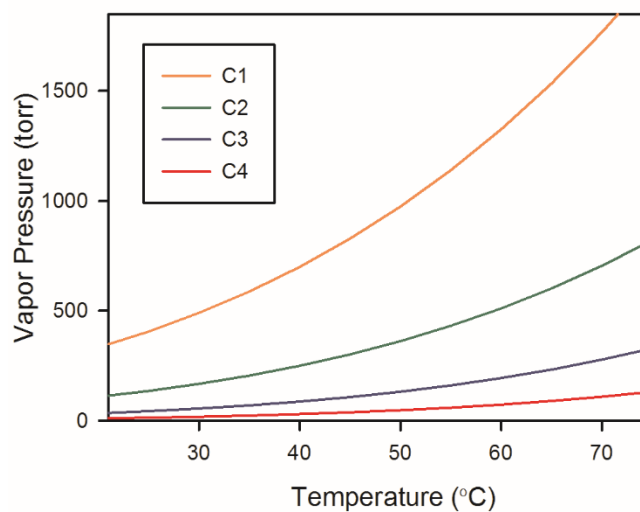


Figure 5. Vapor pressure of 1-iodoalkanes as a function of temperature are predicted using published coefficients in the Antoine equation by Li et al.³⁸ Increasing carbon number has a significant effect on the vapor pressure of the 1-iodoalkane species.

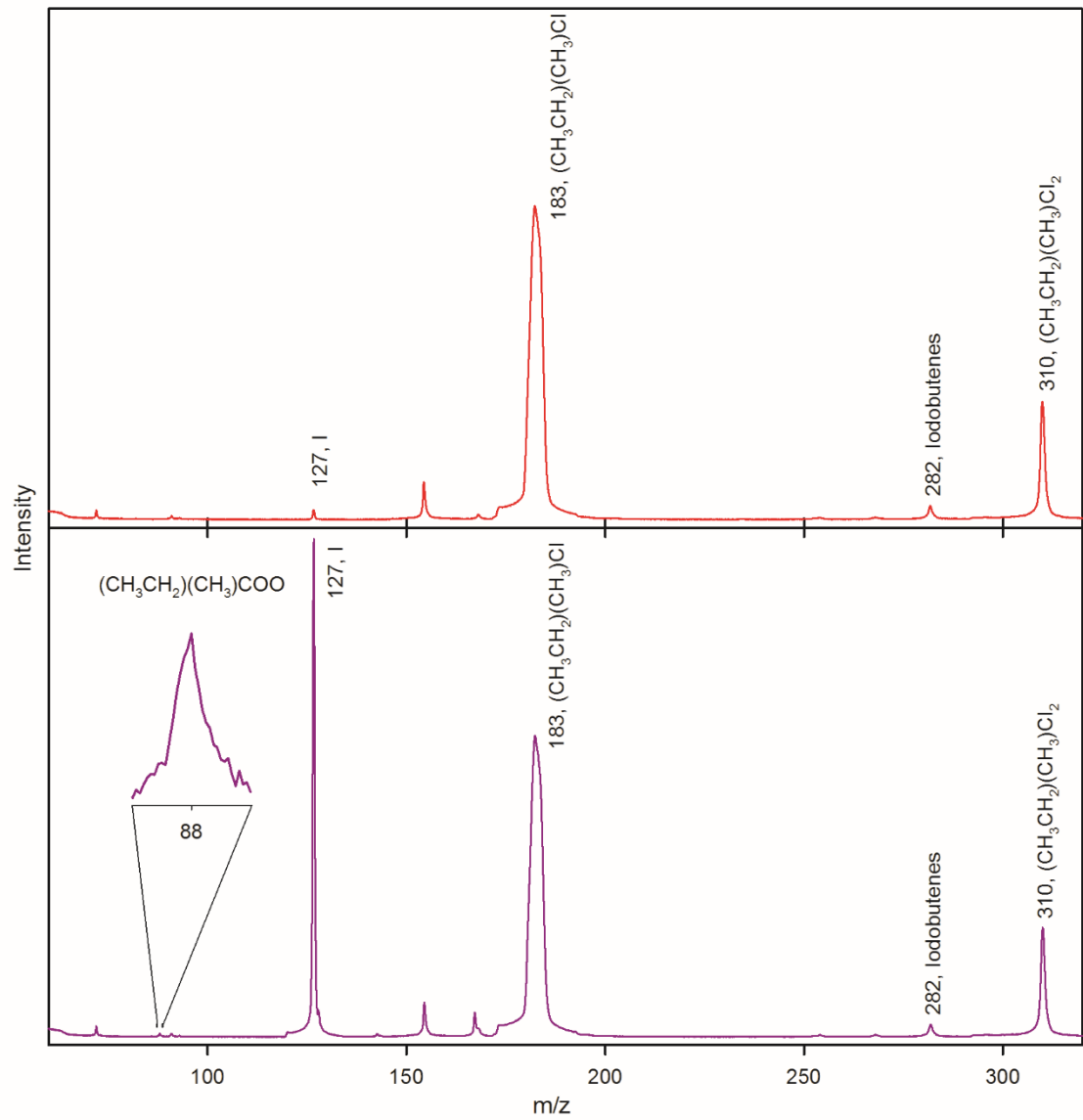


Figure 6. (Upper) Mass spectrum of $(\text{CH}_3\text{CH}_2)(\text{CH}_3)\text{CI}_2$ diiodoalkane precursor seeded in an O_2/Ar carrier gas, heated ($44\text{ }^\circ\text{C}$), and probed with VUV radiation in a TOF-MS. Observation of several mass channels ($m/z = 310\ \text{C}_4\text{H}_8\text{I}_2$, $m/z = 254\ \text{I}_2$, $m/z = 183\ \text{C}_4\text{H}_8\text{I}$, $m/z = 127\ \text{I}$) demonstrate photoionization of the $(\text{CH}_3\text{CH}_2)(\text{CH}_3)\text{CI}_2$ precursor. (Lower) Mass spectrum of $(\text{CH}_3\text{CH}_2)(\text{CH}_3)\text{CI}_2$ precursor with 248 nm photolysis along the capillary prior to photoionization. Significant enhancement of the I-atom ($m/z = 127$) mass channel upon 248 nm photolysis is indicative of photolysis of the C-I bond to produce a monoiodoalkane radical. Subsequent reaction of the resultant monoiodoalkane radical with O_2 produces the corresponding $(\text{CH}_3\text{CH}_2)(\text{CH}_3)\text{COO}$ ($m/z = 88$) Criegee intermediate photoionization signal, as shown in the inset of the lower panel. (Upper) Mass spectrum of $(\text{CH}_3\text{CH}_2)(\text{CH}_3)\text{CI}_2$ diiodoalkane precursor seeded in an O_2/Ar carrier gas, heated ($44\text{ }^\circ\text{C}$), and probed with VUV radiation in a TOF-MS. Observation of several mass channels ($m/z = 310\ \text{C}_4\text{H}_8\text{I}_2$, $m/z = 254\ \text{I}_2$, $m/z = 183\ \text{C}_4\text{H}_8\text{I}$, $m/z = 127\ \text{I}$) demonstrate photoionization of the $(\text{CH}_3\text{CH}_2)(\text{CH}_3)\text{CI}_2$ precursor. (Lower) Mass spectrum of $(\text{CH}_3\text{CH}_2)(\text{CH}_3)\text{CI}_2$ precursor with 248 nm photolysis along the capillary prior to photoionization. Significant enhancement of the I-atom ($m/z = 127$) mass channel upon 248 nm photolysis is indicative of photolysis of the C-I bond to produce a monoiodoalkane radical. Subsequent reaction of the resultant monoiodoalkane radical with O_2 produces the corresponding $(\text{CH}_3\text{CH}_2)(\text{CH}_3)\text{COO}$ ($m/z = 88$) Criegee intermediate photoionization signal, as shown in the inset of the lower panel.

IV. Future Directions

Future experiments to heat the diiodoalkane precursor and enhance the vapor pressure are desirable to study larger Criegee intermediates such as $(\text{CH}_3\text{CH}_2)(\text{CH}_3)\text{COO}$ or a five-carbon tertbutyl- substituted Criegee intermediate $((\text{CH}_3)_3\text{CCHO})$. One prototypical Criegee intermediate of particular interest would contain a vinyl substituent that extends conjugation of the carbonyl oxide group π -system as discussed in Chapter 6. However, synthesis of a geminal diiodoalkene precursor to generate a vinyl-substituted isoprene-derived Criegee intermediate poses a new challenge. The presence of a C=C double bond in a ketone or aldehyde starting material and corresponding hydrazone species now provides an additional location at which iodine may add under ambient conditions, thereby producing a diiodoalkane species and eliminating the double bond of interest.^{39, 40} A different synthetic method to generate a diiodoalkene precursor for a vinyl-substituted isoprene-derived Criegee intermediate is presented in Chapter 6. The low vapor pressure associated with increased molecular mass of the precursor poses an additional challenge for future experiments and may be overcome by heating the precursor sample.

Acknowledgements

The authors thank Prof. David Chenoweth and his research group, especially Dr. Robert Rarig, Dr. Yitao Zhang, Dr. Roy Malamakal, and Daniel Wu for helpful discussions and providing work space for synthesis of the precursors. The authors thank Dr. George Furst and Dr. Jun Gu for assistance in obtaining NMR spectra. The authors also thank Dr.

Rakesh Kohli and Dr. Charles W. Ross III for assistance in obtaining GC-MS and HRMS spectra.

References

- ¹ L. Vereecken, and J. S. Francisco, *Chem. Soc. Rev.* **41**, 6259 (2012).
- ² D. Johnson, and G. Marston, *Chem. Soc. Rev.* **37**, 699 (2008).
- ³ M. S. Alam, M. Camredon, A. R. Rickard, T. Carr, K. P. Wyche, K. E. Hornsby, P. S. Monks, and W. J. Bloss, *Phys. Chem. Chem. Phys.* **13**, 11002 (2011).
- ⁴ A. A. Presto, and N. M. Donahue, *J. Phys. Chem. A* **108**, 9096 (2004).
- ⁵ J. H. Kroll, S. R. Sahay, J. G. Anderson, K. L. Demerjian, and N. M. Donahue, *J. Phys. Chem. A* **105**, 4446 (2001).
- ⁶ G. T. Drozd, T. Kurten, N. M. Donahue, and M. I. Lester, *J. Phys. Chem. A* **121**, 6036 (2017).
- ⁷ T. L. Nguyen, H. Lee, D. A. Matthews, M. C. McCarthy, and J. F. Stanton, *J. Phys. Chem. A* **119**, 5524 (2015).
- ⁸ M. S. Alam, A. R. Rickard, M. Camredon, K. P. Wyche, T. Carr, K. E. Hornsby, P. S. Monks, and W. J. Bloss, *J. Phys. Chem. A* **117**, 12468 (2013).
- ⁹ Y. Fang, F. Liu, S. J. Klippenstein, and M. I. Lester, *J. Chem. Phys.* **145**, 044312 (2016).
- ¹⁰ H.-L. Huang, W. Chao, and J. J.-M. Lin, *Proc. Natl. Acad. Sci.* **112**, 10857 (2015).
- ¹¹ T. R. Lewis, M. A. Blitz, D. E. Heard, and P. W. Seakins, *Phys. Chem. Chem. Phys.* **17**, 4859 (2015).

- ¹² J. M. Beames, F. Liu, L. Lu, and M. I. Lester, *J. Am. Chem. Soc.* **134**, 20045 (2012).
- ¹³ J. M. Beames, F. Liu, L. Lu, and M. I. Lester, *J. Chem. Phys.* **138**, 244307 (2013).
- ¹⁴ F. Liu, J. M. Beames, A. M. Green, and M. I. Lester, *J. Phys. Chem. A* **118**, 2298 (2014).
- ¹⁵ R. Chhantyal-Pun, O. Welz, J. D. Savee, A. J. Eskola, E. P. F. Lee, L. Blacker, H. R. Hill, M. Ashcroft, M. A. H. Khan, G. C. Lloyd-Jones, L. Evans, B. Rotavera, H. Huang, D. L. Osborn, D. K. W. Mok, J. M. Dyke, D. E. Shallcross, C. J. Percival, A. J. Orr-Ewing, and C. A. Taatjes, *J. Phys. Chem. A* **121**, 4 (2017).
- ¹⁶ M. J. Newland, A. R. Rickard, M. S. Alam, L. Vereecken, A. Munoz, M. Rodenas, and W. J. Bloss, *Phys. Chem. Chem. Phys.* **17**, 4076 (2015).
- ¹⁷ A. Novelli, K. Hens, C. Tatum Ernest, M. Martinez, A. C. Nölscher, V. Sinha, P. Paasonen, T. Petäjä, M. Sipilä, T. Elste, C. Plass-Dülmer, G. J. Phillips, D. Kubistin, J. Williams, L. Vereecken, J. Lelieveld, and H. Harder, *Atmos. Chem. Phys.* **17**, 7807 (2017).
- ¹⁸ C. A. Taatjes, D. E. Shallcross, and C. J. Percival, *Nat. Chem.* **6**, 461 (2014).
- ¹⁹ C. Giorio, S. J. Campbell, M. Bruschi, F. Tampieri, A. Barbon, A. Toffoletti, A. Tapparo, C. Paijens, A. J. Wedlake, P. Grice, D. J. Howe, and M. Kalberer, *J. Am. Chem. Soc.* **139**, 3999 (2017).
- ²⁰ R. Yajima, Y. Sakamoto, S. Inomata, and J. Hirokawa, *J. Phys. Chem. A*, **Accepted**, (2017).
- ²¹ J. P. Hakala, and N. M. Donahue, *J. Phys. Chem. A* **120**, 2173 (2016).

- ²² Y. Liu, F. Liu, S. Liu, D. Dai, W. Dong, and X. Yang, *Phys. Chem. Chem. Phys.* **19**, 20786 (2017).
- ²³ T. L. Malkin, A. Goddard, D. E. Heard, and P. W. Seakins, *Atmos. Chem. Phys.* **10**, 1441 (2010).
- ²⁴ C. C. Womack, M.-A. Martin-Drumel, G. G. Brown, R. W. Field, and M. C. McCarthy, *Sci. Adv.* **1**, (2015).
- ²⁵ O. Welz, J. D. Savee, D. L. Osborn, S. S. Vasu, C. J. Percival, D. E. Shallcross, and C. A. Taatjes, *Science* **335**, 204 (2012).
- ²⁶ J. H. Lehman, H. Li, and M. I. Lester, *Chem. Phys. Lett.* **590**, 16 (2013).
- ²⁷ E. P. F. Lee, D. K. W. Mok, D. E. Shallcross, C. J. Percival, D. L. Osborn, C. A. Taatjes, and J. M. Dyke, *Chem. Eur. J.* **18**, 12411 (2012).
- ²⁸ R. L. Letsinger, and C. W. Kammeyer, *J. Am. Chem. Soc.* **73**, 4476 (1951).
- ²⁹ E. C. Friedrich, S. N. Falling, and D. E. Lyons, *Synth. Commun.* **5**, 33 (1975).
- ³⁰ A. Pross, and S. Sternhell, *Aust. J. Chem.* **23**, 989 (1970).
- ³¹ C. Cabezas, J.-C. Guillemin, and Y. Endo, *The Journal of Chemical Physics* **146**, 174304 (2017).
- ³² G. R. Newkome, and D. L. Fishel, *J. Org. Chem.* **31**, 677 (1966).
- ³³ S. M. Agten, D. P. L. Suylen, and T. M. Hackeng, *Bioconjugate Chem.* **27**, 42 (2016).
- ³⁴ J. Andrés, L. R. Domingo, M. T. Picher, and V. S. Safont, *Int. J. Quantum Chem.* **66**, 9 (1998).
- ³⁵ M. C. Smith, W. Chao, K. Takahashi, K. A. Boering, and J. J.-M. Lin, *J. Phys. Chem. A* **120**, 4789 (2016).

- ³⁶ A. M. Green, V. P. Barber, Y. Fang, S. J. Klippenstein, and M. I. Lester, Proc. Natl. Acad. Sci., **Accepted**.
- ³⁷ N. M. Donahue, S. A. Epstein, S. N. Pandis, and A. L. Robinson, Atmos. Chem. Phys. **11**, 3303 (2011).
- ³⁸ J. C. M. Li, and F. D. Rossini, J. Chem. Eng. Data **6**, 268 (1961).
- ³⁹ C. J. Michejda, R. L. Ayres, and E. P. Rack, J. Am. Chem. Soc. **93**, 1389 (1971).
- ⁴⁰ G. Sumrell, B. M. Wyman, R. G. Howell, and M. C. Harvey, Can. J. Chem. **42**, 2710 (1964).

CHAPTER 6

Observation of an isoprene-derived Criegee intermediate: Methylvinylketone oxide

The experimental research was performed with Prof. Marsha I. Lester in the *Department of Chemistry, University of Pennsylvania*. Synthesis and characterization of the diiodoalkene precursor was performed in collaboration with graduate student Nisalak Trongsiwat and Prof. Patrick J. Walsh in the *Department of Chemistry, University of Pennsylvania*.

I. Introduction

Isoprene is the most abundant nonmethane volatile organic compound in the troposphere, with global emissions on the order of 500 Tg each year.^{1,2} Nearly 90% of isoprene emissions are from biogenic sources (i.e. foliar emissions).¹ Although the abundance of both isoprene (2-methyl-1,3-butadiene, $\text{CH}_2=\text{C}(\text{CH}_3)-\text{CH}=\text{CH}_2$) and ozone (O_3) varies by region, concentrations can be as much as 2 ppb isoprene and nearly 20 ppb ozone in tropical rainforest environments.³ Isoprene ozonolysis is a significant source of hydroxyl (OH) radical^{4,5} the primary oxidant of trace atmospheric species.⁵ According to the 2003 TORCH and 1999-2000 PUMA field campaigns in the United Kingdom, alkene ozonolysis is responsible for approximately a third of OH production in the daytime and nearly all OH production in the nighttime.⁶⁻⁸

Isoprene is highly reactive with atmospheric oxidants such as OH radical, nitrate (NO_3) radical, and ozone due to the presence of two double bonds and a methyl substituent.⁹⁻¹¹ OH and NO_3 are known to abstract a hydrogen atom from the methyl group or add to a double bond of isoprene.¹⁰ Both of these reactions produce a carbon centered radical species that may undergo addition of O_2 to form highly oxygenated radical species and ultimately produce secondary organic aerosols (SOA).^{1, 12, 13} Isoprene ozonolysis has also been implicated in the generation of SOA.¹³ Processes contributing to the formation of SOA have a significant impact on global climate.¹⁴

Ozonolysis of isoprene may occur by addition of O_3 at two distinct C=C double bond locations to produce two different primary ozonide species in a highly exothermic process (ca. 50 kcal mol^{-1}).⁵ Subsequent decomposition of the primary ozonide generates

one of three Criegee intermediates and a corresponding carbonyl coproduct, as shown in Figure 1.^{15, 16} Due to the asymmetry of each double bond site, two possible Criegee intermediates are formed following decay of each primary ozonide. Ozonolysis at the C₃=C₄ bond will form CH₂OO (formaldehyde oxide) or MACR-OO (methacrolein oxide, CH₃(CH₂=)CCH(OO)) and corresponding coproducts are methacrolein (CH₃(CH₂=)CCHO) or formaldehyde (H₂CO), respectively. Ozonolysis at the C₁=C₂ bond results in CH₂OO or MVK-OO (methylvinylketone oxide, CH₂=CHC(CH₃)OO) with coproducts of methylvinylketone (CH₂=CHC(CH₃)O) or formaldehyde, respectively. The estimated branching ratio reported by Nguyen *et al.* for CH₂OO : MACR-OO : MVK-OO is 0.576 : 0.192 : 0.232.¹⁵ These estimates are based on a previous evaluation¹⁷ of ozone addition to isoprene (at C₁=C₂ or C₃=C₄ double bond sites) and the branching for decomposition of the resultant primary ozonides to Criegee intermediates.¹⁵ Although CH₂OO is the major Criegee intermediate formed from isoprene ozonolysis, MVK-OO has a substantial branching fraction.¹⁵

Significant experimental and theoretical efforts have been made to understand the reaction mechanisms following addition of ozone across the C=C double bonds of isoprene, in particular processes that ultimately yield OH radicals.^{5, 7, 11, 16, 18} OH radicals have been indirectly detected from isoprene ozonolysis using OH scavenger or tracer species.¹⁹⁻²² The use of OH scavengers (e.g. cyclohexane) results in reaction to form a new species (e.g. cyclohexanone) that is detected.⁴ In contrast, OH tracer species (e.g. m-xylene) react with OH and a loss of the tracer species is measured.⁴ There is some discrepancy in reported OH yields from isoprene ozonolysis, ranging from 0.19 to 0.68

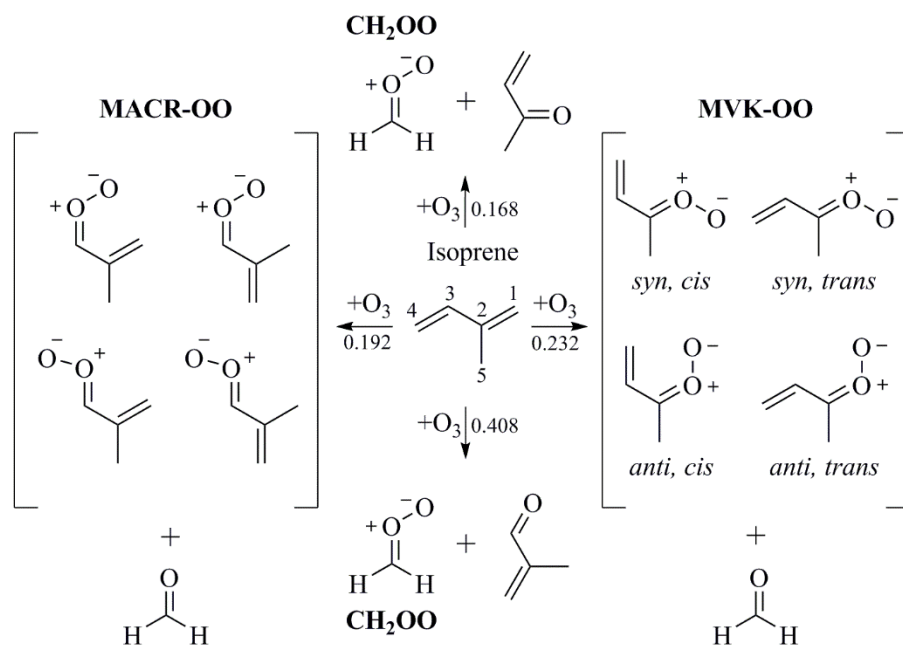


Figure 1. Summary of products from isoprene (2-methyl-1,3-butadiene, $\text{CH}_2=\text{C}(\text{CH}_3)\text{-CH}=\text{CH}_2$) ozonolysis. Three possible Criegee intermediates and corresponding ketone or aldehyde coproducts are formed from isoprene ozonolysis. Addition of ozone at the isoprene $\text{C}_3=\text{C}_4$ bond results in two Criegee intermediates, CH_2OO and MACR-OO (methacrolein oxide, $\text{CH}_3(\text{CH}_2=)\text{CCH}(\text{OO})$). Ozone addition at the isoprene $\text{C}_1=\text{C}_2$ bond produces two Criegee intermediates CH_2OO and MVK-OO (methylvinylketone oxide, $\text{CH}_2=\text{CHC}(\text{CH}_3)\text{OO}$). The relative yield of Criegee intermediates is based on the estimated branching ratio (from Ref. 15) for CH_2OO : MACR-OO : MVK-OO of 0.576 : 0.192 : 0.232. There are four conformers of MVK-OO: two with a methyl group *syn* to the terminal oxygen of the carbonyl oxide group and two with a methyl group that are *anti* to the terminal oxygen. The four conformers are further distinguished by *cis/trans* notation that describes the orientation of the vinyl substituent relative to the carbonyl $\text{C}=\text{O}$ group.

depending on the method of detection.^{4, 19, 20, 23} A theoretical atmospheric model by Malkin *et al.* predicts an OH yield of 0.27, which is in good agreement with their experimentally observed OH yield from isoprene ozonolysis of 0.26 from OH scavenger, OH tracer, and kinetic methods under atmospheric conditions.⁴ Laser-induced fluorescence (LIF) measurements allow for direct detection of OH radicals produced from isoprene ozonolysis at low pressure²⁴ and under atmospheric conditions (beyond the high pressure limit).²⁵

This work focuses on a vinyl-substituted isoprene-derived MVK-OO Criegee intermediate that is expected to be a significant source of OH radicals. There are four conformers of MVK-OO, shown in Figure 1, classified into two subsets (*syn* and *anti*) that describe the location of the methyl substituent with respect to the terminal oxygen of the carbonyl oxide group. Within these subsets are two additional conformers designated *cis* or *trans* that describe the relative position of the vinyl substituent (towards or away) from the carbonyl C=O group. Similar to other *syn* alkyl-substituted Criegee intermediates,^{26, 27} the two *syn* conformers are more stable (by ca. 1-2 kcal mol⁻¹) than the two *anti* conformers due to an intramolecular stabilization between an α -hydrogen on the methyl substituent and the terminal oxygen of the carbonyl oxide group.¹⁶ Isomerization between the *syn* and *anti* conformers (ca. 22-26 kcal mol⁻¹) is predicted to be much higher than isomerization between *cis* and *trans* conformers (ca. 8 kcal mol⁻¹).²⁸ Analogous to other *syn* alkyl-substituted Criegee intermediate systems, theory predicts that the unimolecular decay of *syn* MVK-OO is primarily via a 1,4 H-atom transfer mechanism of an α -hydrogen of the alkyl group to the terminal oxygen and subsequent decomposition

to OH products.^{16, 18, 28} Both prompt and thermal unimolecular decay of *syn* alkyl-substituted Criegee intermediates contribute to OH radical production under atmospheric conditions.^{29, 30} Unimolecular decay of *anti* conformers of MVK-OO is expected to proceed via a ring-closure mechanism through a higher barrier to a dioxirane species that may undergo further decomposition,^{16, 28} as found for other *anti* alkyl-substituted Criegee intermediates.^{18, 31, 32}

Although CH₂OO and *anti*-CH₃CHOO are highly reactive with water and water dimer,^{18, 33, 34} a prior experiment by Nguyen *et al.* did not show evidence of significant bimolecular reaction between *anti* MVK-OO and (H₂O)_n.¹⁵ This experiment relied on a variety of techniques (including gas-chromatography flame-ionization detection, Fourier-transform infrared (FTIR) detection, time-of-flight aerosol mass spectrometry, LIF, and chemical ionization mass spectrometry (CIMS)) to detect many products of isoprene ozonolysis, but did not directly detect Criegee intermediates.¹⁵ The lack of evidence for bimolecular reaction of MVK-OO and water was not attributed to slow rates of reaction between MVK-OO and (H₂O)_n, but rather to inefficient stabilization under atmospheric conditions.^{15, 28} However, earlier theoretical calculations predict significant stabilization of both *syn* MVK-OO (54%) and *anti* MVK-OO (34%) under atmospheric conditions.³⁵

Criegee intermediates, generated from ozonolysis of isoprene, have been observed indirectly via detection of H₂SO₄ products utilizing CIMS.³⁶ Criegee intermediates can oxidize SO₂ to produce SO₃ and a corresponding ketone or aldehyde.³⁶ Subsequent reaction of SO₃ with H₂O produces H₂SO₄.³⁶ To date, there has been no direct detection of vinyl-substituted Criegee intermediates that are derived from isoprene ozonolysis.

Collaboration with Prof. William Dailey and Prof. Patrick Walsh and his group has led to synthesis of a diiodoalkene precursor, which produces a resonance-stabilized monoiodoalkene radical upon UV photolysis. The monoiodoalkene radical is expected to react with O₂ and yield MVK-OO. As a result, this laboratory reports the first direct detection of an isoprene-derived vinyl-substituted Criegee intermediate, MVK-OO, an important species formed in isoprene ozonolysis.

II. Materials and Methods

A. Synthesis and characterization of precursor

Nisalak Trongsirawat and Prof. Patrick Walsh have made a *Z/E* mixture of 1,3-diiodobut-2-ene following the general procedures of Manickam *et al.*³⁷ Briefly, anhydrous zinc chloride (290.3 mg, Sigma Aldrich, ≥98%) was added under nitrogen atmosphere to a solution of but-2-yn-1-ol (1.0 g, Alfa Aesar, 98%) in dry dichloromethane (10 mL). The reaction mixture was cooled to -40 °C using an acetonitrile/dry ice bath. Trimethylsilyl iodide (4.4 mL, Alfa Aesar, 97%) was added slowly over 40 minutes in the dark. The reaction mixture was slowly warmed to 0 °C over a 1 hour period and left stirring at room temperature overnight. The crude product was filtered over a bed of celite and concentrated in vacuo. The product was further purified via column chromatography and vacuum distillation (b.p. 67-69 °C) to yield a brown oil (1.3 grams, 30% yield, *Z/E* ~ 10/1). The product was verified by ¹HNMR. ¹HNMR (500 MHz, CDCl₃): *Z*-1,3-diiodobut-2-ene δ 5.7 (q, 1H), 3.9 (d, 2H), δ 2.5 (d, 3H). *E*-1,3-diiodobut-2-ene δ 6.0 (q, 1H), 4.4 (d, 2H), δ 1.7 (d, 3H).

Following optimization of an older procedure, shown in Figure 2, that does not require a zinc chloride catalyst,³⁸ but-2-yn-1-ol (0.54 mL, Alfa Aesar, 98%) was diluted in dry ether and the mixture was cooled to -40 °C. Trimethylsilyl iodide (TMSI, 2.23 mL, Alfa Aesar, 97%) was added slowly in the dark and with rapid stirring. Following addition of TMSI, the reaction mixture was slowly warmed to 20 °C and left to stir for an hour. The reaction mixture was quenched with a saturated sodium thiosulfate solution. The product was extracted with ether and dried over sodium sulfate. The product was purified via thin layer chromatography in hexanes to yield a brown oil (1.85 grams, 84% yield, Z/E ~ 5/1). ¹HNMR (500 MHz, CDCl₃): *Z*-1,3-diiodobut-2-ene δ 5.7 (q, 1H), 3.9 (d, 2H), δ 2.5 (d, 3H). *E*-1,3-diiodobut-2-ene δ 6.0 (q, 1H), 4.4 (d, 2H), δ 1.7 (d, 3H). HRMS (EI): m/z calculated for (*Z/E*)-1,3-diiodobut-2-ene 307.8559, observed 307.8560. The full ¹HNMR spectrum can be found in Figure S1 in Supplementary Materials.

The (*Z/E*)-1,3-diiodobut-2-ene precursor was further characterized via UV-Vis spectroscopy. Dilute solutions of (*Z/E*)-1,3-diiodobut-2-ene (0.07 mol/L) and CH₂I₂ (0.19 mol/L) in hexanes were prepared and the UV-Vis spectra, shown in Figure 3, were obtained with a spectrophotometer (Jasco V-650). Comparison of the UV-Vis spectra of CH₂I₂ in both polar and nonpolar solvents as compared to the gas phase UV spectrum has indicated virtually no shift in peak absorption wavelengths.³⁹ Therefore the peak UV absorption of (*Z/E*)-1,3-diiodobut-2-ene is anticipated to exhibit no significant shift due to solvent effects.

The strong UV-induced electronic excitation of (*Z/E*)-1,3-diiodobut-2-ene is expected to exhibit a similar excited state dynamic as that of CH₂I₂. The UV spectrum of

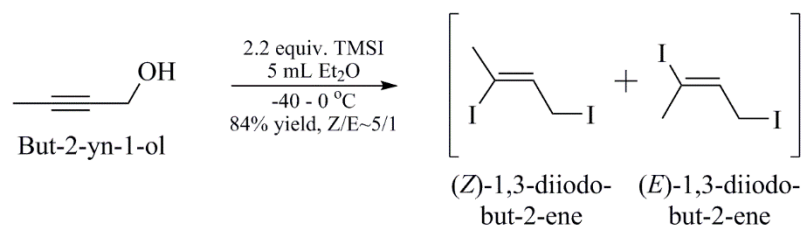


Figure 2. Synthesis of diiodoalkane precursor (*Z/E*)-1,3-diiodobut-2-ene from but-2-yn-1-ol following the methods of Ref. 38.

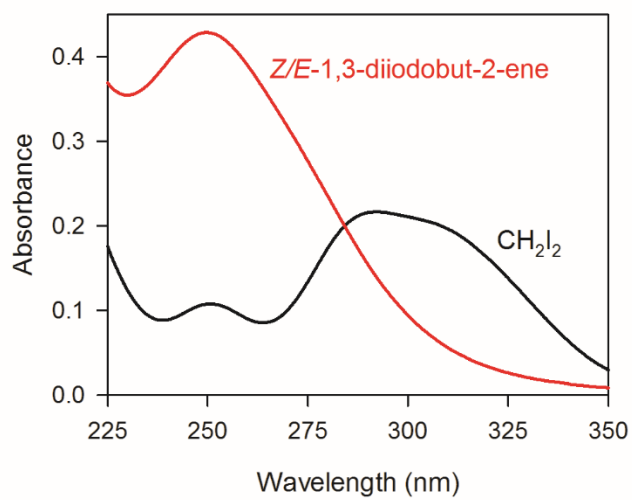


Figure 3. UV-Vis spectra for (*Z/E*)-1,3-diiodobut-2-ene (red, 0.07 mol/L) and CH₂I₂ (black, 0.19 mol/L) in hexanes.

CH₂I₂ is described by a convolution of four partially overlapping Gaussian bands, each assigned to a transition accessing an excited electronic state.⁴⁰ The two lower excited states of CH₂I₂ are repulsive and produce iodine atoms.⁴¹ This laboratory has found that 248 nm excitation to the third excited state of CH₂I₂ is also repulsive along the C-I coordinate. Upon 248 nm excitation of CH₂I₂, the majority of the available energy is partitioned into internal energy of the CH₂I iodoalkyl fragment.⁴² No information is available regarding the excited electronic states or dynamics of the (*Z/E*)-1,3-diiodobut-2-ene precursor. However, it is clear from the UV-Vis spectra that (*Z/E*)-1,3-diiodobut-2-ene has a stronger absorption than CH₂I₂ at 248 nm. In general, it is known that the excited state may have lower barriers to isomerization between *Z/E* conformers.^{43, 44} It is anticipated that the strong absorption of the 1,3-diiodobut-2-ene precursor at 248 nm may result in *Z/E* isomerization prior to C-I bond dissociation.

In addition, the FTIR spectrum of the (*Z/E*)-1,3-diiodobut-2-ene precursor on a KBr plate was obtained with an FTIR spectrometer (Thermo Scientific, Nicolet iS5). The observed FTIR spectrum is presented in Figure S2 in Supplementary Materials. Calculated vibrational frequencies of the (*Z/E*)-1,3-diiodobut-2-ene precursor (detailed in Sec. II. C) are given in Table S1 according to the numbering of atoms shown in Figure S3. High frequency (ca. 2900-2960 cm⁻¹) vibrations are assigned to the methyl CH stretch. CH scissor and CH wag vibrational modes appear in the 1000-1500 cm⁻¹ energy region. The sharp feature at ca. 1630 cm⁻¹ is attributed to the alkene C=C stretch. The very strong C-I stretches appear at ca. 500 cm⁻¹.

B. Generation of MVK-OO and Detection in a TOF-MS

Photoionization detection of Criegee intermediates with VUV radiation in a Wiley-McLaren linear time-of-flight mass spectrometer (TOF-MS, RM Jordan) has been described previously.^{26, 27, 45} Briefly, the diiodoalkene precursor ((*Z/E*)-1,3-diiodobut-2-ene) seeded in a 20% O₂/Ar carrier gas (10 psig) is pulsed through a heated (45 °C) nozzle (1 mm orifice) into a quartz capillary tube reactor (1 inch length, 1 mm orifice). The precursor is photolyzed along the length of the capillary using the cylindrically focused 248 nm output (25 mJ/pulse) of a KrF excimer laser to induce dissociation of the allylic C-I bond of the precursor. Subsequent reaction of the monoiodoalkene radical with O₂ displaces the remaining iodine atom to form the MVK-OO Criegee intermediate. The MVK-OO is collisionally stabilized, cooled in a free jet expansion, and probed 4 cm downstream using 10.5 eV (118 nm) vacuum ultraviolet (VUV) radiation.

The sample is loaded behind the armature of a pulsed valve (Parker General Valve Series 9). The valve is encased in an aluminum block, which makes thermal contact with a Peltier thermoelectric heating module (Laird Technologies, PC4) that results in a temperature differential between the hot side and cool side of the module. The temperature of the cool side of the heating module is maintained by thermal exchange with a water line. Thermal contact is made at every interface with thermal silicone compound (Wakefield-Vette). The temperature was monitored with a thermocouple (Cole-Parmer, Type K digital thermometer).

The fixed 118 nm VUV is generated by frequency-tripling the focused ($f = 30$ cm, UV fused silica lens) third harmonic output (355 nm, 40 mJ/pulse) of an Nd:YAG laser (Continuum Powerlite 9010) in a phase-matched Xe/Ar ($\sim 1:10$) cell. The VUV is refocused ($f = 20$, MgF₂ lens) at the center of the interaction region in a TOF-MS where it is intersected by a counterpropagating focused UV beam. The residual 355 nm is spatially separated from the VUV due to the difference in focal properties.

OH radicals generated in the capillary from decomposition of energized Criegee intermediates are cooled in a supersonic expansion to the lowest rovibrational X²Π_{3/2} ($v=0, J=1.5$) state and observed via $1 + 1'$ resonance enhanced multiphoton ionization (REMPI). The OH X²Π_{3/2} ($v=0, J=1.5$) radicals are excited to the well-characterized OH A²Σ⁺ ($v=1, J=2.5$) state via focused UV excitation resonant on the OH A²Σ⁺-X²Π (1,0) R₁(1.5) transition. The VUV radiation is introduced after 100 ns to induce ionization. The UV radiation (2 mJ/pulse) is generated by frequency-doubling the fundamental output of a Nd:YAG (Continuum 8000, 532 nm) pumped dye laser (ND6000, Rhodamine 590). For UV depletion measurements, several UV wavelengths are generated by doubling the output of the Nd:YAG pumped dye laser with the use of different dyes (Rhodamine 590, DCM, LDS698).

In general, the bond dissociation energy of an R-X species, where X is a halogen is inversely related to the stability of the corresponding alkyl radical (R[•]).⁴⁶ The (*Z/E*)-1,3-diodobut-2-ene precursor contains two C-I bonds, allylic (at C₍₁₎) and vinylic (at C₍₃₎), and is shown in Figure 4. The allylic C-I bond at C₍₁₎ is weaker due to the resonance stabilization of the resultant allyl radical. As a result, 248 nm photolysis is

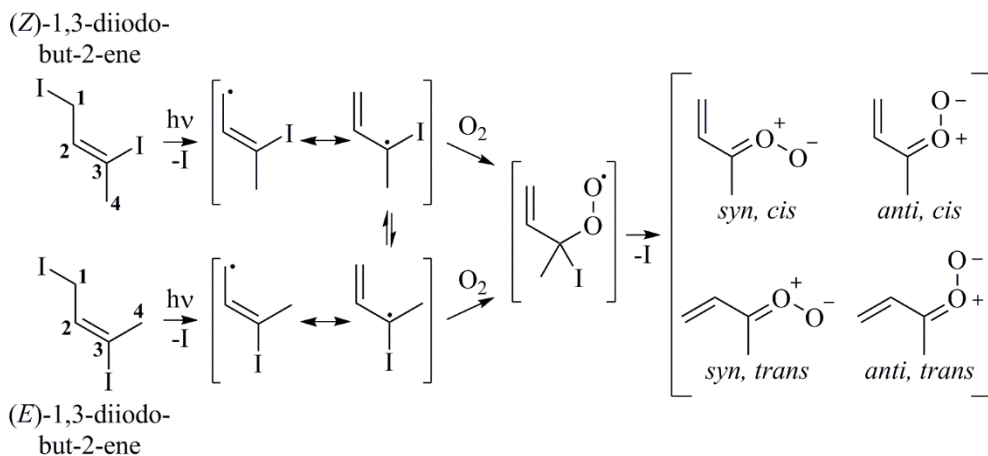


Figure 4. Schematic for generation of methylvinylketone oxide (MVK-OO) Criegee intermediates. UV photolysis of (Z/E)-1,3-diiodobut-2-ene precursor yields resonance stabilized monoiodoalkene radicals. Addition of O₂ to the monoiodoalkene radicals displaces the remaining iodine atom and generates four possible conformers of the MVK-OO Criegee intermediate. The low calculated barrier (ca. 14 kcal mol⁻¹) for rotation of the vinyl group between monoiodoalkene radicals and even lower calculated barrier (ca. 5 kcal mol⁻¹) for the iodoalkene peroxy radical suggests that all four MVK-OO conformers will be generated. The two *syn* conformers are more stable than the two *anti* conformers due to an intramolecular interaction between the terminal oxygen and α -hydrogen of the methyl group. *Cis/trans* notation describes the orientation of the vinyl group with respect to the carbonyl C=O group.

expected to dissociate the weaker C₍₁₎-I bond to produce an allylic monoiodoalkene radical.

The allylic monoiodoalkene radical can be viewed as a superposition of two resonance structures. The more stable and therefore preferred structure will possess a radical on the carbon that has a higher degree of substitution ($3^\circ > 2^\circ > 1^\circ$).⁴⁶ Therefore, subsequent reaction with O₂ is expected to preferentially occur at the more stable, secondary carbon radical site. Addition of O₂ to the resonance stabilized monoiodoalkene radical will displace the remaining iodine atom to produce the MVK-OO Criegee intermediate, analogous to previous experiments.^{26, 27, 45} Both *Z/E* diiodoalkene conformers are expected to produce all four MVK-OO conformers, as discussed later.

C. Theoretical Calculations

Optimized geometries, Gibbs free energies (at 1300 K), and relative ground state energies including harmonic zero-point energy corrections (ZPE), of the four MVK-OO conformers are calculated at the CCSD/6-311+G(d,p) level of theory using the Gaussian 09 program suite.⁴⁷ The vertical excitation energies are determined from the difference between the cation and ground state energies evaluated with B3LYP and CCSD theoretical methods. Vertical excitations for each MVK-OO conformer to the excited B electronic state are calculated at the CASPT2/aug-cc-pVTZ level of theory using the MOLPRO v2010.1 package,⁴⁸ based on the CCSD/6-311+G(d,p) optimized geometries.

(*Z/E*)-1,3-diiodobut-2-ene precursor geometries (Figure S3 in Supplementary Materials) are optimized at the B3LYP/6-311+G(d,p) level of theory, where the basis set

is obtained from the EMSL basis set exchange.^{49, 50} The harmonic fundamental vibrational frequencies of the precursor are calculated and presented in Table S1 in Supplementary Materials. The assignments for vibrational modes of (*Z/E*)-1,3-diiodobut-2-ene precursors are based on the numbering of atoms presented in Figure S3 of Supplementary Materials.

The monoiodoalkene radical and iodoalkene peroxy radical (shown in Figure 4) geometries are also optimized at the B3LYP/6-311+G(d,p) level of theory, where the basis set is obtained from the EMSL basis set exchange.^{49, 50} The rotational barriers of the vinyl group of the monoiodoalkene radical and iodoalkene peroxy radical are calculated based on a relaxed potential energy surface scan of the I-C-C=C dihedral angle with a 10 degree step size at the B3LYP/6-311+G(d,p) level of theory.

III. Results and Discussion

The (*Z/E*)-1,3-diiodobut-2-ene precursor is detected by 10.5 eV (118 nm) VUV photoionization on the $m/z = 308$ parent mass channel in a TOF-MS as shown in the upper panel of Figure 5. Several other fragment mass channels including I ($m/z = 127$), C₄H₆I ($m/z = 181$), and I₂ ($m/z = 254$) are observed upon photoionization of the (*Z/E*)-1,3-diiodobut-2-ene precursor. A small signal at the $m/z = 85$ mass channel is attributed to photoionization of dichloromethane (DCM), which is a solvent used in the synthetic procedure. The lower panel of Figure 5 shows the TOF mass spectrum obtained when 248 nm excimer radiation is introduced to photolyze the precursor in an O₂/Ar gas mixture within the quartz capillary reactor tube prior to VUV photoionization. The inset of the lower panel displays the $m/z = 86$ mass channel, tentatively attributed to the

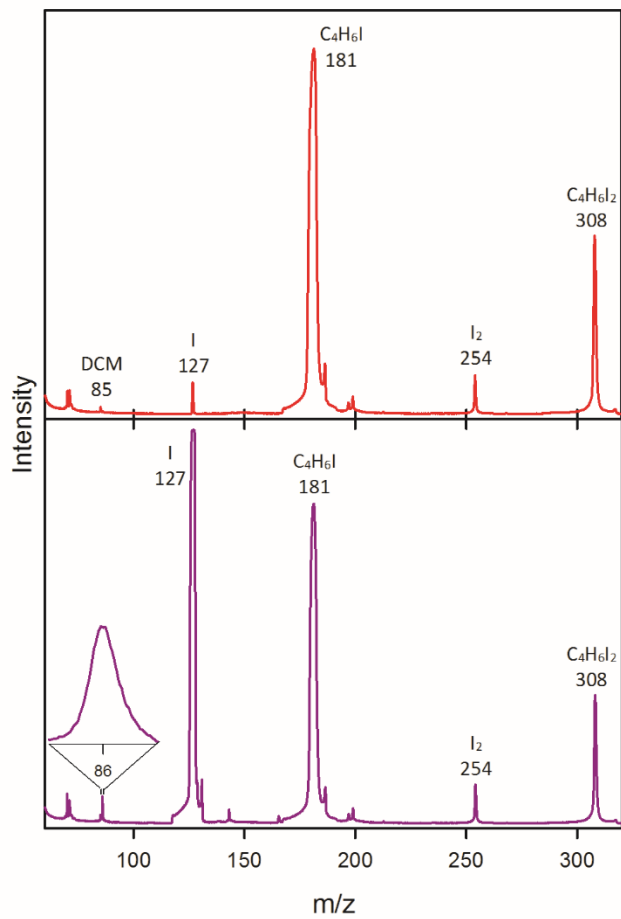


Figure 5. (Upper) TOF mass spectrum of (*Z/E*)-1,3-diiodobut-2-ene precursor sample (heated to 45 °C) obtained upon 118 nm VUV photoionization. Mass channels ($m/z = 308$ C₄H₆I₂, $m/z = 181$ C₄H₆I, $m/z = 127$ I, $m/z = 254$ I₂) show that the precursor is photoionized. Residual dichloromethane (DCM, $m/z = 85$) from the synthetic workup is observed. (Lower) TOF mass spectrum of precursor sample in a 20% O₂/Ar carrier gas with 248 nm photolysis along the quartz capillary tube reactor and 118 nm VUV photoionization. Inset shows excimer induced signal on the $m/z = 86$ mass channel. No signal on the $m/z = 86$ mass channel is evident with the VUV probe laser only. This is consistent with photolysis of the diiodoalkene precursor C-I bond and subsequent reaction with O₂. Thus, the $m/z = 86$ mass channel is tentatively assigned to the MVK-OO Criegee intermediate.

MVK-OO Criegee intermediate. The $m/z = 86$ mass channel only appears upon excimer photolysis of the precursor. This is consistent with 248 nm photolysis of the diiodoalkene precursor producing the monoiodoalkene radical $C_4H_6I + I$. Subsequent reaction of C_4H_6I with O_2 generates the MVK-OO Criegee intermediate.

The distribution of (*Z/E*)-1,3-diiodobut-2-ene precursor is not expected to affect the relative population of MVK-OO conformers. The monoiodoalkene radical (see Figure 4) has a low computed barrier for rotation of the vinyl substituent (ca. 14 kcal mol⁻¹). Addition of O_2 yields an iodoalkene peroxy radical intermediate (Figure 4) that is predicted to have an even lower barrier for rotation of the vinyl group (ca. 5 kcal mol⁻¹). These barriers are much lower than the high degree of internal excitation anticipated for C_4H_6I , as found previously for the monoiodoalkyl radical species (CH_2I , ca. 35 kcal mol⁻¹), following CH_2I_2 photolysis.⁴² Therefore, rotation of the vinyl groups of iodoalkene and/or iodoalkene peroxy radicals are anticipated to be facile and all four MVK-OO conformers may be generated. The calculated relative energies of these MVK-OO conformers, listed in Table 1 and shown in Figure 6, are in close agreement with prior calculations for three of the four MVK-OO conformers.^{16, 23, 28, 51} There is some discrepancy in the literature regarding the relative energy of the *syn, cis* conformer with respect to the lowest energy *syn, trans* conformer. The present study indicates that the relative energy of the *syn, cis* conformer is nearly 0.5 kcal mol⁻¹ lower in energy than several previous calculations,^{16, 23, 28, 51} and nearly 0.5 kcal mol⁻¹ higher in energy than the most recent calculation.¹⁸ The ordering of conformers based on relative energy is consistent across all studies.

Table 1. Relative energies, including harmonic zero-point energy corrections, of MVK-OO conformers are calculated at the CCSD/6-311+G(d,p) level of theory. The two *syn* conformers are more stable than the two *anti* conformers due to an intramolecular interaction between the terminal oxygen of the carbonyl oxide group and an α -hydrogen of the -CH₃ group. The population is estimated assuming a Boltzmann distribution utilizing the calculated relative Gibbs free energies of each conformer.

MVK-OO conformer	Relative Energy (kcal mol ⁻¹)	Relative Gibbs Energy (kcal mol ⁻¹) (T = 1300 K)	Relative Population (T = 1300 K)
<i>anti, cis</i>	2.32	2.21	0.15
<i>anti, trans</i>	1.94	1.43	0.20
<i>syn, cis</i>	1.06	0.29	0.31
<i>syn, trans</i>	0.00	0.00	0.34

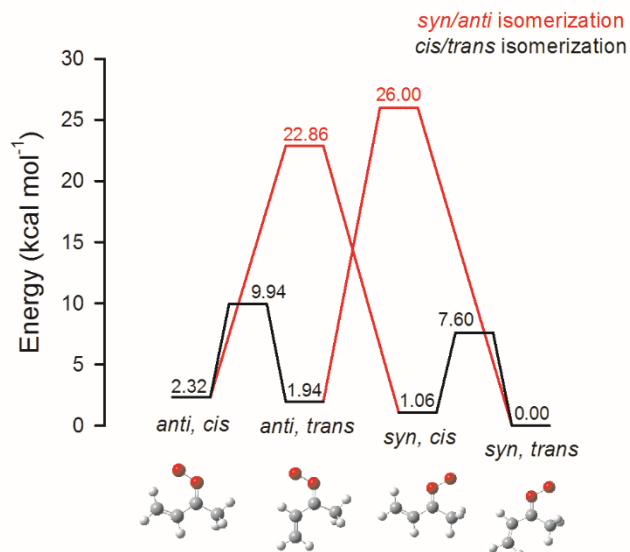


Figure 6. Relative energies of MVK-OO conformers are evaluated at the CCSD/6-311+G(d,p) level of theory and include harmonic zero-point energy corrections. Barriers for *syn/anti* and *cis/trans* isomerization are from Ref. 28. The *cis/trans* isomerization barriers are relative to the more stable *syn, trans* and *anti, trans* conformers. The *syn/anti* isomerization barriers are relative to the more stable *syn, cis* and *syn, trans* conformers.

A simple model is implemented to estimate the relative MVK-OO conformer abundance based on a Boltzmann distribution utilizing calculated Gibbs free energies ($\Delta G = -RT\ln(K)$) at a specified temperature T, where K is the ratio of conformer populations.⁵²⁻⁵⁴ The relative abundance of multiple conformers of other Criegee intermediates, such as CH₃CHOO and (CH₃CH₂)(CH₃)COO, have been successfully estimated with this approach.^{26, 55, 56} The calculated Gibbs free energies (at an estimated T~1300 K) for the MVK-OO conformers and the corresponding relative populations are given in Table 1. The effective temperature of 1300 K is estimated based on the *syn/anti* ratio of 0.7/0.3 for CH₃CHOO observed by Sheps et al. following 266 nm photolysis of CH₃CHI₂ in the presence of O₂.⁵⁷ This model predicts that the lower energy *syn* MVK-OO conformers will have a larger population than the higher energy *anti* conformers, and all four conformers will be populated.

After the MVK-OO conformers are cooled in the supersonic expansion (~10 K), interconversion between *syn/anti* and *cis/trans* conformers will not occur due to substantial barriers between conformers.²⁸ Isomerization between *syn/anti* conformers has a high calculated barrier (ca. 22-26 kcal mol⁻¹) due to the double bond character of the carbonyl oxide group.²⁸ The calculated barrier for *cis/trans* isomerization (ca. 8 kcal mol⁻¹) via rotation of the vinyl substituent is significantly lower, but still too high to enable *cis/trans* isomerization under jet-cooled conditions.²⁸

Vertical ionization energies (VIE) are calculated and given in Table 2 to show that the four MVK-OO conformers can be detected with 10.5 eV photoionization. The calculated VIE (ca. 8.5 eV) are nearly 2 eV lower than the 10.5 eV VUV radiation,

Table 2. Calculated vertical ionization energies at the CCSD/6-311+G(d,p) and B3LYP/6-311+G(d,p) levels of theory for each MVK-OO conformer.

MVK-OO conformer	Calculated VIE (eV) (CCSD/6-311+G(d,p))	Calculated VIE (eV) (B3LYP/6-311+G(d,p))
<i>anti, cis</i>	8.32	8.69
<i>anti, trans</i>	8.18	8.55
<i>syn, cis</i>	8.20	8.54
<i>syn, trans</i>	8.22	8.59

therefore all four conformers should be observed. The possibility of fragmentation upon photoionization cannot be eliminated.

Significant UV-induced depletions on the MVK-OO ($m/z = 86$) mass channel are observed at three wavelengths (281 nm, 317 nm, 350 nm) and shown in Figure 7. UV excitation depletes the ground state population and results in reduced photoionization signals for the Criegee intermediate mass channel. The depletion measurements indicate UV absorption by one or more MVK-OO conformers. In previous studies of CH₂OO and various alkyl-substituted Criegee intermediates,^{26, 27, 45, 58} UV excitation from the ground state to an excited B state is observed as ground state depletions, and was attributed to strong UV absorption and rapid excited state dissociation dynamics along the O-O coordinate.^{58, 59}

High level theoretical calculations predict that each conformer will have a different peak absorption wavelength and transition strength, as shown in Table 3. For comparison, a similar level calculation is given for CH₂OO. The peak absorption wavelength of two conformers (*anti, trans* and *syn, cis*) are predicted shift to longer wavelength (~400 nm and 375 nm) relative to the UV spectrum of CH₂OO. The other two conformers (*anti, cis* and *syn, trans*) have similar calculated peak absorption wavelengths (~350-360 nm) as CH₂OO. The ground state energies of the four conformers are similar (within ~0.04-0.09 eV; ~1-2 kcal mol⁻¹), therefore the change in the calculated B-X transition is largely due to the stability of the excited B state.

It is anticipated that the UV spectra of the four MVK-OO conformers may be overlapping based on the broad (ca. 40 nm FWHM) UV spectra of previously observed

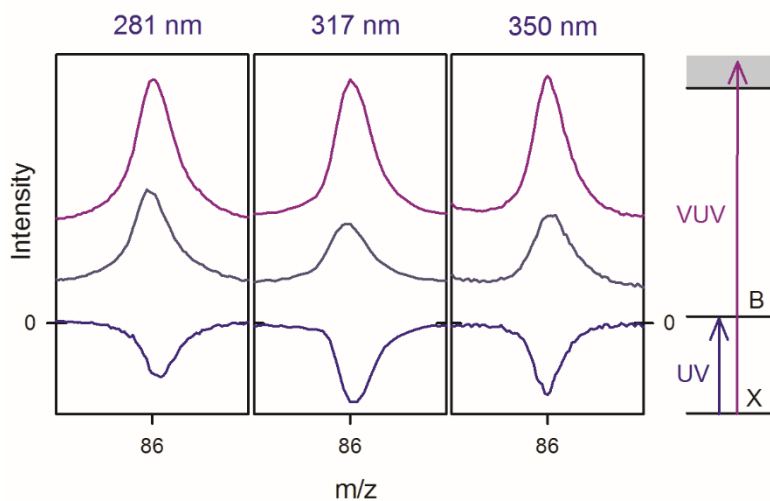


Figure 7. (Left) Depletions on the $m/z = 86$ mass channel have been observed at three UV wavelengths (281 nm, 317 nm, 350 nm), suggestive of a broad UV absorption. The subtraction of the UV pump + VUV probe signal (grey) from the VUV probe only signal (purple) results in the depleted signal (blue). (Right) Scheme demonstrates detection from the ground state to above the photoionization threshold via VUV (purple) laser excitation. UV (blue) excitation to an excited B state prior to photoionization results in removal of population from the ground state, observed as a depletion in the $m/z = 86$ mass channel.

Table 3. Vertical B-X excitation energies are calculated at the CASPT2/aug-cc-pVTZ level of theory for each MVK-OO conformer and CH₂OO.^a The corresponding peak UV absorption wavelength and transition strength is also provided.

MVK-OO conformer	Calculated B-X excitation energy (eV)	Predicted peak UV absorption (nm)	Transition Strength
<i>anti, cis</i>	3.45	359	0.167
<i>anti, trans</i>	3.13	396	0.196
<i>syn, cis</i>	3.31	375	0.206
<i>syn, trans</i>	3.53	351	0.246
CH ₂ OO	3.56	348	0.110

^a B. Marchetti, personal communication (2017)

CH₂OO and alkyl-substituted Criegee intermediate systems.^{26, 27, 45} Observation of a significant UV-induced depletion at 351 nm indicates that one or more MVK-OO conformers is present and is a strong UV absorber. It is anticipated that two conformers (*syn, cis* and *anti, trans*) will be the primary absorbers at longer wavelengths near 400 nm. Observation of significant depletions at shorter wavelengths (281 nm and 317 nm) may arise from another $\pi^* \leftarrow \pi$ transition. Additional $\pi\pi^*$ excited states have been observed for species with extended π -systems such as phenol and aniline,^{60, 61} and may also affect the UV spectrum of MVK-OO.

Stable isomers (i.e. ester species) may be generated, via isomerization through a dioxirane intermediate, and photoionized at 10.5 eV.⁵ For example, methyl propenoate has an adiabatic ionization energy (AIE) of 10.0 eV and vinyl acetate has an AIE of 9.4 eV.⁶² Thus, these species may appear on the same $m/z = 86$ mass channel. However, these isomers lack a $\pi^* \leftarrow \pi$ transition characteristic of the carbonyl oxide species^{26, 27, 45} and therefore are not expected to absorb UV radiation or undergo a UV-induced depletion at 350 nm. Vinyl acetate cannot contribute to the observed depletions because it absorbs only at ≤ 250 nm.⁶³ There is no UV absorption data for methyl propenoate at the wavelengths of interest. However, similar ester species exhibit UV absorptions that peak near 215 nm,⁶⁴ outside of the 281-350 nm region where significant UV-induced depletions of the $m/z = 86$ mass channel is observed. Thus, these isomers are unlikely to contribute to the UV-induced depletion of the $m/z = 86$ photoionization signal.

Another stable isomer is a 5-membered ring structure (dioxole) formed from the electrocyclicization of MVK-OO, as predicted by Kuwata *et al.*²⁸ This species could also

arise from addition of O₂ to the monoiodoalkene radical following photolysis of the (Z/E)-1,3-diiodobut-2-ene precursor, as shown in Figure 8 for (Z)-1,3-diiodobut-2-ene. There is no information on the synthesis or UV characterization of dioxole. In addition, this dioxole species has not been observed previously.

Finally, *syn* conformers of the MVK-OO Criegee intermediate are predicted to be a major source of OH radicals, as has been observed for other *syn* alkyl-substituted Criegee intermediates.^{65,66} *Anti* conformers of MVK-OO are not anticipated to be a significant source of OH radical.^{16,35} Stable isomers such as dioxole, methyl propenoate, and vinyl acetate are also not expected to be a significant source of OH, as there is no clear pathway for production of OH radical.¹⁵ A $m/z = 17$ photoionization signal, attributed to OH radicals, has been observed concurrently with the MVK-OO Criegee intermediate mass channel ($m/z = 86$) in a TOF-MS, as shown in Figure 9. The OH radicals are generated in the capillary reactor tube, cooled in the supersonic expansion, and probed in the ground rovibrational state, X²Π_{3/2} ($v=0, J=1.5$) via A-X (1,0) resonant UV excitation on the R₁(1.5) transition. Subsequent VUV excitation at 10.5 eV provides sufficient energy to exceed the ionization threshold for OH radicals and produce OH⁺. The 10.5 eV radiation is the same laser used for photoionization of MVK-OO. The OH⁺ signal is not detected when the UV laser is off or off-resonance, confirming that the $m/z = 17$ photoionization signal arises from OH radicals. Furthermore, the OH⁺ signal requires excimer photolysis of the precursor/O₂ gas mixture, suggesting that OH radicals are produced from the decay of energized MVK-OO. The relative OH yield, determined by scaling the intensity of the OH photoion signal by the intensity of the MVK-OO

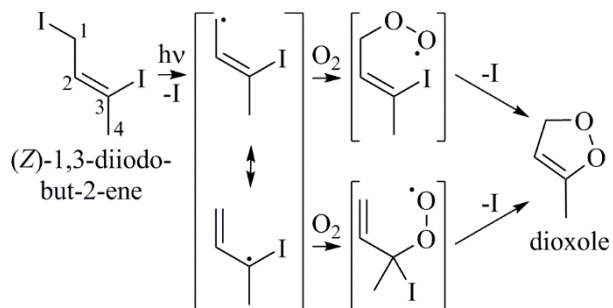


Figure 8. A cyclic dioxole isomer ($m/z = 86$) may be formed from reaction of O_2 with iodoalkene radicals (C_4H_6I), which are generated from photolysis of (Z)-1,3-diiodobut-2-ene (shown) or (*E*)-1,3-diiodobut-2-ene (not shown).

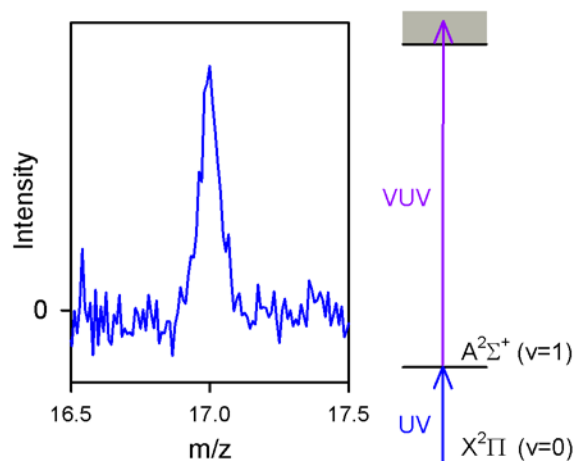


Figure 9. (Left) $1 + 1'$ REMPI photoionization of OH radicals ($m/z = 17$) detected concurrently with MVK-OO Criegee intermediates ($m/z = 86$, not shown), in a TOF-MS. (Right) $1 + 1'$ REMPI scheme utilizes resonant OH A-X (1,0) $R_1(1.5)$ UV excitation with fixed frequency VUV ionization at 118 nm.

($m/z = 86$) photoion signal, is provided in Table 4 and compared to that of several other Criegee intermediates in similar experiments.

OH yields have been shown to increase with increased alkylation of Criegee intermediates, whether they are generated from diiodo precursors^{26, 27} or ozonolysis of a corresponding symmetric alkene.⁶⁷⁻⁶⁹ The relative OH yield observed for MVK-OO is greater than CH₂OO, when generated from their corresponding diiodo precursors. This is expected because MVK-OO contains a methyl group and can undergo an intramolecular 1,4 H-atom transfer to ultimately yield OH products. CH₂OO does not contain an alkyl group and follows a ring closure pathway through a dioxirane intermediate to several products, including a minor channel to OH radical.^{31, 70} Although *syn* MVK-OO is anticipated to be the primary source of OH from isoprene ozonolysis, a direct comparison cannot be made between the OH yield of MVK-OO in the current study and OH generated from ozonolysis of isoprene. The current study examines OH generated from only MVK-OO.

IV. Conclusions and Future Directions

The synthesis of a diiodoalkene precursor, (*Z/E*)-1,3-diiodobut-2-ene, has permitted generation of a vinyl-substituted isoprene-derived Criegee intermediate, MVK-OO, which has been directly detected via 10.5 eV photoionization in a TOF-MS. The observed parent ($m/z = 86$) photoionization signal may contain contributions from four *syn/anti* and *cis/trans* conformers. UV-induced depletion of the MVK-OO photoionization signal suggests a strong UV transition at 350 nm, which is similar to strong $\pi^* \leftarrow \pi$ transitions localized on the carbonyl oxide group in other Criegee

Table 4. Relative OH yield intensity scaled to the intensity of the corresponding Criegee intermediate signal observed in a TOF-MS compared to reported OH yields from ozonolysis of symmetric alkenes, when possible.

Criegee intermediate	Alkene	Reported OH yield	Observed OH signal ratio
CH ₂ OO	Ethene	0.18 ^a	1 ^e
CH ₃ CHOO	<i>E</i> -2-butene	0.64 ^b	4 ^e
(CH ₃) ₂ COO	2,3-dimethyl-2-butene	0.91 ^b	6 ^e
CH ₃ CH ₂ CHOO	<i>E</i> -3-hexene	0.53 ^{b,c}	10 ^e
MVK-OO	Isoprene	0.26 ^d	2 ^f
MACR-OO			
CH ₂ OO			

^a From Ref. 68.

^b From Ref. 67.

^c From Ref. 69.

^d From Ref. 4. Isoprene ozonolysis produces three Criegee intermediates: MVK-OO, MACR-OO, CH₂OO.

^e From Ref. 27.

^f OH generated from unimolecular decay of MVK-OO only.

intermediates. Concurrent detection of OH radicals suggests that MVK-OO is produced with internal excitation and some conformers undergo unimolecular decay to OH products. This work provides the first steps towards understanding the fundamental spectroscopy, dynamics, and kinetics of an isoprene-derived Criegee intermediate, MVK-OO. Future work to deduce the branching ratios for the four conformers, characterize the MVK-OO UV absorption spectrum, and understand the dynamics of unimolecular decay are desirable. Other Criegee intermediates of interest include MACR-OO and pinene-derived Criegee intermediates, if suitable precursors can be synthesized.

Acknowledgements

The authors thank Prof. William Dailey (Penn), for suggesting the use of a resonance stabilized diiodoalkene precursor, Prof. Patrick Walsh (Penn) and graduate student Nisalak Trongsiwat (Penn) for synthesis of the diiodoalkene precursor, Dr. Barbara Marchetti (Penn) for calculations presented in Table 3, and Dr. Charles Ross III (Penn) for assistance in obtaining a HRMS spectrum of the precursor.

References

- ¹ F. Pacifico, S. P. Harrison, C. D. Jones, and S. Sitch, *Atmos. Environ.* **43**, 6121 (2009).
- ² J. O. Nriagu, *Gaseous pollutants: Characterization and cycling* (John Wiley & Sons, Inc, New York, 1992), Vol. 24.

- ³ J. Lelieveld, T. M. Butler, J. N. Crowley, T. J. Dillon, H. Fischer, L. Ganzeveld, H. Harder, M. G. Lawrence, M. Martinez, D. Taraborrelli, and J. Williams, *Nature* **452**, 737 (2008).
- ⁴ T. L. Malkin, A. Goddard, D. E. Heard, and P. W. Seakins, *Atmos. Chem. Phys.* **10**, 1441 (2010).
- ⁵ D. Johnson, and G. Marston, *Chem. Soc. Rev.* **37**, 699 (2008).
- ⁶ K. M. Emmerson, N. Carslaw, D. C. Carslaw, J. D. Lee, G. McFiggans, W. J. Bloss, T. Gravestock, D. E. Heard, J. Hopkins, T. Ingham, M. J. Pilling, S. C. Smith, M. Jacob, and P. S. Monks, *Atmos. Chem. Phys.* **7**, 167 (2007).
- ⁷ L. Vereecken, D. R. Glowacki, and M. J. Pilling, *Chem. Rev.* **115**, 4063 (2015).
- ⁸ R. M. Harrison, J. Yin, R. M. Tilling, X. Cai, P. W. Seakins, J. R. Hopkins, D. L. Lansley, A. C. Lewis, M. C. Hunter, D. E. Heard, L. J. Carpenter, D. J. Creasey, J. D. Lee, M. J. Pilling, N. Carslaw, K. M. Emmerson, A. Redington, R. G. Derwent, D. Ryall, G. Mills, and S. A. Penkett, *Sci. Total. Environ.* **360**, 5 (2006).
- ⁹ R. Atkinson, and J. Arey, *Acc. Chem. Res.* **31**, 574 (1998).
- ¹⁰ B. J. Finlayson-Pitts, and J. N. Pitts, *Chemistry of the Upper and Lower Atmosphere* (Academic Press, San Diego, 2000).
- ¹¹ L. Vereecken, and J. S. Francisco, *Chem. Soc. Rev.* **41**, 6259 (2012).
- ¹² H. Gong, A. Matsunaga, and P. J. Ziemann, *J. Phys. Chem. A* **109**, 4312 (2005).
- ¹³ J. H. Kroll, and J. H. Seinfeld, *Atmos. Environ.* **42**, 3593 (2008).
- ¹⁴ M. C. Jacobson, H. C. Hansson, K. J. Noone, and R. J. Charlson, *Rev. Geophys.* **38**, 267 (2000).

- ¹⁵ T. B. Nguyen, G. S. Tyndall, J. D. Crouse, A. P. Teng, K. H. Bates, R. H. Schwantes, M. M. Coggon, L. Zhang, P. Feiner, D. O. Miller, K. M. Skog, J. C. Rivera-Rios, M. Dorris, K. F. Olson, A. Koss, R. J. Wild, S. S. Brown, A. H. Goldstein, J. A. de Gouw, W. H. Brune, F. N. Keutsch, J. H. Seinfeld, and P. O. Wennberg, *Phys. Chem. Chem. Phys.* **18**, 10241 (2016).
- ¹⁶ D. Zhang, and R. Zhang, *J. Am. Chem. Soc.* **124**, 2692 (2002).
- ¹⁷ S. M. Aschmann, and R. Atkinson, *Environ. Sci. Technol.* **28**, 1539 (1994).
- ¹⁸ K. T. Kuwata, M. R. Hermes, M. J. Carlson, and C. K. Zogg, *J. Phys. Chem. A* **114**, 9192 (2010).
- ¹⁹ R. Atkinson, S. M. Aschmann, J. Arey, and B. Shorees, *J. Geophys. Res.* **97**, 6065 (1992).
- ²⁰ S. E. Paulson, R. C. Flagan, and J. H. Seinfeld, *Int. J. Chem. Kinet.* **24**, 103 (1992).
- ²¹ S. E. Paulson, A. D. Sen, P. Liu, J. D. Fenske, and M. J. Fox, *Geophys. Res. Lett.* **24**, 3193 (1997).
- ²² A. G. Lewin, D. Johnson, D. W. Price, and G. Marston, *Phys. Chem. Chem. Phys.* **3**, 1253 (2001).
- ²³ R. Gutbrod, E. Kraka, R. N. Schindler, and D. Cremer, *J. Am. Chem. Soc.* **119**, 7330 (1997).
- ²⁴ N. M. Donahue, J. H. Kroll, J. G. Anderson, and K. L. Demerjian, *Geophysical Research Letters* **25**, 59 (1998).
- ²⁵ M. S. Alam, A. R. Rickard, M. Camredon, K. P. Wyche, T. Carr, K. E. Hornsby, P. S. Monks, and W. J. Bloss, *J. Phys. Chem. A* **117**, 12468 (2013).

- ²⁶ J. M. Beames, F. Liu, L. Lu, and M. I. Lester, *J. Chem. Phys.* **138**, 244307 (2013).
- ²⁷ F. Liu, J. M. Beames, A. M. Green, and M. I. Lester, *J. Phys. Chem. A* **118**, 2298 (2014).
- ²⁸ K. T. Kuwata, L. C. Valin, and A. D. Converse, *J. Phys. Chem. A* **109**, 10725 (2005).
- ²⁹ J. H. Kroll, S. R. Sahay, J. G. Anderson, K. L. Demerjian, and N. M. Donahue, *J. Phys. Chem. A* **105**, 4446 (2001).
- ³⁰ G. T. Drozd, T. Kurten, N. M. Donahue, and M. I. Lester, *J. Phys. Chem. A* **121**, 6036 (2017).
- ³¹ T.-N. Nguyen, R. Putikam, and M. C. Lin, *J. Chem. Phys.* **142**, 124312 (2015).
- ³² C. Yin, and K. Takahashi, *Phys. Chem. Chem. Phys.* **19**, 12075 (2017).
- ³³ W. Chao, J.-T. Hsieh, C.-H. Chang, and J. J.-M. Lin, *Science* **347**, 751 (2015).
- ³⁴ T. R. Lewis, M. A. Blitz, D. E. Heard, and P. W. Seakins, *Phys. Chem. Chem. Phys.* **17**, 4859 (2015).
- ³⁵ D. Zhang, W. Lei, and R. Zhang, *Chem. Phys. Lett.* **358**, 171 (2002).
- ³⁶ M. Sipilä, T. Jokinen, T. Berndt, S. Richters, R. Makkonen, N. M. Donahue, R. L. Mauldin III, T. Kurtén, P. Paasonen, N. Sarnela, M. Ehn, H. Junninen, M. P. Rissanen, J. Thornton, F. Stratmann, H. Herrmann, D. R. Worsnop, M. Kulmala, V. M. Kerminen, and T. Petäjä, *Atmos. Chem. Phys.* **14**, 12143 (2014).
- ³⁷ G. Manickam, U. Siddappa, and Y. Li, *Tetrahedron Lett.* **47**, 5867 (2006).
- ³⁸ J.-L. Gras, Y. Y. Kong Win Chang, and M. Bertrand, *Tetrahedron Lett.* **23**, 3571 (1982).
- ³⁹ W. M. Kwok, and D. L. Phillips, *J. Chem. Phys.* **104**, 2529 (1996).

- ⁴⁰ M. Ito, P.-K. C. Huang, and E. M. Kosower, *Trans. Farad. Soc.* **57**, 1662 (1961).
- ⁴¹ M. Kawasaki, S. J. Lee, and R. Bersohn, *J. Chem. Phys.* **63**, 809 (1975).
- ⁴² J. H. Lehman, H. Li, and M. I. Lester, *Chem. Phys. Lett.* **590**, 16 (2013).
- ⁴³ C.-P. Liu, J. J. Newby, C. W. Müller, H. D. Lee, and T. S. Zwier, *J. Phys. Chem. A* **112**, 9454 (2008).
- ⁴⁴ J. J. Newby, C. W. Müller, C.-P. Liu, and T. S. Zwier, *J. Am. Chem. Soc.* **132**, 1611 (2010).
- ⁴⁵ J. M. Beames, F. Liu, L. Lu, and M. I. Lester, *J. Am. Chem. Soc.* **134**, 20045 (2012).
- ⁴⁶ N. Isaacs, *Physical Organic Chemistry* (Longman Scientific & Technical, 1995).
- ⁴⁷ Gaussian09, M. J. Frisch, G. W. Trucks, H. B. Schlegel, G. E. Scuseria, M. A. Robb, J. R. Cheeseman, G. Scalmani, V. Barone, B. Mennucci, G. A. Petersson, H. Nakatsuji, M. Caricato, X. Li, H. P. Hratchian, A. F. Izmaylov, J. Bloino, G. Zheng, J. L. Sonnenberg, M. Hada, M. Ehara, K. Toyota, R. Fukuda, J. Hasegawa, M. Ishida, T. Nakajima, Y. Honda, O. Kitao, H. Nakai, T. Vreven, J. A. Montgomery, Jr., J. E. Peralta, F. Ogliaro, M. Bearpark, J. J. Heyd, E. Brothers, K. N. Kudin, V. N. Staroverov, R. Kobayashi, J. Normand, K. Raghavachari, A. Rendell, J. C. Burant, S. S. Iyengar, J. Tomasi, M. Cossi, N. Rega, J. M. Millam, M. Klene, J. E. Knox, J. B. Cross, V. Bakken, C. Adamo, J. Jaramillo, R. Gomperts, R. E. Stratmann, O. Yazyev, A. J. Austin, R. Cammi, C. Pomelli, J. W. Ochterski, R. L. Martin, K. Morokuma, V. G. Zakrzewski, G. A. Voth, P. Salvador, J. J. Dannenberg, S. Dapprich, A. D. Daniels, Ö. Farkas, J. B. Foresman, J. V. Ortiz, J. Cioslowski, and D. J. Fox, *Gaussian 09* (Gaussian, Inc., Wallingford CT, 2009).

- ⁴⁸ MOLPRO, version 2010.1, a package of ab initio programs, H.-J. Werner, P. J. Knowles, G. Knizia, F. R. Manby, M. Schütz, P. Celani, T. Korona, R. Lindh, A. Mitrushenkov, G. Rauhut, K. R. Shamasundar, T. B. Adler, R. D. Amos, A. Bernhardsson, A. Berning, D. L. Cooper, M. J. O. Deegan, A. J. Dobbyn, F. Eckert, E. Goll, C. Hampel, A. Hesselmann, G. Hetzer, T. Hrenar, G. Jansen, C. Köppl, Y. Liu, A. W. Lloyd, R. A. Mata, A. J. May, S. J. McNicholas, W. Meyer, M. E. Mura, A. Nicklass, D. P. O'Neill, P. Palmieri, K. Pflüger, R. Pitzer, M. Reiher, T. Shiozaki, H. Stoll, A. J. Stone, R. Tarroni, T. Thorsteinsson, M. Wang, and A. Wolf, see <http://www.molpro.net>.
- ⁴⁹ D. Feller, *J. Comp. Chem.* **17**, 1571 (1996).
- ⁵⁰ K. L. Schuchardt, B. T. Didier, T. Elsethagen, L. Sun, V. Gurumoorthi, J. Chase, J. Li, and T. L. Windus, *J. Chem. Inf. Model.* **47**, 1045 (2007).
- ⁵¹ P. Aplincourt, and J. M. Anglada, *J. Phys. Chem. A* **107**, 5798 (2003).
- ⁵² V. A. Shubert, E. E. Baquero, J. R. Clarkson, W. H. James, J. A. Turk, A. A. Hare, K. Worrel, M. A. Lipton, D. P. Schofield, K. D. Jordan, and T. S. Zwier, *J. Chem. Phys.* **127**, 234315 (2007).
- ⁵³ A. Kaczor, I. D. Reva, L. M. Proniewicz, and R. Fausto, *J. Phys. Chem. A* **110**, 2360 (2006).
- ⁵⁴ S. Blanco, J. C. López, S. Mata, and J. L. Alonso, *Angew. Chem. Int. Ed.* **49**, 9187 (2010).
- ⁵⁵ C. Cabezas, J.-C. Guillemin, and Y. Endo, *J. Chem. Phys.* **146**, 174304 (2017).
- ⁵⁶ C. Cabezas, J.-C. Guillemin, and Y. Endo, *J. Chem. Phys.* **145**, 224314 (2016).
- ⁵⁷ L. Sheps, A. M. Scully, and K. Au, *Phys. Chem. Chem. Phys.* **16**, 26701 (2014).

- ⁵⁸ H. Li, Y. Fang, J. M. Beames, and M. I. Lester, *J. Chem. Phys.* **142**, 214312 (2015).
- ⁵⁹ H. Li, Y. Fang, N. M. Kidwell, J. M. Beames, and M. I. Lester, *J. Phys. Chem. A* **119**, 8328 (2015).
- ⁶⁰ G. M. Roberts, C. A. Williams, J. D. Young, S. Ullrich, M. J. Paterson, and V. G. Stavros, *J. Am. Chem. Soc.* **134**, 12578 (2012).
- ⁶¹ G. A. King, T. A. A. Oliver, M. G. D. Nix, and M. N. R. Ashfold, *J. Phys. Chem. A* **113**, 7984 (2009).
- ⁶² J. Wang, B. Yang, T. A. Cool, and N. Hansen, *Int. J. Mass Spectrom.* **292**, 14 (2010).
- ⁶³ W. D. Paist, E. R. Blout, F. C. Uhle, and R. C. Elderfield, *J. Org. Chem.* **06**, 273 (1941).
- ⁶⁴ H. E. Ungnade, and I. Ortega, *J. Am. Chem. Soc.* **73**, 1564 (1951).
- ⁶⁵ F. Liu, J. M. Beames, and M. I. Lester, *J. Chem. Phys.* **141**, 234312 (2014).
- ⁶⁶ F. Liu, J. M. Beames, A. S. Petit, A. B. McCoy, and M. I. Lester, *Science* **345**, 1596 (2014).
- ⁶⁷ G. E. Orzechowska, and S. E. Paulson, *Atmos. Environ.* **36**, 571 (2002).
- ⁶⁸ S. E. Paulson, J. D. Fenske, A. D. Sen, and T. W. Callahan, *J. Phys. Chem. A* **103**, 2050 (1999).
- ⁶⁹ J. H. Kroll, N. M. Donahue, V. J. Cee, K. L. Demerjian, and J. G. Anderson, *J. Am. Chem. Soc.* **124**, 8518 (2002).
- ⁷⁰ T. L. Nguyen, H. Lee, D. A. Matthews, M. C. McCarthy, and J. F. Stanton, *J Phys Chem A* **119**, 5524 (2015).

APPENDIX I

UV + VUV double-resonance studies of autoionizing Rydberg states of the hydroxyl radical supplementary material

This work has been published as supplementary material in the *Journal of Chemical Physics*, **144**, 184311 (2016) and is a supplement to Chapter 2 of this thesis. The research and was performed with postdoctoral researcher Dr. Fang Liu and Prof. Marsha I. Lester in the *Department of Chemistry, University of Pennsylvania*.

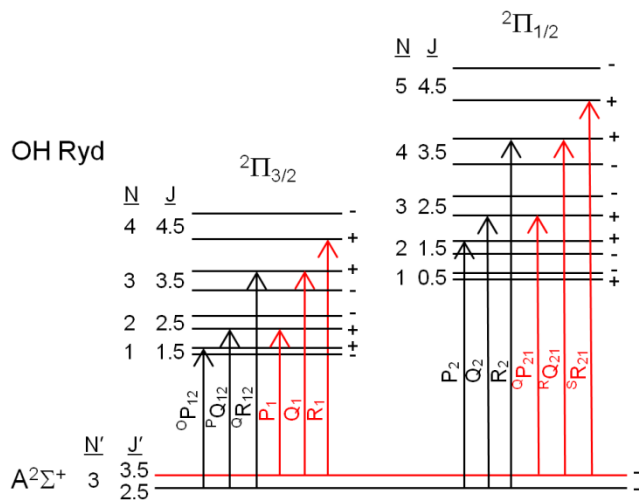


Figure S1. Schematic diagram illustrating the six allowed transitions from the OH $A^2\Sigma^+$ ($v'=1, J'=3.5, N'=3, F_1'$) state (red) to OH $^2\Pi_{\Omega}$ ($v=0$) Ryd states. Also shown are the six allowed transitions from the OH $A^2\Sigma^+$ ($v'=1, J'=2.5, N'=3, F_2'$) state (black) to OH $^2\Pi_{\Omega}$ ($v=0$) Ryd states. The OH $A^2\Sigma^+$ ($v'=1, N'=3$) state has two nearly degenerate spin-rotation levels.

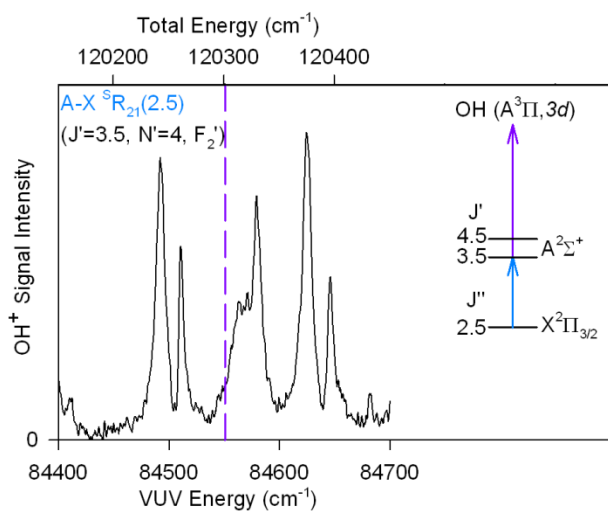


Figure S2. VUV spectrum accessing OH [$A^3\Pi, 3d$] ($v=0$) Rydberg states from OH $A^2\Sigma^+$ ($v'=1, N'=4, J'=3.5, F_2'$) level with OH⁺ detection. The intermediate level is prepared by UV excitation on the OH $A^2\Sigma^+ - X^2\Pi$ (1,0) $^sR_{21}(2.5)$ line. See Figure 2 caption of main text for additional details.

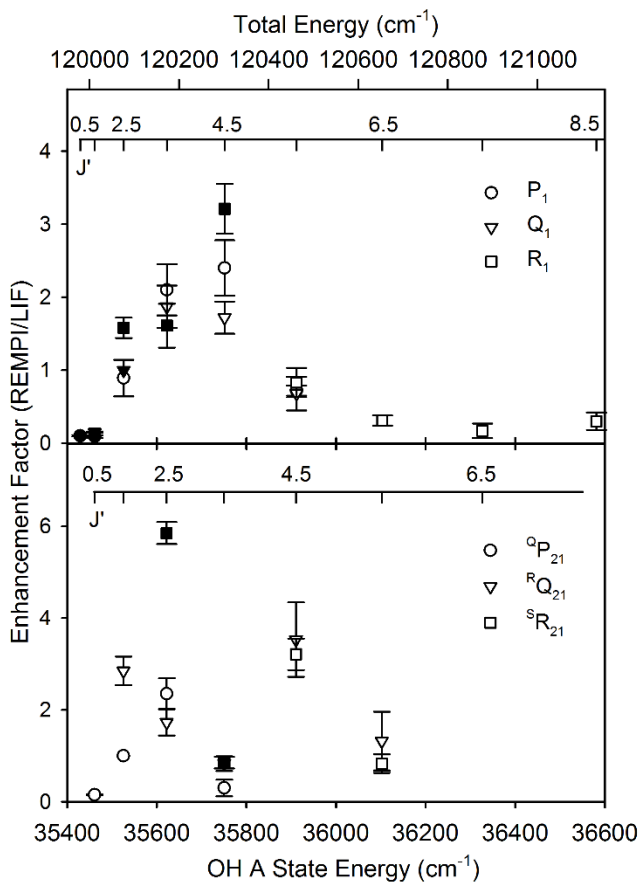


Figure S3. Enhancement factors (REMPL/LIF) previously reported for main branch (top panel) and satellite lines (bottom panel) in the OH A²Σ⁺ - X²Π (1,0) region, accessing F₁' and F₂' fine structure levels of the OH A²Σ⁺ state, respectively. The enhancement factors are plotted versus OH A state energy on the lower axis and total energy on the upper axis. The OH A²Σ⁺ (v'=1, J', N', F₁') rotational levels are labeled with comb ticks indicating J'. The intermediate OH A²Σ⁺ levels studied in the present work are highlighted with filled symbols. This figure is adapted from the main text and supplementary information of J. M. Beames, F. Liu, and M. I. Lester, *Mol. Phys.* **112**, 897 (2013).

Table S1. Peak positions (cm^{-1}), FWHM (cm^{-1}), and assignments of OH Rydberg levels and VUV transitions observed from initially prepared OH $A^2\Sigma^+$ ($v'=1, J', N', F_1'$) levels via specific OH $A^2\Sigma^+ - X^2\Pi$ transitions.

OH $A^2\Sigma^+$ ($v'=1$) intermediate level via $A^2\Sigma^+ - X^2\Pi$ Transition	VUV Peak Position ^a (cm^{-1})	FWHM ^a (cm^{-1})	Rydberg Level Assignment	$^2\Pi_{\Omega}$ Ryd - $A^2\Sigma^+$ VUV Transition
$J'=0.5, N'=0, F_1'$ via $A^2\Sigma^+ - X^2\Pi$ $P_1(1.5)$	84647.5	12.2	$^2\Pi_{3/2,\text{lower}}(J=1.5, F_1, -)$	$R_1(0.5)$
	84710.2	3.2	$^2\Pi_{1/2,\text{upper}}(J=0.5, F_2, -)$	$^RQ(0.5)$
	84740.4	9.5	$^2\Pi_{1/2,\text{lower}}(J=1.5, F_2, -)$	$^SR(0.5)$
	84762.6	7.5	$^2\Pi_{1/2,\text{upper}}(J=1.5, F_2, -)$	$^SR(0.5)$
$J'=0.5, N'=1, F_2'$ via $A^2\Sigma^+ - X^2\Pi$ $Q_2(0.5)$	84616.8	15.3	$^2\Pi_{3/2,\text{lower}}(J=1.5, F_1, +)$	$^QR(0.5)$
	84695.8	5.1	$^2\Pi_{1/2,\text{lower}}(J=1.5, F_2, +)$	$R_2(0.5)$
	84719.6	12.8	$^2\Pi_{1/2,\text{upper}}(J=1.5, F_2, +)$	$R_2(0.5)$
$J'=1.5, N'=1, F_1'$ via $A^2\Sigma^+ - X^2\Pi$ $P_1(2.5)$	84617.8	15.2	$^2\Pi_{3/2,\text{lower}}(J=1.5, F_1, +)$	$Q_1(1.5)$
	84637.0	8.6	$^2\Pi_{3/2,\text{upper}}(J=1.5, F_1, +)$	$Q_1(1.5)$
	84647.3	6.8	$^2\Pi_{1/2,\text{lower}}(J=0.5, F_2, +)$	$^QP(1.5)$
	84667.0	7.0	$^2\Pi_{3/2,\text{lower}}(J=2.5, F_1, +)$	$R_1(1.5)$
	84687.4	3.4	$^2\Pi_{1/2,\text{upper}}(J=0.5, F_2, +)$	$^QP(1.5)$
$J'=1.5, N'=1, F_1'$ via $A^2\Sigma^+ - X^2\Pi$ $Q_1(1.5)$	84719.0	11.5	$^2\Pi_{1/2,\text{upper}}(J=1.5, F_2, +)$	$^RQ(1.5)$
	84618.5	14.8	$^2\Pi_{3/2,\text{lower}}(J=1.5, F_1, +)$	$Q_1(1.5)$
	84637.2	7.4	$^2\Pi_{3/2,\text{upper}}(J=1.5, F_1, +)$	$Q_1(1.5)$
	84647.6	8.5	$^2\Pi_{1/2,\text{lower}}(J=0.5, F_2, +)$	$^QP(1.5)$
	84666.8	6.5	$^2\Pi_{3/2,\text{lower}}(J=2.5, F_1, +)$	$R_1(1.5)$
$J'=1.5, N'=2, F_2'$ via $A^2\Sigma^+ - X^2\Pi$ $R_2(0.5)$	84687.3	3.5	$^2\Pi_{1/2,\text{upper}}(J=0.5, F_2, +)$	$^QP(1.5)$
	84718.7	11.0	$^2\Pi_{1/2,\text{upper}}(J=1.5, F_2, +)$	$^RQ(1.5)$
	84550.9	8.9	$^2\Pi_{3/2,\text{lower}}(J=1.5, F_1, -)$	$^PQ(1.5)$
	84571.1	9.5	$^2\Pi_{3/2,\text{upper}}(J=1.5, F_1, -)$	$^PQ(1.5)$
	84591.5	5.9	$^2\Pi_{1/2,\text{lower}}(J=0.5, F_2, -)$	$P_2(1.5)$
	84605.8	6.3	$^2\Pi_{3/2,\text{lower}}(J=2.5, F_1, -)$	$^QR(1.5)$
	84625.0	7.8		c
84665.7	9.1	$^2\Pi_{1/2,\text{upper}}(J=1.5, F_2, -)$	$Q_2(1.5)$	
84692.5	12.2	$^2\Pi_{1/2,\text{lower}}(J=2.5, F_2, -)$	$R_2(1.5)$	
84720.0	4.9	$^2\Pi_{1/2,\text{upper}}(J=2.5, F_2, -)$	$R_2(1.5)$	

$J'=2.5, N'=2, F_1'$ via $A^2\Sigma^+ - X^2\Pi$ $R_1(1.5)$	84551.8	9.3	${}^2\Pi_{3/2,\text{lower}}(J=1.5, F_1, -)$	$P_1(2.5)$
	84571.9	9.9	${}^2\Pi_{3/2,\text{upper}}(J=1.5, F_1, -)$	$P_1(2.5)$
	84591.4	5.9	${}^2\Pi_{1/2,\text{lower}}(J=0.5, F_2, -)$	$P_2(1.5)^b$
	84606.5	9.0	${}^2\Pi_{3/2,\text{lower}}(J=2.5, F_1, -)$	$Q_1(2.5)$
	84615.6	3.0	${}^2\Pi_{1/2,\text{upper}}(J=0.5, F_2, -)$	$P_2(1.5)^b$
	84627.2	4.1		c
	84635.3	9.7	${}^2\Pi_{3/2,\text{upper}}(J=2.5, F_1, -)$	$Q_1(2.5)$
	84665.8	6.8	${}^2\Pi_{1/2,\text{upper}}(J=1.5, F_2, -)$	${}^Q P(2.5)$
	84690.2	8.2	${}^2\Pi_{1/2,\text{lower}}(J=2.5, F_2, -)$	${}^R Q(2.5)$
	84696.4	4.5	${}^2\Pi_{3/2,\text{lower}}(J=3.5, F_1, -)$	$R_1(2.5)$
84720.8	6.6	${}^2\Pi_{1/2,\text{upper}}(J=2.5, F_2, -)$	${}^R Q(2.5)$	
$J'=2.5, N'=2, F_1'$ via $A^2\Sigma^+ - X^2\Pi$ $Q_1(2.5)$	84552.2	8.9	${}^2\Pi_{3/2,\text{lower}}(J=1.5, F_1, -)$	$P_1(2.5)$
	84571.3	7.8	${}^2\Pi_{3/2,\text{upper}}(J=1.5, F_1, -)$	$P_1(2.5)$
	84591.2	7.4	${}^2\Pi_{1/2,\text{lower}}(J=0.5, F_2, -)$	$P_2(1.5)^b$
	84606.4	5.4	${}^2\Pi_{3/2,\text{lower}}(J=2.5, F_1, -)$	$Q_1(2.5)$
	84615.9	3.3	${}^2\Pi_{1/2,\text{upper}}(J=0.5, F_2, -)$	$P_2(1.5)^b$
	84627.6	6.2		c
	84635.9	9.0	${}^2\Pi_{3/2,\text{upper}}(J=2.5, F_1, -)$	$Q_1(2.5)$
	84667.5	6.4	${}^2\Pi_{1/2,\text{upper}}(J=1.5, F_2, -)$	${}^Q P(2.5)$
	84692.8	13.2	${}^2\Pi_{3/2,\text{lower}}(J=3.5, F_1, -)$ or ${}^2\Pi_{1/2,\text{lower}}(J=2.5, F_2, -)$	$R_1(2.5)$ or ${}^R Q(2.5)$
	84722.7	8.9	${}^2\Pi_{1/2,\text{upper}}(J=2.5, F_2, -)$	${}^R Q(2.5)$
$J'=2.5, N'=3, F_2'$ via $A^2\Sigma^+ - X^2\Pi$ ${}^S R_{21}(1.5)$	84545.1	12.2	${}^2\Pi_{3/2,\text{upper}}(J=2.5, F_1, +)$	${}^P Q(2.5)$
	84590.3	10.4		c
	84616.7	7.9	${}^2\Pi_{3/2,\text{lower}}(J=3.5, F_1, +)$	${}^Q R(2.5)$
	84631.5	6.6	${}^2\Pi_{3/2,\text{upper}}(J=3.5, F_1, +)$	${}^Q R(2.5)$
	84658.8	9.5		c
	84668.0	6.6	${}^2\Pi_{1/2,\text{lower}}(J=3.5, F_2, +)$	$R_2(2.5)$
$J'=2.5, N'=3, F_2'$ via $A^2\Sigma^+ - X^2\Pi$ $R_2(1.5)$	84545.0	13.8	${}^2\Pi_{3/2,\text{upper}}(J=2.5, F_1, +)$	${}^P Q(2.5)$
	84588.3	3.7		c
	84616.0	7.2	${}^2\Pi_{3/2,\text{lower}}(J=3.5, F_1, +)$	${}^Q R(2.5)$
	84630.7	7.5	${}^2\Pi_{3/2,\text{upper}}(J=3.5, F_1, +)$	${}^Q R(2.5)$
	84658.8	10.1		c
	84667.4	7.3	${}^2\Pi_{1/2,\text{lower}}(J=3.5, F_2, +)$	$R_2(2.5)$
$J'=3.5, N'=3, F_1'$ via $A^2\Sigma^+ - X^2\Pi$ $R_1(2.5)$	84544.0	11.2	${}^2\Pi_{3/2,\text{upper}}(J=2.5, F_1, +)$	$P_1(3.5)$
	84556.3	7.3	${}^2\Pi_{1/2,\text{upper}}(J=1.5, F_2, +)$	$P_2(2.5)^b$
	84607.8	9.3	${}^2\Pi_{1/2,\text{lower}}(J=2.5, F_2, +)$	${}^Q P(3.5)$

	84635.6	4.0	${}^2\Pi_{1/2,\text{upper}}(J=2.5, F_2, +)$	${}^Q P(3.5)$
	84667.8	10.2	${}^2\Pi_{1/2,\text{lower}}(J=3.5, F_2, +)$	${}^R Q(3.5)$
J'=4.5, N'=4, F ₁ ' via A ² Σ ⁺ - X ² Π R ₁ (3.5)	84491.8	8.9		d
	84511.1	4.2		d
	84541.8	10.2		d
	84551.0	6.6		d
	84587.6	12.1		d
	84625.5	8.3		d
	84645.8	8.5		d
J'=3.5, N'=4, F ₂ ' via A ² Σ ⁺ - X ² Π ^S R ₂₁ (2.5)	84492.3	8.7		e
	84511.2	4.2		e
	84564.5	19.5		e
	84579.9	8.8		e
	84624.9	9.2		e
	84646.5	5.8		e

^a Uncertainties in the peak position and FWHM are from the estimated VUV linewidth of ~0.1-1.0 cm⁻¹. See main text.

^b Extra lines in the VUV spectra (denoted with *) attributed to simultaneous preparation of nearly degenerate (spin-rotation) A²Σ⁺ levels in the A-X excitation step.

^c Unassigned lines.

^d Prominent lines tentatively attributed to Q₁ (and/or P₁) lines terminating in the lower and upper ${}^2\Pi_{3/2}$ states and ${}^Q P_{21}$ lines terminating in the lower and upper ${}^2\Pi_{1/2}$ states.

^e Prominent lines tentatively attributed to ${}^Q R$ (and/or ${}^P Q$) lines terminating in the lower and upper ${}^2\Pi_{3/2}$ states and Q₂ lines terminating in the lower and upper ${}^2\Pi_{1/2}$ states.

Table S2. Relative energies (cm⁻¹) of observed ²Π Ryd levels, depicted in Figure 6 of main text, sorted by rotational level (J) and parity (+/-).

	² Π _{3/2, lower}		² Π _{1/2, lower}	
J	(+)	(-)	(+)	(-)
0.5			31.8	39.6
1.5	1.6	0.0	79.9	91.9
2.5	51.3	54.6	153.5	140.8
3.5	161.2	143.3	212.9	
	² Π _{3/2, upper}		² Π _{1/2, upper}	
J	(+)	(-)	(+)	(-)
0.5			71.3	63.4
1.5	21.3	19.8	102.9	115.0
2.5	89.6	84.3	181.5	169.6
3.5	176.2			

APPENDIX II

Selective deuteration illuminates the importance of tunneling in the unimolecular decay of Criegee intermediates to hydroxyl radical products supplementary material

This work has been submitted as supplementary material to the Proceedings of the National Academy of Sciences (2017, DOI: 10.1073/pnas.1715014114) and is a supplement to Chapter 4 of this thesis. The experimental research and was performed with graduate students Victoria Barber, Yi Fang, and Prof. Marsha I. Lester in the *Department of Chemistry, University of Pennsylvania*. Theoretical calculations were performed in collaboration with Stephen J. Klippenstein in the *Chemical Sciences and Engineering Division, Argonne National Laboratory*.

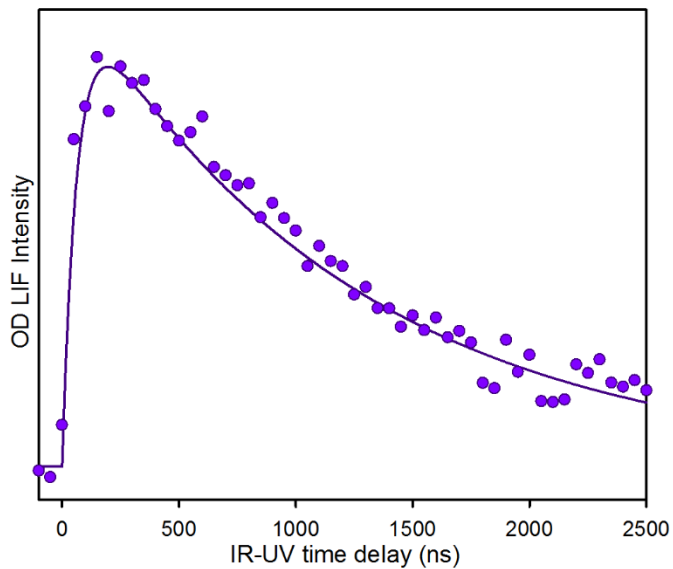


Figure S1. Temporal profile of OD products arising from IR excitation of the *syn*-CD₃CHOO Criegee intermediate at 6055.0 cm⁻¹. The OD LIF intensity is recorded as a function of IR-UV time delay. A step size of 50 ns is used to record a longer time scan to determine the fall off time, ($k_{\text{fall}} = 8.0 \pm 0.5 \times 10^5 \text{ s}^{-1}$), which arises from molecules moving out of the UV probe laser region. The uncertainty ($\pm 1\sigma$) is derived from repeated measurements.

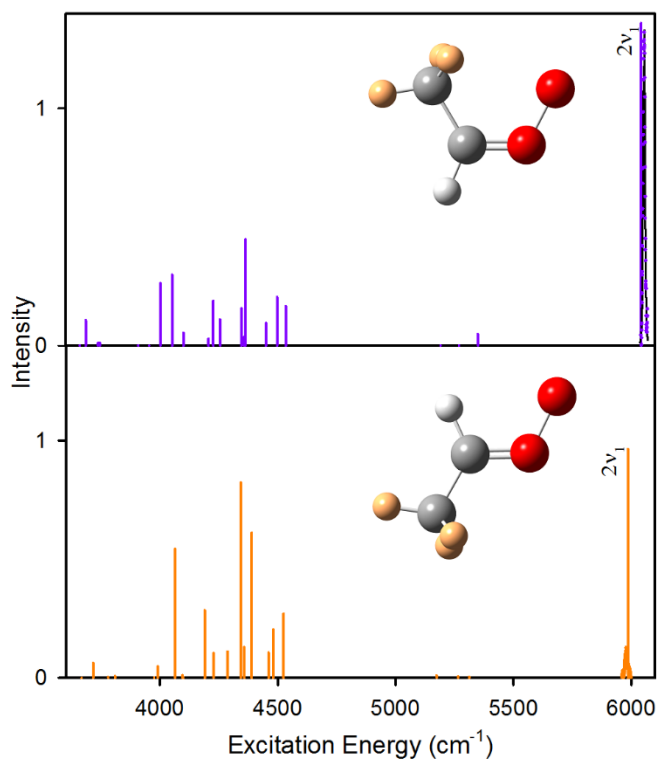


Figure S2. Calculated anharmonic IR stick spectrum for *syn*- (purple, upper panel) and *anti*- (orange, lower panel) conformers of selectively deuterated CD₃CHOO at the B2PLYPD3/cc-pVTZ level of theory. Experimental IR action spectral features observed (upper panel; purple data, black fit) at 6055.0 cm⁻¹ with OD LIF detection attributed to *syn*-CD₃CHOO and (lower panel; orange data and fit) at 5979.0 cm⁻¹ with OH LIF detection ascribed to *anti*-CD₃CHOO.

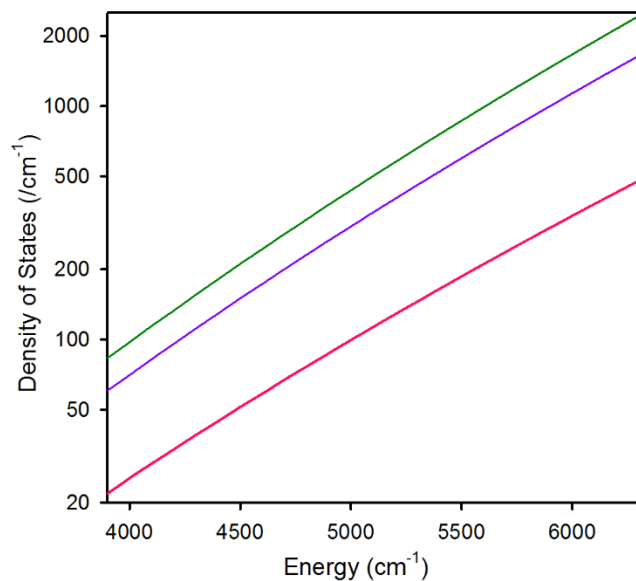


Figure S3. Density of reactant states per cm^{-1} for *syn*-CH₃CHOO (red), *syn*-CD₃CHOO (purple) and *syn*-CD₃CDOO (green) on semi-log scale. The density of states are calculated using the Densum program in the Multiwell suite (1). The methyl torsion is treated as a one-dimensional hindered rotor.

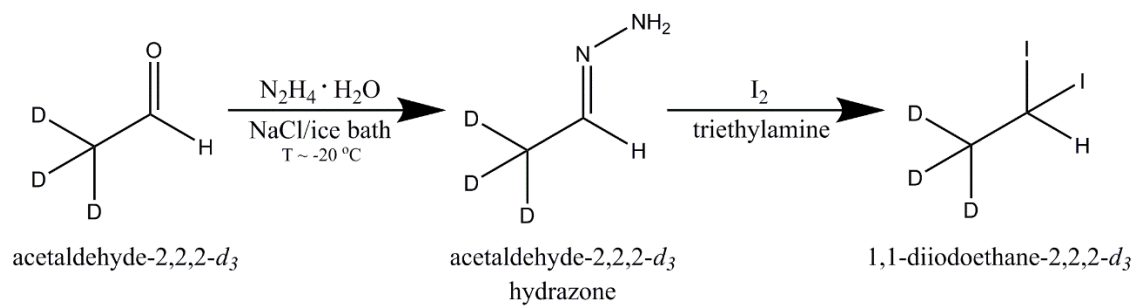


Figure S4. Schematic of Synthesis of 1,1-diiodoethane-2,2,2-*d*₃.

Table S1. Fundamental harmonic and anharmonic vibrational frequencies and descriptions computed for *syn*-CD₃CDOO, *syn*-CD₃CHOO, and *anti*-CD₃CHOO in C_s symmetry.

Mode	Symmetry	Harmonic Frequency ^a (cm ⁻¹)	Anharmonic Frequency ^b (cm ⁻¹)	Description
<i>syn</i> -CD ₃ CDOO				
v ₁	A'	2383.0	2285.9	Carbonyl oxide CD stretch
v ₂	A'	2352.0	2267.0	Methyl in-plane CD stretch
v ₃	A'	2186.7	2108.0	Methyl out-of-plane symmetric CD stretch
v ₄	A'	1455.1	1412.3	CO stretch
v ₅	A'	1182.4	1153.3	Methyl umbrella
v ₆	A'	1062.0	1035.3	Carbonyl oxide CD in-plane wag
v ₇	A'	1048.5	1015.8	Methyl symmetric scissor
v ₈	A'	970.4	951.5	CCO bend
v ₉	A'	856.3	839.6	OO stretch
v ₁₀	A'	806.2	792.6	CC stretch
v ₁₁	A'	601.6	594.6	COO bend
v ₁₂	A'	277.6	261.5	DCCOO ring closure
v ₁₃	A''	2285.8	2203.1	Methyl out-of-plane asymmetric CD stretch
v ₁₄	A''	1044.5	1024.8	Methyl asymmetric scissor
v ₁₅	A''	883.4	867.1	CCO out of plane bend
v ₁₆	A''	530.9	520.5	Carbonyl oxide out-of-plane CH wag
v ₁₇	A''	406.8	393.5	CCOO out-of-plane ring distortion
v ₁₈	A''	145.3	143.5	<i>syn</i> -methyl torsion
<i>syn</i> -CD ₃ CHOO				
v ₁	A'	3226.1	3099.7	Carbonyl oxide CH stretch
v ₂	A'	2353.0	2263.1	Methyl in-plane CD stretch
v ₃	A'	2186.9	2105.8	Methyl out-of-plane symmetric CD stretch
v ₄	A'	1504.3	1459.0	CO stretch
v ₅	A'	1308.4	1270.2	Carbonyl oxide CH in-plane wag
v ₆	A'	1172.5	1145.9	Methyl umbrella
v ₇	A'	1048.6	1023.7	Methyl symmetric scissor
v ₈	A'	987.2	967.5	CCO bend
v ₉	A'	886.2	868.6	OO stretch
v ₁₀	A'	834.8	818.1	CC stretch
v ₁₁	A'	608.0	600.9	COO bend
v ₁₂	A'	278.1	265.3	DCCOO ring closure
v ₁₃	A''	2285.9	2204.3	Methyl out-of-plane asymmetric CD stretch
v ₁₄	A''	1046.0	1019.2	Methyl asymmetric scissor
v ₁₅	A''	935.4	911.0	CCO out of plane bend
v ₁₆	A''	678.4	661.6	Carbonyl oxide out-of-plane CH wag

ν_{17}	A''	407.9	397.0	CCOO out-of-plane ring distortion
ν_{18}	A''	146.3	147.8	<i>anti</i> -methyl torsion

a. Harmonic frequencies are calculated at the CCSD(T)/cc-pVTZ level of theory.

b. Anharmonic frequencies are calculated by adding B2PLYPD3/cc-pVTZ anharmonic corrections to the reference harmonic values.

c. For *anti*-CD₃CHOO, both harmonic and anharmonic frequencies are calculated at the B2PLYPD3/cc-pVTZ level of theory.

Table S2. Strongest IR transitions predicted with second order vibrational perturbation theory (VPT2) using B2PLYPD3/cc-pVTZ level of theory for *syn*-CD₃CDOO, *syn*-CD₃CHOO, and *anti*-CD₃CHOO from 3900 to 6300 cm⁻¹ with assignments, wavenumbers and intensities.

Assignment	Wavenumber (cm ⁻¹)	IR intensity (km mol ⁻¹)
<i>syn</i> -CD ₃ CDOO		
v ₃ + v ₁₃	4253.8	0.11
2v ₁₃	4343.1	0.16
2v ₂	4499.8	0.25
2v ₁	4537.1	0.73
v ₁ + v ₂	4560.1	0.13
<i>syn</i> -CD ₃ CHOO		
v ₁ + v ₉	4003.1	0.26
v ₁ + v ₈	4052.7	0.30
v ₁ + v ₆	4226.8	0.19
v ₃ + v ₁₃	4255.9	0.11
2v ₁₃	4345.3	0.16
v ₁ + v ₅	4363.6	0.45
v ₂ + v ₁₃	4450.2	0.10
2v ₂	4497.5	0.21
v ₁ + v ₄	4534.5	0.17
2v ₁	6042.5	1.36
<i>anti</i> -CD ₃ CHOO		
v ₁ + v ₁₀	4063.8	0.55
v ₁ + v ₇	4189.5	0.29
2v ₄	4227.6	0.10
v ₃ + v ₄	4286.2	0.11
v ₁ + v ₆	4343.4	0.82
v ₂ + v ₄	4357.2	0.13
2v ₃	4388.7	0.61
v ₂ + v ₃	4460.1	0.11
2v ₂	4480.8	0.20
v ₁ + v ₅	4523.7	0.27
2v ₁	5986.1	0.97

Table S3. Computed harmonic and anharmonic frequencies for the transition states (TS) of *syn*-CD₃CHOO and *syn*-CD₃CDOO.

Mode	<i>syn</i> -CD ₃ CHOO TS		<i>syn</i> -CD ₃ CDOO TS	
	^a Harmonic Frequency (cm ⁻¹)	^b Anharmonic Frequency (cm ⁻¹)	^a Harmonic Frequency (cm ⁻¹)	^b Anharmonic Frequency (cm ⁻¹)
v ₁	3213.7	3093.2	2392.5	2313.9
v ₂	2389.5	2306.5	2376.7	2290.2
v ₃	2264.9	2171.9	2262.7	2179.9
v ₄	1528.7	1487.2	1480.6	1438.8
v ₅	1341.1	1314.0	1340.0	1312.9
v ₆	1278.5	1243.3	1238.7	1208.5
v ₇	1239.6	1213.4	1058.0	1030.9
v ₈	1046.5	1019.2	1008.0	986.5
v ₉	993.2	972.0	967.5	947.1
v ₁₀	947.9	926.9	904.1	888.9
v ₁₁	886.4	867.5	846.1	829.3
v ₁₂	878.0	866.1	806.9	792.2
v ₁₃	728.3	714.9	716.6	703.1
v ₁₄	667.8	656.7	644.2	632.8
v ₁₅	620.3	607.4	558.4	546.8
v ₁₆	455.4	445.5	446.8	437.6
v ₁₇	417.8	405.1	416.8	404.6
v ₁₈	1253.4 <i>i</i>	1324.8 <i>i</i>	1250.2 <i>i</i>	1321.3 <i>i</i>

a. Harmonic frequencies are calculated at the CCSD(T)/cc-pVTZ level of theory.

b. Anharmonic frequencies are calculated by adding B2PLYPD3/cc-pVTZ anharmonic corrections to the reference harmonic values.

Table S4. RRKM rates and lifetimes calculated for unimolecular decay of *syn*-CD₃CHOO and *syn*-CD₃CDOO using asymmetric Eckart or semi-classical transition state theory (SCTST) model for tunneling.

Energy (cm ⁻¹)	SCTST		Eckart	
	Rate (s ⁻¹)	Lifetime (ns)	Rate (s ⁻¹)	Lifetime (ns)
<i>syn</i> -CD ₃ CHOO				
3000	96.3	1.04 x 10 ⁷	73.9	1.35 x 10 ⁷
3100	1.51 x 10 ²	6.62 x 10 ⁶	1.19 x 10 ²	8.42 x 10 ⁶
3200	2.35 x 10 ²	4.26 x 10 ⁶	1.86 x 10 ²	5.36 x 10 ⁶
3300	3.65 x 10 ²	2.74 x 10 ⁶	3.12 x 10 ²	3.21 x 10 ⁶
3400	5.69 x 10 ²	1.76 x 10 ⁶	4.93 x 10 ²	2.03 x 10 ⁶
3500	8.79 x 10 ²	1.14 x 10 ⁶	8.23 x 10 ²	1.21 x 10 ⁶
3600	1.36 x 10 ³	7.35 x 10 ⁵	1.24 x 10 ³	8.08 x 10 ⁵
3700	2.10 x 10 ³	4.76 x 10 ⁵	2.01 x 10 ³	4.97 x 10 ⁵
3800	3.24 x 10 ³	3.08 x 10 ⁵	3.10 x 10 ³	3.22 x 10 ⁵
3900	4.97 x 10 ³	2.01 x 10 ⁵	5.02 x 10 ³	1.99 x 10 ⁵
4000	7.65 x 10 ³	1.31 x 10 ⁵	7.71 x 10 ³	1.30 x 10 ⁵
4100	1.17 x 10 ⁴	8.56 x 10 ⁴	1.21 x 10 ⁴	8.26 x 10 ⁴
4200	1.79 x 10 ⁴	5.59 x 10 ⁴	1.86 x 10 ⁴	5.38 x 10 ⁴
4300	2.72 x 10 ⁴	3.67 x 10 ⁴	2.87 x 10 ⁴	3.49 x 10 ⁴
4400	4.16 x 10 ⁴	2.41 x 10 ⁴	4.45 x 10 ⁴	2.25 x 10 ⁴
4500	6.30 x 10 ⁴	1.59 x 10 ⁴	6.94 x 10 ⁴	1.44 x 10 ⁴
4600	9.58 x 10 ⁴	1.04 x 10 ⁴	1.05 x 10 ⁵	9.49 x 10 ³
4700	1.45 x 10 ⁵	6.91 x 10 ³	1.59 x 10 ⁵	6.27 x 10 ³
4800	2.19 x 10 ⁵	4.57 x 10 ³	2.43 x 10 ⁵	4.12 x 10 ³
4900	3.30 x 10 ⁵	3.03 x 10 ³	3.72 x 10 ⁵	2.69 x 10 ³
5000	4.97 x 10 ⁵	2.01 x 10 ³	5.61 x 10 ⁵	1.78 x 10 ³
5100	7.46 x 10 ⁵	1.34 x 10 ³	8.48 x 10 ⁵	1.18 x 10 ³
5200	1.12 x 10 ⁶	8.94 x 10 ²	1.26 x 10 ⁶	7.91 x 10 ²
5300	1.67 x 10 ⁶	5.99 x 10 ²	1.91 x 10 ⁶	5.23 x 10 ²
5400	2.49 x 10 ⁶	4.02 x 10 ²	2.83 x 10 ⁶	3.53 x 10 ²
5500	3.68 x 10 ⁶	2.72 x 10 ²	4.23 x 10 ⁶	2.37 x 10 ²
5600	5.42 x 10 ⁶	1.84 x 10 ²	6.20 x 10 ⁶	1.61 x 10 ²
5700	7.91 x 10 ⁶	1.26 x 10 ²	9.05 x 10 ⁶	1.11 x 10 ²
5800	1.14 x 10 ⁷	88.0	1.29 x 10 ⁷	77.3
5900	1.61 x 10 ⁷	62.3	1.83 x 10 ⁷	54.8
6000	2.21 x 10 ⁷	45.3	2.50 x 10 ⁷	39.9
6100	2.95 x 10 ⁷	33.8	3.34 x 10 ⁷	30.0

6200	3.83×10^7	26.1	4.30×10^7	23.2
6300	4.84×10^7	20.7	5.41×10^7	18.5
6400	6.00×10^7	16.7	6.71×10^7	14.9
6500	7.37×10^7	13.6	8.22×10^7	12.2
6600	8.98×10^7	11.1	1.00×10^8	9.98
6700	1.09×10^8	9.18	1.21×10^8	8.25
6800	1.31×10^8	7.64	1.45×10^8	6.91
6900	1.56×10^8	6.40	1.73×10^8	5.79
7000	1.85×10^8	5.41	2.03×10^8	4.92
<i>syn</i> -CD ₃ CDOO				
3000	71.9	1.39×10^7	45.8	2.19×10^7
3100	1.11×10^2	9.01×10^6	74.8	1.34×10^7
3200	1.75×10^2	5.71×10^6	1.22×10^2	8.22×10^6
3300	2.71×10^2	3.69×10^6	1.87×10^2	5.35×10^6
3400	4.23×10^2	2.36×10^6	3.13×10^2	3.19×10^6
3500	6.50×10^2	1.54×10^6	5.01×10^2	1.99×10^6
3600	1.01×10^3	9.89×10^5	7.94×10^2	1.26×10^6
3700	1.56×10^3	6.43×10^5	1.25×10^3	7.99×10^5
3800	2.41×10^3	4.15×10^5	1.96×10^3	5.10×10^5
3900	3.68×10^3	2.72×10^5	3.09×10^3	3.23×10^5
4000	5.66×10^3	1.77×10^5	4.76×10^3	2.10×10^5
4100	8.64×10^3	1.16×10^5	7.45×10^3	1.34×10^5
4200	1.33×10^4	7.53×10^4	1.15×10^4	8.71×10^4
4300	2.02×10^4	4.96×10^4	1.79×10^4	5.60×10^4
4400	3.07×10^4	3.26×10^4	2.72×10^4	3.67×10^4
4500	4.66×10^4	2.15×10^4	4.25×10^4	2.36×10^4
4600	7.08×10^4	1.41×10^4	6.45×10^4	1.55×10^4
4700	1.07×10^5	9.35×10^3	9.84×10^4	1.02×10^4
4800	1.62×10^5	6.18×10^3	1.50×10^5	6.68×10^3
4900	2.43×10^5	4.11×10^3	2.26×10^5	4.42×10^3
5000	3.67×10^5	2.72×10^3	3.45×10^5	2.90×10^3
5100	5.50×10^5	1.82×10^3	5.19×10^5	1.93×10^3
5200	8.24×10^5	1.21×10^3	7.79×10^5	1.28×10^3
5300	1.23×10^6	8.13×10^2	1.17×10^6	8.58×10^2
5400	1.83×10^6	5.46×10^2	1.75×10^6	5.72×10^2
5500	2.71×10^6	3.69×10^2	2.58×10^6	3.87×10^2
5600	3.99×10^6	2.51×10^2	3.80×10^6	2.63×10^2
5700	5.81×10^6	1.72×10^2	5.52×10^6	1.81×10^2
5800	8.36×10^6	1.20×10^2	7.95×10^6	1.26×10^2
5900	1.18×10^7	84.7	1.11×10^7	89.8
6000	1.63×10^7	61.4	1.54×10^7	65.1

6100	2.18×10^7	45.9	2.05×10^7	48.9
6200	2.84×10^7	35.3	2.66×10^7	37.6
6300	3.60×10^7	27.8	3.37×10^7	29.7
6400	4.50×10^7	22.2	4.19×10^7	23.9
6500	5.57×10^7	18.0	5.17×10^7	19.3
6600	6.84×10^7	14.6	6.34×10^7	15.8
6700	8.34×10^7	12.0	7.74×10^7	12.9
6800	1.01×10^8	9.92	9.32×10^7	10.7
6900	1.21×10^8	8.27	1.11×10^8	8.99
7000	1.44×10^8	6.97	1.32×10^8	7.56

Supplementary Materials and Methods

A. Synthesis and characterization of precursor

1,1-diiodoethane-2,2,2- d_3 (CD_3CHI_2) was synthesized following the general procedures of Friedrich et al. (1) as shown in Scheme S1. Acetaldehyde-2,2,2- d_3 (1 mL, 99% purity, 98% D, Sigma Aldrich) chilled to $\sim 0^\circ C$ was added to hydrazine monohydrate (4 mL, >99% purity, Alfa Aesar) maintained at ca. $-20^\circ C$ in a NaCl/ice bath ($\sim 1:3$) with rapid stirring to produce the acetaldehyde hydrazone species. The chilled reaction was allowed to stir for 1 hour. The crude hydrazone species was extracted with dichloromethane (5 x 5 mL, $0^\circ C$) and dried over sodium sulfate. The dried hydrazone solution was chilled in an ice water bath. Triethylamine (5 mL, >99% purity, Fisher Scientific) was added and the mixture was again chilled in an ice bath. Solid iodine (>99.8% purity, Sigma Aldrich) was added slowly with rapid stirring until no more N_2 gas was evolved and the solution was a deep red/brown color. The crude product was washed successively with water, a saturated sodium thiosulfate solution, 3N HCl, and brine. The product was dried over magnesium sulfate, concentrated in vacuo, and purified via Kugelrohr distillation to yield a reddish oil (1.25 g, 26% yield). Analytical results: 1H NMR (500 MHz, $CDCl_3$) δ 5.20 (s). 2H NMR (77 MHz, $CHCl_3$) δ 2.88 (s). ^{13}C NMR (125 MHz, $CDCl_3$) δ 38.22 ($J(^{13}C-^2H) = 19.94$ Hz), -39.14. HRMS (EI) m/z calculated for CD_3CHI_2 284.8591, observed 284.8570.

The NMR shifts for CD_3CHI_2 are compared with those for a similar partially deuterated diiodoethane species, CH_3CDI_2 , reported previously by Anson et al. (2). The 1HNMR of CD_3CHI_2 obtained in the present work exhibits an analogous chemical shift as

that observed in the $^2\text{HNMR}$ for CH_3CDI_2 (3). In addition, the $^2\text{HNMR}$ of CD_3CHI_2 shows a similar chemical shift as the $^1\text{HNMR}$ for CH_3CDI_2 (3). The $^{13}\text{CNMR}$ spectrum of CD_3CHI_2 contains two unique carbons at similar chemical shifts as those reported for CH_3CDI_2 (2). Furthermore, high-resolution mass spectrometry (HRMS) employing an electron impact source has identified the parent mass for CD_3CHI_2 (calculated $m/z = 284.8591$; observed $m/z = 284.8570$). The combination of $^1\text{HNMR}$, $^2\text{HNMR}$, $^{13}\text{CNMR}$, and HRMS demonstrates that the CD_3CHI_2 isotopologue has been synthesized.

Acetaldehyde (CH_3CHO) can undergo a well-known keto-enol tautomerization in which a methyl proton can transfer to the oxygen atom to form vinyl alcohol ($\text{CH}_2=\text{CHOH}$). The $-\text{OH}$ proton in vinyl alcohol is acidic and thereby available to undergo H/D exchange with solvent molecules. Previous theoretical work has established that acetaldehyde is the more stable conformer (8-14 kcal/mol) with a significant barrier to tautomerization (70-90 kcal/mol) (3). In the present synthesis, the brief exposure time to nondeuterated solvents and lack of heating minimize the possibility of tautomerization from acetaldehyde to vinyl alcohol, which could facilitate H/D exchange. Indeed, no loss of deuteration is observed in producing CD_3CHI_2 from CD_3CHO .

B. Experimental and theoretical methods

The experimental method for producing *syn*- CH_3CHOO Criegee intermediates in a pulsed supersonic expansion have been described previously (4-6). In the present study, selectively deuterated *syn*- CD_3CHOO is generated by 248 nm photolysis of the

CD₃CHI₂ precursor and subsequent reaction of the CD₃CHI radical with O₂ (20% O₂/Ar at 25 psig) (7).

Tunable IR radiation (~20 mJ/pulse, 6.0 ns FWHM, 0.15 cm⁻¹ bandwidth) is obtained from the signal output of an optical parametric oscillator/amplifier (Laservision OPO/OPA) pumped by an injection-seeded Nd:YAG laser (Continuum Precision II 8000, 1064 nm, 10 Hz). The UV radiation (~2 mJ/pulse, 5.7 ns FWHM, 0.08 cm⁻¹ bandwidth) is generated by frequency-doubling the output of a Nd:YAG (Continuum 7020, 532 nm, 20 Hz) pumped dye laser (ND6000, Rhodamine 640/Rhodamine 610 dye mixture). As described (5), a convolution of the IR and UV pulse profiles yields an experimental time resolution of $\Delta t = 5.0 \pm 0.1$ ns. The IR and UV laser beams are spatially overlapped and gently focused to ~2 mm diameter as they intersect the pulsed supersonic expansion in the collision-free region (ca. 1 cm downstream).

The UV probe radiation is fixed on the OD A²Σ⁺ - X²Π_{3/2} (1,0) Q₁(3.5) line, as the OD X²Π_{3/2} (v=0, J=3.5) product state is found to have the largest population. OD A²Σ⁺ - X²Π_{3/2} (1,1) emission is collected. Active background subtraction (IR on – IR off) is used to remove OD background (IR off) arising from unimolecular decay of energized Criegee intermediates in the capillary, and subsequent cooling in the supersonic expansion. An analogous scheme is used for detecting OH products.

The infrared spectra of selectively deuterated *syn*-CD₃CHOO and fully deuterated *syn*-CD₃CDOO are computed from anharmonic frequencies and intensities calculated using the B2PLYPD3/cc-pVTZ method/basis with second order vibrational perturbation theory (VPT2) using the Gaussian program suite (Version 09; ref. 8). Previously, the

rovibronic properties and energies of the *syn*-CH₃CHOO Criegee intermediate, the TS barrier, and the VHP incipient product required for the kinetic rate calculations were obtained from high level electronic structure theory [CCSD(T,full)/CBS with various corrections] with anharmonic zero-point energy (ZPE) (5). The energies of the stationary points along the *syn*-CH₃CHOO, *syn*-CD₃CHOO, and *syn*-CD₃CDOO reaction coordinates are equivalent aside from ZPE corrections. The ZPE for the deuterated species are evaluated at the CCSD(T)/cc-pVTZ level of theory with anharmonic B2PLYPD3/cc-pVTZ zero point energy corrections.

The microcanonical rate constant $k(E)$ at a given energy E is given by (9):

$$k(E) = \frac{\sigma_{eff} G^\ddagger(E - E_0)}{\sigma_{eff}^\ddagger h N(E)}$$

Here, E_0 is the TS energy barrier, $G^\ddagger(E - E_0)$ is the sum of states at the TS, $N(E)$ is the density of states of the Criegee intermediate, and h is Planck's constant. The effective symmetry numbers σ_{eff} are 1 for the reactants and 1/2 for the transition states. The methyl torsion is treated as a one-dimensional hindered rotor and all other modes are treated as rigid-rotor harmonic oscillators. The MULTIWELL software package (10) is used to evaluate $k(E)$ for the SCTST calculations.

Master equation modeling of the thermal rate constants including tunneling are well reproduced by modified Arrhenius expressions: $k(T) = 2.76 \times 10^{-73} T^{27.88} \exp(3978/T)$ for *syn*-CH₃CHOO (6), $k(T) = 9.18 \times 10^{-73} T^{28.23} \exp(1870/T)$ for selectively deuterated *syn*-CD₃CHOO, and $k(T) = 7.32 \times 10^{-73} T^{28.28} \exp(1850/T)$ for fully deuterated *syn*-CD₃CDOO. In the absence of tunneling, the thermal rate constants are well fit by an

Arrhenius expression with activation energies equivalent to the computed TS barriers. The thermal decay rates for selectively and fully deuterated Criegee intermediates are nearly indistinguishable from one another under atmospheric conditions.

References

1. Friedrich EC, Falling SN, Lyons DE (1975) A convenient synthesis of ethylidene iodide. *Synth Commun* 5(1):33-36.
2. Anson CE, et al. (1994) Assignments of the infrared and Raman spectra of the $\text{Os}_2(\mu_2\text{-CHCH}_3)$ group of $[(\mu_2\text{-CHCH}_3)\text{Os}_2(\text{CO})_8]$ and of its d^1 and d^4 isotopologs as models for the spectra of such ethylidene groups on metal surfaces. *J Am Chem Soc* 116:3058-3062.
3. Andrés J, Domingo LR, Picher MT, Safont VS (1998) Comparative theoretical study of transition structures, barrier heights, and reaction energies for the intramolecular tautomerization in acetaldehyde/vinyl alcohol and acetaldimine/vinylamine systems. *Int J Quantum Chem* 66:9-24.
4. Fang Y, et al. (2016) Deep tunneling in the unimolecular decay of CH_3CHOO Criegee intermediates to OH radical products. *J Chem Phys* 145:234308.
5. Fang Y, et al. (2016) Communication: Real time observation of unimolecular decay of Criegee intermediates to OH radical products. *J Chem Phys* 144:061102.
6. Liu F, Beames JM, Petit AS, McCoy AB, Lester MI (2014) Infrared-driven unimolecular reaction of CH_3CHOO Criegee intermediates to OH radical products. *Science* 345:1596-1598.

7. Taatjes CA, et al. (2013) Direct measurements of conformer-dependent reactivity of the Criegee intermediate CH₃CHOO. *Science* 340:177-180.
8. Frisch MJ, et al. (2009) *Gaussian 09* (Gaussian, Inc., Wallingford CT).
9. Baer T, Hase WL (1996) *Unimolecular Reaction Dynamics theory and Experiments* (Oxford Univ Press, New York).
10. Barker JR, et al. (2016) MultiWell Program Suite (University of Michigan, Ann Arbor, MI), Version Multiwell-2016) Available at clasp-research.engin.umich.edu/multiwell/. Accessed February 8, 2017.

APPENDIX III

Synthesis of precursors and experimental studies of larger Criegee intermediates
supplementary material

This work is a supplement to Chapter 5 of this thesis. The experimental research and was performed with Prof. Marsha I. Lester in the *Department of Chemistry, University of Pennsylvania*.

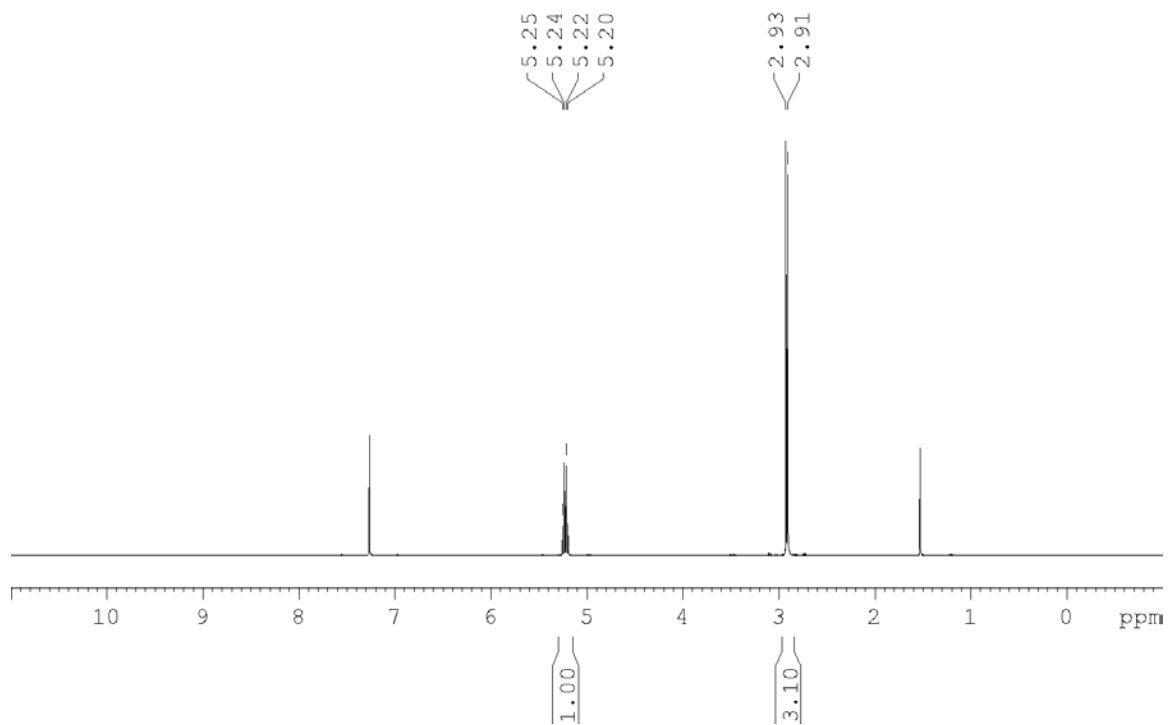


Figure S1. ¹H NMR of CH₃CHCl₂ in CDCl₃: δ 2.9 (d, 3H), 5.2 (q, 1H).

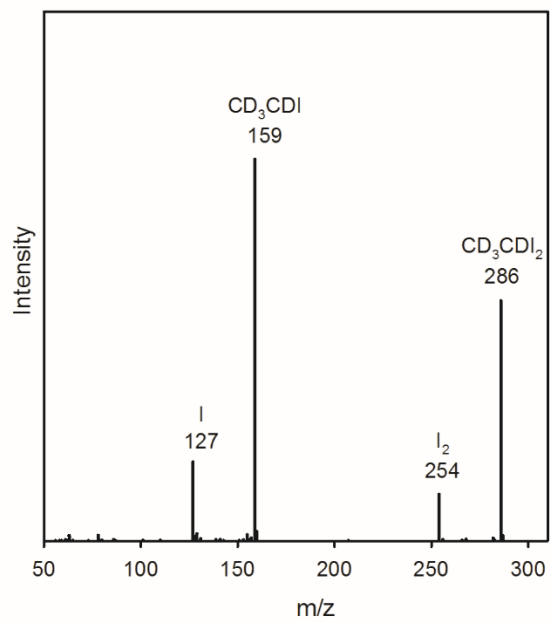


Figure S2. GC-MS (EI) of CD₃CDI₂.

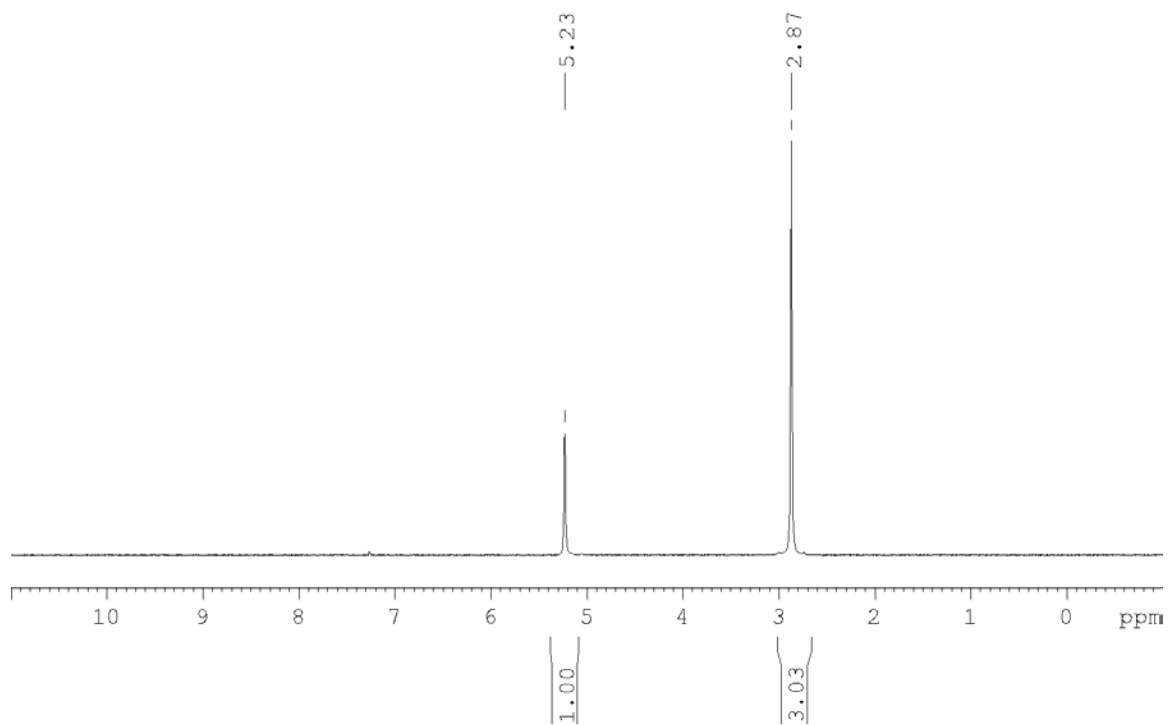


Figure S3. ^2H NMR of CD_3CDI_2 in CHCl_3 : δ 2.9 (s, 3D), 5.2 (s, 1D).

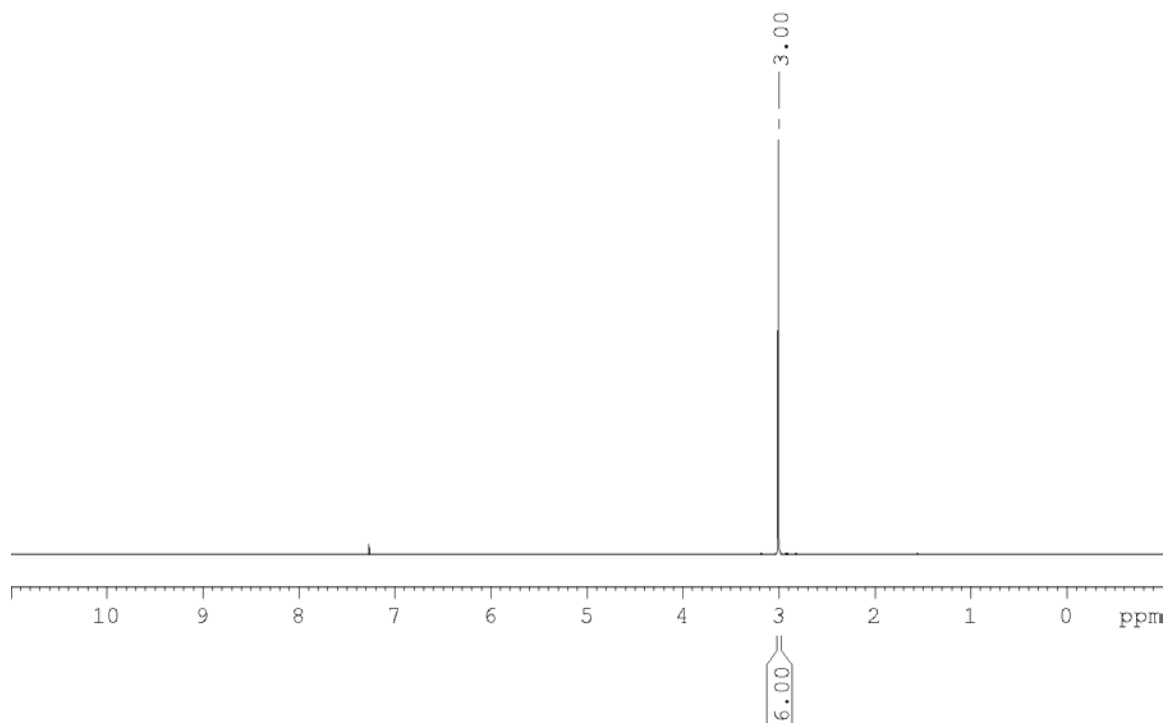


Figure S4. ^1H NMR of $(\text{CH}_3)_2\text{Cl}_2$ in CDCl_3 : δ 3.0 (s, 6H).

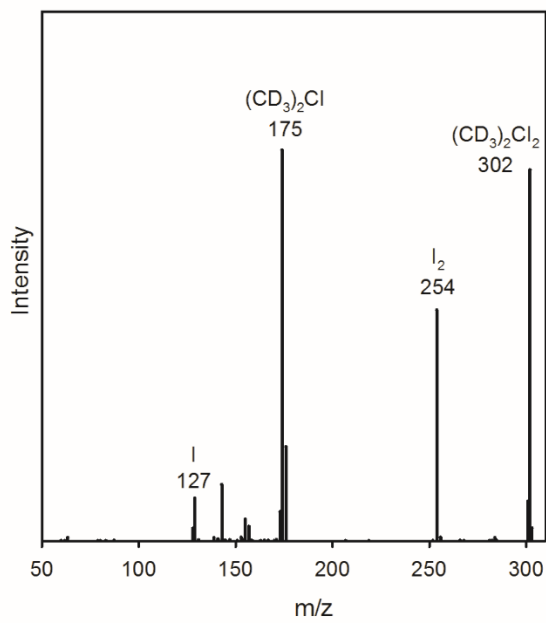


Figure S5. GC-MS (EI) of $(CD_3)_2Cl_2$.

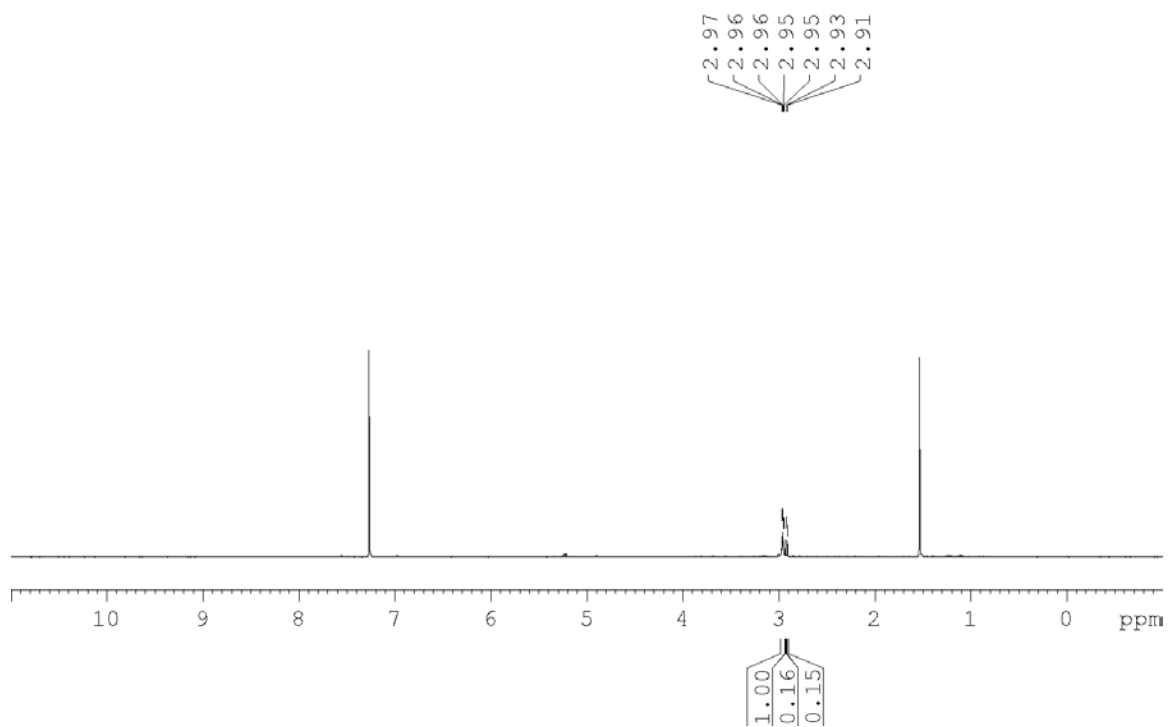


Figure S6. ¹H NMR of (CD₃)₂Cl₂ in CDCl₃. Some intensity at ca. δ 3.0 indicates slight loss of deuteration.

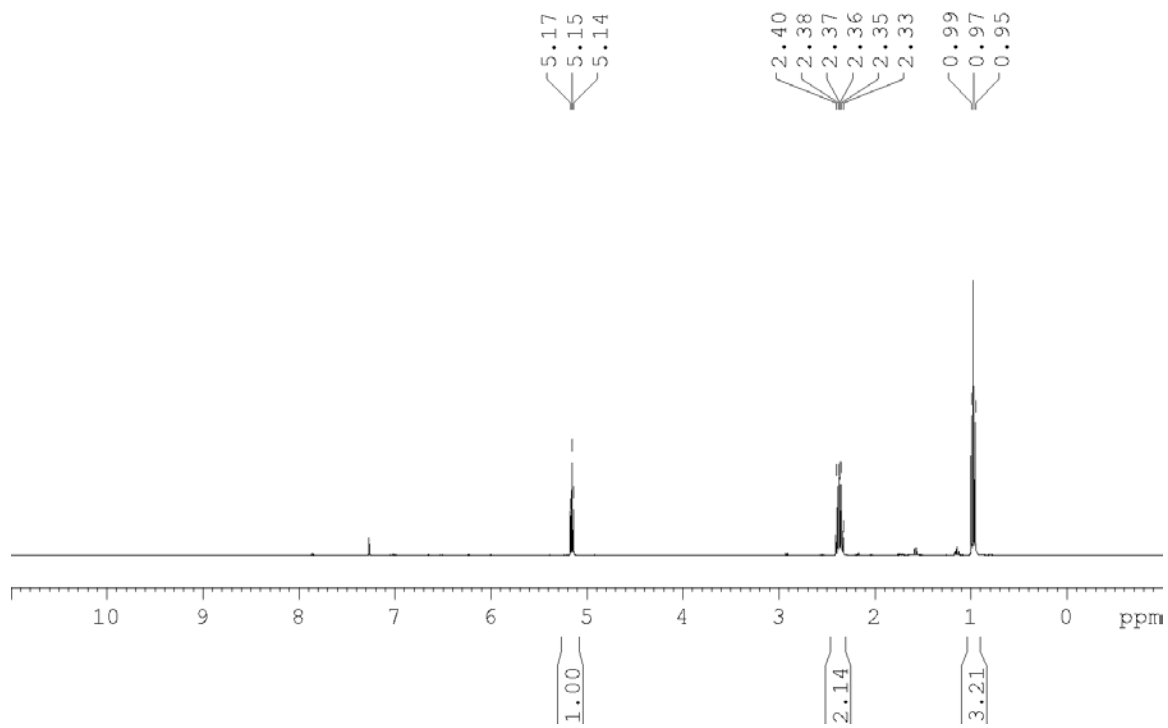


Figure S7. ^1H NMR of $\text{CH}_3\text{CH}_2\text{CHI}_2$ in CDCl_3 : δ 1.0 (t, 3H), 2.4 (m, 2H), 5.1 (t, 1H).

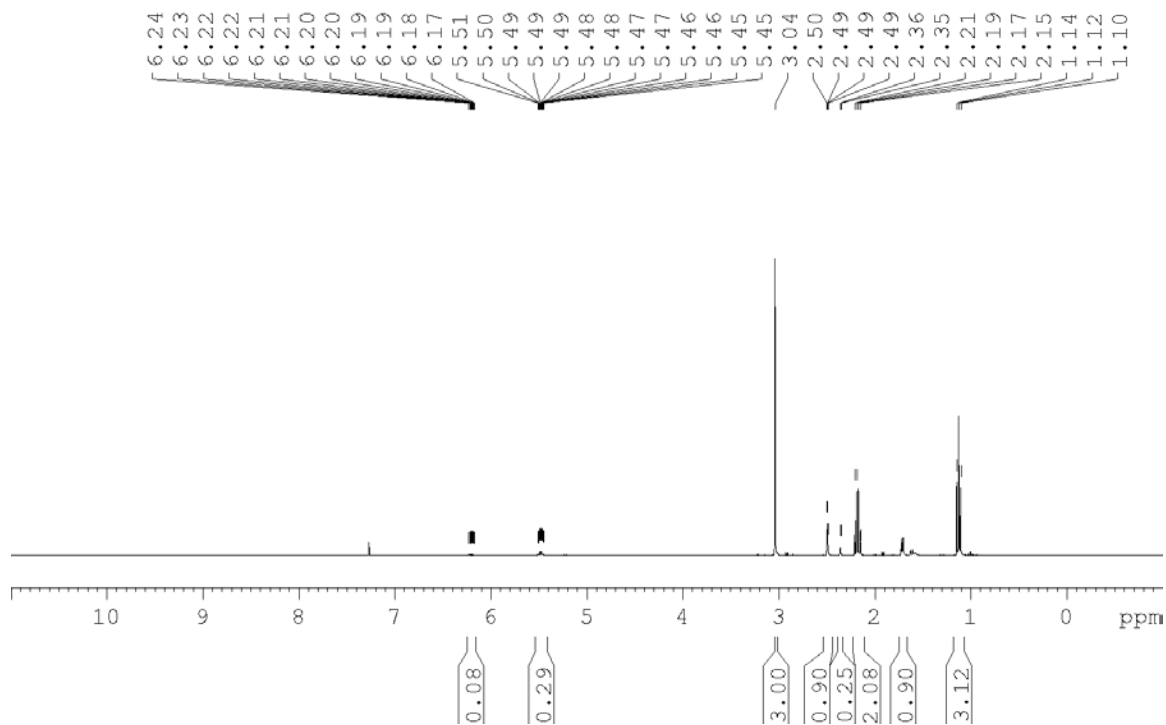


Figure S8. ^1H NMR of $(\text{CH}_3\text{CH}_2)(\text{CH}_3)\text{Cl}_2$ in CDCl_3 : δ 1.1 (t, 3H), 2.2 (q, 2H), 3.0 (s, 3H). The impurities are identified as *cis*-2-iodobut-2-ene that has a signature vinylic H, which appears at δ 6.2 (qq, 1H), and *trans*-iodobut-2-ene, which appears at δ 5.5 (qq, 1H). The relative yields of diiodoalkane precursor $\text{CH}_3\text{CH}_2)(\text{CH}_3)\text{Cl}_2$ (73%) to *cis/trans*-2-iodobut-2-ene (27%) are determined by ^1H NMR.

APPENDIX IV

Observation of an isoprene-derived Criegee intermediate: Methylvinylketone oxide
supplementary material

This work is a supplement to Chapter 6 of this thesis. The experimental research and was performed with Prof. Marsha I. Lester in the *Department of Chemistry, University of Pennsylvania*.

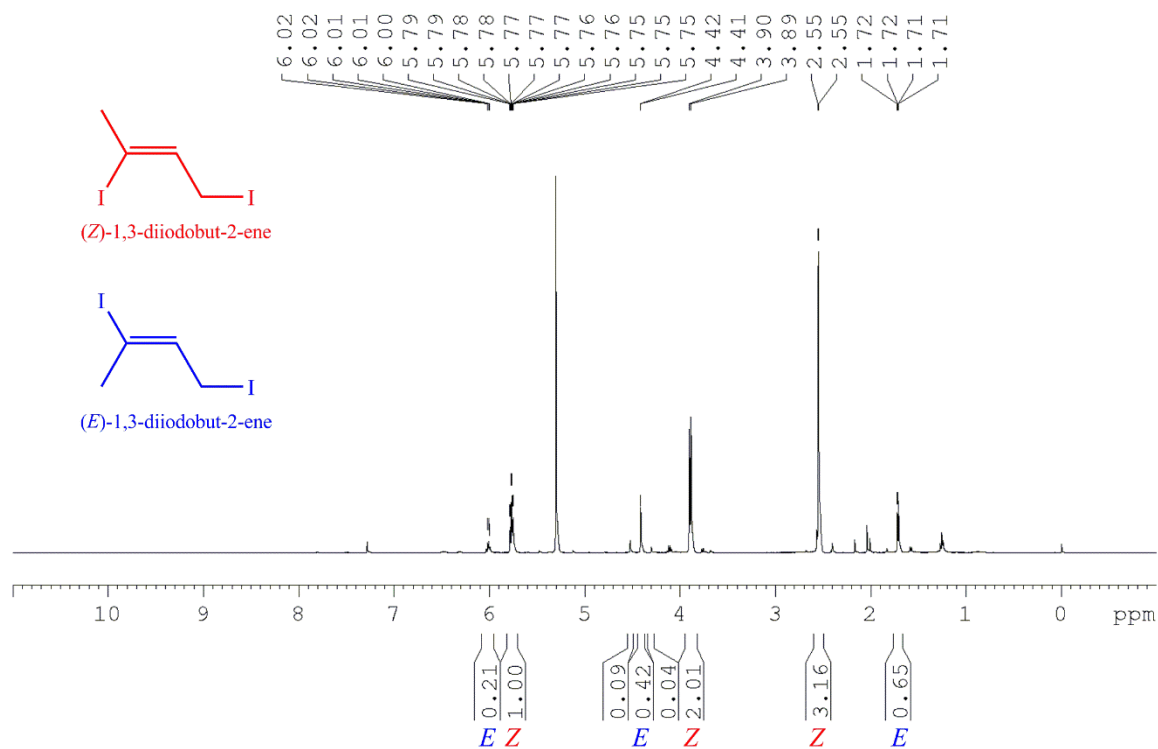


Figure S1. ^1H NMR of (*Z*)-1,3-diiodobut-2-ene (red) and (*E*)-1,3-diiodobut-2-ene mixture (blue): *Z*-1,3-diiodobut-2-ene δ 5.7 (q, 1H), 3.9 (d, 2H), δ 2.5 (d, 3H), *E*-1,3-diiodobut-2-ene δ 6.0 (q, 1H), 4.4 (d, 2H), δ 1.7 (d, 3H). The ~ 5:1 ratio is determined by the normalized integrated intensity of the methine hydrogen of (*Z*)-1,3-diiodobut-2-ene (δ 5.7 ppm, 1H, 1.00 integrated intensity) to the methine hydrogen of (*E*)-1,3-diiodobutene (δ 6.0 ppm, 1H, 0.21 integrated intensity).

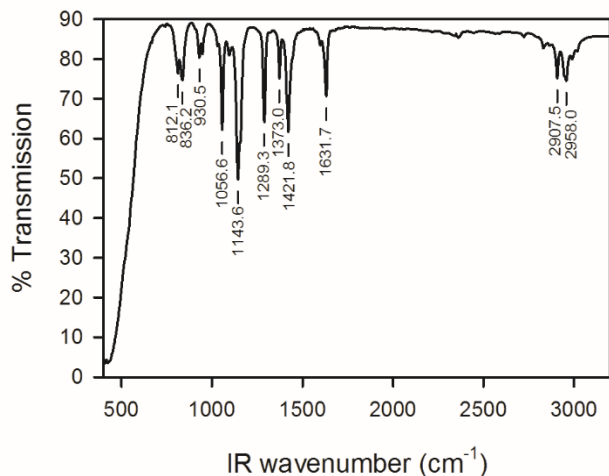


Figure S2. FTIR spectrum of (*Z*)-1,3-diiodobut-2-ene and (*E*)-1,3-diiodobut-2-ene mixture from 400-3200 cm^{-1} . High frequency vibrations at ca. 2900-2960 cm^{-1} are assigned to the methyl CH stretch based on the calculated vibrational frequencies of (*Z/E*)-1,3-diiodobut-2-ene given in Table S1. Several CH scissor and CH wag vibrational modes appear in the 1000-1500 cm^{-1} energy region. The sharp feature at ca. 1630 cm^{-1} is the alkene C=C stretch. The C-I stretches appear at ca. 500 cm^{-1} and are very strong.

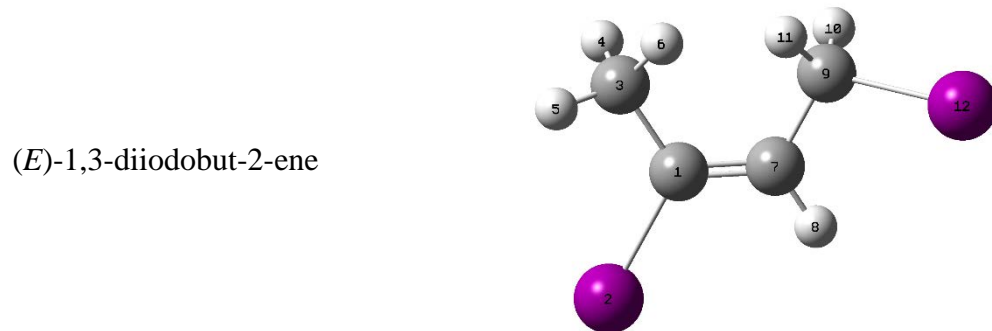
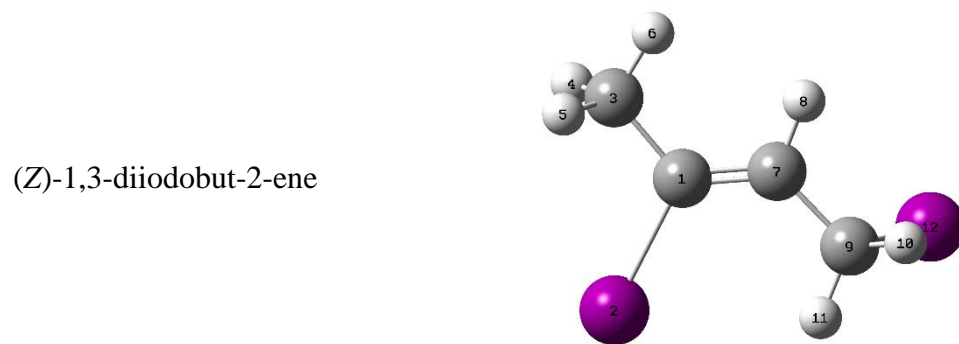


Figure S3. (Z)-1,3-diiodobut-2-ene and (E)-1,3-diiodobut-2-ene precursor geometries with number labeling of atoms.

Table S1. Calculated vibrational modes for (*Z*)-1,3-diiodobut-2-ene and (*E*)-1,3-diiodobut-2-ene at the B3LYP/6-311+G(d,p) level of theory. Both species are C₁ symmetry. Labeling is based on the numbering of atoms in Figure S3.

Mode	Harmonic Frequency (cm ⁻¹)	Description
(Z)-1,3-diiodobut-2-ene		
v ₁	3188.26	Out-of-phase C ₍₉₎ H ₍₁₀₎ H ₍₁₁₎ stretch
v ₂	3122.74	Methine C ₍₇₎ H ₍₈₎ stretch
v ₃	3116.08	In-phase C ₍₉₎ H ₍₁₀₎ H ₍₁₁₎ stretch
v ₄	3098.29	Methyl C ₍₃₎ H ₍₅₎ stretch
v ₅	3086.90	Out-of-phase C ₍₃₎ H ₍₄₎ H ₍₅₎ stretch
v ₆	3025.73	In-phase methyl CH stretch
v ₇	1689.03	Alkene C ₍₁₎ =C ₍₇₎ stretch
v ₈	1488.99	Alkyl C ₍₉₎ H ₍₁₀₎ H ₍₁₁₎ scissor
v ₉	1473.87	Methyl C ₍₃₎ H ₍₄₎ H ₍₅₎ scissor
v ₁₀	1468.68	Methyl C ₍₃₎ H ₍₅₎ wag
v ₁₁	1415.24	Methyl umbrella
v ₁₂	1328.24	Methine C ₍₇₎ H ₍₈₎ wag
v ₁₃	1184.79	Alkyl C ₍₉₎ H ₍₁₁₎ wag
v ₁₄	1183.29	Alkyl C ₍₉₎ H ₍₁₀₎ wag
v ₁₅	1108.01	C ₍₇₎ -C ₍₉₎ stretch
v ₁₆	1073.02	Alkyl C ₍₃₎ H ₍₆₎ wag
v ₁₇	1062.65	Methyl C ₍₃₎ H ₍₄₎ H ₍₅₎ wag
v ₁₈	978.94	C ₍₁₎ -C ₍₃₎ stretch
v ₁₉	866.49	Methine C ₍₇₎ H ₍₈₎ wag
v ₂₀	821.07	Alkyl C ₍₉₎ H ₍₁₀₎ H ₍₁₁₎ wag
v ₂₁	548.83	C ₍₁₎ I ₍₂₎ stretch
v ₂₂	521.17	C ₍₉₎ I ₍₁₂₎ stretch
v ₂₃	426.64	C ₍₃₎ C ₍₁₎ C ₍₇₎ twist
v ₂₄	407.90	C ₍₁₎ C ₍₇₎ C ₍₉₎ bend
v ₂₅	294.73	I ₍₂₎ C ₍₁₎ C ₍₃₎ bend
v ₂₆	262.31	I ₍₂₎ C ₍₁₎ C ₍₇₎ H ₍₄₎ dihedral twist
v ₂₇	195.76	Methyl rotor
v ₂₈	182.31	I ₍₂₎ C ₍₁₎ C ₍₇₎ bend
v ₂₉	96.82	C ₍₇₎ C ₍₉₎ I ₍₁₂₎ wag
v ₃₀	25.53	Alkyl C ₍₉₎ H ₍₁₀₎ H ₍₁₁₎ I ₍₁₂₎ rotor
(E)-1,3-diiodobut-2-ene		
v ₁	3195.77	Out-of-phase C ₍₉₎ H ₍₁₀₎ H ₍₁₁₎ stretch

v ₂	3173.73	Methine C ₍₇₎ H ₍₈₎ stretch
v ₃	3123.31	In-phase C ₍₉₎ H ₍₁₀₎ H ₍₁₁₎ stretch
v ₄	3107.94	Methyl C ₍₃₎ H ₍₅₎ stretch
v ₅	3089.48	Out-of-phase C ₍₃₎ H ₍₄₎ H ₍₅₎ stretch
v ₆	3033.61	In-phase methyl CH stretch
v ₇	1675.57	Alkene C ₍₁₎ =C ₍₇₎ stretch
v ₈	1495.29	Alkyl C ₍₉₎ H ₍₁₀₎ H ₍₁₁₎ scissor
v ₉	1474.18	Methyl C ₍₃₎ H ₍₄₎ H ₍₅₎ scissor
v ₁₀	1470.23	Methyl C ₍₃₎ H ₍₅₎ wag
v ₁₁	1416.57	Methyl umbrella
v ₁₂	1368.71	Methine C ₍₇₎ H ₍₈₎ wag
v ₁₃	1180.37	Alkyl C ₍₉₎ H ₍₁₁₎ wag
v ₁₄	1166.85	Alkyl C ₍₉₎ H ₍₁₀₎ wag
v ₁₅	1081.36	C ₍₇₎ -C ₍₉₎ stretch
v ₁₆	1076.61	Alkyl C ₍₃₎ H ₍₆₎ wag
v ₁₇	1058.83	Methyl C ₍₃₎ H ₍₄₎ H ₍₅₎ wag
v ₁₈	934.47	C ₍₁₎ -C ₍₃₎ stretch
v ₁₉	891.04	Methine C ₍₇₎ H ₍₈₎ wag
v ₂₀	842.88	Alkyl C ₍₉₎ H ₍₁₀₎ H ₍₁₁₎ wag
v ₂₁	613.73	C ₍₁₎ I ₍₂₎ stretch
v ₂₂	505.32	C ₍₉₎ I ₍₁₂₎ stretch
v ₂₃	422.73	C ₍₃₎ C ₍₁₎ C ₍₇₎ twist
v ₂₄	353.35	C ₍₁₎ C ₍₇₎ C ₍₉₎ bend
v ₂₅	293.08	I ₍₂₎ C ₍₁₎ C ₍₃₎ bend
v ₂₆	255.18	I ₍₂₎ C ₍₁₎ C ₍₇₎ H ₍₄₎ dihedral twist
v ₂₇	199.44	I ₍₂₎ C ₍₁₎ C ₍₇₎ bend
v ₂₈	155.86	Methyl rotor
v ₂₉	53.50	C ₍₇₎ C ₍₉₎ I ₍₁₂₎ wag
v ₃₀	47.90	Alkyl C ₍₉₎ H ₍₁₀₎ H ₍₁₁₎ I ₍₁₂₎ rotor
